Exploration du diagramme de phase Fe-Ni-Cr-O en couches minces : de l'analyse microscopique à l'analyse macroscopique

Alban Simonnot

université PARIS-SACLAY

Exploration of the Fe-Ni-Cr-O phase diagram in thin films: from microscopic to macroscopic analysis

Exploration du diagramme de phase Fe-Ni-Cr-O en couches minces : de l'analyse microscopique à l'analyse macroscopique

Thèse de doctorat de l'université Paris-Saclay
École doctorale n°564, Physique en Île-de-France (PIF)
Spécialité de doctorat : Physique
Graduate School : Physique. Référent : Faculté des sciences d'Orsay

Thèse préparée dans l'unité de recherche **Service de recherche en Corrosion et Comportement des Matériaux** (Université Paris-Saclay, CEA) sous la direction de **Jean-Baptiste MOUSSY**, directeur de recherche, et la co-direction de **Alain CHARTIER**, directeur de recherche

Thèse soutenue à Paris-Saclay, le 05 novembre 2024, par

Alban SIMONNOT

Composition du Jury

Membres du jury avec voix délibérative

Yves DUMONT Professeur, Université Versailles Saint-Quentin-en-Yvelines	Président
Pascal THIBAUDEAU Directeur de recherche, CEA/DAM Le Ripault	Rapporteur & Examinateur
Franck VIDAL Professeur, Sorbonne Université	Rapporteur & Examinateur
Aurore FINCO Chargée de recherche CNRS, Université de Montpellier	Examinatrice
Bénédicte WAROT-FONROSE Directrice de recherche CNRS, CEMES-CNRS, Université de Toulouse	Examinatrice

THÈSE DE DOCTORAT
NNT : 2024UPASP143

université PARIS-SACLAY | ÉCOLE DOCTORALE Physique en Île-de-France (PIF)

Titre : Exploration du diagramme de phase Fe-Ni-Cr-O en couches minces : de l'analyse microscopique à l'analyse macroscopique

Mots clés : films minces épitaxiés, spinelles, structure fine, modélisation

Résumé : Les oxydes de fer, nickel et chrome, avec la structure spinelle ou halite, représentent une part importante du système quaternaire Fe-Ni-Cr-O. Ils sont aussi bien présents dans les couches de corrosion des aciers inoxydables que dans des dispositifs de la spintronique. L'objectif de cette thèse est de relier des observations microscopiques comme l'occupation des sites cationiques de la structure spinelle à des grandeurs macroscopiques comme les propriétés magnétiques. Pour cela, des couches minces « modèles » épitaxiées seront synthétisées. Des outils de modélisation de spectres ont permis l'interprétation fine des mesures expérimentales.

La première partie de la thèse est dédié à la structure halite et à la modélisation des phénomènes de paroi de domaine antiferromagnétiques dans l'oxyde de nickel (NiO). Les calculs ont été accomplis à l'aide de la dynamique atomistique de spins (ASD). Ces calculs montrent l'organisation à l'échelle atomique des parois, et les propriétés macroscopiques comme l'épaisseur de paroi et le champ de fuite ont été obtenues. Nos calculs montrent une dépendance de la longueur de paroi avec l'inverse de la racine carrée de la constante d'anisotropie, ce qui permet d'extrapoler les simulations et de les comparer à des mesures expérimentales. Ces comparaisons ont permis une réinterprétation de celles-ci.

La deuxième partie de cette thèse est dédiée à l'étude des oxydes de structure spinelle, à base de fer, nickel et chrome. L'objectif est de relier la structure fine, c'est-à-dire l'ordre cationique dans les sites interstitiels de la structure cristallographique aux propriétés macroscopiques comme le paramètre de maille ou le comportement magnétique. Pour cela, des films minces cristallins de type $Fe_{\alpha}Ni_{\beta}Cr_{\gamma}O_4$ ont été synthétisés par épitaxie par jets moléculaires assistée par un plasma d'oxygène atomique. Une étude approfondie des propriétés structurales, chimiques et magnétiques des échantillons a été effectuée. L'utilisation de techniques avancées, comme l'absorption X, le dichroïsme magnétique circulaire ou la diffraction résonnante, associées à des calculs de multiplets, a permis d'extraire le degré d'oxydation et l'environnement de champ cristallin des différents cations. Les résultats montrent (*i*) que le chrome est exclusivement en position octaédrique (O_h), au degré d'oxydation III, (*ii*) que le nickel est aussi principalement en position O_h, au degré d'oxydation II, à l'exception des échantillons les plus riches en chrome, dans lesquels on observe des cations Ni^{2+} en site tétraédrique (T_d) et (*iii*) que les cations de fer sont à la fois au degré d'oxydation II et III, dans les sites O_h et T_d. Cette répartition cationique a été utilisée dans un modèle permettant de connaître le paramètre de maille théorique et les angles entre les sites cationiques. Ces calculs ont été comparés avec les paramètres magnétiques (champ coercitif, aimantation). Les échantillons possédant les moins bonnes propriétés magnétiques sont aussi ceux ayant les angles entre sites cationiques les plus éloignés des angles favorisant les interactions d'échange magnétique.

Title : Exploration of the Fe-Ni-Cr-O phase diagram in thin films: from microscopic to macroscopic analysis

Keywords : epitaxial thin film, spinel, fine structure, modeling

Abstract : Iron-nickel-chromium oxides, in the structure spinel or halite, are an important part of the Fe-Ni-Cr-O quaternary system. They are present in the corrosion layers of stainless steels as well as in spintronic devices. The aim of this thesis is to link microscopic observations such as the occupation of cationic sites in the spinel structure to macroscopic quantities such as magnetic properties. To this end, epitaxial model thin films will be synthesized. The use of theoretical models has enabled fine interpretation of experimental measurements.

The first part of the thesis is dedicated to the halite structure and to the modeling of antiferromagnetic domain wall phenomena in nickel oxide (NiO). The simulations were performed using atomistic spin dynamics. These simulations allow to obtain the atomic-scale organization of the walls, and macroscopic properties such as wall width and stray field. Our simulations show a dependence of the wall width on the inverse of the square root of the anisotropy constant, enabling the simulations to be extrapolated and compared with experiment. These comparisons enable experimental measurements to be reinterpreted.

The second part of this thesis is dedicated to the study of oxides with spinel structure, composed of iron, nickel and chromium. The aim is to link fine structure, *i.e.* cationic order in interstitial sites of the crystallographic structure, to macroscopic properties such as lattice parameter or magnetic behavior. Spinel $Fe_{\alpha}Ni_{\beta}Cr_{\gamma}O_4$ thin films were synthesized by atomic oxygen plasma-assisted molecular beam epitaxy. An in-depth study of the structural, chemical and magnetic properties of the samples was carried out. Advanced techniques such as X-ray absorption, circular magnetic dichroism and resonant diffraction, combined with multiplet calculations, have made it possible to extract the oxidation state and crystal field environment of the various cations. The results show (*i*) that chromium is exclusively in the octahedral position (O_h), oxidation state III, (*ii*) that nickel is also mainly in the O_h position, oxidation state II, with the exception of the more enriched chromium samples, in which some Ni^{2+} in the tetrahedral site (T_d) was observed, and (*iii*) that iron cations are in both oxidation states II and III, in the Oh and Td sites. This cationic distribution was used in a model to derive the theoretical lattice parameter and angles between cationic sites. These calculations are then compared with the magnetic parameters. The samples with the lowest magnetic parameters are also those with the angles between cationic sites furthest from the angles favoring magnetic exchange.

Membre de l'équipe encadrante

Frédéric MISERQUE Chargé de recherche, CEA Saclay

A ma Claire, toute ma gratitude et mon amour.

Acknowlegments

I would like to express my sincerest gratitude to the members of my jury committee: Pr. Yves Dumont, president, Dr. Pascal Thibaudeau and Pr. Franck Vidal as reporters and Dr. Aurore Finco, Dr. Benedicte Warot-Finrose as examiners for taking the time to read this thesis and to participate in the thesis defence.

I would like to extend my gratitude to all colleagues, friends and family members who contributed to this project.

I would like to express my sincerest gratitude to all those who have supervised me throughout this process, in particular my PhD director Jean-Baptiste Moussy and my supervisors Alain Chartier and Frédéric Miserque. I have benefited considerably from the opportunity to engage in discussion with my colleagues, and I am grateful for the insights I have gained from each of them. I would like to express my gratitude to Jean-Baptiste for his patience and willingness to respond to my questions concerning the synthesis. The samples, which have been subjected to exhaustive analysis, are also a little bit his. I would like to express my gratitude to Alain for his assistance and for engaging in discussions about theoretical methods. It was consistently resfreshing, joyful and encouraging. I would also like to express my gratitude to Frédéric for our numerous discussions on the subject of spectroscopy and for his patience, both during the synchrotron runs and in the writing of this thesis.

I would also like to thank all the collaborators that I have worked with during my thesis:

- Dr Alina Vlad and Dr Antoine Barbier for our fruitful collaboration at the SiXS beamline, Synchrotron Soleil.
- Dr. Patrick Schick, Dr. Edwige Otero for our colloboration at the Deimos beamline, Synchrotron Soleil.
- Dr. Pamela Pinho, for the XMCD experiments performed at ESRF and our discussions during the synchrotron runs.

During my PhD years, I was hosted by two different institutions of the CEA Paris-Saclay: *Laboratoire Nano-Magnétisme et Oxydes* (SPEC/LNO) and *Laboratoire de Modélisation, de Thermodynamique et de Thermochimie* (SCCME/LM2T). I would like to thank once again all my colleagues, my fellow PhD student, in particular Eloi de Villoutrey, with whom I have the happiness to share my office. Special thanks to Dr. Sylvie Chatain and Dr. Cyrille Barreteau for being part of my thesis counselling. Finally I want to thank the 'MBE team': Dr. Helene Magnan, Dr.

Antoine Barbier and Frédéric Merlet for their help and encouragement, despite the many machine breakdowns.

Finally, I would like to thanks my family, and my wife Claire. Without her, I would not be here today.

Articles and communications

Article:

A. Simonnot, F. Miserque, J-B. Moussy, J-Y. Chauleau, M. Viret and A. Chartier, Atomic scale structure of Domain Walls in NiO (*in progress*)

Communications:

A. Simonnot, F. Miserque, J-B. Moussy, J-Y. Chauleau, M. Viret and A. Chartier, Atomic scale simulations of Domain Walls in NiO, *European Conference Physics of Magnetism 2023*, Poznan, June 26-30, 2023

A. Simonnot, F. Miserque, J-B. Moussy, J-Y. Chauleau, M. Viret and A. Chartier, Atomic scale structure of Domain Walls in NiO, *Colloque Louis Néel*, Sète, November 13-16, 2023

Poster:

A. Simonnot, F. Miserque, A. Chartier and J-B. Moussy, Nickel and Chromium Substitution in $Fe_{3-x-y}Ni_yCr_xO_4$ Epitaxial Thin Films, *Colloque Louis Néel*, Sète, November 13-16, 2023

Contents

List of figures viii

List of tables xvii

Acronyms xx

Résumé de la thèse en français xxi

1 Introduction: The Fe-Ni-Cr-O system 1

1.1 The Fe-Ni-Cr-O quaternary system 2

1.2 Structure, research fields and spintronics applications of NiO 4

1.2.1 Crystallographic and magnetic structure 4

1.2.2 Research fields of NiO 5

1.2.3 Antiferromagnetic materials applications in spintronics 5

1.3 Structure, physicochemical properties, corrosion context and spintronics applications of the spinel phase of Fe-Ni-Cr-O quaternary system 7

1.3.1 Crystallographic structure 7

1.3.2 Magnetic structures within the spinel structure 9

1.3.3 Physicochemical properties of particular compounds in the spinel area of the quaternary Fe-Ni-Cr-O 11

1.3.4 Binaries between the end members of the spinel area 13

1.3.5 Spinel phase of the Fe-Ni-Cr-O system in different domains 23

1.3.6 Spinel phases containing Fe, Ni and Cr in spintronics context 23

1.3.7 Spinel phases containing Fe, Ni and Cr in corrosion context 24

1.4 Objectives and organization of the manuscript 26

1.5 Bibliography 27

2 Atomic scale structure of Domain Walls in NiO 39

2.1 Magnetic structure of NiO 40

2.2 Methods for domain wall simulation 42

2.2.1 Heisenberg Hamiltonian 42

2.2.2 Super-exchange and anisotropy constants determination 44

2.2.3 Description of domain walls 46

2.2.4 Construction of domain walls 48

2.2.5 Symmetry considerations 51

2.3 Techniques for domain wall analysis 52

2.3.1 Stereographic projection ... 52
2.3.2 XMLD-PEEM ... 54
2.3.3 Nitrogen Vacancy Magnetometry ... 56
2.4 Atomic structure of Domain Wall in NiO ... 58
2.4.1 Rotation of atomic spins throughout S domain walls ... 58
2.4.2 Rotation of atomic spins throughout T domain walls ... 60
2.4.3 Geometrical requirement of the splitting zone ... 62
2.5 Physical properties of domain wall in NiO ... 64
2.5.1 Simulated domain walls vs stray fields ... 64
2.5.2 Widths of domain walls from XMLD-PEEM ... 66
2.5.3 Extrapolation of simulated domain walls ... 69
2.5.4 Comparison of simulated domain walls with experiment ... 70
2.6 Conclusions ... 72
2.7 Bibliography ... 74

3 Experimental techniques and simulation methods ... 77

3.1 Epitaxial growth by Oxygen-Assisted Molecular Beam Epitaxy ... 78
3.2 Structural characterization of thin films ... 82
3.2.1 Reflection High Energy Electron Diffraction ... 82
3.2.2 X-ray methods and thin film specifications ... 84
3.2.3 X-ray Reflectivity of thin films ... 86
3.2.4 X-ray Diffraction of thin films ... 87
3.3 Chemical characterization of thin films ... 90
3.3.1 Theoretical considerations ... 90
3.3.2 Quantification of the stoichiometry of the thin films ... 92
3.4 Fine structure characterization of thin films ... 94
3.4.1 X-ray Absorption Spectroscopy and X-Ray magnetic circular dichroism ... 94
3.4.2 Resonant X-ray diffraction ... 97
3.5 Simulation of XMCD and RXD spectra ... 100
3.5.1 Quanty simulation of XMCD spectra ... 100
3.5.2 FDMNES simulations of RXD spectra ... 102
3.6 Magnetic characterization of thin films ... 104
3.7 Bibliography ... 107

4 Crystalline growth, structure and magnetic properties of spinel thin films ... 110

4.1 OA-MBE growth of spinel thin films 111
4.1.1 Substrates choice and preparation 111
4.1.2 Exploratory strategies in a quaternary system 112
4.1.3 Epitaxial growth of $Fe_{\alpha}Ni_{\beta}Cr_{\gamma}O_4$ spinel thin films 112
4.2 Monitoring the film growth with RHEED measurements 114
4.2.1 RHEED images of the substrates 114
4.2.2 Evolution of the RHEED images during growth 116
4.2.3 In-plane lattice parameter determination 118
4.3 Chemical composition determination 120
4.3.1 Quantification challenges for $Fe_{\alpha}Ni_{\beta}Cr_{\gamma}O_4$ thin films 120
4.3.2 Chemical composition deduced from XPS 121
4.3.3 Evolution in the XPS spectra according to the stoichiometry 123
4.4 Structural investigations of spinel thin films 127
4.4.1 Sample thickness investigations with XRR 127
4.4.2 Lattice parameters and crystalline quality analysis via XRD 129
4.5 Magnetic investigation 135
4.6 Conclusions 141
4.7 Bibliography 142

5 Fine structure investigation 144

5.1 X-ray magnetic circular dichroism fine structure investigation 145
5.1.1 Experimental conditions 145
5.1.2 Theoretical curves calculations with Quanty 146
5.1.3 Considerations on the fitting of XMCD spectra 148
5.1.4 Chromium $L_{2,3}$ edges XMCD spectra 150
5.1.5 Nickel $L_{2,3}$ edges XMCD spectra 151
5.1.6 Iron $L_{2,3}$ edges XMCD spectra 152
5.1.7 Trends in specific series 156
5.1.8 Theoretical model for species distribution 156
5.1.9 Low temperatures XMCD spectra 158
5.1.10 XMCD Hysteresis loops 163
5.2 Resonant X-ray diffraction fine structure investigation 165
5.2.1 Exploitation of RXD to obtain the fine structure 165
5.2.2 SiXS indexation of the reciprocal space and implications 166
5.2.3 Data analysis 168

5.2.4 Understanding parameters with FDMNES simulations 171
5.2.5 Comparisons of RXD data with FDMNES simulations 172
5.2.6 Cationic distribution with (531) signal features 177
5.2.7 Comparison between RXD and XMCD regarding the cationic distribution 179
5.3 Conclusions 180
5.3.1 Conclusions on the XMCD experiment 180
5.3.2 Conclusions on the RXD experiment 181
5.4 Bibliography 182
6 **Relations between the fine structure and crystallography or magnetic behavior**. 183
6.1 Fine structure relation with crystallographic structure 184
6.1.1 Model of theoretical lattice parameter 184
6.1.2 Application to $Fe_{\alpha}Ni_{\beta}Cr_{\gamma}O_4$ spinel thin films 186
6.1.3 Cationic distribution with lattice parameter 190
6.2 Correlations between the lattice parameter and the cationic ordering of the spinel thin films 192
6.2.1 Isoconcentrations in chromium: $Fe_{\alpha}Ni_{\beta}Cr_{\gamma}O_4$ with γ fixed 192
6.2.2 Isoconcentrations in nickel: $Fe_{\alpha}Ni_{\beta}Cr_{\gamma}O_4$ with β fixed 197
6.2.3 Conclusions on the relation between the fine structure and the cationic ordering 203
6.3 Correlations between cationic ordering and magnetic properties 205
6.3.1 Angle calculation 205
6.3.2 Link between magnetic properties and calculated angles 207
6.3.3 Magnetic properties variation for chromium enriched samples 209
6.3.4 Magnetic properties variation for low chromium content sample 210
6.3.5 Conclusions on the relation between fine structure and magnetic properties 211
6.4 Bibliography 212
7 **Conclusions and Perspectives** 214
7.1 Bibliography 220

Liste of Figures

Chapter 1: Introduction: The Fe-Ni-Cr-O system

Figure 1.1: Quaternary representation of the Fe-Ni-Cr-O system. 2

Figure 1.2: Crystallographic structure of NiO. The green circles represent Ni atoms, while the red ones depict oxygen anions. 4

Figure 1.3: Schematic illustration of a solar cell proposed by Ukoba et al.[25] 5

Figure 1.4: Unit cell of a spinel structure. The T_d sites are highlighted in orange, while the O_h sites are depicted in gray. 8

Figure 1.5: Schematic illustration of the magnetic exchange interaction in Fe_3O_4. The orange color represents the T_d sites, while the green color depicts the O_h sites. Due to crystal field effect, the 3d orbitals of the O_h sites are split into the triply degenerate low-energy t2g states and doubly degenerated high-energy eg states, whereas the T_d site cations exhibit two low-energy e states and three high-energy t2 states. Extracted from Pinho[62]. 10

Figure 1.6: Schematic illustration of the different binaries system in the quaternary diagram. 13

Figure 1.7: Evolution of the lattice parameter as a function of the Cr doping. The gray crosses present the variations in bulk samples, while the red crosses depict the variations for thin films. Adapted from Pinho[52]. 14

Figure 1.8: Temperature phase diagram of $Fe_\alpha Cr_{3-\alpha}O_4$. Figure adapted from Ma et al.[83] 15

Figure 1.9: Evolution of the lattice parameter in $Fe_{3-\beta}Ni_\beta O_4$ from different works for nanoparticles (NPs) and thin films (TFs). 17

Figure 1.10: Evolution of the percentages of spinel phase (a) and eskolaite phase (b) depending of α in $Ni_{1-\alpha}Fe_\alpha Cr_2O_4$. Adapted from Gilabert et al.[101] 18

Figure 1.11: Comparison of the lattice parameter evolution with the prediction of Vegard's law (ideal solid solution between $NiCr_2O_4$ and $FeCr_2O_4$). 19

Figure 1.12: Lattice parameter as a function of the Cr content (γ) in $NiCr_2O_4$-$NiFe_2O_4$ binary system from Ziemniak[86], Allen[103], Hosterman[104], Lee[106], Jahan[107] and Rais[105] 20

Figure 1.13: Evolution of the Curie temperature as a function of the Cr content (γ). from Lee[106], Jahan[107] and Rais[105]. The red triangle represent the T_C of $NiCr_2O_4$ (80 K). 21

Figure 1.14: Measured solvus in the $Ni(Fe_{1-n}Cr_n)_2O_4$ (2n = γ) spinel binary: EDX

(Energy-Dispersive X-ray, open circles) and EMPA (Electron MicroProbe Analysis, filled circles). Arrows show solvus based on observed cation distributions between octahedral and tetrahedral sites at room temperature. Extracted from Ziemniak et al.[86] 22

Figure 1.15: a) TEM cross-section picture of the corrosion layer observed on an A690 alloy (Ni – 10 % Fe – 30 % Cr in weight) in primary environment. b) Magnified HRTEM picture on the alloy-spinel interface. c) Schematic illustration of the different phases observed. Adapted from Marchetti[127]. 25

Chapter 2: Atomic scale struture of Domain Walls in NiO

Figure 2.1: a) T directions in a cubic lattice. b) In the case of T [111] domain, the T and S directions are indicated. 41

Figure 2.2: Schematic illustration of the super-exchange constants. The green circles represent the Ni atoms, while the red one depict O atoms. The blue planes depict the T1 planes ([111]) and the yellow arrows represent the magnetostriction linked to T1. 43

Figure 2.3: Normalized staggered magnetization M_S (T) function of the temperature, calculated using the Heisenberg Hamiltonian (see Equation (2.1)) with J_2= - 26 meV. 46

Figure 2.4: Schematic illustration of the two possible orientations of a magnetic transition wall for T1 (blue plane) to T4 (green plane). The transparent black planes represent (100) and (011) planes. 47

Figure 2.5: Schematic illustration of the DW construction. The top figure represents the construction of S walls, while the two bottom figures depict the construction of $T_{(100)}$ and $T_{(110)}$ DW, respectively. 50

Figure 2.6: Schematic illustration of one stereographic projection in the T1 plane. The distinct S direction are indicated by orange arrows, while the (100) plane is illustrated in grey. 52

Figure 2.7: Stereographic projection for $T_{(100)}$ (a) and $T_{(110)}$ (b) walls 54

Figure 2.8: XMLD-PEEM contrast variation in function of ω, angle between the surface normal and the incoming polarized light. Adapted from Arai et al.[30] 55

Figure 2.9: Illustration of the simulated NVM setup. 57

Figure 2.10: a) Schematic representation of a S 60° DW. b) Schematic representation of a S 120° DW. The T1 planes are depicted in cyan, and the red and blue arrows represent the atomic structure of the DW, which is the transparent black plane. 58

Figure 2.11: Stereographic projection of spins for S 60° (a) and for S 120° (b). 6

KuT = J_2 is employed in both simulations. 59

Figure 2.12: Stereographic projection of spins. Figures (a) and (b) correspond, respectively, to $T_{(100)}$ DW (T1S1-T4S3) and to $T_{(110)}$ DW (T1S2-T2S2), which are both viewed from the (111) surface. The anisotropy constant is set at 10 KuT = J2. The remaining symbols are identical to those depicted in Figure 2.11. 60

Figure 2.13: Schematic illustration of the geometrical requirement of the splitting zone. 62

Figure 2.14: Schematic representation of the splitting zone. 63

Figure 2.15: Spin projections (upper panel), and stray field (bottom panel) for S 60° DW (T1S3-T1S2) (a) and S 120° DW (T1S3-T1S2) (b), seen from the (1 1 1) surface and plotted as a function of their positions (nm) in the simulation cell with 6 KuT = J_2. Normalized intensities of spin projections $I_{L,R}$ are reported for u_{T1S3} (blue line) and u_{T1S2} (orange line) directions. The rectangular function Π (green line) indicates the width δ (nm). The stray field intensity is shown (red line - quoted Norm in μT) with its B_x, B_y, and B_z components (respectively, blue, orange, and green lines). 64

Figure 2.16: First panels illustrate spin projections, second panels present the deviation angle from the optimal AF alignment of spins (quoted splitting, in degrees), and lower panels show the stray field. Figures (a) and (b) pertain, respectively, to $T_{(100)}$ DW (T1S1-T4S3) and to $T_{(110)}$ DW (T1S2-T2S2), which are both viewed from the (111) surface. The anisotropy constant is set at 10 KuT = J2. The deviation angles are shown as gray crosses. They are fitted using a Lorentzian function for which the FHWM is reported. The remaining symbols are identical to those depicted in Figure 2.15. 65

Figure 2.17: Evolution of the widths (in nm) of S60° and S120°, $T_{(100)}$ and $T_{(110)}$ DWs as a function of KuT calculated from spins projections. The super-exchange constants were maintained at a fixed value. 70

Figure 2.18: Widths (in nm) of DWs measured by Arai[30] using XMLD-PEEM images (histogram in black) and fitting (green lines) using one Gaussian function for S120° DW (a) and two Gaussian functions (blue and red lines) for each T DW ($T_{(011)}$ for (b) and $T_{(001)}$ for (c)). 71

Chapter 3: Experimentals techniques and simulation methods

Figure 3.1: Schematic illustration of the AO-MBE apparatus. Adapted from Vila-Fungueiriño et al.[4]. 78

Figure 3.2: The OA-MBE setup developed in CEA-SPEC. 79

Figure 3.3: Schematic illustration of RHEED patterns for different surface

morphologies. The first column depicts a schematic illustration of the growing layer, the second illustrates the expected RHEED pattern and the third column presents one experimental example. 83

Figure 3.4: Schematic illustration of the various angles employed in a thin film diffractometer, from Harrington et al.[7] 85

Figure 3.5: Effect of roughness variation (a), density variation (b), and thickness variation (c) on the resulting signal in XRR. 87

Figure 3.6: XPS Fe-2p core levels spectra for different reference iron oxides[15]. ..91

Figure 3.7: Schematic illustration of a XMCD experiment. The left circular X-rays probe spin-up electrons, while the right circular X-rays probe spin-down electrons. 96

Figure 3.8: Energy variation of the two terms of the anomalous scattering in the case of iron, in multiple of scattering of one electron ($2.82e^{-15}$ m) 98

Figure 3.9: Energy level diagram illustrating the 3d orbitals splitting for an O_h anionic arrangement and a T_d anionic arrangement. Energy between orbitals is given in terms of crystal field parameters. 101

Figure 3.10: Hysteresis loop of a spinel sample before (a) and after (b) the subtraction of the linear diamagnetic contribution (which is indicated in orange) and normalization. 105

Chapter 4: Crystalline growth, structure and magnetic properties of spinel thin films

Figure 4.1: RHEED patterns of an $MgAl_2O_4$ (001) (or MAO) substrate. A schematic illustration of the reciprocal space with the two crystallographic directions of observation is shown. 114

Figure 4.2: RHEED patterns of MAO (111) and α-Al_2O_3 (0001) substrates. The black and orange arrows refer, respectively, to α-Al_2O_3 and MAO orientation of the reciprocal space. The green and blue arrows refers to [110] and [112] directions, with a reorientation of the reciprocal space of 30° between the sapphire and the MAO structures. 115

Figure 4.3: RHEED patterns recording during the growth of a spinel sample on MAO (001) (up) and MA0 (111) (down). 116

Figure 4.4: RHEED patterns recorded during the growth of the spinel sample 19 on α-Al_2O_3 (0001). 117

Figure 4.5 Evolution of the in-plane interreticular distance in the two RHEED directions. 119

Figure 4.6: Fe 2p core levels spectra obtained with a Al Kα X-ray source. The blue curve represents a spectrum without iron ($NiCr_2O_4$), while the orange curve depicts a sample with iron. 120

Figure 4.7: XPS 3p core levels spectrum on a spinel oxide layer recorded with a X-ray Al Kα source. 121

Figure 4.8: Chemical composition of thin films obtained by XPS measurements represented in a quaternary phase diagram. The red squares represent the $Fe_{3-\gamma}Cr_\gamma O_4$ samples synthesized in a previous PhD. work[9] 123

Figure 4.9: Normalized and Shirley background subtracted XPS Fe 2p core levels spectra for $Ni_\beta Fe_{3-\beta}O_4$ thin film series. 123

Figure 4.10: Normalized and Shirley background subtracted XPS Fe 2p core levels spectra for $Fe_{2.60-\gamma}Ni_{0.40}Cr_\gamma O_4$ (left) and $Fe_{2.20-\beta}Ni_\beta Cr_{0.80}O_4$ (right) series. 124

Figure 4.11: Normalized and Shirley subtracted background XPS Ni 2p core levels spectra for $Ni_\beta Fe_{3-\beta}O_4$ series (left) and zoom on the $2p_{3/2}$ peak for samples for $Fe_{2-\gamma}Ni_1Cr_\gamma O_4$ series (right). 125

Figure 4.12: Normalized and Shirley subtracted XPS Cr 2p core levels spectra. 126

Figure 4.13: X-ray reflectivity curves for different samples. The experimental curves are represented by the blue lines, while the fitted curves are depicted by the orange curves. 127

Figure 4.14: X-ray diffraction in out-of-plane configuration for the sample $Fe_{1.44}Ni_{0.45}Cr_{1.11}O_4$. The blue curve represents the XRD data. In inset: the rocking curve for the (222) peak. 129

Figure 4.15: Out-of-plane lattice parameters in hexagonal convention (in Å) indicated in the quaternary diagram. 131

Figure 4.16: Comparison between the XRR thickness and the Scherrer thickness. The blue crosses represent the different samples. 131

Figure 4.17: In-plane XRD measurement (H00 scan) for the sample $Fe_{1.20}Ni_{0.24}Cr_{1.56}O_4$. The blue curve represents the XRD data, and the orange curve depicts the Gaussian fit. 132

Figure 4.18: In-plane lattice parameter in hexagonal convention (in Å) indicated in the quaternary diagram. 133

Figure 4.19: Magnetic hysteresis loops obtained at three temperatures for $Fe_{2.07}Ni_{0.39}Cr_{0.54}O_4$. 135

Figure 4.20: M_S at 10 K (a), 100 K (b) and 300 K (c) for each sample composition. 137

Figure 4.21: M_R at 10 K (a), 100 K (b) and 300 K (c) for each sample composition.

..... 138

Figure 4.22: H_C at 10 K (a), 100 K (b) and 300 K (c) for each sample composition. 139

Figure 4.23: a) Hysteresis loops at T= 300 K for $NiCr_2O_4$ (001) and (111) samples. b) Hysteresis loops at 300 K, 100 K and 10 K for (111) sample. 140

Chapter 5: Fine structure investigation

Figure 5.1: Calculated XMCD spectra of chromium (a), iron (b), and nickel (c) species with parameters described in Table 5.2. 148

Figure 5.2: Fe L_3 edge XMCD spectrum of $Fe_{1.44}Ni_{0.45}Cr_{1.11}O_4$ sample at 300 K, adjusted manually. The color curve are identical to the Figure 5.1. 149

Figure 5.3: XMCD spectra at the chromium $L_{2,3}$ edges, at T = 300 K, for low-to-medium chromium content (a) and high chromium content (b). 150

Figure 5.4: XMCD spectra at the nickel $L_{2,3}$ edges, at T = 300 K, for low-to-medium chromium content (a) and high chromium content (b). 151

Figure 5.5: XMCD Ni L_3 edge fit for $Fe_{1.20}Ni_{0.24}Cr_{1.56}O_4$ at 300 K. 152

Figure 5.6: Iron L_3 edge XMCD spectra at T = 300 K for selected samples..... 152

Figure 5.7: Quaternary plot of the occupancy (in absolute value) of all iron species. The results concerning $FeTd3+$, $FeTd2+$, $FeOh3+$, and $FeOh2+$ are illustrated in a), b), c) and d), respectively. 155

Figure 5.8: Fitted XMCD iron L_3 edge spectra at T = 300 K with constraints. The sample has $Fe_{1.80}Ni_{0.69}Cr_{0.51}O_4$ stoichiometry. 157

Figure 5.9: Quaternary plot of δ, the inversion parameter..... 158

Figure 5.10: Comparison of normalized Cr $L_{2,3}$ edges XMCD spectra at T = 300 K and low temperatures (T = 4 K or 107 K). The normalization is done by the maximum for (a) and (b), and by the minimum for (c) and (d). 159

Figure 5.11: Comparison of normalized XMCD spectra at 300 K and low temperatures at the Ni $L_{2,3}$ edges. 160

Figure 5.12 Comparison of normalized Fe $L_{2,3}$ edges XMCD spectra at 300 K and low temperature (T = 4 K or 20 K). 161

Figure 5.13 Magnetic XMCD hysteresis loops of different samples for each species at T = 300 K. 163

Figure 5.14: Three-dimensional representation of the (622) peak at the Ni K edge for the $Fe_{1.71}Ni_{0.57}Cr_{0.72}O_4$ sample. 169

Figure 5.15: Cartography (ω, E) of a RXD experiment. 169

Figure 5.16: Example of background (bk) removal for data of Figure 5.14..... 170

Figure 5.17: Simulated RXD signal as a function of the aggregate radius (a) and as a function of the in-plane lattice parameter (b). The aggregate radius is R = 5.0 Å for (b)..... 171

Figure 5.18: Simulated RXD signal at the iron K edge for the (622) peak (a) and the (531) peak (b) as a function of the cationic site of iron..... 172

Figure 5.19: Raw data obtained for RXD signals at the Ni K edge of $Fe_{1.71}Ni_{0.57}Cr_{0.72}O_4$ (a) and the resulting treatment (b)..... 173

Figure 5.20: Normalized experimental and simulated RXD signals at the Ni K edge for the $Fe_{1.71}Ni_{0.57}Cr_{0.72}O_4$ sample..... 174

Figure 5.21: Normalized experimental and simulated RXD signals at the Fe K edge for the $Fe_{1.71}Ni_{0.57}Cr_{0.72}O_4$ sample. The diffraction peaks (440), (311), (531), and (511) are represented in (a), (b), (c), and (d), respectively. 175

Figure 5.22: Normalized RXD signal at the Fe K edge and comparison with FDMNES calculations for the $Fe_{2.43}Ni_{0.21}Cr_{0.36}O_4$ sample. 176

Figure 5.23: Normalized RXD signal at the Fe K edge and comparison with FDMNES calculations for the $Fe_{1.44}Ni_{0.45}Cr_{1.11}O_4$ sample 176

Figure 5.24: Variations of the normalized (531) signal for different cationic repartition. The curves presented in a) and b) have been divided by their minimums, while the curves presented in c) and d) have been divided by their maximums..... 178

Chapter 6: Relations between the fine structure and crystallography or magnetic behavior

Figure 6.1: Theoretical lattice parameter (c_{th}) compared to the experimental lattice parameter (c_{exp}) for the different samples. 186

Figure 6.2: Theoretical lattice parameter compared to the experimental lattice parameter, in the revised model..... 188

Figure 6.3: Anion parameter u" obtained through r_{Oh} in function of u', obtained through r_{Td}. The crosses represent the different parts, which can be read on the left. The red circles represent the inversion parameter..... 189

Figure 6.4: Average anion parameter (u_{avg}) as a function of the inversion parameter (δ). The black line is a linear fit without the points at δ = 1..... 189

Figure 6.5: u_{avg} for the revised model is represented in the quaternary plot..... 190

Figure 6.6: Schematic illustration of several isolines in the quaternary system. 192

Figure 6.7: Isolines of chromium concentration. 192

Figure 6.8: Lattice parameter variations as a function of β in the series $Fe_{3-\beta-\gamma}Ni_{\beta}Cr_{\gamma}O_4$ 193

Figure 6.9: Lattice parameter evolution as a function of β in the Fe_3O_4-$NiFe_2O_4$ binary system extracted from [5–9]. 193

Figure 6.10: Variations of the lattice parameter with the mean cationic radius in $Fe_{3-\beta}Ni_{\beta}Cr_0O_4$. The lattice parameter (red curve) is indicated at the left, the mean cationic radius at the right. r_{Td} is shifted by +0.2 Å. 194

Figure 6.11: Variations of the lattice parameter with the mean cationic radius in $Fe_{2.5-\beta}Ni_{\beta}Cr_{0.5}O_4$. The lattice parameter (pink curve) is indicated at the left, the mean cationic radius at the right. r_{Td} is shifted by +0.2 Å. 195

Figure 6.12: Variations of the lattice parameter with the mean cationic radius in $Fe_{1.96-y}Ni_yCr_{1.04}O_4$. The lattice parameter (purple curve) is indicated at the left, the mean cationic radius at the right. r_{Td} is shifted by +0.2 Å. 196

Figure 6.13: Isolines of nickel concentration. 197

Figure 6.14: Lattice parameter variations function of γ in $Fe_{3-\beta-\gamma}Ni_{\beta}Cr_{\gamma}O_4$. 198

Figure 6.15: Evolution of the lattice parameter as a function of the Cr doping. The red crosses present the bulk variations, while the gray crosses depict the thin film variations. Adapted from Pinho[12]. 199

Figure 6.16: Variations of the lattice parameter with the mean cationic radius in $Fe_{3.0-\gamma}Ni_0Cr_{\gamma}O_4$. The lattice parameter (red curve) is indicated at the left, the mean cationic radius at the right. r_{Td} is shifted by +0.2 Å. 199

Figure 6.17: Variations of the lattice parameter with the mean cationic radius in $Fe_{2.75-\gamma}Ni_{0.25}Cr_{\gamma}O_4$ (a) and in $Fe_{2.60-\gamma}Ni_{0.40}Cr_{\gamma}O_4$ (b). The lattice parameter (cyan and pink curves) is indicated at the left, the mean cationic radius at the right. r_{Td} is shifted by +0.2 Å. 200

Figure 6.18: Evolution of the lattice parameter as a function of the chromium content in the $Fe_{2.0-\gamma}Ni_{1.0}Cr_{\gamma}O_4$ series in this work and coming from different authors. 201

Figure 6.19: Variations of the lattice parameter with the mean cationic radius in $Fe_{2.05-\gamma}Ni_{0.95}Cr_{\gamma}O_4$. The lattice parameter (purple curve) is indicated at the left, the occupancies at the right. r_{Td} is shifted by +0.15 Å. 202

Figure 6.20: Most favorable bond angles for effective magnetic interactions and super-exchanges mechanisms. Extracted from Yan et al.[22] 205

Figure 6.21: Various angles presented in the quaternary diagram. θ_1 (a), θ_3 (b), and θ_5 (c) correspond to the angle between O_h and T_d sites, O_h and O_h sites and T_d

and T_d sites, respectively. 207

Figure 6.22: M_S variations at T = 300 K as a function of u_{avg} (a), θ_1 (b), θ_3 (c), and θ_5 (d). 208

Figure 6.23: M_R (a) and H_C (b) variations at 300 K as a function of u_{avg}. 208

Figure 6.24: Separation in two zone of magnetic properties variations. 209

Figure 6.25: Variations of M_S (a) and H_C (b) as a function of the chromium content and variations of M_R (c) and (d) as a function of the chromium and nickel content respectively. 210

Figure 6.26: Variations of M_S (a), M_R (b), and H_C (c) as a function of the $FeOh2+$ content. 211

Liste of Tables

Chapter 2: Atomic scale struture of Domain Walls in NiO

Table 2.1: Summary of the twelve magnetic domains in NiO. The contraction axis (T direction, the FM planes alternating directions) and the S domain (easy axis direction for atomic spins) are highlighted. The three S directions are all at 90° with respect to the contraction axis. 41

Table 2.2: Theoretical and experimental J_1 and J_2 (in meV). The employed technique is presented in first column, while the J_1 and J_2 are depicted in the final two columns. 44

Table 2.3: Summary of simulated DWs with the main parameters indicated. 49

Table 2.4: Summary of the observed symmetry between the different T-S domains for $T_{(100)}$ and $T_{(110)}$ DWs. 51

Table 2.5: Mechanisms of spin rotations for S domain walls. The first column present the two TS domains imposed at the right and at the left of the simulation lox. The second column depict the rotation mechanism. 59

Table 2.6: Mechanism of spin rotations for T domain walls. The T DWs are classified according to the symmetry considerations of the Table 2.4. The mechanism are divided into two groups. The first group undergoes a total 120° rotation, whereas the other group undergoes an overall 180° rotation. 61

Table 2.7: Widths of S DWs and T DWs, calculated from atomic spins projections for different domains and for two different surfaces. The column with $\mathrm{KuT} = 0.005$ meV reports the widths obtained by extrapolating the simulations (± 10 %). The experimental values are extracted from the work of Arai et al.[30] (see text for details). The behaviors of spins are determined from stereographic projections (see Table 2.5 and Table 2.6). * denotes values obtained by projections. 67

Chapter 4: Crystalline growth, structure and magnetic properties of spinel thin films

Table 4.1: Summary of the growth conditions of samples selected in this thesis manuscript. 113

Table 4.2: Composition of studied $Fe_{\alpha}Ni_{\beta}Cr_{\gamma}O_4$ samples. 122

Table 4.3: Structural information extracted from XRR. * and ** indicate MAO (001) and MAO (111) substrate. For *, the Scherrer thickness (S) is indicated. 128

Table 4.4: Summary of the structural information obtained with XRD measurements. * and ** indicate MAO (001) and MAO (111) substrates. 130

Table 4.5: Summary of the in-plane lattice parameter measurements. * and ** indicate MAO (001) and MAO (111) substrates. 133

Table 4.6: Summary of the magnetic parameters for all samples extracted from VSM measurements. M_S, M_R and H_C are noted in $kA.m^{-1}$. * and ** indicate samples grown on MAO (001) and MAO (111) substrates..... 136

Chapter 5: Fine structure investigation

Table 5.1: Experimental conditions for XAS/XMCD acquisitions on spinel oxide layers..... 145

Table 5.2: Parameters used in Quanty simulations. 147

Table 5.3: Information extracted from the nickel L_3 edge XMCD fits..... 151

Table 5.4: Iron cationic distribution and inversion parameter obtained from the iron L_3 edge XMCD fits, at T =300 K. (E) indicates ESRF experiments. * indicates a $NiTd2+$ contribution. 153

Table 5.5: Total occupancy of the two samples exhibiting $NiTd2+$. 154

Table 5.6: Occupancies extracted from the nickel L_3 edge XMCD fits, at T = 300 K and 4K. 160

Table 5.7: Occupancies extracted from the iron L_3 edge XMCD fits, at low temperatures..... 162

Table 5.8: Coercive fields (H_C) at 300 K, in $kA.m^{-1}$, extracted from the XMCD hysteresis loops..... 164

Table 5.9 Peaks of the RXD experiment. The three lattice conventions are indicated..... 167

Table 5.10 Summary of the RXD experiments conducted..... 168

Table 5.11: Cationic repartition used for the FDMNES calculations (in fractional site occupancy). 173

Table 5.12 Summary of the cationic distribution obtained through XMCD and RXD fits. 179

Chapter 6: Relations between the fine structure and crystallography or magnetic behavior

Table 6.1: Effective ionic radius extracted from Shannon[4] for the different species. 184

Table 6.2: Revised model applied on different spinel oxide thin films probed by XMCD. * indicates a $NiTd2+$ contribution..... 187

Table 6.3: Summary of the cationic distribution tested for the two samples not previously examined in XMCD. 191

Table 6.4: Variations of cationic iron species for the different chromium isolines. LP means lattice parameter. 197

Table 6.5: Variations of cationic iron species for the different nickel isolines. .. 202

Table 6.6: Equations for distances and angles displayed in Figure 6.20. 206

Table 6.7: Angles between the different sites for sample studied in XMCD. 206

Acronyms

AF	AntiFerromagnetic
AO-MBE	Assisted Oxygen-plasma Molecular Beam Epitaxy
APB	Anti-Phase Boundary
ASD	Atomistic Spin Dynamics
BE	Binding Energy
CFM	Crystal Fiel Multiplet
EDX	Energy Dispersive X-ray spectroscopy
EELS	Electron Energy-Loss Spectroscopy
EMPA	Electron MicroProbe Analysis
EXAFS	Extended X-ray Absorption Fine Structure
FM	FerroMagnetic
FWHM	Full Width at Half Maximum
GIXD	Grazing Incidence X-ray Diffraction
MAO	$MgAl_2O_4$
PBC	Periodic Boundaries Conditions
PLD	Pulsed Laser Deposition
PPMS	Physical Properties Measurement System
RC	Rocking Curve
RHEED	Reflection High-Energy Electron Diffraction
RXD	Resonant X-ray Diffraction
TEY	Total Electron Yield
TFY	Total Fluorescence Yield
UHV	UltraHigh Vacuum
VSM	Vibrating Sample Magnetometer
XANES	X-ray Absorption Near-Edge Structure
XAS	X-ray Absorption Spectroscopy
XMCD	X-ray Magnetic Circular Dichroism
XPS	X-ray Photoemission Spectroscopy
XRD	X-Ray Diffraction
XRR	X-Ray Reflectivity

Résumé de la thèse en français

Cette thèse est divisée en deux parties distinctes, chacune employant sa propre méthodologie. Cette section présente un rapide résumé des principaux résultats obtenues dans chacune des deux parties.

La première partie de cette thèse est dédiée à l'étude des parois de domaines magnétiques dans le composé antiferromagnétique de l'oxyde de nickel. Cette partie utilise la dynamique atomique de spin.

NiO a été sélectionné car il représente l'un des composes contenant uniquement un métal de transition dans le diagramme de phase quaternaire Fe-Ni-Cr-O. L'oxyde de nickel présente une structure antiferromagnétique complexe (type G). Dans ce type de composé, deux directions sont importantes : les directions [111] (4 possibilités, domaines "T"), qui sont la direction d'alternance antiferromagnétique d'un ensemble de plans (111) ferromagnétiquement alignés dans le plan, et les directions [11$\bar{2}$] (3 possibilités, domaines "S"), qui sont les directions faciles d'aimantation dans les plans (111). Cela donne un total de 12 domaines magnétiques différents.

Pour simuler cette texture magnétique complexe, deux constantes uniaxiales d'anisotropie ont été introduites dans l'Hamiltonien du système. Cela permet la simulation des domaines "T" et "S". La seconde décision pour les simulations a été d'utiliser des valeurs élevées pour les constantes d'anisotropie (de l'ordre de la constante de super échange J_2), dans le but de simuler les parois de domaines magnétiques dans des boites de simulation de taille raisonnable. Avec ces deux décisions prises, les parois S et T ont été simulé avec succès.

En ce qui concerne les parois S, uniquement les parois S 60° et S 120° ont été simulé avec succès, alors que les parois S 180° ont été uniquement obtenues comme interférences parasites dans les autres simulations. A l'échelle atomique, la structure de ces parois révèle une rotation à 60° ou à 120° du vecteur antiferromagnétique. Les propriétés physiques de ces parois S ont aussi été obtenues, grâce à des simulations de pseudo XMLD-PEEM et de NVM. Le pseudo XMLD-PEEM montre un comportement symétrique des deux côtés de la paroi de domaine, alors que les images simulées de NVM présentent des variations dans la composante x, y ou z du signal, pendant que la norme reste constante à travers la paroi de domaine.

La paroi de domaine T révèle un comportement plus complexe. L'épaisseur de la paroi est le résultat de deux contributions distinctes. La première partie est une rotation du vecteur antiferromagnétique, qui transitionne par la direction

commune aux deux plans T. La deuxième partie, plus intriguant, est l'existence d'une zone de split (schéma Figure 1). Cette zone est une conséquence de la nature antiferromagnétique de NiO. Dans cette zone, les spins atomiques maintiennent leur alignement antiferromagnétique entre plans T, tout en brisant leur alignement ferromagnétique dans chaque plan T. Ce mouvement complexe est géométriquement obligatoire pour passer d'un plan T à l'autre. L'épaisseur de ces parois observes en pseudo XMLD-PEEM montre un comportement asymétrique, lié à la présence de la zone de split. Plus grande est la rotation nécessaire pour atteindre la direction d'arrivée depuis la direction de départ, plus grande est l'épaisseur.

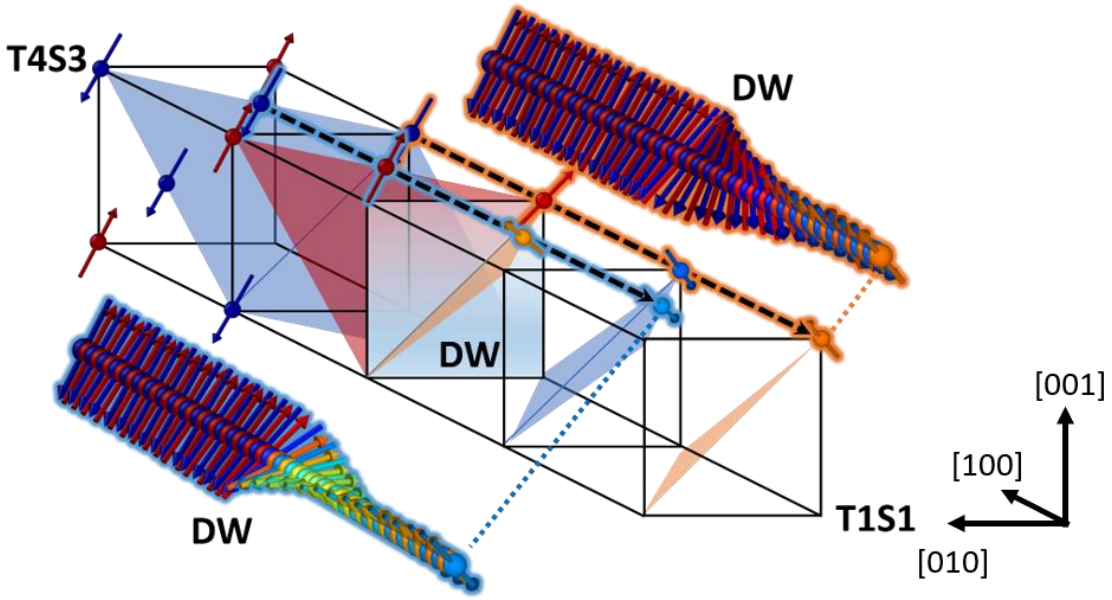

Figure 1: Représentation schématique du mécanisme du split entre deux domaines T.

Ce mécanisme identifié de corrélation entre l'épaisseur et la rotation fournit un critère pertinent de distinction entre parois de domaine T. Cela a permis de séparer les quatre parois de domaines T différents, indépendantes par symétrie, d'être séparée entre un singulet et un triplet. Cette séparation singulet/triplet n'a pas été accomplie dans les expériences de mesures d'épaisseurs entreprises par Arai *et al.*[1]. Les simulations entreprises avec des valeurs décroissantes de K_u^T, de J_2 à 1/10 de J_2, indiquent une dépendance linéaire entre l'épaisseur de la paroi de domaine et la racine de $1/K_u^T$.

L'ajustement de cette dépendance en fonction du singulet ou du triplet a permis une nouvelle interprétation des épaisseurs expérimentales, avec une distinction faite dans les distributions mesurées par Arai *et al.*[1] grâce à la séparation singulet/triplet.

L'étude NVM menée révèle un signal fort d'environ 20 µT, sur la surface (111). Ce signal est exclusivement observé quand le domaine T est aligné avec la surface d'observation. Le signal diminue rapidement après le passage de la paroi de domaine.

Quelques perspectives ouvertes par ce travail peuvent être discutées. Une version customisée du code de simulation Vampire[2–4] a été utilisée pour étudier un composé avec deux constantes d'anisotropie. De la même manière, d'autres systèmes antiferromagnétiques ayant deux constant d'anisotropie peuvent être simulé, comme CoO ou MnO. Ces systèmes sont intéressants pour des applications en spintronique, même si leur température de Néel (T_N) est en dessous de 300 K. Un autre système antiferromagnétique intéressant pour la spintronique est Cr_2O_3. Plusieurs équipes ont tentées d'augmenter la T_N grâce à de l'ingénierie de la contrainte[5]. Le code Vampire pourrait être utilisé pour étudier la structure antiferromagnétique et les différents paramètres influençant l'épaisseur des parois de domaine dans ces systèmes. Des structures plus complexes peuvent être simulées dans l'oxyde de nickel comme un croisement entre une paroi $T_{(100)}$ et une paroi $T_{(110)}$. Dans d'autres codes de simulation, l'ajout de la dynamique de spin avec la dynamique atomique peut ouvrir la possibilité de simuler la formation des parois de domaine, par exemple dans la couche d'oxydes se formant sur un alliage de nickel.

La deuxième partie de cette thèse est dédiée à la croissance cristalline de couches minces dans le système quaternaire Fe-Ni-Cr-O et les relations entre la structure fine (la position des cations dans la maille) et les propriétés cristallographiques ou magnétiques.

Dans le chapitre 4, il est montré qu'il est possible de faire croitre des couches minces épitaxiées de composition $Fe_\alpha Ni_\beta Cr_\gamma O_4$ et d'orientation (111) sur α-Al_2O_3 (0001) pour différentes compositions en α, β, γ. Pour des compositions très riches en chrome (γ), l'utilisation d'un substrat de type spinelle ($MgAl_2O_4$ avec les orientations (001) ou (111)) a été nécessaire pour élaborer des oxydes de structure spinelle. La composition en α, β ou γ a été contrôlée précisément par l'utilisation de cellules à effusion individuelles dans un appareil d'épitaxie par jets moléculaires assistée par plasma d'oxygène (AO-MBE). Les images de diffraction des électrons de hautes énergies (RHEED), eneregistré en temps réel, montre une excellente épitaxie des couches d'oxydes, avec un mode de croissance 2D et une faible rugosité. Ces analyses sont confirmées par la reflectometrie des rayons X (XRR). La composition chimique de chaque échantillon a été sondé rigoureusement en utilisant la spectrocopie de photoémission des rayons X (XPS). Le centre et le bas de la zone spinelle a été exploré, tandis que la zone en-haut à gauche (zone autour de $NiCr_2O_4$, avec un faible contenu en fer) et la zone en-haut

à droite (zone autour de $NiFe_2O_4$, faible contenu en chrome) sont plus difficiles à explorer. Une analyse rigoureuse par diffraction des rayons X (XRD) a permis de montrer l'excellente qualité cristalline des couches et de déterminer les relations d'épitaxie entre les substrats sélectionnés et la struture spinelle, et les paramètres de maille en fonction de la stoichiométrie (Figure 2).

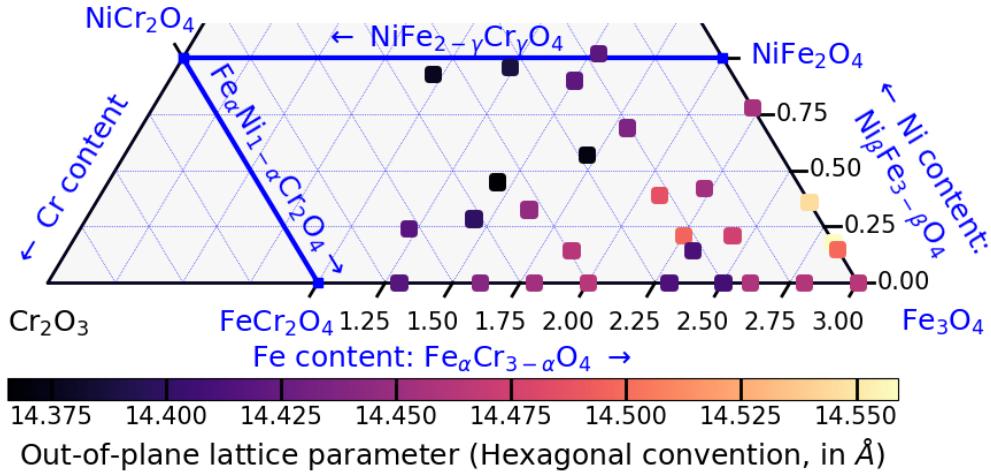

Figure 2 : Paramètre de maille en dehors du plan en convention hexagonale (en Å) indiqués dans le diagramme quaternaire.

Dans le chapitre 5, la distribution dans les sites cationiques dans les différents échantillons $Fe_\alpha Ni_\beta Cr_\gamma O_4$ a été étudiée en utilisant deux techniques basées sur des rayonnements synchrotron : dichroïsme magnétique circulaire des rayons X (XMCD) et diffraction résonante des rayons X (RXD). En XMCD, l'ajustement de chaque transition L_3 de chaque élément (Fe, Ni ou Cr) a été entrepris avec succès en utilisant la contribution théorique de chaque espèce cationique. Le chrome est uniquement Cr^{3+}, dans les sites O_h. Le nickel possède la valence 2+ et est localisé dans les sites O_h, même si pour deux échantillons, la présence de Ni^{2+} dans les sites T_d peut être observe, sans explication claire. En développant l'expérience de RXD (sur la transition K du Ni et du Fe), l'étude de certains pics de diffraction nous a permis de sonder à nouveau la distribution cationique. La simulation de ces spectres a été entreprise à l'aide de FDMNES. Les courbes expérimentales et théoriques sont en bon accord. La distribution cationique pressentie pour les simulations avec FCMNES est donc correcte. Cela signifie aussi qu'il n'y a pas de Ni^{2+} dans les sites T_d, et que le ratio de fer entre les sites T_d et O_h est correct. De plus, ces deux techniques sont en bon accord l'une avec l'autre.

Dans le chapitre 6, la distribution cationique dans les sites obtenue au chapitre 5 a été utilisé dans un modèle reliant la struture fine et le paramètre de maille expérimental. Cela a permis de calculer le paramètre d'anion et le paramètre de maille théorique. Depuis ces deux valeurs, il est également possible d'obtenir les différents angles entre les sites cationiques dans la structure spinelle. Avec ce

modèle et la connaissance du paramètre de maille expérimentale, une première approximation de la distribution cationique peut être établie. Les relations entre le paramètre de maille et la structure fine est étudiée dans deux cas différents : isoconcentrations en nickel et en chrome. Les isoconcentrations en fer comportent trop peu d'échantillons pour en tirer des tendences. Les isoconcentrations en nickel ont révélé des mécanismes intéressants. En effet, à β= 0, trois régions (frontières à 0.5 et à 1.0) ont été identifié. L'augmentation de β a entraîné la fusion progressive de la région II avec la région I pour β = 0,25 et β = 0,40. A β= 1, la région II a disparu et seules deux régions sont observées. En ce qui concerne les isolignes de chrome, à γ = 0, le paramètre de maille présente deux régions (augmentation suivie d'une diminution) avec une limite à β = 0,4. La même tendance a été observée pour γ = 0,5, alors qu'à γ = 1,04, deux régions de paramètres de maille presque identiques sont séparées par une chute du paramètre de maille, passant de la région I à la région II. En ce qui concerne les propriétés magnétiques, deux régions ont été observées. Les échantillons ayant un paramètre de position de l'oxygène, u, proche de la valeur idéale de 0,375 présentent les propriétés magnétiques les plus élevées. Cette valeur idéale de u est liée aux différents angles associés aux interactions de super échange. En diminuant la valeur u, l'interaction de super échange magnétique diminue. Les échantillons à forte teneur en chrome (γ > 0,60) présentent des propriétés magnétiques médiocres en raison des différences entre les angles expérimentaux et les valeurs théoriques idéales. Les paramètres M_S et H_C sont liés à la teneur en chrome tandis que le paramètre M_R semble être lié à la teneur en nickel. Dans les échantillons ayant les meilleures propriétés magnétiques (γ < 0.60), une correlation avec $Fe_{O_h}^{2+}$ a été identifié pour M_S et M_R. Le parameter H_C ne montre pas de correlation claire avec $Fe_{O_h}^{2+}$.

Quelques perspectives de ce travail peuvent être discutées. Concernant la croissance de nouveaux échantillons $Fe_\alpha Ni_\beta Cr_\gamma O_4$, une zone a été peu explorée ($NiCr_2O_4$ avec peu de fer). La sélection d'un substrat avec la structure spinelle a été une bonne décision pour l'élaboration de la sotichiométrie $NiCr_2O_4$ avec la structure spinelle.

Une autre expérience à entreprendre sur ces échantillons, notamment dans le domaine de la corrosion, est la mesure de la résistivité électrique. Un des paramètres clés contrôlant la corrosion est la conductivité électrique de la couche intermédiaire entre l'alliage et l'environnement corrosif. Pour obtenir ces valeurs, des mesures de résistivité en fonction de la température devront être menées dans le futur. La compréhension des liens entre la résistivité et la structure fine pourront être utilisé ultérieurement dans des modèles pour la corrosion.

Bibliographie

(1) Arai, K.; Okuda, T.; Tanaka, A.; Kotsugi, M.; Fukumoto, K.; Ohkochi, T.; Nakamura, T.; Matsushita, T.; Muro, T.; Oura, M.; Senba, Y.; Ohashi, H.; Kakizaki, A.; Mitsumata, C.; Kinoshita, T. Three-Dimensional Spin Orientation in Antiferromagnetic Domain Walls of NiO Studied by x-Ray Magnetic Linear Dichroism Photoemission Electron Microscopy. *Phys. Rev. B* **2012**, *85* (10), 104418. https://doi.org/10.1103/PhysRevB.85.104418.

(2) Evans, R. F. L.; Fan, W. J.; Chureemart, P.; Ostler, T. A.; Ellis, M. O. A.; Chantrell, R. W. Atomistic Spin Model Simulations of Magnetic Nanomaterials. *J. Phys.: Condens. Matter* **2014**, *26* (10), 103202. https://doi.org/10.1088/0953-8984/26/10/103202.

(3) Evans, R. F. L.; Atxitia, U.; Chantrell, R. W. Quantitative Simulation of Temperature-Dependent Magnetization Dynamics and Equilibrium Properties of Elemental Ferromagnets. *Phys. Rev. B* **2015**, *91* (14), 144425. https://doi.org/10.1103/PhysRevB.91.144425.

(4) Jenkins, S.; Chantrell, Roy. W.; Evans, R. F. L. Atomistic Simulations of the Magnetic Properties of Ir x Mn 1 − x Alloys. *Phys. Rev. Materials* **2021**, *5* (3), 034406. https://doi.org/10.1103/PhysRevMaterials.5.034406.

(5) Kota, Y.; Imamura, H.; Sasaki, M. Strain-Induced Néel Temperature Enhancement in Corundum-Type Cr_2O_3 and Fe_2O_3. *Appl. Phys. Express* **2013**, *6* (11), 113007. https://doi.org/10.7567/APEX.6.113007.

1 INTRODUCTION: THE FE-NI-CR-O SYSTEM

This PhD thesis is based on a thorough study of structural and physicochemical properties of the Fe-Ni-Cr-O system in thin films. In particular, the corundum and spinel phases are the subject of an extensive research in the context of corrosion of stainless steels. In addition, these materials have also been identified as potential candidates for spintronics applications due to their intriguing magnetic properties. The following chapter provides an overview of the different crystalline structures which can be found in this quaternary system, including a description of their structural and physical properties and an examination of their potential applications.

1 INTRODUCTION: THE FE-NI-CR-O SYSTEM

1.1 THE FE-NI-CR-O QUATERNARY SYSTEM

The Fe-Ni-Cr-O quaternary system, illustrated in Figure 1.1, comprises a range of materials, which have been extensively studied for potential applications in different research fields such as geology[1–3], metallurgy[4–6], corrosion[7,8], electronics[9], or spintronics[10]. In this Fe-Ni-Cr-O system, solid oxide phases can exhibit multiple crystallographic structures such as the halite, the corundum or the spinel phases. All of these oxides exhibit magnetic properties.

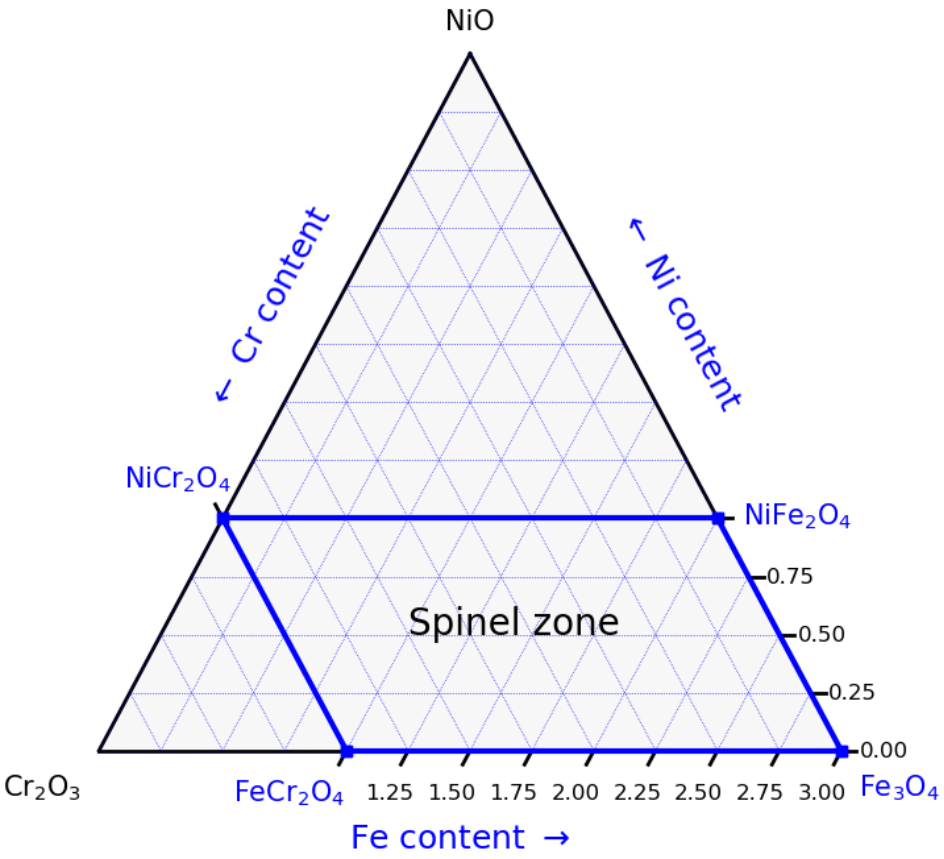

Figure 1.1: Quaternary representation of the Fe-Ni-Cr-O system.

The first crystallographic structure is the halite, like the rocksalt (NaCl) one, composed of divalent cations. The space group is 225, $Fm\bar{3}m$ (according to the International Tables[11]). The two representing components are NiO and FeO. The wüstite (FeO) exhibits a non-stoichiometric rocksalt structure, resulting from the slight oxidation of some Fe^{2+} cations in Fe^{3+} cations, while the NiO phase is stoichiometric. The FeO phase is only stable above 843 K and under conditions of minimal oxygen pressure (pO_2 varying from 10^{-6} to 10^{-25} atm depending of the temperature). At temperature below 843 K, FeO undergoes decomposition, yielding Fe and Fe_3O_4. FeO is antiferromagnetic below 200 K, while NiO have an antiferromagnetic ordering below 523 K as explained in details below.

The corundum phase is composed of trivalent cations, arranged in the example hexagonal α-Al_2O_3-type structure (space group 167, $R\bar{3}c$, according to the International Tables[11]). The two representative materials of this structure are α-Cr_2O_3 and α-Fe_2O_3. A complete binary solution is observed between Fe_2O_3 (hematite) and Cr_2O_3 (eskolaite). These phases are stable under a wide range of temperatures and pressures[12]. The Ni_2O_3 phase can be observed as a result of irradiation of the NiO phase[13]. However, it is more accurately described as a deficient NiO form than as a corundum phase[14]. Cr_2O_3 and Fe_2O_3 can tolerate small to medium amount of Ni in their structure[15,16] (15 % for Fe_2O_3 and 10 % for Cr_2O_3). No binary system exists between Ni_2O_3 and the two corundum structures, as the structures are not identical. Cr_2O_3 and Fe_2O_3 are typical antiferromagnetic materials with Neel temperatures around 307 K and 950 K respectively.

The last crystallographic structure to be discussed is the spinel one. The structure is composed of divalent and trivalent cations, arranged in the $MgAl_2O_4$-type structure (space group 227, $Fd\bar{3}m$, according to the International Tables[11]). This structure is observed in several materials within the Fe-Ni-Cr-O system. These materials include Fe_3O_4, $FeCr_2O_4$, $NiCr_2O_4$, or $NiFe_2O_4$.

The spinel phase ($Fe_\alpha Ni_\beta Cr_\gamma O_4$ with α + β + γ = 3) displays a greater range of variations in the composition because this structure is able to accept divalent and trivalent cations. The oxides previously mentioned: Fe_3O_4, $FeCr_2O_4$, $NiCr_2O_4$, and $NiFe_2O_4$ represent the four corners of the spinel zone labelled in blue in Figure 1.1. It should be noted that the Cr_3O_4 and Ni_3O_4 phases are not observed experimentally. The spinel area does not extend over the top corner and left corner of the ternary NiO-Cr_2O_3-Fe_3O_4 system. In the upward direction, the spinel zone ends at 1.0 of Ni, while in the leftward direction, the spinel zone terminates at 2.0 of chromium. This is due to the fact that chromium forms preferentially trivalent cations, while nickel prefers divalent cations. Iron is able to form both divalent and trivalent cations, which is the reason why Fe_3O_4 (magnetite) is observed in nature.

The present work is focused on two stable oxides phases present in the quaternary Fe-Ni-Cr-O system: NiO and the spinel phase. The objectives of this thesis are distinct. Concerning NiO, the interest is focused on its potential applications in antiferromagnetic spintronics through the description of the magnetic domain walls. Concerning the Fe-Ni-Cr-O system, the fine structure of these spinel phases (*i.e.* the cationic ordering) plays a key role for understanding the physicochemical properties (magnetism and conductivity in the context of nanomagnetism and corrosion). The following sections present an overview of the structural and physicochemical properties of NiO and spinel phases.

1.2 STRUCTURE, RESEARCH FIELDS AND SPINTRONICS APPLICATIONS OF NIO

This section is divided into three distinct parts. The first part presents the crystallographic and complex magnetic structure of NiO. Then, the second part outlines some research fields using the physical properties of NiO. The final part presents more specifically the applications of NiO in the field of antiferromagnetic spintronics.

1.2.1 Crystallographic and magnetic structure

Under standard conditions of pressure and temperature, NiO represents the most stable form of nickel oxide. The crystallographic structure of NiO, illustrated by Figure 1.2, is a rock salt type, belonging to the space group 225 ($Fm\bar{3}m$). The nickel and oxygen ions are arranged alternatively in the three directions of space on a fcc cubic lattice. The conventional unit cell contains four formula units and the lattice parameters are a = b = c = 4.18 Å[17]. The oxygen anions and nickel cations are situated in the *4b* and *4a* Wyckoff positions. The *4a* position encompasses the origin of the cell.

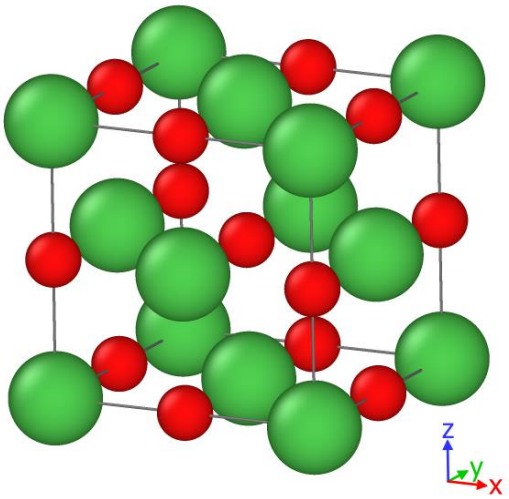

Figure 1.2: Crystallographic structure of NiO. The green circles represent Ni atoms, while the red ones depict oxygen anions.

Below its Néel temperature of 523 K[17], NiO exhibits an antiferromagnetic (AF) structure. The crystallographic structure and the magnetic order are interrelated through the phenomenon of magnetostriction[18,19]. The extensive description of the magnetic order and the magnetostriction phenomenon are detailed in chapter 2.

1.2.2 Research fields on NiO

NiO is employed for its electrical and magnetic properties. Its magnetic properties are detailed are discussed in detail in the next subsection. Its electrical properties, in particular its insulating properties and its good absorption at the surface for organic components make NiO a promising candidate for use in gas sensors[20,21]. Additionally, NiO is utilized in electronics devices, including batteries[22], dielectric devices[23] and thin film transistors[24]. The integration of NiO into sophisticated multilayers structures offers promising applications in solar cells[25], as illustrated in Figure 1.3.

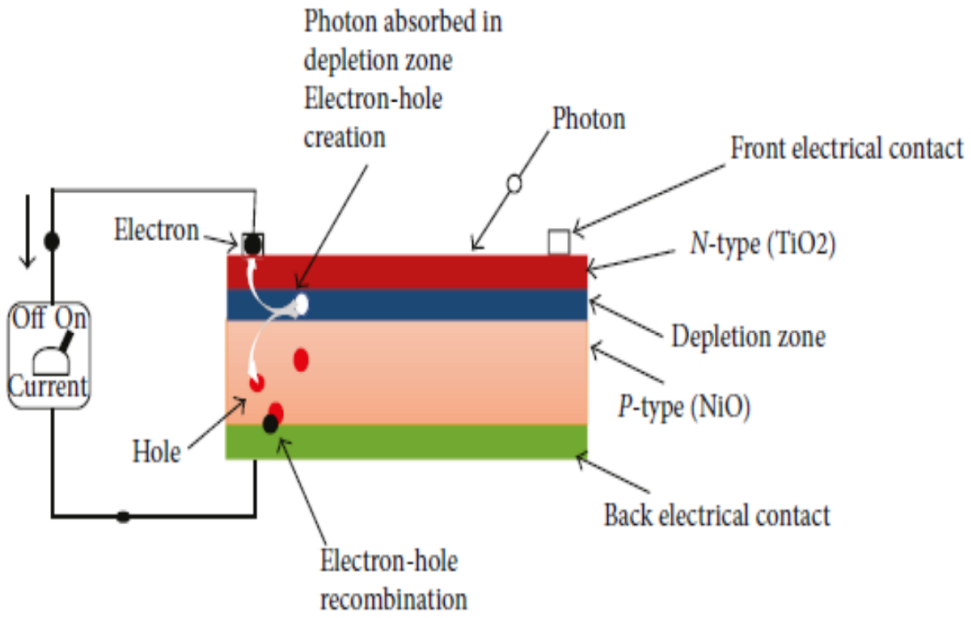

Figure 1.3: Schematic illustration of a solar cell proposed by Ukoba et al.[25]

Additionally, NiO has been observed in the corrosion layers of multiple Ni-based alloys. It is present at the surface of a clean Ni sample immersed in a NaCl solution[26] at ambient temperature. In more challenging conditions (700 °C and sulfuric conditions), NiO is also present[27]. In fused nitrates, the film of NiO is reported to be a barrier against further corrosion[28]. In molten carbonates, the NiO film is observed to include Ni^{3+} cations and accordingly nickel cation vacancies[28].

1.2.3 Antiferromagnetic materials applications in spintronics

The potential applications of AF, and therefore of NiO, materials in spintronics have recently been the subject of considerable interest[29–31]. In comparison to their ferromagnetic (FM) counterparts, they offer three notable advantages.

The first advantage is their immunity to external electromagnetic interference. Their compensated magnetic structure exhibits a better resistance to perturbing magnetic fields, thereby rendering them insensitive to external perturbations. The second advantage of AF materials is their capacity for high-density data storage. Indeed, the magnetic domains in which the information is written do not interact dipolarly between them. The final advantage of these materials is their operational frequency. Indeed, their inherent THz dynamics allows operation in the domain of the picosecond, thereby enhancing performance.

However, several issues remains before their effective utilization in spintronic devices. For instance, the read/write operation has been studied, but for now, no process made the unanimity and it is device dependent[32]. For instance, in FM spin-valves, the exchange coupling between FM and AF layers is used as a mean to write magnetic state in the AF layer. In nickel oxide (NiO), which represents one of the corner of the quaternary system of Fe-Ni-Cr-O, one scheme has been proposed[33], which is the introduction of spin current to flip the S state of the NiO layer. Before proposing read/write operation, the magnetic state must be established.

The stabilization of a single magnetic state is already challenging. In the absence of any driving force, like applying strain[34,35] or magnetic field[36,37], a complex magnetic structure is observed in NiO. Between these spins structures, the transition zone is called Domain Wall (DW). Consequently, spins transport that can reach tens of nanometers in a single domain[38], reveals itself more complex in complex spin structure. At the opposite, DWs can be used as magnetic recording media, by exploiting the DWs movements[39], or the magnetoelastic interactions between them[40].

While DWs are a common feature of NiO, their atomic-scale structure remains poorly documented. They were initially identified through XMLD-PEEM[41], a sophisticated X-ray absorption technique based on synchrotron radiation. Several studies have tried to clarify the DWs structure and behavior in NiO by using different techniques[42–45]. These experiments can be interpreted with macrospin models[46], conventional micromagnetic[47] or atomic spin dynamics[33]. This last method has the advantage to provide a more detailed description, with less assumptions and maintaining a classical description of spins.

A part of this work is dedicated to the analysis of the magnetic ordering in NiO. The complex magnetic structure of NiO leads to the apparition of DWs between two magnetic orientations of the AF vector, which will be the central focus of the chapter 2.

1.3 STRUCTURE, PHYSICOCHEMICAL PROPERTIES, CORROSION CONTEXT AND SPINTRONICS APPLICATIONS OF THE SPINEL PHASE OF FE-NI-CR-O QUATERNARY SYSTEM

This section is divided into three distinct parts. The first part presents the crystallographic and ferrimagnetic structure of the spinel phase. The second part presents a comprehensive review of the literature on specific spinel compounds (Fe_3O_4, $NiFe_2O_4$, $FeCr_2O_4$ and $NiCr_2O_4$) within the quaternary Fe-Ni-Cr-O system. Additionally, it encompasses a detailed examination of the binaries formed between these compounds. The final part provides an overview of the diverse research areas in which these materials are used, with a specific emphasis on their applications in spintronics applications and corrosion studies.

1.3.1 Crystallographic structure

The crystallographic structure of spinel is described by the space group 227, $Fd\bar{3}m$ in the International Tables[11]. The conventional cubic unit cell contains eight formula units, and the overall conventional unit cell contains 32 anions and 24 cations, for a total of 56 atoms (see Figure 1.4). The oxygen anion sublattice forms a pseudo-cubic close packed structure at Wyckoff position *32e*. The metallic cations occupy one-eighth of the tetrahedral interstices (Wyckoff position *8a*) and half of the octahedral interstices (Wyckoff position *16d*). Eight of the cations are situated in tetrahedral sites, while the remaining sixteen are located in octahedral sites. The tetrahedral sites constitute a diamond cubic sublattice with a lattice parameter equal to the lattice parameter of the spinel. Each tetrahedral site is isolated from the others. The octahedron are arranged in lines oriented along the [110] directions. The octahedron are connected by edges along these lines. In the remainder of this thesis, the tetrahedral sites will be referred to as T_d sites, and the octahedral sites will be referenced as O_h sites.

Two possible descriptions of this structure exist in the International Tables[11]. The first description (1) has its origin on a T_d site ($\bar{4}3m$), whereas the second possible description (2) has its origin on a vacancy of an O_h site ($\bar{3}m$)[48]. It is possible to transition between the two descriptions. Whatever the convention utilized, the Wyckoff positions of ions remain identical. For the rest of this manuscript, the $\bar{4}3m$ (1) convention is employed. Figure 1.4 illustrates this convention.

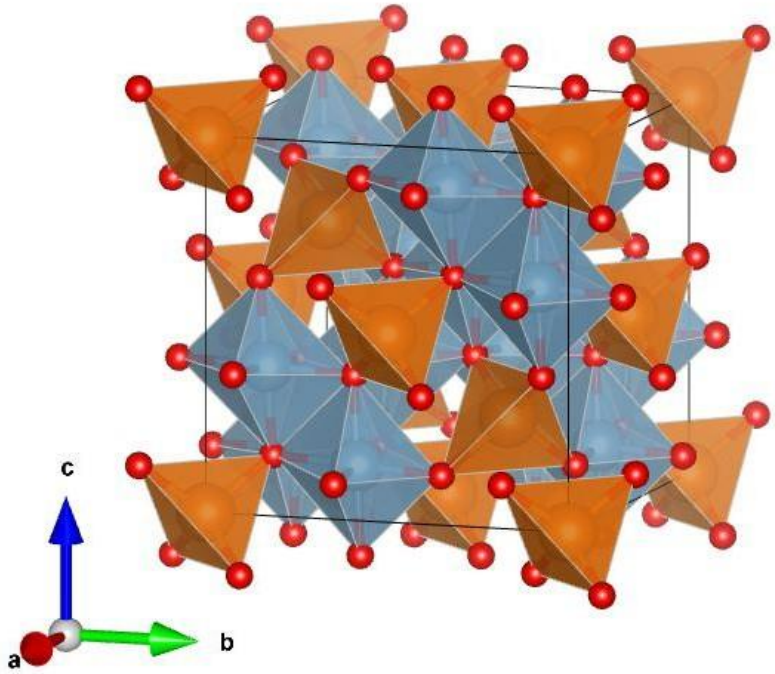

Figure 1.4: Unit cell of a spinel structure. The T_d sites are highlighted in orange, while the O_h sites are depicted in gray.

Two additional parameters are required to fully describe the cubic spinel structure. The first parameter is the anion parameter: u. Indeed, oxygen atoms do not form a cubic close-packed structure. A slight deviation in position of oxygen anions is parametrized by this anion parameter. In the case of a perfect close packed structure, the anion parameter is u = 0.375 in the $\bar{4}3m$ adopted convention. The second parameter is the inversion parameter: δ. Indeed, the cationic distribution is not fixed within the spinel structure. The divalent cations, depending on the chemical species, may exhibit a preference for either O_h or T_d sites. This cationic arrangement is noted with the inversion parameter δ, which varies between 0 and 1. When δ is equal to zero, all divalent cations are placed in T_d sites. This is the normal spinel structure. When δ is equal to one, all the divalent cations are located in O_h sites. This is the inverse spinel structure. The cationic distribution can be summarized as follows (for example $NiCr_2O_4$, a normal spinel with δ = 0): $(Ni^{2+}_{1-\delta=1}Cr^{3+}_{\delta=0})_{Td}[Ni^{2+}_{\delta=0}Cr^{3+}_{2-\delta=2}]_{Oh}O_4$. $()_{Td}$ and $[]_{Oh}$ indicate the composition in T_d and O_h sites, respectively. The 2 in subscript of trivalent Cr cations indicates the presence of two times more O_h sites than T_d sites.

A notable characteristic of spinel phases is their ability to accommodate a significant degree of cationic disorder within the crystallographic structure. In the Fe-Ni-Cr-O system, the accepted cations are divalent (II) and trivalent (III). However, some spinels are able to accept (IV) and (VI) cations, accompanied by two (II) and (I) cations, respectively[48].

In the field of nanometric samples (nanoparticles or thin films), the adopted method of synthesis influences the overall cationic distribution. In the context of nanoparticles[49], the synthesis method of co-precipitation results in different inversion parameters in function of the second cation (M) for MFe_2O_4. In thin films, the synthesis of $CoFe_2O_4$ results in an inversion parameter of 0.88[50], which is close to the inverse spinel structure (δ = 1) exhibited in the bulk material.

The cationic arrangement has a significant influence on the physicochemical properties of the spinel structure. To illustrate, the radii of cationic species increase when transitioning from a T_d environment to an O_h environment[51]. This has an impact on the resulting lattice parameter of the crystallographic structure. This change in lattice parameter influence the distance between two O_h sites, and thus for example the conductivity through the hopping mechanism[52].

Some authors have investigated the preference of different cations for T_d or O_h sites[53,54]. The calculations presented by Navrotsky[53] are based on thermodynamic considerations, while the calculations of Dunitz[54] are based on the crystal field. In both cases, the order of stabilization energy in O_h sites is the following: Cr^{3+}, Ni^{2+}, Fe^{2+} and Fe^{3+}. This indicates that trivalent chromium exhibits a strong preference for O_h sites, followed by divalent Ni. In contrast, divalent iron exhibits a slight preference for O_h sites, whereas the trivalent iron does not display a preference for either sites.

1.3.2 Magnetic structures within the spinel structure

Spinels present various magnetic structures. The theory of ferrimagnetism for the spinel phase has been first introduced by Néel[55]. He proposed that the magnetic interactions between cations of the same sublattice (T_d-T_d and O_h-O_h interactions) are ferromagnetic and weak, while the interactions between cations of distinct sublattice (T_d-O_h interactions) are antiferromagnetic and strong. The net result of these interactions is an antiparallel alignment of spins in the T_d and O_h sites. The net magnetic moment (μ_{total}) is defined as the difference between the O_h (μ_{Oh}) and the T_d (μ_{Td}) magnetic moments:

$$\mu_{total} = \sum \mu_{Oh} - \sum \mu_{Td} \qquad (1.1)$$

The phenomenon of producing an ordered magnetic field through the interaction of elements is referred to as exchange interaction. The direct exchange interaction is a consequence of the overlap of two atomic orbitals belonging to two neighboring atoms or ions. Furthermore, in an oxide material, the magnetic exchange interaction occurs through an oxygen anion, and is referred as super-exchange. The magnetic cations are too distant to establish a conventional exchange interaction through orbitals; the oxygen serves as an intermediary in

this process. The theory of super-exchange interactions was first introduced by Kramers[56] and then developed by Anderson[57,58], Goodenough[59,60], and Kanamori[61]. A number of rules have been proposed to determine the theoretical sign and intensity of the magnetic interactions. The essential information to be retained is that the primary parameter is the degree of orbitals overlapping. The degree of overlapping is influenced by the crystalline geometry. Of particular interest are the angles between the metallic cations and the oxygen anions (Me-O-Me, where Me represents the metallic cation) and the metal-metal distance. Strong overlapping results in strong coupling. To illustrate, the T_d-T_d interaction is relatively weak due to the significant distance T_d-T_d.

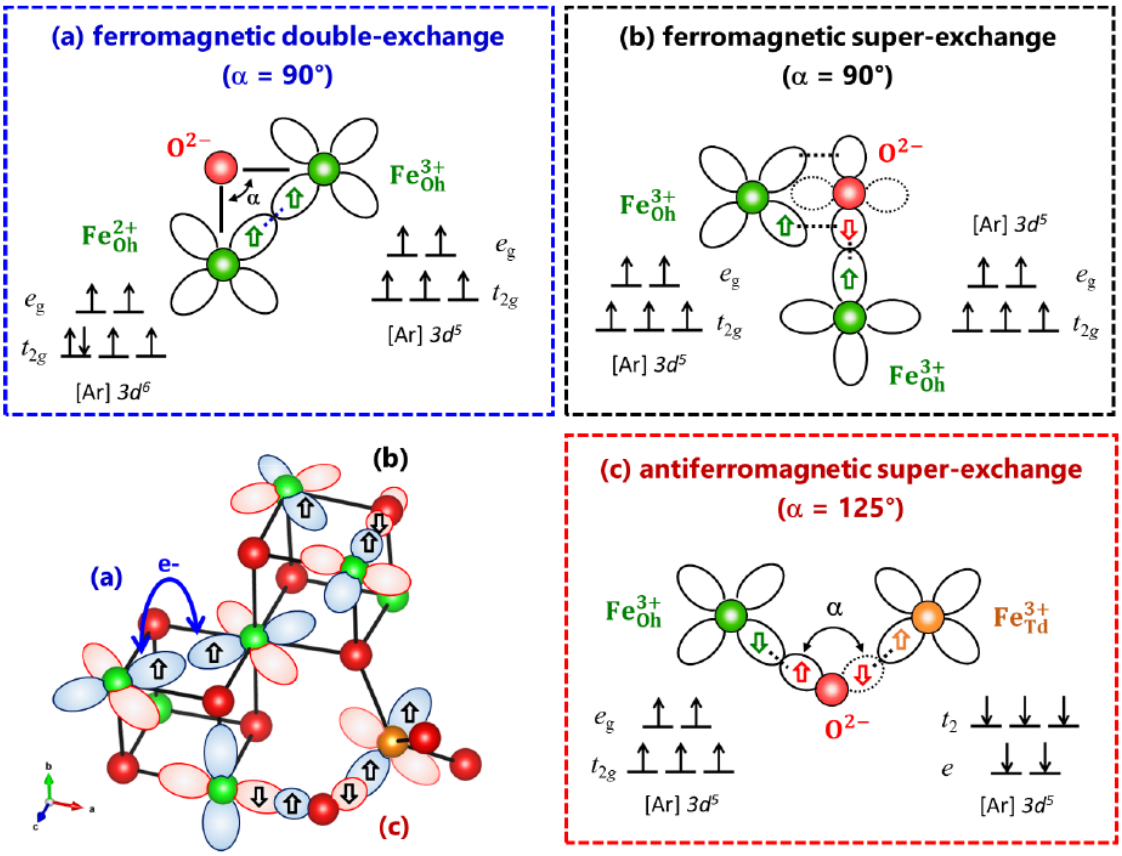

Figure 1.5: Schematic illustration of the magnetic exchange interaction in Fe_3O_4. The orange color represents the T_d sites, while the green color depicts the O_h sites. Due to crystal field effect, the 3d orbitals of the O_h sites are split into the triply degenerate low-energy t_{2g} states and doubly degenerated high-energy e_g states, whereas the T_d site cations exhibit two low-energy e states and three high-energy t_2 states. Extracted from Pinho[62].

The different super-exchange interactions in Fe_3O_4 are illustrated in *Figure 1.5*. The interacting orbitals are the *2p* orbitals for oxygen anions, and *3d* orbitals for

cations. An angle of 180° between two cations results in the maximum antiferromagnetic coupling[57,58]. This 180° configuration does not occur in spinel. However, the 125° angle of T_d-O_h exchange yields a significant antiferromagnetic interaction (configuration c). Two potential interactions occur in the O_h-O_h configuration. The first one (a) is the Zener double exchange[63]. It occurs due to the electron transfer from Fe^{2+} to Fe^{3+}. This interaction is relatively weak and often masked by the superexchange at 90° (b). The latter results in a subtle ferromagnetic interaction.

Following Néel's introduction of the ferrimagnetism in the spinel phase, other researchers demonstrated the existence of alternative magnetic structures within the spinel phase. The replacement of magnetic cations with other magnetic or non-magnetic cations results in the dilution of certain interactions[64]. In particular, when the O_h-O_h interaction is no longer negligible in comparison to the T_d-O_h interaction, the O_h sites can be divided into two distinct sublattices, with an angle between each other and the T_d sites. This triangular configuration was first proposed by Yafet and Kittel[65]. The angle formed by the magnetization between the different magnetic sublattices is referred to as the Yafet-Kittel angle, or the canting angle. The canted configuration is the reason for the lower magnetic moment observed in chromites[66] ($Fe_{3-x}Cr_xO_4$ series) compared to Fe_3O_4.

1.3.3 Physicochemical properties of particular compounds in the spinel area of the quaternary Fe-Ni-Cr-O

This section describe the crystallographic and magnetic structure (and the eventual transitions) of the four corners of the spinel area depicted in Figure 1.1. The considered compounds are: Fe_3O_4, $NiFe_2O_4$, $FeCr_2O_4$ and $NiCr_2O_4$.

1.3.3.1 Magnetite (Fe_3O_4)

Fe_3O_4 (or magnetite) is a compound situated at the bottom right corner of the spinel region. Fe_3O_4 has an inverse spinel structure ($\delta = 1$), with Fe^{2+} ions situated at the Oh sites, and Fe^{3+} ions distributed between the T_d and O_h sites. This ordering can be summarized by the following formula: $(Fe^{3+})_{Td}[Fe^{2+}Fe^{3+}]_{Oh}O_4$. This oxide is ferrimagnetic, with a Curie temperature of 850 K [67] and has a lattice parameter of 8.37-8.41 Å[68–70].

At low temperatures, Fe_3O_4 undergoes a structural transition. This phenomenon is due to the charge ordering of Fe^{2+} and Fe^{3+} ions at the O_h sites. This transition is called the Verwey transition[71] and occurs at 120 K for pure Fe_3O_4. The low-temperature phase of the magnetite remains a topic of debate. Some researchers propose a monoclinic cell structure[72], while others observe deviations from the proposed monoclinic cell[73].

Above the Verwey transition at 120 K, Fe_3O_4 exhibits a rather low metallic behavior. Below the Verwey transition, the magnetite exhibits an isolating behavior. The conduction mechanism is a combination of two distinct phenomena[74]. The first phenomenon is that of band conductivity, while the second is that of hopping conductivity. This hopping is attributed to the electronic transfer between Fe^{3+} and Fe^{2+} in O_h sites. The maximum conductivity is observed at 350 K, where the two mechanisms are of equal magnitude. Another exciting property of this oxide is its half-metallic behavior. This effect induces the existence of a fully spin-polarized current for one spin direction at the Fermi level. This behavior can be used in spintronics devices such as magnetic tunnel junction[75].

1.3.3.2 Trevorite ($NiFe_2O_4$)

The $NiFe_2O_4$ (trevorite) compound is placed in the top right corner of the spinel region. $NiFe_2O_4$ crystallizes in an inverse spinel structure ($\delta = 1$), with Ni^{2+} ions located in the Oh sites, and Fe^{3+} ions distributed between the T_d and O_h sites. The formula is $(Fe^{3+})_{Td}[Ni^{2+}Fe^{3+}]_{Oh}O_4$. This oxide is also ferrimagnetic, with a Curie temperature of 843 K[76], and has a lattice parameter of 8.32-8.34 Å in bulk[77–79].

Stoichiometric $NiFe_2O_4$ has an insulating behavior.; However, modifying the sintering temperature allows for the reduction of Fe^{3+} to Fe^{2+}, enabling the hopping mechanism[80] to occur. Consequently, the oxide is less insulating.

1.3.3.3 Iron chromite ($FeCr_2O_4$)

The $FeCr_2O_4$ (iron chromite) compound is located at the lower left corner of the spinel region. $FeCr_2O_4$ crystallizes in a normal spinel structure ($\delta = 0$), with Fe^{2+} ions located on the T_d sites, and Cr^{3+} ions exclusively occupying the O_h sites. The formula is now $(Fe^{2+})_{Td}[Cr_2^{3+}]_{Oh}O_4$. This oxide exhibits a lattice parameter of 8.37-8.38 Å[66,81,82].

$FeCr_2O_4$ displays two structural transitions and two magnetic transitions. By decreasing the temperature, the first transition is a structural transition from the cubic spinel phase to a tetragonal phase (with $c/a < 1$) at 140 K[66,83,84], attributed to a Jahn-Teller effect. This effect occurs when an energy degenerate system distorts itself in order to reduce its energy, thereby removing the degeneracy. Then, a magnetic transition linked with a structural transition is observed at approximately 90 K. The compound is then ferrimagnetic and has an orthorhombic structure. By decreasing the temperature further, a final transition is observed at 40 K, where a conical spin ordering is present.

1.3.3.4 Nickel chromite ($NiCr_2O_4$)

The $NiCr_2O_4$ (nickel chromite) compound is located in the top right corner of the spinel region. $NiCr_2O_4$ has a normal spinel structure ($\delta = 0$), with Ni^{2+} ions located on the T_d sites, and Cr^{3+} ions exclusively occupying the O_h sites. The formula can be expressed as: $(Ni^{2+})_{Td}[Cr_2^{3+}]_{Oh}O_4$. This oxide exhibits a lattice parameter of 8.31-8.32 Å[85,86]. The $NiCr_2O_4$ electrical behavior suggests a semiconducting behavior[87].

$NiCr_2O_4$ also exhibits two magnetic transitions and two structural transitions. By decreasing the temperature, the first transition, occurring at 320 K is a structural transition from cubic to tetragonal lattice (with $c/a > 1$)[88,89]. This transition is driven by the Jahn-Teller effect of Ni^{2+}. At the Curie temperature of around 80 K[89,90], a magnetic transition coupled to a structural transition occurs. The compound is ferrimagnetic and has an orthorhombic structure. A last magnetic transition observed is the apparition of a conical spin ordering at 30 K[90].

A few preliminary observations can be done on the magnetic properties of these spinel compounds. The inverse spinel structure exhibits a higher Curie temperature than the normal spinel structure. The Cr doping with $\gamma = 2.0$ in $Fe_\alpha Ni_\beta Cr_\gamma O_4$ gives rise to complex structural and magnetic transitions.

1.3.4 Binaries between the end members of the spinel area

The following section examine the properties of the intermediary materials situated between the aforementioned four initial compounds. These zones of the phase diagram of the spinel area have been the subject of previous studies, with samples synthesized under different forms (bulk, nanoparticles, thin films…). These different synthesis methods diverge from the AO-MBE process selected in this work. We will discuss the four binaries, along the samples synthesis processes, comprising Fe_3O_4-$FeCr_2O_4$ (the bottom gray line of the spinel region), Fe_3O_4-$NiFe_2O_4$ (red line), $FeCr_2O_4$-$NiCr_2O_4$ (left green line) and $NiFe_2O_4$-$NiCr_2O_4$ (top blue line) systems labelled in Figure 1.5.

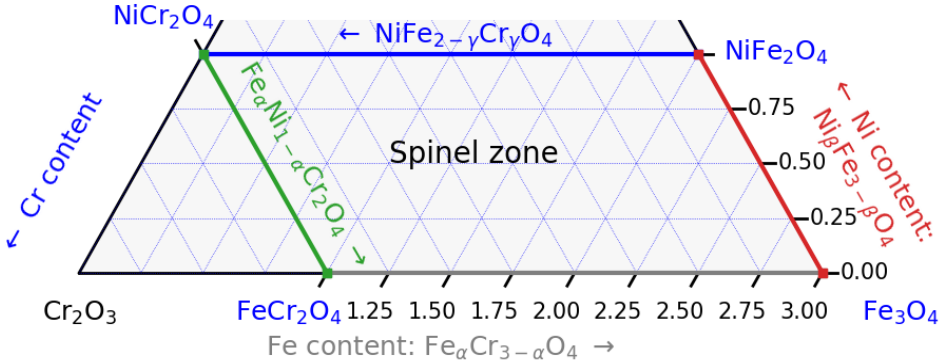

Figure 1.6: Schematic illustration of the different binaries system in the quaternary diagram.

1.3.4.1 Fe_3O_4-$FeCr_2O_4$ binary system

The binary system Fe_3O_4-$FeCr_2O_4$ is the bottom line of the spinel region. The two end members exhibit an opposite cationic repartition. Fe_3O_4 has an inverse spinel structure, while $FeCr_2O_4$ has a normal spinel structure. The binary system has been studied by different teams. Ma *et al.*[83], Robbins *et al.*[91] or Francombe *et al.*[66] have performed measurements of the structure (lattice parameter), as well as investigations on the magnetic and structural transitions for bulk compounds. In the case of thin films, a previous study has been done in our team[62]. The evolution of the lattice parameter as a function of the chromium content shows three different regions[66,82], as illustrated in Figure 1.7.

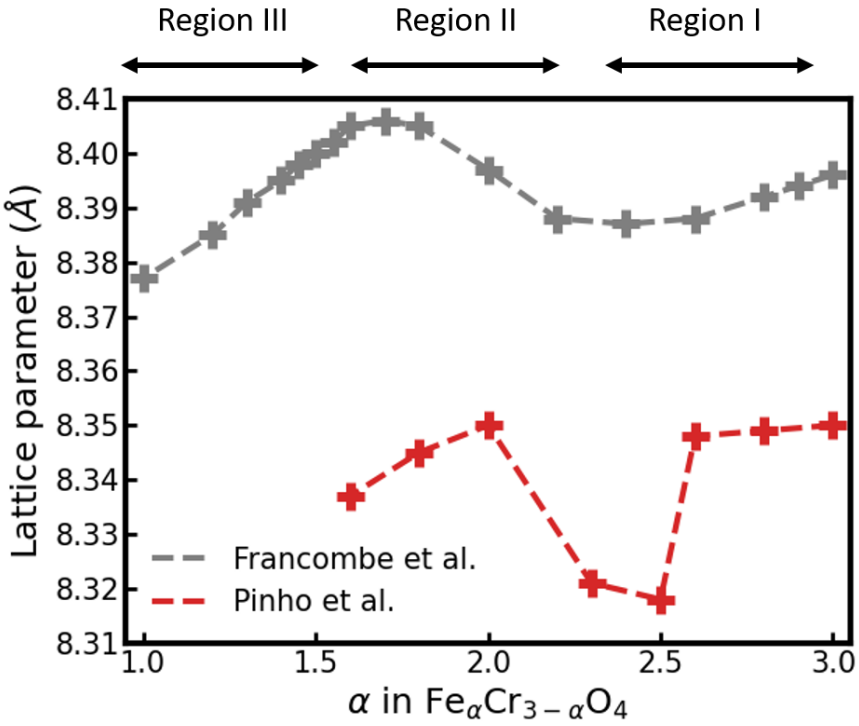

Figure 1.7: Evolution of the lattice parameter as a function of the Cr doping. The gray crosses present the variations in bulk samples, while the red crosses depict the variations for thin films. Adapted from Pinho[52].

The region I shows a transition from an inverse spinel to an intermediate inversion. This region extends from α = 3.0 to α = 2.4. The decrease in lattice parameter is attributed to the smaller cationic radius of Cr^{3+} compared to Fe^{3+} in O_h sites (61.5 pm versus 64.5 pm[51]). In the region II, the spinel inversion remains intermediate, between α = 2.4 and α = 1.7. The lattice parameter increases due to the progressive filling of the T_d sites by Fe^{2+}. Their cationic radius is 63 pm, in comparison to the radius of 49 pm for Fe^{3+} cations in the T_d sites. The region III displays a significant decrease in the lattice parameter. It extends from α = 1.7 to

α = 1.0. The spinel structure is of intermediate inversion and reaches a normal spinel at α = 1. The decrease is predominantly attributable to the diminished cationic radius of cations in O_h sites.

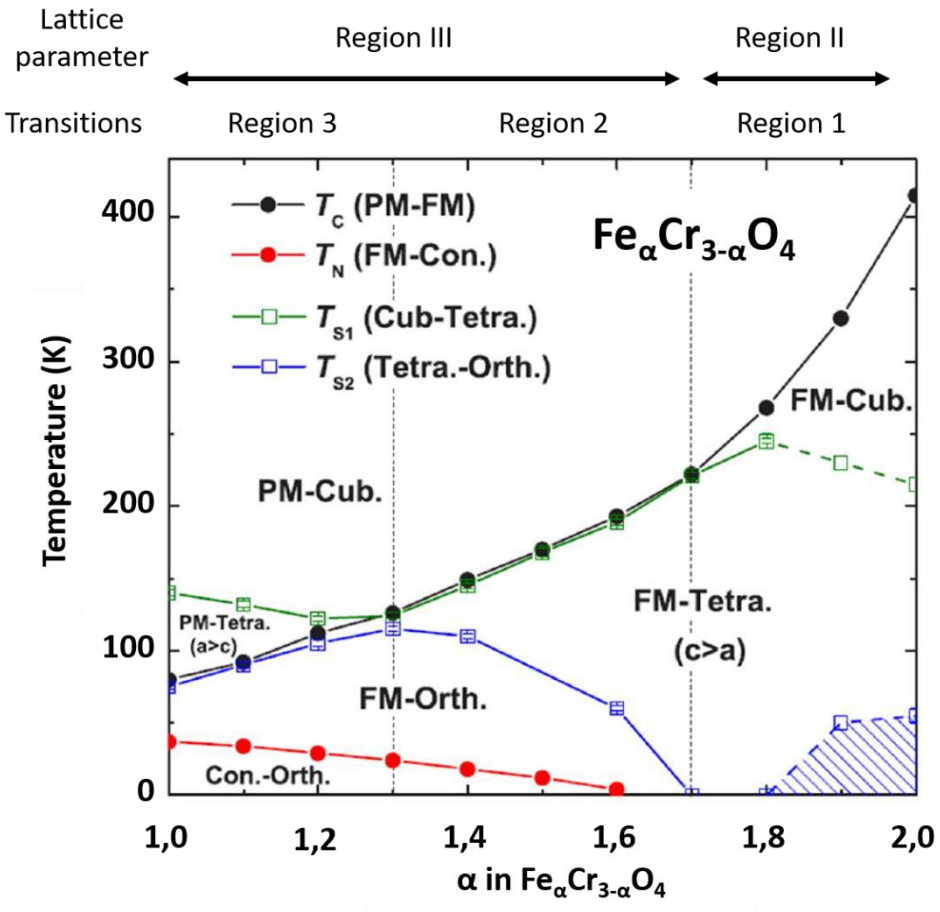

Figure 1.8: Temperature phase diagram of $Fe_\alpha Cr_{3-\alpha}O_4$. Figure adapted from Ma et al.[83].

The complete description of the crystalline and magnetic transitions in Fe_2CrO_4-$FeCr_2O_4$ is presented in Figure 1.8. T_C is the paramagnetic-to-collinear ferrimagnetic phase transition temperature, T_N is the collinear-to-conical ferrimagnetic phase transition temperature, T_{S1} is the cubic-to-tetragonal lattice transition temperature, and T_{S2} is the tetragonal-to-orthorhombic lattice transition temperature. The solid lines show the structural and magnetic transitions, while the dashed lines display the possible structural distortions.

Three distinct regions can be discussed as described in the article[83]. The first region is observed when α is below 1.3 (region 3). In this region, the spinel phase exhibits the normal spinel configuration (δ = 0). Two principal magnetic transitions are observed: the paramagnetic to collinear ferrimagnetic transition (T_C) and the collinear to conical Yafet-Kittel transition (T_N). A reduction in

chromium content (α increasing) results in an increase in T_C, but a decrease in T_N. From a crystallographic point of view, two distinct crystallographic transitions are observed, a transition from cubic to tetragonal (with c/a < 1) at T_{S1}, and a transition from tetragonal to orthorhombic at T_{S2}. A reduction in chromium content induces a decrease for T_{S1}, while T_{S2} increases, until the two temperatures become the same, at 110 K, for α = 1.3. The initial crystallographic transition T_{S1} is not associated with a magnetic ordering, whereas the subsequent crystallographic T_{S2} coincides with the first magnetic ordering (T_C).

In the second region (region 2, 1.3 < α < 1.7), the materials exhibit an intermediate spinel inversion (0 < δ < 1). Four transitions in the magnetic and crystallographic structure are still discernible. In contrast to the observations made in region 3, the variations are in opposition to the aforementioned trends. Specifically, the T_C and T_{S1} values increase with a reduction of the Cr content, while the T_N and T_{S2} values decrease, reaching 0 at α = 1.7. Below T_{S1}, the tetragonal phase exhibits c/a > 1. The initial crystallographic transition T_{S1} is associated with the magnetic transition T_C. The subsequent crystallographic transition occurs without changing the magnetic phase.

The third region is obtained with α > 1.7 (region 1). The spinel inversion is intermediate (0 < δ < 1). The compounds are purely cubic and the crystallographic transitions T_{S1} and T_{S2} disappeared. The T_C increases more abruptly in comparison to the other regions. No correlation was identified between structural and magnetic transitions.

1.3.4.2 Fe_3O_4-$NiFe_2O_4$ binary system

The binary system Fe_3O_4-$NiFe_2O_4$ is the right line of the spinel region. The two end members exhibit an inverse spinel structure with a high T_C of approximately 850 K. It is anticipated that Ni^{2+} cations will progressively replace Fe^{2+} cations in the O_h sites, and the lattice parameter variations will be linear.

From a thermodynamic standpoint, the spinel phase ($Fe_{3-\beta}Ni_\beta O_4$)is stable up to β = 1.0 of Ni[92], which represents the upper limit of this binary spinel system. In contrast to bulk properties, the Curie temperature remains constant in the case of fine particles[93].

The impact of progressive Ni doping on the lattice parameters of magnetite has been studied by different authors, with investigations on nanoparticles[94–98] and thin films[99,100]. A summary of these variations can be found in Figure 1.9.

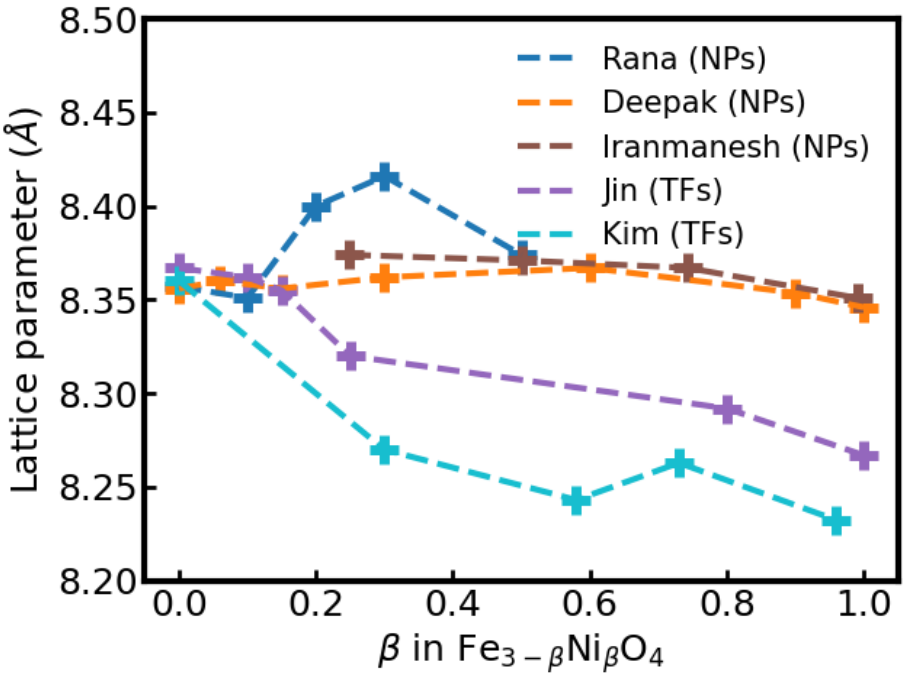

Figure 1.9: Evolution of the lattice parameter in $Fe_{3-\beta}Ni_{\beta}O_4$ from different works for nanoparticles (NPs) and thin films (TFs).

The lattice parameter exhibits notable variations according to the synthesis method. In nanoparticles (NPs), Iranmanesh *et al.*[96] or in thin films (TFs) Jin *et al.*[99], observed a continuous decrease in the lattice parameter with the increasing Ni content. This is probably due to the smaller cationic radius of Ni^{2+} in an O_h environment (69 pm) in comparison with the radius of Fe^{2+} in an O_h environment 78 pm[51]). In other publications (Rana *et al.*[98] or Deepak *et al.*[97]), an initial increase in the lattice parameter can be observed, followed by a decrease with the Ni content.

The values reported by Jin *et al.*[99] and Kim *et al.*[100] are lower than the values reported by the other studies, probably due to the fact that the thin film deposition was done on MgO and α-Al_2O_3 (0001) substrates, respectively. The strain imposed by the substrate induces a reduction of the lattice parameter. Kim *et al.*[100] has grown polycrystalline thin films on α-Al_2O_3 (0001) substrates, which is the substrate also selected in this study. The authors have observed a tetragonal distortion for samples with a Ni content greater than 0.57, whereas those with a Ni content below 0.3 remain cubic. The evolution of the lattice parameter is also reported in Figure 1.9 with an equivalent a_{cubic} ($a_{cubic}^3 = a_{tetra}^2 c_{tetra}$) in order to be compared with the other works. The remaining reported values, despite some variations, converge toward a similar range (from 8.37 Å for $Ni_{0.5}Fe_{2.5}O_4$ to 8.35 Å for $NiFe_2O_4$) for compounds close to $NiFe_2O_4$.

1.3.4.3 $FeCr_2O_4$-$NiCr_2O_4$ binary system

This pseudo binary system $FeCr_2O_4$-$NiCr_2O_4$ represent the left line of the spinel region and has not been explored in details. The two end members of this binary exhibit a normal spinel structure, with a low Curie temperature. It is probably due to a gradual substitution of Fe^{2+} cations by Ni^{2+} cations in T_d sites.

To the best of our knowledge, the work of Gilabert *et al.*[101] is the only article which describes this binary system with measurements of the lattice parameters. This part of the spinel region is at the intersection of two ternary systems (Ni-Cr-O and Ni-Fe-O systems). And, only two studies have explored this binary spinel solution from a thermodynamic perspective: Kjellqvist *et al.*[12] and Kurepin *et al.*[102]. No evolution of the Curie temperature with the iron content is reported in the literature.

In the work of Gilabert[101], the measured lattice parameters indicate that the as-synthesized spinel samples exhibit the expected stoichiometry. However, after post-synthesis (calcination at 800 or 1000 °C, in O_2 or N_2), a unique spinel phase of $NiCr_2O_4$, without any iron (or $FeCr_2O_4$ when no Ni is introduced in the reaction mix) is observed. Figure 1.10 shows the progressive vanishing of the spinel phase with the calcination temperature. It should be noted that the $FeCr_2O_4$ phase is not thermodynamically stable below 1400°C[12]. In the post synthesis treatment, the oxidizing conditions favor the formation of Fe^{3+}. Consequently, the eskolaite (Cr_2O_3 enriched with iron) phase becomes more prevalent.

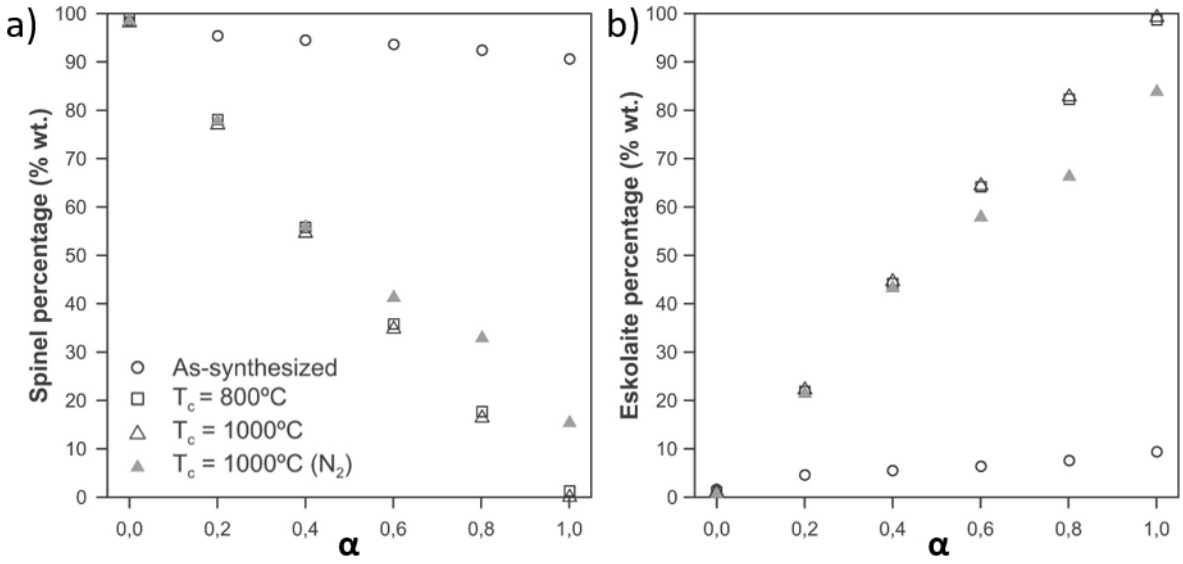

Figure 1.10: Evolution of the percentages of spinel phase (a) and eskolaite phase (b) depending of α in $Ni_{1-\alpha}Fe_\alpha Cr_2O_4$. Adapted from Gilabert et al.[101].

This is evidenced by the percentage of each phase present in the resulting mixture (Figure 1.10). The reaction mixture following synthesis exhibits a predominantly spinel phase, with an increase in eskolaite phase in a linear manner with α in post-treatment. The use of N_2 during the calcination process has been demonstrated to facilitate the preservation of the spinel phase at 10% within the total phase composition, in the instance where α = 1.

The evolution of the lattice parameter of the as-synthesized and post-treated samples is illustrated in Figure 1.11. It can be observed that the as-synthesized and samples treated in oxidizing conditions exhibit the same behavior. Their lattice parameters are slightly below the expected one in the case of an ideal solid solution (Vegard's law). Increasing the calcination temperature T_C results in a reduction in the lattice parameter. In order to elucidate the parabolic decline observed in the treated sample exposed to an N_2 atmosphere, the authors has formulated the following hypothesis. The transformation of the spinel phase into the eskolaite phase is accompanied by the transport of Fe^{3+} cations into the growing eskolaite phase, which results in the formation of vacancies in the spinel structure. Furthermore, the application of an inert atmosphere results in the loss of oxygen anions. As a result, the iron and oxygen vacancies lead to a notable reduction in the lattice parameter.

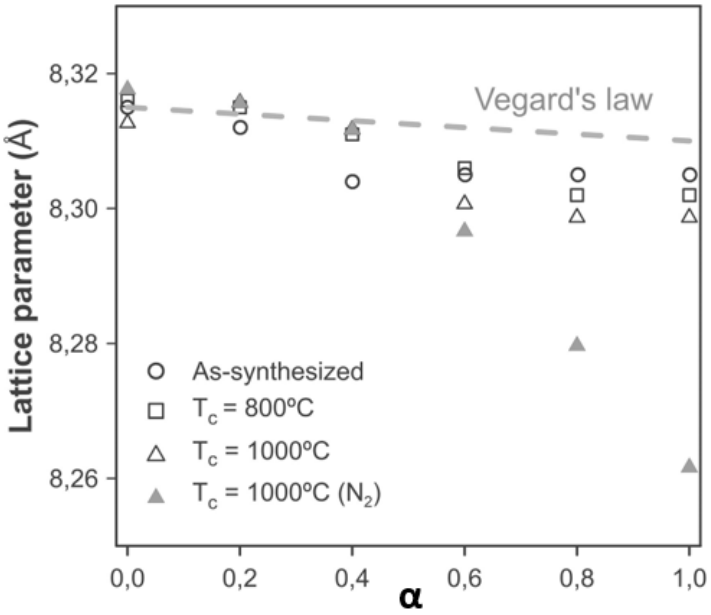

Figure 1.11: Comparison of the lattice parameter evolution with the prediction of Vegard's law (ideal solid solution between $NiCr_2O_4$ and $FeCr_2O_4$).

Concerning the cationic distribution, the authors postulated that Ni^{2+} is gradually replaced by Fe^{2+} on T_d sites.

The replacement of Ni atoms by Fe ones in T_d sites is, in fact, a more complex process, as the $FeCr_2O_4$ phase is not thermodynamically stable. This binary system represents the intersection of two ternary systems (Ni-Fe-O and Ni-Cr-O). This is a potential explanation of the few available experimental data.

1.3.4.4 $NiFe_2O_4$-$NiCr_2O_4$ binary system

The two end members of this binary system $NiFe_2O_4$-$NiCr_2O_4$ (top line of spinel region) exhibit an opposed cationic arrangement. $NiFe_2O_4$ has an inverse spinel structure with a high Curie temperature, whereas $NiCr_2O_4$ has a normal spinel structure, with a low Curie temperature. The lattice parameter should display significant variations to accommodate this opposed cationic distribution.

A number of authors have performed experimental studies on this system[86,103–108]. The majority of authors have used synthesis methods yielding to ceramic[103] or powdered[86,104] materials. The only study on nanoparticles[108] exhibited lattice parameters markedly exceeding the others values, thus this study has been rejected for the rest of this discussion.

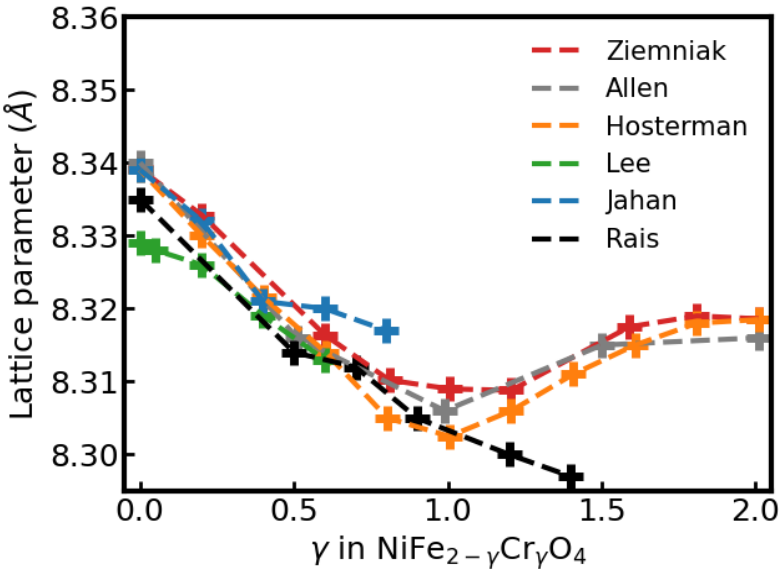

Figure 1.12: Lattice parameter as a function of the Cr content (γ) in $NiCr_2O_4$-$NiFe_2O_4$ binary system from Ziemniak[86], Allen[103], Hosterman[104], Lee[106], Jahan[107] and Rais[105].

The lattice parameters measured by the different authors as a function of the Fe content are illustrated in Figure 1.12. The $NiFe_2O_4$ compound is situated at the left side of the diagram (γ = 0.0), while the $NiCr_2O_4$ compound is located on the right (γ = 2.0). The reported values for the lattice parameters are coherent. It is noteworthy that the compound $NiCr_2O_4$ exhibits a tetragonal structure below 320 K. The reported lattice parameters for this compound are consistent with a cubic-

like lattice parameter. The cubic-equivalent structure is established as having the same volume as the tetragonal one ($a_{cubic}^3 = a_{tetra}^2 c_{tetra}$).

A linear decreasing is observed between $NiFe_2O_4$ and $NiFeCrO_4$ (γ = 1.0), followed by a linear increasing between $NiFeCrO_4$ and $NiCr_2O_4$ (γ = 2.0). The proposed mechanism for the lattice parameter variations is supported by Mossbauer studies[105] and is as follows. Starting from $NiFe_2O_4$, the Cr^{3+} cations substitute for the Fe^{3+} cations in the O_h sites. The smaller cationic radius (61.5 pm for Cr^{3+} in O_h sites, compared to 64.5 pm for Fe^{3+} in O_h sites[51]) results in a decrease in the lattice parameter, as the system transitions from $NiFe_2O_4$ to $NiFeCrO_4$ (γ = 0.0 to γ = 1.0). At $NiFeCrO_4$, the cationic organization is represented by the formula $(Fe)_{Td}[NiCr]_{Oh}O_4$. Subsequently, the Cr content continues to increase in O_h sites, forcing Ni atoms to relocate in T_d sites. This results in a reduction of iron in the T_d sites. The cationic radii of Fe^{3+} are 49 pm for T_d sites and 64.5 pm for O_h sites, while the radii for Ni^{2+} are 55 pm for T_d sites and 69 pm for O_h sites. The T_d site size exhibits an increase, while the O_h decrease slightly. The net result is an increase in the lattice parameter from $(Fe)_{Td}[NiCr]_{Oh}O_4$ (γ = 1.0) to $(Ni)_{Td}[Cr_2]_{Oh}O_4$ (γ = 2.0).

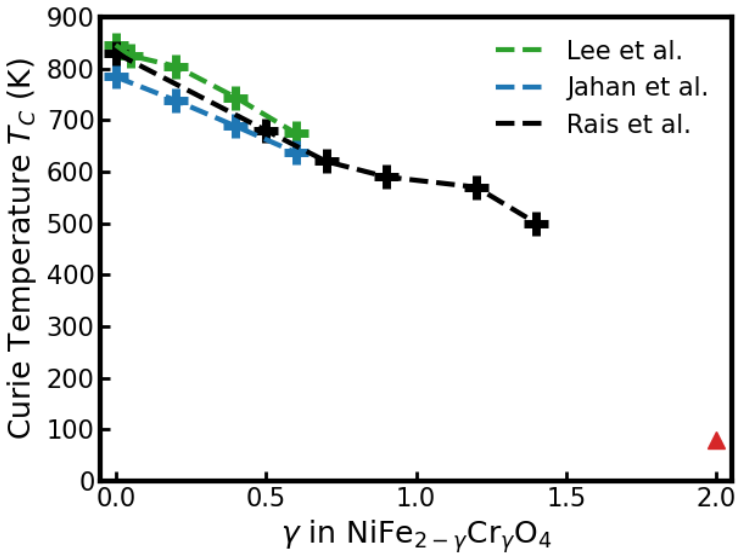

Figure 1.13: Evolution of the Curie temperature as a function of the Cr content (γ). from Lee[106], Jahan[107] and Rais[105]. The red triangle represent the T_C of $NiCr_2O_4$ (80 K).

The Curie temperature has also been studied by some groups[105,106,109]. The results are presented in Figure 1.13. A general linear decrease is observed when going from $NiFe_2O_4$ to $NiFeCrO_4$. These three studies present some discrepancies in the reported value of T_C. However, similar variations are observed. The samples measured by Rais *et al.* exhibited a magnetic temperature of compensation, T_K.

This phenomenon is associated to the magnetic ordering and manifests as a zero in the M_S (T) curve. At T_K, the compound exhibits an AF alignment, which results in zero net magnetization. Subsequent to this temperature point, the compound exhibits a remaining magnetization. The compensation temperatures converge with the Curie temperature at γ = 1.7.

Because no study is available between γ = 1 and γ = 2, it is anticipated that the linear decrease between $NiFeCrO_4$ and $NiCr_2O_4$ will be more pronounced than that observed between $NiFe_2O_4$ and $NiFeCrO_4$.

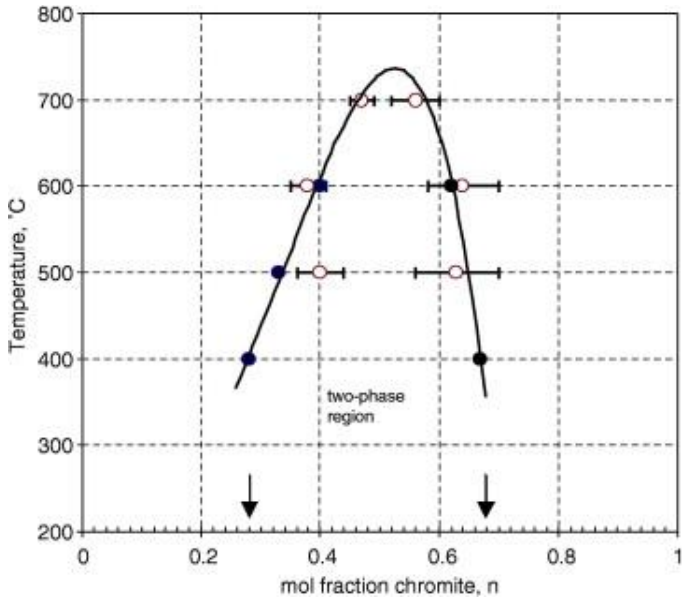

Figure 1.14: Measured solvus in the $Ni(Fe_{1-n}Cr_n)_2O_4$ (2n = γ) spinel binary: EDX (Energy-Dispersive X-ray, open circles) and EMPA (Electron MicroProbe Analysis, filled circles). Arrows show solvus based on observed cation distributions between octahedral and tetrahedral sites at room temperature. Extracted from Ziemniak et al.[86].

Ziemniak[86] observed the presence of an miscibility gap. The miscibility gap is observed below 1000 K and is characterized by a two-phase region extending from n = 0.27 to n = 0.67 (γ = 0.54 to γ = 1.34) at room temperature. In order to obtain the two phases, the samples were synthesized in molten salts and maintained at distinct temperatures (400 to 700°C) for an extended period of time (one month to six months). This miscibility gap is unlikely to be observed in this study.

1.3.5 Spinel phase of the Fe-Ni-Cr-O system in different domains

The oxides composed of iron, nickel and chromium elements exhibit a wide range of applications in different research fields.

In the context of geology and metallurgy, magnetite (Fe_3O_4) is identified as the most abundant iron mineral on Earth, while chromite ($FeCr_2O_4$) is established as the primary source of chromium. Chromium is considered a crucial element in the production of stainless steel, as it is the constituent responsible for conferring corrosion resistance properties to these materials.

Some of the compounds in this system display also a semi-conductor behavior. The band gap can be engineered to match the wavelengths of visible light, enabling visible light harvesting for use in photovoltaic or photocatalytic applications[110–113].

Additionally, these compounds have applications in the fields of medicine and biology. The potential of magnetite nanoparticles as a drug delivery system has been the subject of some research[114].

Our interest for investigating the structural and physicochemical properties of spinels comprising Fe, Ni, and Cr elements is related to two distinct contexts: corrosion and spintronics.

1.3.6 Spinel phases containing Fe, Ni and Cr in spintronics context

Concerning the field of spintronics (demanding monocrystalline samples with precise chemical composition), Fe_3O_4 exhibits a half-metallic behavior at room temperature. A half-metal is defined as a material exhibiting a conductivity only for electrons with one spin direction. Consequently, the conduction electrons are fully spin-polarized. A lot of researches have been dedicated to the use of this property for spintronics applications such as tunneling magnetoresistance (TMR) in magnetic tunnel junctions[75,115,116] or spin field-effect transistors[117–119].

The conductive behavior of thin films of $NiFe_2O_4$ are dependent on the synthesis conditions. It has the potential for exhibiting conductive behavior with spin polarization up to 45 % at room temperature[10]. However, when this oxide is insulating, it can be also integrated in magnetic tunnel barrier for spin filtering applications[120].

The $Fe_{3-x}Cr_xO_4$ series exhibits Curie temperatures below room temperature for highest Cr content ($x > 1.2$), thereby limiting the applications of this series in spintronics. However, the magnetic phase diagram is complex with exciting magnetic and electric properties[52,62].

The growth of thin films of materials with magnetic properties (and other properties such as optical, ferroelectricity, etc.) is a crucial step in the development of modern spintronic applications. The lattice parameter, or the growth directions have significant impact on the magnetic properties of the samples. Spinel phases of varying compositions can be grown on different substrates, which influence the lattice parameter. $NiFe_2O_4$ can be grown on $SrTiO_3$ (001)[121,122], silicon (100)[123], $MgAl_2O_4$ (001)[124] or $ZnGa_2O_4$ (001)[125], among other substrates. The common point of all these substrates is that the growth is oriented along the [001] direction.

In this study, the selected substrate is α-Al_2O_3 (0001). It has been previously demonstrated that Fe_3O_4 or $NiFe_2O_4$ exhibit excellent growth on α-Al_2O_3 (0001)[126]. Given the orientation of α-Al_2O_3 (0001), spinel phases will grow in the direction [111]. This orientation will enrich the possibilities for spintronics devices by adding new surfaces. More recently, in our laboratory, we have demonstrated that it is possible to elaborate $Fe_{3-x}Cr_xO_4$ thin films on α-Al_2O_3 (0001) with a controlled chromium content and tunable electric and magnetic properties[52].

1.3.7 Spinel phases containing Fe, Ni and Cr in corrosion context

The fundamental criteria for a steel to be classified as stainless steel are the presence of iron, carbon, and a minimum of 18% chromium and 12% nickel in weight. Other alloys frequently used in industrial settings for their corrosion resistance properties include Fe-Cr and Ni-Cr alloys. When exposed to varying oxidizing environments (steam, hot water), a complex multiphasic layer is formed. The corrosion layer contains corundum (Cr_2O_3), spinels (Fe_3O_4) or halite-type phases (NiO or FeO) with diverse compositions in iron, nickel and chromium[127].

The oxidation resistance of stainless steel is primarily associated with the formation of a protective layer of Cr_2O_3[128]. The spinel phase, and in particular magnetite is well documented to offer minimal to no corrosion resistance due to its conductive behavior. However, in Fe-Cr[129] as in Ni-Cr[127] alloys, the spinel phase governs the electronic and cationic transport between the alloy and the surrounding environment. As an intermediate between the alloy and the environment, the physicochemical properties of the spinel phase play a pivotal role in determining the future evolution of corrosion.

Despite this key role in the corrosion mechanism, there is still much to know regarding the transport properties of spinel phases in the context of corrosion. This is due to the complex multiphasic corrosion layer, the variable composition, the poor crystallinity, and the complex microstructure. For example, the Figure 1.15 presents some results from a study[127] conducted on a Ni-Cr alloy corroded in primary cooling circuit condition of pressurized water nuclear reactor.

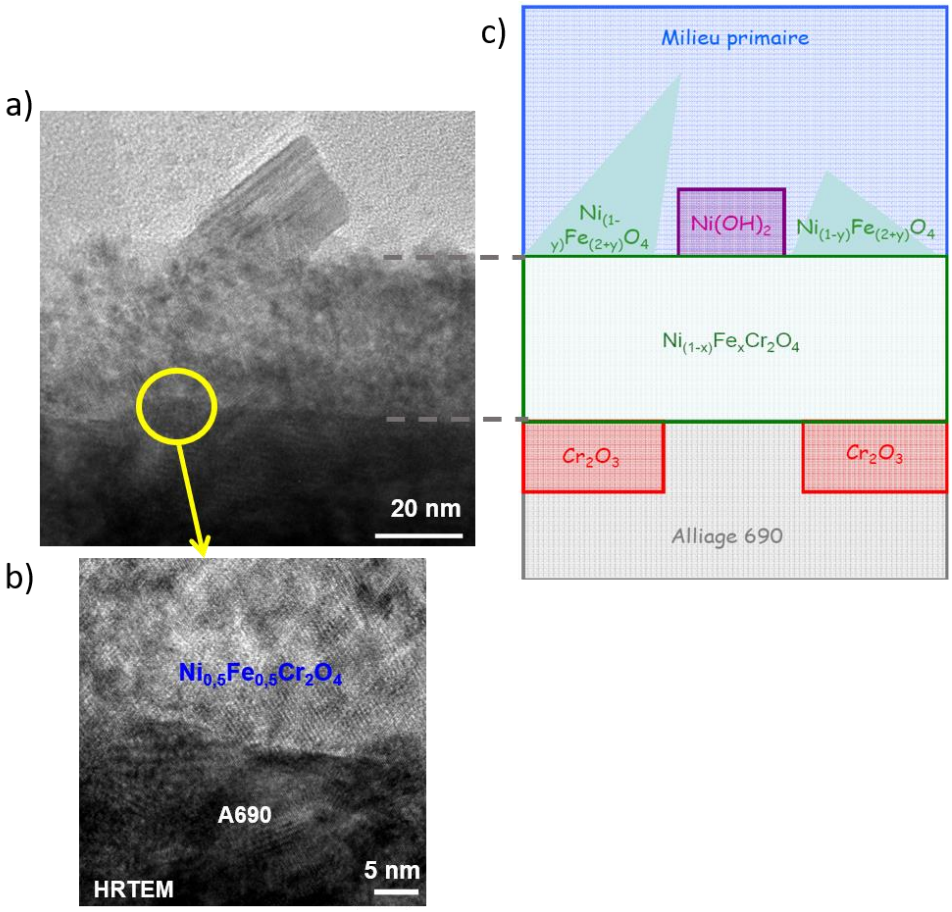

Figure 1.15: a) TEM cross-section picture of the corrosion layer observed on an A690 alloy (Ni – 10 % Fe – 30 % Cr in weight) in primary environment. b) Magnified HRTEM picture on the alloy-spinel interface. c) Schematic illustration of the different phases observed. Adapted from Marchetti[127].

As illustrated in Figure 1.15 (c), the various phases of the Fe-Ni-Cr-O quaternary system are present. Nodules of halite-like (NiO) and trevorite-like ($NiFe_2O_4$) phases are present at the top of the corrosion layer. The interfacial layer, which regulates cationic and electronic transport, is a chromite spinel phase ($FeCr_2O_4$), more or less enriched with nickel. Additionally, some inclusions of corundum-like (Cr_2O_3) structure are observed. As evidenced by the magnified HRTEM image of the alloy-spinel interface presented in (b), this region is poorly crystallized and exhibits a complex microstructure (grain boundaries, variable composition). The variable compositions are illustrated by the diverse stoichiometries (expressed as x or y) observed in the nodules and the chromite phase in (c).

1.4 OBJECTIVES AND ORGANIZATION OF THE MANUSCRIPT

In summary, this thesis will be dedicated to the synthesis of model systems with the objectives of using these systems in spintronics devices or elucidating the intricate behavior of corrosion layers. The second objective of this work is to probe the correlations between the magnetic properties and the fine structure, *i.e.* the cationic distribution within the O_h and T_d sites.

The first part of this thesis will be dedicated to a theoretical investigation of simulated domain walls (DWs) in NiO (Chapter 2). The complete magnetic structure of NiO and its description in terms of called "T" and "S" domains will be performed. Subsequently, the complex magnetic structure will be described with a three-part Heisenberg Hamiltonian. The Vampire code[130,131] will be used to solve the Hamiltonian and providing as output the magnetic structure. Then, the magnetic structure will be used for calculations in order to characterize the physical properties of the DWs. The atomic-scale behavior of the domain walls (DWs) will be first described, and subsequently, the properties of the simulated DWs will be discussed.

The second part of this thesis will be dedicated to the spinel phase of the Fe-Ni-Cr-O quaternary system. In the chapter 3, the experimental and simulations methods will be explained. This Chapter 3 includes the theoretical basis to understand the different techniques and the different information extracted from each of these techniques. In Chapter 4, the growth of $Fe_\alpha Ni_\beta Cr_\gamma O_4$ ($\alpha + \beta + \gamma = 3$) epitaxial thin films will be described with the objectives to obtain their magnetic properties for spintronics applications and their structural properties for corrosion applications. We will see that these layers, with $0 < \gamma < 2$ and $0 < \beta < 1$, can be synthesized by oxygen-assisted molecular beam epitaxy (OA-MBE). Structural data will be obtained by using electron diffraction (RHEED) and X-ray diffraction (XRD). Then, the chemical compositions will be probed by X-ray photoelectron spectroscopy (XPS). The magnetic properties will be analyzed for different compositions by vibrating sample magnetometry (VSM). In Chapter 5, the cationic distribution in the O_h and T_d sites of the spinel structure will be probed. For doing that, collaborations will be done with the synchrotron SOLEIL, and two techniques will be developed: Resonant X-ray diffraction (RXD) on the "SiXS" beamline and X-ray absorption spectroscopy (XAS/XMCD) on the "Deimos" beamline. Additionally, some hysteresis loops will be recorded on the "Deimos" beamline in order to probe the magnetic arrangement in the spinel phase. In Chapter 6, a model linking the fine structure and the lattice parameter will be explained and subsequently applied to the synthesized samples. Based on this model, a comprehensive study of the relationships between the fine structure and the magnetic properties will be discussed. In Chapter 7, some conclusions will be drawn and some limitations and perspectives will be discussed.

1.5 BIBLIOGRAPHY

(1) Giuliani, G.; Ohnenstetter, D.; Fallick, A. E.; Groat, L.; Fagan, A. J. THE GEOLOGY AND GENESIS OF GEM CORUNDUM DEPOSITS. In *Geology of Gem Deposits Second Edition*; Groat, L. A., Ed.; Mineralogical Association of Canada, 2014; Vol. 44, p 0. https://doi.org/10.3749/9780921294696.ch02.

(2) Simonet, C.; Fritsch, E.; Lasnier, B. A Classification of Gem Corundum Deposits Aimed towards Gem Exploration. *Ore Geology Reviews* **2008**, *34* (1), 127–133. https://doi.org/10.1016/j.oregeorev.2007.09.002.

(3) Arai, S. Characterization of Spinel Peridotites by Olivine-Spinel Compositional Relationships: Review and Interpretation. *Chemical Geology* **1994**, *113* (3), 191–204. https://doi.org/10.1016/0009-2541(94)90066-3.

(4) Decterov, S. A. Thermodynamic Modelling of the Al2O3-CaO-CoO-CrO-Cr2O3-FeO-Fe2O3-MgO-MnO-NiO-SiO2-S System and Applications in Ferrous Process Metallurgy.

(5) Luz, A. P.; Martinez, A. G. T.; Braulio, M. A. L.; Pandolfelli, V. C. Thermodynamic Evaluation of Spinel Containing Refractory Castables Corrosion by Secondary Metallurgy Slag. *Ceramics International* **2011**, *37* (4), 1191–1201. https://doi.org/10.1016/j.ceramint.2010.11.043.

(6) Rao, G. M.; Akhil, M.; Das, B.; Khan, A. R.; Patra, A.; Chaira, D. Development and Characterization of Nano-Al2O3, Cr2O3, and TiO2 Dispersed Mo Alloys Fabricated by Powder Metallurgy. *J. of Materi Eng and Perform* **2023**, *32* (4), 1683–1706. https://doi.org/10.1007/s11665-022-07215-3.

(7) Cho, M.-K.; Hong, G.-G.; Lee, S.-K. Corrosion of Spinel Clinker by CaO–Al2O3–SiO2 Ladle Slag. *Journal of the European Ceramic Society* **2002**, *22* (11), 1783–1790. https://doi.org/10.1016/S0955-2219(01)00509-X.

(8) Jastrzębska, I.; Ludwig, M.; Śnieżek, E.; Kalęba, A.; Drożdż, P.; Szczerba, J. Corrosion Study of Novel Cr-Free Alumina-Spinel Refractory Material Dedicated to the Copper Industry. *Journal of the European Ceramic Society* **2022**, *42* (15), 7311–7327. https://doi.org/10.1016/j.jeurceramsoc.2022.08.038.

(9) Šutka, A.; Gross, K. A. Spinel Ferrite Oxide Semiconductor Gas Sensors. *Sensors and Actuators B: Chemical* **2016**, *222*, 95–105. https://doi.org/10.1016/j.snb.2015.08.027.

(10) Lüders, U.; Barthélémy, A.; Bibes, M.; Bouzehouane, K.; Fusil, S.; Jacquet, E.; Contour, J.-P.; Bobo, J.-F.; Fontcuberta, J.; Fert, A. NiFe2O4: A Versatile Spinel Material Brings New Opportunities for Spintronics. *Advanced Materials* **2006**, *18* (13), 1733–1736. https://doi.org/10.1002/adma.200500972.

(11) *International Tables for Crystallography*, 2016th ed.; Vol. A.

(12) Kjellqvist, L.; Selleby, M.; Sundman, B. Thermodynamic Modelling of the Cr–Fe–Ni–O System. *Calphad* **2008**, *32* (3), 577–592. https://doi.org/10.1016/j.calphad.2008.04.005.

(13) Jouini, K.; Raouafi, A.; Dridi, W.; Daoudi, M.; Mustapha, B.; Chtourou, R.; Hosni, F. Investigation of Gamma-Ray Irradiation Induced Phase Change from NiO to Ni2O3 for Enhancing Photocatalytic Performance. *Optik* **2019**, *195*, 163109. https://doi.org/10.1016/j.ijleo.2019.163109.

(14) Blume, R.; Calvet, W.; Ghafari, A.; Mayer, T.; Knop-Gericke, A.; Schlögl, R. Structural and Chemical Properties of NiO $_x$ Thin Films: Oxygen Vacancy Formation in O $_2$ Atmosphere. *ChemPhysChem* **2023**, *24* (23), e202300231. https://doi.org/10.1002/cphc.202300231.

(15) Liu, Y.; Yu, Y.-X.; Zhang, W.-D. Photoelectrochemical Properties of Ni-Doped Fe2O3 Thin Films Prepared by Electrodeposition. *Electrochimica Acta* **2012**, *59*, 121–127. https://doi.org/10.1016/j.electacta.2011.10.051.

(16) Fan, Z.; Zhu, M.; Pan, S.; Ge, J.; Hu, L. Giant Photoresponse Enhancement in Cr2O3 Films by Ni Doping-Induced Insulator-to-Semiconductor Transition. *Ceramics International* **2021**, *47* (10, Part A), 13655–13659. https://doi.org/10.1016/j.ceramint.2021.01.226.

(17) Hutchings, M. T.; Samuelsen, E. J. Measurement of Spin-Wave Dispersion in NiO by Inelastic Neutron Scattering and Its Relation to Magnetic Properties. *Phys. Rev. B* **1972**, *6* (9), 3447–3461. https://doi.org/10.1103/PhysRevB.6.3447.

(18) Yamada, T.; Saito, S.; Shimomura, Y. Magnetic Anisotropy, Magnetostriction, and Magnetic Domain Walls in NiO. II. Experiment. *J. Phys. Soc. Jpn.* **1966**, *21* (4), 672–680. https://doi.org/10.1143/JPSJ.21.672.

(19) Nakahigashi, K. Crystal Structure of Antiferromagnetic NiO Determinded by X Ray Topography. *Journal of the physical Society of Japan* **1975**.

(20) Hotový, I.; Huran, J.; Spiess, L.; Čapkovic, R.; Haščík, Š. Preparation and Characterization of NiO Thin Films for Gas Sensor Applications. *Vacuum* **2000**, *58* (2), 300–307. https://doi.org/10.1016/S0042-207X(00)00182-2.

(21) Dirksen, J. A.; Duval, K.; Ring, T. A. NiO Thin-Film Formaldehyde Gas Sensor. *Sensors and Actuators B: Chemical* **2001**, *80* (2), 106–115. https://doi.org/10.1016/S0925-4005(01)00898-X.

(22) Danjumma, S. G.; Abubakar, Y.; Suleiman, S. Nickel Oxide (NiO) Devices and Applications: A Review. *International Journal of Engineering Research & Technology* **2019**, *8* (4). https://doi.org/10.17577/IJERTV8IS040281.

(23) Jamwal, G.; Prakash, J.; Chandran, A.; Gangwar, J.; Srivastava, A. K.; Biradar, A. M. Effect of Nickel Oxide Nanoparticles on Dielectric and Optical Properties of Nematic Liquid Crystal. *AIP Conference Proceedings* **2015**, *1675* (1), 030065. https://doi.org/10.1063/1.4929281.

(24) Li, X.; Lin, T.; Shin, J.; Jang, J. P-191L: Late-News Poster: Solution Processed P-Channel Oxide Thin Film Transistor Employing Metal Doped Nickel Oxide. *SID Symposium Digest of Technical Papers* **2016**, *47* (1), 1221–1224. https://doi.org/10.1002/sdtp.10845.

(25) Ukoba, K. O.; Inambao, F. L.; Eloka-Eboka, A. C. Fabrication of Affordable and

Sustainable Solar Cells Using NiO/TiO2 P-N Heterojunction. *International Journal of Photoenergy* **2018**, *2018* (1), 6062390. https://doi.org/10.1155/2018/6062390.

(26) Onyeachu, B. I.; Oguzie, E. E.; Ukaga, I. C.; Njoku, D. I.; Peng, X. Ni Corrosion Product Layer During Immersion in a 3.5% NaCl Solution: Electrochemical and XPS Characterization: *Port. Electrochim. Acta* **2017**, *35* (3), 127–127. https://doi.org/10.4152/pea.201703127.

(27) Gheno, T.; Gleeson, B. On the Hot Corrosion of Nickel at 700 °C. *Oxid Met* **2015**, *84* (5), 567–584. https://doi.org/10.1007/s11085-015-9588-6.

(28) Tzvetkoff, T.; Gencheva, P. Mechanism of Formation of Corrosion Layers on Nickel and Nickel-Based Alloys in Melts Containing Oxyanions—a Review. *Materials Chemistry and Physics* **2003**, *82* (3), 897–904. https://doi.org/10.1016/j.matchemphys.2003.08.001.

(29) Baltz, V.; Manchon, A.; Tsoi, M.; Moriyama, T.; Ono, T.; Tserkovnyak, Y. Antiferromagnetic Spintronics. *Reviews of Modern Physics* **2018**, *90* (1), 015005. https://doi.org/10.1103/RevModPhys.90.015005.

(30) Gomonay, E. V.; Loktev, V. M. Spintronics of Antiferromagnetic Systems (Review Article). *Low Temperature Physics* **2014**, *40* (1), 17–35. https://doi.org/10.1063/1.4862467.

(31) Gomonay, O.; Jungwirth, T.; Sinova, J. Concepts of Antiferromagnetic Spintronics. *physica status solidi (RRL) – Rapid Research Letters* **2017**, *11* (4), 1700022. https://doi.org/10.1002/pssr.201700022.

(32) Jungwirth, T.; Marti, X.; Wadley, P.; Wunderlich, J. Antiferromagnetic Spintronics. *Nature Nanotech* **2016**, *11* (3), 231–241. https://doi.org/10.1038/nnano.2016.18.

(33) Chirac, T.; Chauleau, J.-Y.; Thibaudeau, P.; Gomonay, O.; Viret, M. Ultrafast Antiferromagnetic Switching in NiO Induced by Spin Transfer Torques. *Phys. Rev. B* **2020**, *102* (13), 134415. https://doi.org/10.1103/PhysRevB.102.134415.

(34) Srinivasan, G.; Seehra, M. S. Magnetic Susceptibilities, Their Temperature Variation, and Exchange Constants of NiO. *Phys. Rev. B* **1984**, *29* (11), 6295–6298. https://doi.org/10.1103/PhysRevB.29.6295.

(35) Barra, A.; Ross, A.; Gomonay, O.; Baldrati, L.; Chavez, A.; Lebrun, R.; Schneider, J. D.; Shirazi, P.; Wang, Q.; Sinova, J.; Carman, G. P.; Kläui, M. Effective Strain Manipulation of the Antiferromagnetic State of Polycrystalline NiO. *Applied Physics Letters* **2021**, *118* (17), 172408. https://doi.org/10.1063/5.0046255.

(36) Sapozhnik, A. A.; Filianina, M.; Bodnar, S. Yu.; Lamirand, A.; Mawass, M.-A.; Skourski, Y.; Elmers, H.-J.; Zabel, H.; Kläui, M.; Jourdan, M. Direct Imaging of Antiferromagnetic Domains in ${\mathrm{Mn}}_{2}\mathrm{Au}$ Manipulated by High Magnetic Fields. *Phys. Rev. B* **2018**, *97* (13), 134429.

https://doi.org/10.1103/PhysRevB.97.134429.

(37) Kinoshita, T.; Wakita, T.; Sun, H.; Tohyama, T.; Harasawa, A.; Kiwata, H.; Ulrich Hillebrecht, F.; Ono, K.; Matsushima, T.; Oshima, M.; Ueno, N.; Okuda, T. Antiferromagnetic Domain Structure Imaging of Cleaved NiO(100) Surface Using Nonmagnetic Linear Dichroism at O K Edge: Essential Effect of Antiferromagnetic Crystal Distortion. *J. Phys. Soc. Jpn.* **2004**, *73* (11), 2932–2935. https://doi.org/10.1143/JPSJ.73.2932.

(38) Ikebuchi, T.; Kobayashi, Y.; Sugiura, I.; Shiota, Y.; Ono, T.; Moriyama, T. Long-Distance Spin Current Transmission in Single-Crystalline NiO Thin Films. *Appl. Phys. Express* **2021**, *14* (12), 123001. https://doi.org/10.35848/1882-0786/ac3575.

(39) Spethmann, J.; Grünebohm, M.; Wiesendanger, R.; von Bergmann, K.; Kubetzka, A. Discovery and Characterization of a New Type of Domain Wall in a Row-Wise Antiferromagnet. *Nat Commun* **2021**, *12* (1), 3488. https://doi.org/10.1038/s41467-021-23760-2.

(40) Bossini, D.; Pancaldi, M.; Soumah, L.; Basini, M.; Mertens, F.; Cinchetti, M.; Satoh, T.; Gomonay, O.; Bonetti, S. Ultrafast Amplification and Nonlinear Magnetoelastic Coupling of Coherent Magnon Modes in an Antiferromagnet. *Phys. Rev. Lett.* **2021**, *127* (7), 077202. https://doi.org/10.1103/PhysRevLett.127.077202.

(41) Stöhr, J.; Scholl, A.; Regan, T. J.; Anders, S.; Lüning, J.; Scheinfein, M. R.; Padmore, H. A.; White, R. L. Images of the Antiferromagnetic Structure of a NiO(100) Surface by Means of X-Ray Magnetic Linear Dichroism Spectromicroscopy. *Phys. Rev. Lett.* **1999**, *83* (9), 1862–1865. https://doi.org/10.1103/PhysRevLett.83.1862.

(42) Arai, K.; Okuda, T.; Tanaka, A.; Kotsugi, M.; Fukumoto, K.; Ohkochi, T.; Nakamura, T.; Matsushita, T.; Muro, T.; Oura, M.; Senba, Y.; Ohashi, H.; Kakizaki, A.; Mitsumata, C.; Kinoshita, T. Three-Dimensional Spin Orientation in Antiferromagnetic Domain Walls of NiO Studied by x-Ray Magnetic Linear Dichroism Photoemission Electron Microscopy. *Phys. Rev. B* **2012**, *85* (10), 104418. https://doi.org/10.1103/PhysRevB.85.104418.

(43) Meer, H.; Wust, S.; Schmitt, C.; Herrgen, P.; Fuhrmann, F.; Hirtle, S.; Bednarz, B.; Rajan, A.; Ramos, R.; Niño, M. A.; Foerster, M.; Kronast, F.; Kleibert, A.; Rethfeld, B.; Saitoh, E.; Stadtmüller, B.; Aeschlimann, M.; Kläui, M. Laser-Induced Creation of Antiferromagnetic 180-Degree Domains in NiO/Pt Bilayers. *Advanced Functional Materials* **2023**, *33* (21), 2213536. https://doi.org/10.1002/adfm.202213536.

(44) Schmitt, C.; Baldrati, L.; Sanchez-Tejerina, L.; Schreiber, F.; Ross, A.; Filianina, M.; Ding, S.; Fuhrmann, F.; Ramos, R.; Maccherozzi, F.; Backes, D.; Mawass, M.-A.; Kronast, F.; Valencia, S.; Saitoh, E.; Finocchio, G.; Kläui, M. Identification of Néel Vector Orientation in Antiferromagnetic Domains Switched by Currents in Ni O / Pt Thin Films. *Phys. Rev. Applied* **2021**, *15* (3),

034047. https://doi.org/10.1103/PhysRevApplied.15.034047.
(45) Schmitt, C.; Sanchez-Tejerina, L.; Filianina, M.; Fuhrmann, F.; Meer, H.; Ramos, R.; Maccherozzi, F.; Backes, D.; Saitoh, E.; Finocchio, G.; Baldrati, L.; Kläui, M. Identifying the Domain-Wall Spin Structure in Antiferromagnetic NiO/Pt. *Phys. Rev. B* **2023**, *107* (18), 184417. https://doi.org/10.1103/PhysRevB.107.184417.
(46) Roth, W. L. Neutron and Optical Studies of Domains in NiO. *Journal of Applied Physics* **1960**, *31* (11), 2000–2011. https://doi.org/10.1063/1.1735486.
(47) Moriyama, T.; Sánchez-Tejerina, L.; Oda, K.; Ohkochi, T.; Kimata, M.; Shiota, Y.; Nojiri, H.; Finocchio, G.; Ono, T. Micromagnetic Understanding of Evolutions of Antiferromagnetic Domains in NiO. *Phys. Rev. Materials* **2023**, *7* (5), 054401. https://doi.org/10.1103/PhysRevMaterials.7.054401.
(48) Sickafus, K. E.; Wills, J. M.; Grimes, N. W. Structure of Spinel. *Journal of the American Ceramic Society* **1999**, *82* (12), 3279–3292. https://doi.org/10.1111/j.1151-2916.1999.tb02241.x.
(49) Lyder Andersen, H.; Saura-Múzquiz, M.; Granados-Miralles, C.; Canévet, E.; Lock, N.; Christensen, M. Crystalline and Magnetic Structure–Property Relationship in Spinel Ferrite Nanoparticles. *Nanoscale* **2018**, *10* (31), 14902–14914. https://doi.org/10.1039/C8NR01534A.
(50) De Santis, M.; Bailly, A.; Coates, I.; Grenier, S.; Heckmann, O.; Hricovini, K.; Joly, Y.; Langlais, V.; Ramos, A. Y.; Richter, C.; Torrelles, X.; Garaudée, S.; Geaymond, O.; Ulrich, O. Epitaxial Growth and Structure of Cobalt Ferrite Thin Films with Large Inversion Parameter on Ag(001). *Acta Cryst B* **2019**, *75* (1), 8–17. https://doi.org/10.1107/S2052520618016177.
(51) Shannon, R. D. Revised Effective Ionic Radii and Systematic Studies of Interatomic Distances in Halides and Chalcogenides. *Acta Cryst A* **1976**, *32* (5), 751–767. https://doi.org/10.1107/S0567739476001551.
(52) Pinho, P. V. B.; Chartier, A.; Menut, D.; Barbier, A.; Hunault, M. O. J. Y.; Ohresser, P.; Marcelot, C.; Warot-Fonrose, B.; Miserque, F.; Moussy, J.-B. Stoichiometry Driven Tuning of Physical Properties in Epitaxial Fe3-xCrxO4 Thin Films. *Applied Surface Science* **2023**, *615*, 156354. https://doi.org/10.1016/j.apsusc.2023.156354.
(53) Navrotsky, A.; Kleppa, O. J. The Thermodynamics of Cation Distributions in Simple Spinels. *Journal of Inorganic and Nuclear Chemistry* **1967**, *29* (11), 2701–2714. https://doi.org/10.1016/0022-1902(67)80008-3.
(54) Dunitz, J. D.; Orgel, L. E. Electronic Properties of Transition-Metal Oxides-II: Cation Distribution amongst Octahedral and Tetrahedral Sites. *Journal of Physics and Chemistry of Solids* **1957**, *3* (3), 318–323. https://doi.org/10.1016/0022-3697(57)90035-5.
(55) Néel, M. L. Propriétés magnétiques des ferrites; ferrimagnétisme et antiferromagnétisme. *Ann. Phys.* **1948**, *12* (3), 137–198.

https://doi.org/10.1051/anphys/194812030137.
(56) Kramers, H. A. L'interaction Entre Les Atomes Magnétogènes Dans Un Cristal Paramagnétique. *Physica* **1934**, *1* (1), 182–192. https://doi.org/10.1016/S0031-8914(34)90023-9.
(57) Anderson, P. W. New Approach to the Theory of Superexchange Interactions. *Phys. Rev.* **1959**, *115* (1), 2–13. https://doi.org/10.1103/PhysRev.115.2.
(58) Anderson, P. W. Ordering and Antiferromagnetism in Ferrites. *Phys. Rev.* **1956**, *102* (4), 1008–1013. https://doi.org/10.1103/PhysRev.102.1008.
(59) Goodenough, J. B. Theory of the Role of Covalence in the Perovskite-Type Manganites [La, M(II)]MnO$_{3}$. *Phys. Rev.* **1955**, *100* (2), 564–573. https://doi.org/10.1103/PhysRev.100.564.
(60) Goodenough, J. B. An Interpretation of the Magnetic Properties of the Perovskite-Type Mixed Crystals *La*1−x*Srx*C*o*O3−λ. *Journal of Physics and Chemistry of Solids* **1958**, *6* (2), 287–297. https://doi.org/10.1016/0022-3697(58)90107-0.
(61) Kanamori, J. Superexchange Interaction and Symmetry Properties of Electron Orbitals. *Journal of Physics and Chemistry of Solids* **1959**, *10* (2), 87–98. https://doi.org/10.1016/0022-3697(59)90061-7.
(62) Pinho, P. V. B. Experimental and Theoretical Study on Fe-Cr-O Thin Films : From Fine Structure to Macroscopic Behavior. phdthesis, Université Paris-Saclay, 2022. https://theses.hal.science/tel-03917144 (accessed 2024-04-19).
(63) Zener, C. Interaction Between the d Shells in the Transition Metals. *Phys. Rev.* **1951**, *81* (3), 440–444. https://doi.org/10.1103/PhysRev.81.440.
(64) O'Reilly, W. The Atomic Basis of Magnetism. In *Rock and Mineral Magnetism*; O'Reilly, W., Ed.; Springer US: Boston, MA, 1984; pp 30–57. https://doi.org/10.1007/978-1-4684-8468-7_3.
(65) Yafet, Y.; Kittel, C. Antiferromagnetic Arrangements in Ferrites. *Phys. Rev.* **1952**, *87* (2), 290–294. https://doi.org/10.1103/PhysRev.87.290.
(66) Francombe, M. H. Lattice Changes in Spinel-Type Iron Chromites. *Journal of Physics and Chemistry of Solids* **1957**, *3* (1), 37–43. https://doi.org/10.1016/0022-3697(57)90045-8.
(67) Steinsvoll, O. Measurements of Critical Exponents and the Magnetic Equation of State in Fe $_3$ O $_4$ by Polarized Neutron Scattering. *Phys. Scr.* **1982**, *26* (2), 119–128. https://doi.org/10.1088/0031-8949/26/2/011.
(68) Liu, X.; Zhong, Z.; Tang, Y.; Liang, B. Review on the Synthesis and Applications of Fe3O4 Nanomaterials. *Journal of Nanomaterials* **2013**, *2013* (1), 902538. https://doi.org/10.1155/2013/902538.
(69) Wang, X.; Liao, Y.; Zhang, D.; Wen, T.; Zhong, Z. A Review of Fe3O4 Thin Films: Synthesis, Modification and Applications. *Journal of Materials Science & Technology* **2018**, *34* (8), 1259–1272.

https://doi.org/10.1016/j.jmst.2018.01.011.

(70) Nakagiri, N.; Manghnani, M. H.; Ming, L. C.; Kimura, S. Crystal Structure of Magnetite under Pressure. *Phys Chem Minerals* **1986**, *13* (4), 238–244. https://doi.org/10.1007/BF00308275.

(71) Verwey, E. J. W.; Heilmann, E. L. Physical Properties and Cation Arrangement of Oxides with Spinel Structures I. Cation Arrangement in Spinels. *The Journal of Chemical Physics* **1947**, *15* (4), 174–180. https://doi.org/10.1063/1.1746464.

(72) Samuelsen, E. J.; Bleeker, E. J.; Dobrzynski, L.; Riste, T. Neutron Scattering from Magnetite below 119°K. *Journal of Applied Physics* **1968**, *39* (2), 1114–1115. https://doi.org/10.1063/1.1656188.

(73) Medrano, C.; Schlenker, M.; Baruchel, J.; Espeso, J.; Miyamoto, Y. Domains in the Low-Temperature Phase of Magnetite from Synchrotron-Radiation x-Ray Topographs. *Phys. Rev. B* **1999**, *59* (2), 1185–1195. https://doi.org/10.1103/PhysRevB.59.1185.

(74) Ihle, D.; Lorenz, B. Small-Polaron Band versus Hopping Conduction in Fe3O4. *J. Phys. C: Solid State Phys.* **1985**, *18* (21), L647. https://doi.org/10.1088/0022-3719/18/21/004.

(75) Seneor, P.; Fert, A.; Maurice, J.-L.; Montaigne, F.; Petroff, F.; Vaurès, A. Large Magnetoresistance in Tunnel Junctions with an Iron Oxide Electrode. *Applied Physics Letters* **1999**, *74* (26), 4017–4019. https://doi.org/10.1063/1.123246.

(76) Ziemniak, S.; Anovitz, L.; Castelli, R.; Porter, W. Magnetic Contribution to Heat Capacity and Entropy of Nickel Ferrite (NiFe2O4). *Journal of Physics and Chemistry of Solids - J PHYS CHEM SOLIDS* **2006**, *4582*, 1–12. https://doi.org/10.1016/j.jpcs.2006.07.015.

(77) Gopale, S. B.; Kakade, G. N.; Kulkarni, G. D.; Vinayak, V.; Jadhav, S. P.; Jadhav, K. M. X-Ray Diffraction, Infrared and Magnetic Studies of $NiFe_2O_4$ Nanoparticles. *J. Phys.: Conf. Ser.* **2020**, *1644* (1), 012010. https://doi.org/10.1088/1742-6596/1644/1/012010.

(78) Jundale, V. A.; Patil, D. A.; Yadav, A. A. Preparation and Characterization of $NiFe_2O_4$ Thin Films for Supercapacitor Applications. *Phase Transitions* **2022**, *95* (11), 786–802. https://doi.org/10.1080/01411594.2022.2122825.

(79) Liu, J.; Yang, H.; Xue, X. Structure, Morphology, and Magnetic Properties of NiFe2O4 Powder Prepared by Molten Salt Method. *Powder Technology* **2019**, *355*, 708–715. https://doi.org/10.1016/j.powtec.2019.07.047.

(80) Zabotto, F. L.; Gualdi, A. J.; Eiras, J. A.; Oliveira, A. J. A. de; Garcia, D. Influence of the Sintering Temperature on the Magnetic and Electric Properties of NiFe2O4 Ferrites. *Mat. Res.* **2012**, *15*, 428–433. https://doi.org/10.1590/S1516-14392012005000043.

(81) Yearian, H. J.; Kortright, J. M.; Langenheim, R. H. Lattice Parameters of the FeFe(2—x)CrxO4 Spinel System. *The Journal of Chemical Physics* **1954**, *22*

(7), 1196–1198. https://doi.org/10.1063/1.1740331.

(82) Ziemniak, S. E.; Castelli, R. A. Immiscibility in the Fe3O4–FeCr2O4 Spinel Binary. *Journal of Physics and Chemistry of Solids* **2003**, *64* (11), 2081–2091. https://doi.org/10.1016/S0022-3697(03)00237-3.

(83) Ma, J.; Garlea, V. O.; Rondinone, A.; Aczel, A. A.; Calder, S.; Dela Cruz, C.; Sinclair, R.; Tian, W.; Chi, S.; Kiswandhi, A.; Brooks, J. S.; Zhou, H. D.; Matsuda, M. Magnetic and Structural Phase Transitions in the Spinel Compound Fe 1 + x Cr 2 − x O 4. *Phys. Rev. B* **2014**, *89* (13), 134106. https://doi.org/10.1103/PhysRevB.89.134106.

(84) Shirane, G.; Cox, D. E.; Pickart, S. J. Magnetic Structures in FeCr2S4 and FeCr2O4. *Journal of Applied Physics* **1964**, *35* (3), 954–955. https://doi.org/10.1063/1.1713556.

(85) Bakar, S. A.; Soltani, N.; Yunus, W. M. M.; Saion, E.; Bahrami, A. Structural and Paramagnetic Behavior of Spinel NiCr2O4 Nanoparticles Synthesized by Thermal Treatment Method: Effect of Calcination Temperature. *Solid State Communications* **2014**, *192*, 15–19. https://doi.org/10.1016/j.ssc.2014.05.002.

(86) Ziemniak, S. E.; Gaddipati, A. R.; Sander, P. C. Immiscibility in the NiFe2O4–NiCr2O4 Spinel Binary. *Journal of Physics and Chemistry of Solids* **2005**, *66* (6), 1112–1121. https://doi.org/10.1016/j.jpcs.2005.01.009.

(87) Javed, M.; Khan, A. A.; Kazmi, J.; Mohamed, M. A.; Khan, M. N.; Hussain, M.; Bilkees, R. Dielectric Relaxation and Small Polaron Hopping Transport in Sol-Gel-Derived NiCr2O4 Spinel Chromite. *Materials Research Bulletin* **2021**, *138*, 111242. https://doi.org/10.1016/j.materresbull.2021.111242.

(88) Crottaz, O.; Kubel, F.; Schmid, H. Jumping Crystals of the Spinels NiCr2O4 and CuCr2O4. *J. Mater. Chem.* **1997**, *7* (1), 143–146. https://doi.org/10.1039/a604758k.

(89) Tomiyasu, K.; Kagomiya, I. Magnetic Structure of $NiCr_2O_4$ Studied by Neutron Scattering and Magnetization Measurements. *J. Phys. Soc. Jpn.* **2004**, *73* (9), 2539–2542. https://doi.org/10.1143/JPSJ.73.2539.

(90) Ishibashi, H.; Yasumi, T. Structural Transition of Spinel Compound NiCr2O4 at Ferrimagnetic Transition Temperature. *Journal of Magnetism and Magnetic Materials* **2007**, *310* (2, Part 2), e610–e612. https://doi.org/10.1016/j.jmmm.2006.10.1131.

(91) Robbins, M.; Wertheim, G. K.; Sherwood, R. C.; Buchanan, D. N. E. Magnetic Properties and Site Distributions in the System FeCr2O4-Fe3O4(Fe2+Cr2−xFex3+O4. *Journal of Physics and Chemistry of Solids* **1971**, *32* (3), 717–729. https://doi.org/10.1016/S0022-3697(71)80412-2.

(92) Grutzeck, M. W.; Muan, A. Liquid–Solid Equilibria in the System FeO–NiO–Fe2O3–SiO2. *Journal of the American Ceramic Society* **1992**, *75* (6), 1342–1350. https://doi.org/10.1111/j.1151-2916.1992.tb04192.x.

(93) Orehotsky, J.; Davidson, C. R. MAGNETIC PROPERTIES OF FINE PARTICLE

NixFe3 - xO4 SPINELS. *Magnetism letters* **1980**, *1*, 117–122.

(94) Larumbe, S.; Gomez-Polo, C.; Pérez-Landazábal, J. I.; García-Prieto, A.; Alonso, J.; Fdez-Gubieda, M. L.; Cordero, D.; Gómez, J. Ni Doped Fe_3O_4 Magnetic Nanoparticles. *j nanosci nanotechnol* **2012**, *12* (3), 2652–2660. https://doi.org/10.1166/jnn.2012.5769.

(95) Frolova, L. A. Characterization of $Ni_xFe_{3-x}O_4$ Dispersed Particles Obtained by the Plasma Method. *Molecular Crystals and Liquid Crystals* **2018**, *661* (1), 6–11. https://doi.org/10.1080/15421406.2018.1460229.

(96) Iranmanesh, P.; Tabatabai Yazdi, Sh.; Mehran, M. Effect of Ni Substitution on Structural, Optical and Magnetic Properties of Ferrite Nanoparticles Synthesized by Co-Precipitation Route. *Materials Science and Engineering: B* **2019**, *251*, 114442. https://doi.org/10.1016/j.mseb.2019.114442.

(97) Deepak, F. L.; Bañobre-López, M.; Carbó-Argibay, E.; Cerqueira, M. F.; Piñeiro-Redondo, Y.; Rivas, J.; Thompson, C. M.; Kamali, S.; Rodríguez-Abreu, C.; Kovnir, K.; Kolen'ko, Y. V. A Systematic Study of the Structural and Magnetic Properties of Mn-, Co-, and Ni-Doped Colloidal Magnetite Nanoparticles. *J. Phys. Chem. C* **2015**, *119* (21), 11947–11957. https://doi.org/10.1021/acs.jpcc.5b01575.

(98) Rana, G.; Johri, U. C. A Study on Structural and Magnetic Properties of Ni-Substituted Magnetite Nanoparticles. *Journal of Alloys and Compounds* **2013**, *577*, 376–381. https://doi.org/10.1016/j.jallcom.2013.05.184.

(99) Jin, C.; Zhang, Q.; Mi, W. B.; Jiang, E. Y.; Bai, H. L. Tunable Magnetic and Electrical Properties of Polycrystalline and Epitaxial $Ni_xFe_{3-x}O_4$ Thin Films Prepared by Reactive Co-Sputtering. *J. Phys. D: Appl. Phys.* **2010**, *43* (38), 385001. https://doi.org/10.1088/0022-3727/43/38/385001.

(100) Kim, K. J.; Kim, M. H.; Kim, C. S. Structural Phase Transition, Electronic Structure, and Magnetic Properties of Sol-Gel-Prepared Inverse-Spinel Nickel-Ferrites Thin Films. *Journal of Magnetics* **2014**, *19* (2), 111–115. https://doi.org/10.4283/JMAG.2014.19.2.111.

(101) Gilabert, J.; Palacios, M. D.; Orts, M. J.; Mestre, S. Solution Combustion Synthesis of (Ni,Fe)Cr2O4 Pigments: Effect of Post-Synthesis Thermal Treatments. *Ceramics International* **2017**, *43* (15), 12789–12798. https://doi.org/10.1016/j.ceramint.2017.06.168.

(102) Kurepin, V. A.; Kulik, D. A.; Hitpold, A.; Nicolet, M. *Thermodynamic Modelling of Fe-Cr-Ni-Spinel Formation at the Light-Water Reactor Conditions*; 1019–0643; Switzerland, 2002; p 98.

(103) Allen, G. C.; Jutson, J. A.; Tempest, P. A. Characterization of Nickel-Chromium-Iron Spinel-Type Oxides. *Journal of Nuclear Materials* **1988**, *158*, 96–107. https://doi.org/10.1016/0022-3115(88)90159-6.

(104) Hosterman, B. D. Raman Spectroscopic Study of Solid Solution Spinel Oxides, University of Nevada, Las Vegas. https://doi.org/10.34917/2476131.

(105) Rais, A.; Gismelseed, A. M.; Al-Omari, I. A. Cation Distribution and Magnetic

Properties of Nickel-Chromium Ferrites NiCrxFe2-xO4 (0 ≤x ≤ 1.4). *phys. stat. sol. (b)* **2005**, *242* (7), 1497–1503. https://doi.org/10.1002/pssb.200440022.

(106) Lee, S. H.; Yoon, S. J.; Lee, G. J.; Kim, H. S.; Yo, C. H.; Ahn, K.; Lee, D. H.; Kim, K. H. Electrical and Magnetic Properties of NiCrxFe2ÀxO4 Spinel (0 x 0.6). *Materials Chemistry and Physics* **1999**, 6.

(107) Jahan, N.; Chowdhury, F.-Z.; Zakaria, A. K. M. Structural and Electrical Properties of Chromium Substituted Nickel Ferrite by Conventional Ceramic Method. *Materials Science-Poland* **2016**, *34* (1), 185–191. https://doi.org/10.1515/msp-2016-0028.

(108) Azam, M.; Adeela, N.; Khan, U.; Riaz, S.; Iqbal, M.; Naseem, S. Structural and Magnetic Investigations of Cr Substituted NiFe2O4 Nanostructures. *Journal of Alloys and Compounds* **2017**, *698*, 228–233. https://doi.org/10.1016/j.jallcom.2016.12.161.

(109) Jahan, N.; Chowdhury, F.-U.-Z.; Zakaria, A. K. M.; Khan, M. N. I.; Aktar, M. S.; Hakim, M. A. Manipulation of Magnetic Properties of Cr-Substituted Ni Ferrite Synthesized by Conventional Ceramic Technique. *J Supercond Nov Magn* **2017**, *30* (1), 261–268. https://doi.org/10.1007/s10948-016-3713-x.

(110) Chandrasekaran, S.; Bowen, C.; Zhang, P.; Li, Z.; Yuan, Q.; Ren, X.; Deng, L. Spinel Photocatalysts for Environmental Remediation, Hydrogen Generation, CO 2 Reduction and Photoelectrochemical Water Splitting. *Journal of Materials Chemistry A* **2018**, *6* (24), 11078–11104. https://doi.org/10.1039/C8TA03669A.

(111) Tatarchuk, T.; Al-Najar, B.; Bououdina, M.; Ahmed, M. Catalytic and Photocatalytic Properties of Oxide Spinels; 2018. https://doi.org/10.1007/978-3-319-48281-1_158-1.

(112) Kovalenko, A.; Singh Yadav, R.; Pospisil, J.; Zmeskal, O.; Karashanova, D.; Heinrichová, P.; Vala, M.; Havlica, J.; Weiter, M. Towards Improved Efficiency of Bulk-Heterojunction Solar Cells Using Various Spinel Ferrite Magnetic Nanoparticles. *Organic Electronics* **2016**, *39*, 118–126. https://doi.org/10.1016/j.orgel.2016.09.033.

(113) Kirankumar, V. S.; Sumathi, S. A Review on Photodegradation of Organic Pollutants Using Spinel Oxide. *Materials Today Chemistry* **2020**, *18*, 100355. https://doi.org/10.1016/j.mtchem.2020.100355.

(114) Yew, Y. P.; Shameli, K.; Miyake, M.; Ahmad Khairudin, N. B. B.; Mohamad, S. E. B.; Naiki, T.; Lee, K. X. Green Biosynthesis of Superparamagnetic Magnetite Fe3O4 Nanoparticles and Biomedical Applications in Targeted Anticancer Drug Delivery System: A Review. *Arabian Journal of Chemistry* **2020**, *13* (1), 2287–2308. https://doi.org/10.1016/j.arabjc.2018.04.013.

(115) Althammer, M.; Meyer, S.; Nakayama, H.; Schreier, M.; Altmannshofer, S.; Weiler, M.; Huebl, H.; Geprägs, S.; Opel, M.; Gross, R.; Meier, D.; Klewe, C.; Kuschel, T.; Schmalhorst, J.-M.; Reiss, G.; Shen, L.; Gupta, A.; Chen, Y.-T.;

Bauer, G. E. W.; Saitoh, E.; Goennenwein, S. T. B. Quantitative Study of the Spin Hall Magnetoresistance in Ferromagnetic Insulator/Normal Metal Hybrids. *Phys. Rev. B* **2013**, *87* (22), 224401. https://doi.org/10.1103/PhysRevB.87.224401.

(116) Bataille, A. Etude des propriétés physiques des films de Fe3O4 épitaxiés et de la polarisation en spin à l'interface Fe3O4/γ-Al2O3. phdthesis, Université Paris Sud - Paris XI, 2005. https://theses.hal.science/tel-00085941 (accessed 2024-09-16).

(117) Bibes, M.; Barthelemy, A. Oxide Spintronics. *IEEE Transactions on Electron Devices* **2007**, *54* (5), 1003–1023. https://doi.org/10.1109/TED.2007.894366.

(118) Žutić, I.; Fabian, J.; Das Sarma, S. Spintronics: Fundamentals and Applications. *Rev. Mod. Phys.* **2004**, *76* (2), 323–410. https://doi.org/10.1103/RevModPhys.76.323.

(119) Alexe, M.; Ziese, M.; Hesse, D.; Esquinazi, P.; Yamauchi, K.; Fukushima, T.; Picozzi, S.; Gösele, U. Ferroelectric Switching in Multiferroic Magnetite (Fe_3O_4) Thin Films. *Advanced Materials* **2009**, *21* (44), 4452–4455. https://doi.org/10.1002/adma.200901381.

(120) Matzen, S.; Moussy, J.-B.; Wei, P.; Gatel, C.; Cezar, J. C.; Arrio, M. A.; Sainctavit, Ph.; Moodera, J. S. Structure, Magnetic Ordering, and Spin Filtering Efficiency of NiFe2O4(111) Ultrathin Films. *Applied Physics Letters* **2014**, *104* (18), 182404. https://doi.org/10.1063/1.4871733.

(121) Boni, G. A.; Hrib, L.; Porter, S. B.; Atcheson, G.; Pintilie, I.; Rode, K.; Pintilie, L. Electrical Properties of NiFe2O4 Epitaxial Ultra-Thin Films. *J Mater Sci* **2017**, *52* (2), 793–803. https://doi.org/10.1007/s10853-016-0376-8.

(122) Hoppe, M. *Magnetic, Structural, and Electronic Properties of NiFe2O4 Ultrathin Films*; Schriften des Forschungszentrums Jülich Reihe Schlüsseltechnologien; Forschungszentrum Jülich: Jülich, 2016.

(123) Jaffari, G. H.; Rumaiz, A. K.; Woicik, J. C.; Shah, S. I. Influence of Oxygen Vacancies on the Electronic Structure and Magnetic Properties of NiFe2O4 Thin Films. *Journal of Applied Physics* **2012**, *111* (9), 093906. https://doi.org/10.1063/1.4704690.

(124) Klewe, C.; Meinert, M.; Boehnke, A.; Kuepper, K.; Arenholz, E.; Gupta, A.; Schmalhorst, J.-M.; Kuschel, T.; Reiss, G. Physical Characteristics and Cation Distribution of NiFe2O4 Thin Films with High Resistivity Prepared by Reactive Co-Sputtering. *Journal of Applied Physics* **2014**, *115* (12), 123903. https://doi.org/10.1063/1.4869400.

(125) Regmi, S.; Li, Z.; Srivastava, A.; Mahat, R.; KC, S.; Rastogi, A.; Galazka, Z.; Datta, R.; Mewes, T.; Gupta, A. Structural and Magnetic Properties of NiFe2O4 Thin Films Grown on Isostructural Lattice-Matched Substrates. *Applied Physics Letters* **2021**, *118* (15), 152402. https://doi.org/10.1063/5.0047865.

(126) Gota, S.; Moussy, J.-B.; Henriot, M.; Guittet, M.-J.; Gautier-Soyer, M. Atomic-Oxygen-Assisted MBE Growth of Fe3O4 (1 1 1) on α-Al2O3 (0 0 0 1).

Surface Science **2001**, *482–485*, 809–816. https://doi.org/10.1016/S0039-6028(00)01066-9.

(127) Marchetti, L. Corrosion généralisée des alliages à base nickel en milieu aqueux à haute température : Apport à la compréhension des mécanismes. phdthesis, Ecole Nationale Supérieure des Mines de Saint-Etienne, 2007. https://theses.hal.science/tel-00991918 (accessed 2024-08-15).

(128) Mahesh, B. V.; Singh Raman, R. K.; Koch, C. C. Resistance of Nanostructured Fe-Cr Alloys to Oxidative Degradation: Role of Zr and Cr Contents | Metallurgical and Materials Transactions A. **2015**, *46*, 1814–1824.

(129) Wood, G. C. High-Temperature Oxidation of Alloys. **1970**.

(130) Evans, R. F. L.; Fan, W. J.; Chureemart, P.; Ostler, T. A.; Ellis, M. O. A.; Chantrell, R. W. Atomistic Spin Model Simulations of Magnetic Nanomaterials. *J. Phys.: Condens. Matter* **2014**, *26* (10), 103202. https://doi.org/10.1088/0953-8984/26/10/103202.

(131) Evans, R. F. L.; Atxitia, U.; Chantrell, R. W. Quantitative Simulation of Temperature-Dependent Magnetization Dynamics and Equilibrium Properties of Elemental Ferromagnets. *Phys. Rev. B* **2015**, *91* (14), 144425. https://doi.org/10.1103/PhysRevB.91.144425.

2 ATOMIC SCALE STRUCTURE OF DOMAIN WALLS IN NIO

The second chapter of this thesis is a study of the magnetic domain wall (DW) in NiO. Herein, the methodology adopted is atomic spin dynamics, with the Vampire code. After the parameterization of the main variables, two types of DW are simulated. The simulated DWs are analyzed using NVM and XMLD-like techniques. The T-wall, the magnetic transition from one T-domain to another, reveals intriguing mechanisms. Indeed, a splitting zone is observed, corresponding to the breaking of the in-plane FM alignment, while maintaining the overall AF alignment.

2 ATOMIC SCALE STRUCTURE OF DOMAIN WALLS IN NIO

The following sections present the magnetic structure of NiO and the methodology adopted for the simulation of domain walls (DWs). The Hamiltonian comprised three parts. The super-exchange and anisotropy constants are determined, which enables the simulations of "T" and "S" domain walls. Subsequently, the various analytical techniques are outlined. These techniques are inspired from X-ray Magnetic Linear Dichroism (XMLD) and Nitrogen Vacancy Magnetometry (NVM). As a conclusion, the results are presented: the atomic spin behavior and their associated physical properties.

2.1 MAGNETIC STRUCTURE OF NIO

Herein, the structure of NiO is presented, followed by its magnetic structure and the link between the magnetic structure and the crystallographic structure, which is magnetostriction.

The structure of NiO is a rocksalt (halite, space group 225), with a lattice parameter a = 4.17-4.19 Å[1,2]. Below the Néel temperature of 523 K[1–3], NiO exhibits an antiferromagnetic (AF) order of type G. In this specific type of AF order, two directions are of particular importance:

- The stacking direction: the experimentally observed AF order consists of ferromagnetic (FM) planes that alternate in one direction. In the case of NiO, this direction is one of the four [111] directions that exist in a cubic crystal. The four red arrows, illustrated in Figure 2.1 (a), indicate the four equivalent [111] directions (respectively $[111]$, $[\bar{1}11]$, $[1\bar{1}1]$, $[11\bar{1}]$, see Table 2.1). It can be observed that they have a T_d symmetry. Furthermore, the atomic spins are fixed in these (111) planes. These directions are designated as the T-domain.
- The spin direction: in the case of NiO, three easy-axis spin directions are favored. This is one of the six $[11\bar{2}]$ directions. As NiO exhibits AF behavior, only three $[11\bar{2}]$ directions are distinguishable. This direction is referred to as the S-domain. In Figure 2.1 (b), the three in-plane arrows indicate the three $[11\bar{2}]$ directions in the case of T [111] (respectively $[\bar{2}11]$, $[1\bar{2}1]$, $[11\bar{2}]$, see Table 2.1). They point to the three corners of an equilateral triangle. The angle between two S directions is 120°. The two blue colored planes represent the FM planes, which alternate along the out-of-plane arrow (T direction).

Consequently, NiO exhibits 12 distinct magnetic domains within a single crystal.

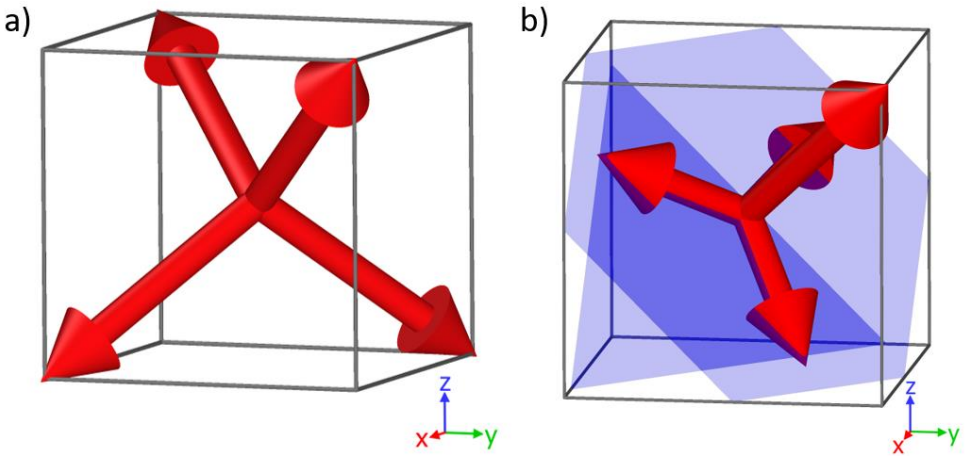

Figure 2.1: a) T directions in a cubic lattice. b) In the case of T [111] domain, the T and S directions are indicated.

Furthermore, the magnetic order of NiO is associated with the crystalline structure of NiO through magnetostriction[2]. A primary deformation is linked to the T-domain, exhibiting a slight contraction along the T-directions (the [111] directions), which removes the degeneracy of the first coordination shell around one Ni atom. The second deformation is linked to the direction of the S-domain ($[\bar{2}11]$ directions), though it is relatively weak and challenging to observe[2,4,5]. In the following discussion, only the magnetostriction associated with the T-domain will be considered.

Table 2.1 provides an overview of the different T domains and their respective S domains. These notations will be utilized throughout the subsequent chapter. For instance, when a T1S2 domain is formed, it refers to a T1 domain, which is characterized by a [111] contraction axis and an easy axis spin direction along $[1\bar{2}1]$, which is the S2 direction corresponding to T1 domain.

Table 2.1: Summary of the twelve magnetic domains in NiO. The contraction axis (T direction, the FM planes alternating directions) and the S domain (easy axis direction for atomic spins) are highlighted. The three S directions are all at 90° with respect to the contraction axis.

	T1	T2	T3	T4
Contraction axis	[111]	$[11\bar{1}]$	$[1\bar{1}1]$	$[\bar{1}11]$
S1	$[\bar{2}11]$	$[\bar{2}1\bar{1}]$	$[\bar{2}\bar{1}1]$	[211]
S2	$[1\bar{2}1]$	$[1\bar{2}\bar{1}]$	[121]	$[\bar{1}\bar{2}1]$
S3	$[11\bar{2}]$	[112]	$[1\bar{1}\bar{2}]$	$[\bar{1}1\bar{2}]$

2.2 METHODS FOR DOMAIN WALL SIMULATION

The adopted methodology to simulate DW is based on Atomic Spin Dynamic (ASD) with the Vampire code[6,7]. This section presents the theoretical considerations, the parametrization of each part of the Hamiltonian and the construction of the DWs.

2.2.1 Heisenberg Hamiltonian

The complex magnetic structure of NiO is described by using a classical Heisenberg Hamiltonian $\mathcal{H}_{TS}$ on a rigid face-centered cubic (fcc) lattice for nickel ions as follow:

$$\mathcal{H}_{TS} = -\sum_{i<j} J_{ij}\boldsymbol{S_i}\boldsymbol{S_j} - K_u^T \sum_i (\boldsymbol{u_T}\cdot\boldsymbol{S_i})^2 - K_u^S \sum_i (\boldsymbol{u_S}\cdot\boldsymbol{S_i})^2 \qquad (2.1)$$

In Equation (2.1), three terms are employed: the first term describes super-exchange interactions in NiO. The second term imposes the T domain, while the third term imposes the S domain.

The first term represents the conventional description of the super-exchange interaction. $\mathbf{S_i}$ and $\mathbf{S_j}$ represent the two interacting spins on site i and j, with the same magnitude of magnetic moment, $||\mathbf{S_i}|| = ||\mathbf{S_j}|| = 2\ \mu_B$. In the case of NiO, super-exchange interactions up to the fourth coordination shell have been obtained[1]. In this instance, the most significant exchanges originate from the first two coordination shells. The two coordination shells and the super-exchange constants between the different Ni atoms are illustrated schematically in Figure 2.2.

The first coordination shell is composed of 12 nearest neighbors (NN) interactions surrounding a central nickel atom, at a distance of $a/\sqrt{2} \approx 2.96$ Å (a=4.18 Å) with the sequence Ni-O-Ni forming an angle of 90° through the O atom. This exchange is modeled with the J_1 constant[1,8], which exhibits a relatively weak magnitude and is FM.

The second coordination shell is made of the six next nearest neighbors (NNN), which are at a distance of 4.18 Å, around the central Ni atom. In this case, the Ni-O-Ni sequence forms an angle of 180° through the O atom. This interaction is described by J_2. J_2 is AF and is at least one order of magnitude above J_1[1,9].

Finally, it is important to consider the magnetostriction of NiO. As previously described elsewhere[10], NiO undergoes a crystalline transition at its Néel temperature, to contract along one of the [111] directions (yellow arrows on Figure 2.2). This is linked to the alternating directions of FM planes (T domains).

To provide a comprehensive description of this phenomenon, the J_1 interaction is split into two groups of six interactions each due to the rhombohedral contraction[10]. This splitting also prevents the stabilization of the incorrect type B structure described by Li[11]. The separation between the two J_1 constants is called ΔJ_1 and is added to the J_1 in-plane (in the same T plane) super-exchange constant, resulting in $J_1^+ = J_1^- + \Delta J_1$. The J_1^+ and J_1^- parameters describe, respectively, the in-plane J_1 interaction and the out-of-plane J_1 interaction. In this manner, spin $\mathbf{S_i}$ exhibits an energy preference for FM alignment with the atomic spins $\mathbf{S_j}$ within the same T-plane, and an AF alignment with the six others out-of-plane.

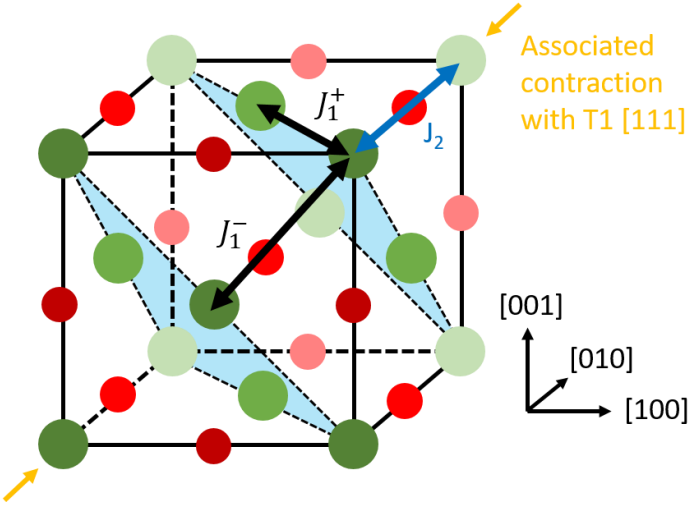

Figure 2.2: Schematic illustration of the super-exchange constants. The green circles represent the Ni atoms, while the red one depict O atoms. The blue planes depict the T1 planes ([111]) and the yellow arrows represent the magnetostriction linked to T1.

The second and third terms in Equation (2.1) describe anisotropy terms that render the T and the S domains, respectively. Both are described with a uniaxial easy axis type of anisotropy. K_u^T is used to render an easy plane orientation, and thus it is chosen negative. Conversely, K_u^S is used to render an easy axis direction, and thus a positive value is used.

The choice of an easy axis anisotropy constant to describe the T and S domains in this Hamiltonian results in the imposition of a single TS domain, which is at odd with others simulations[12], where any S domain can be stabilized from a given T domain (see Table 2.1). However, this constraint is essential for the precise control of the desired TS domain on either side of the DW (see section 2.2.3).

All calculations are conducted using a custom version of the Vampire code[6,7]. In this custom version of the code, two distinct uniaxial constants have been introduced: one for the easy plane orientation K_u^T and another for the easy axis

orientation K_u^S. These two anisotropy constants permits the control of the given TS domain from either side of the magnetic wall.

The supercells employed have dimensions of 26.7×26.7×26.7 nm^3 (1048576 Ni atoms) for an artificially high value of the anisotropy constant K_u^T = J_2. For lower values of the anisotropy constant, down to 10 K_u^T = J_2, supercells with sizes ranging from 106.8×26.7×26.7 nm^3 (4194304 Ni atoms) up to 76×38×38 nm^3 (12058624 Ni atoms) are considered, for $T_{(100)}$ and $T_{(110)}$ DWs, respectively.

The spin configurations are optimized using the Monte Carlo algorithm, which is implemented in the Vampire code, with two stages. The initial stage of the optimization process lasts for 330000 Monte Carlo steps. It begins with a random spin configuration and the application of a high value of ΔJ_1. Subsequently, 320000 Monte Carlo steps are conducted with a reduced value of ΔJ_1 (see below). Each step is conducted at 1 K for DWs. The average configurations are taken from an additional 10000 Monte Carlo steps.

2.2.2 Super-exchange and anisotropy constants determination

The values of the super-exchange constants J_1 and J_2, which relate to the interactions between the central atom and its first and second coordination shells, respectively, have been the subject of numerous experimental[1,3,13–16] and theoretical studies[17–22].

Table 2.2: Theoretical and experimental J_1 and J_2 (in meV). The employed technique is presented in first column, while the J_1 and J_2 are depicted in the final two columns.

Technique	J_1 (meV)	J_2 (meV)
Theoretical		
UHF [18]	0.8	-4.6
CASSCF [18]	0.5	-5.0
CASPT2 [18]	1.2	-16.7
LDA [18]	11.9	-71.3
B3LYP [18]	2.4	-26.7
PBE [22]	1.3	-44.5
Super-exchange [23]	small	-19.8
Experimental		
Neutron scattering [1]	1.35/1.39	-19.0
Raman scattering [13]	small	-18.4

Table 2.2 presents various super-exchange values. While most experimental works report consistent values for both constants, from 1 up to 3 meV for J_1 and from -20 up to -18 meV for J_2, theoretical studies have yielded more disparate results. In particular, theoretical values reported for J_2 range from -71 up to -5 meV[21,22]. It is therefore necessary to investigate their impact on the Néel temperature T_N with the Heisenberg Hamiltonian presented above. For the determination of super-exchange constants, the simulations begin at 1 K with high ΔJ_1 and is repeated with 5 K steps until 801 K is reached.

The adjustment of J_1, ΔJ_1 and J_2 is performed using a single magnetic TS domain, which is defined by the Hamiltonian $\mathcal{H}_{TS}$ (Equation (2.1)). It is evident that the total magnetization of NiO cannot be employed as an order parameter to probe the Néel temperature T_N, as its value is zero. Instead, a staggered magnetization M_S[24] must be calculated for a specific T domain, as defined here:

$$M_s = \left| \sum_i cos(\boldsymbol{Q} \cdot \boldsymbol{r_i}) \cdot \boldsymbol{S_i} \right| \qquad (2.2)$$

In Equation (2.2), the directions of the local spins $\mathbf{S_i}$, situated on position vectors $\mathbf{r_i}$, are inverted with a period defined by $\mathbf{Q}= \pi/a\ \mathbf{u_T}$, where a is the cell parameter and $\mathbf{u_T}$ is the stacking direction of the T domain. As a result, the staggered magnetization M_S exhibits finite values below T_N (see Figure 2.3). The evolution of M_S with temperature T can then be mapped with the following equation:

$$M_s(T) = M_0 \left(1 - \frac{T}{T_N}\right)^{\beta} \qquad (2.3)$$

In Equation (2.3), M_0 represents the staggered magnetization at 0 K (here normalized to $M_0 = 1$), β denotes the critical exponent, and T_N is the Néel temperature.

As might be expected, calculations show that the first neighbor super-exchange constants (J_1^+ and J_1^-) exert a negligible influence on the Néel temperature. It is therefore fixed arbitrarily to 1.76 meV, in agreement with experimental values[1,3,13,15,16]. ΔJ_1 is set to 0.66 meV (thus, J_1^- = 1.76 meV and J_1^+ = 2.42 meV) which is high enough to suppress the degeneracy between the different T domains, to remove the type B structure[11] and to control the T domain wanted. This value is used for the first stage of the optimization of the DWs. It should be noted that ΔJ_1 is decreased to a value of 0.034 meV while the mean of the two previous values is kept constant for the second stage of the optimization mentioned above. Out-of-plane J_1^- and in-plane J_1^+ super-exchange constants are therefore set to 2.078 meV and 2.112 meV, respectively.

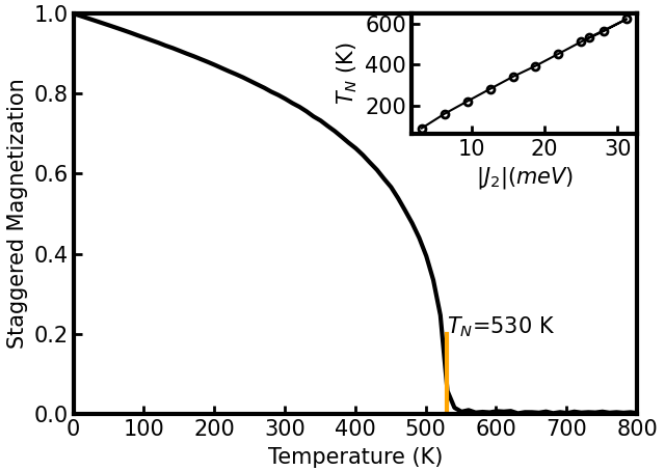

Figure 2.3: Normalized staggered magnetization M_S (T) function of the temperature, calculated using the Heisenberg Hamiltonian (see Equation (2.1)) with J_2= - 26 meV.

The second neighbor super-exchange constant J_2 is intimately related to T_N, as shown by Figure 2.3. T_N varies linearly with J_2 (see the inset of Figure 2.3), and a value of J_2 = - 26 meV gives a Néel temperature T_N = 530 K in good agreement with the experimental value of 523 K[1].

Finally, the ratio of the anisotropy constants K_u^T/K_u^S is fixed at 100 in the range of previous calculations[25,26]. The magnitudes of these parameters have been explored in detail below, with absolute values ranging from 1 to one tenth of J_2 magnitude. Despite the unphysical nature[1] of these values, they permit the simulation of DWs in reasonable supercell sizes and macroscopic situations will be extrapolated from them.

2.2.3 Description of domain walls

Given the presence of 12 magnetic structures within a single crystal, it is reasonable to hypothesize that these domains may interact with one another. In the interaction between two distinct magnetic structures, a magnetic transition zone will be formed, *i.e.* a domain wall, to switch from one domain to the other one. Two different cases can be distinguished. In the first case of DW, a reorientation of the spin vectors occurs without changing the T planes and the contraction axis. This process is designated as an S (spin) domain wall. In the second case of DW, a T DW will be formed, resulting from the alteration of the contraction axis along this wall. This process creates a twin within the crystallographic structure, which is why it is referred to as a T wall.

2.2.3.1 S domain wall

In the case of a S Wall, the T plane remains constant through the DW, while the AF vector undergoes a change from one S domain to another. With one S domain imposed for the left side of the wall, three possibilities for the transition remain:

- S 60° Wall. The magnetic vector will remain on the same T-plane, with a rotation of 60° between the initial and final state. This type of wall has been successfully simulated.
- S 120° Wall. The magnetic vector will remain on the same T-plane too, with a rotation of 120° between the initial and final states. Although the imposed TS at either sides of the DW are identical to those of the S 60° wall (see Table 2.3), the change in direction of rotation, from clockwise to counterclockwise, results in a change in the rotation length, from 60° to 120°. This configuration of wall has been successfully simulated.
- S 180° Wall. This particular S wall is more intricate. Within the same T plane, atomic spins will undergo a transition from one direction to its opposite, thereby effecting a 180° rotation. This particular configuration of wall has not been successfully simulated. It can be observed as an unanticipated outcome in Vampire simulations, yet no proper S 180° wall was obtained for itself.

2.2.3.2 T domain wall

A T wall is generated when a change of T plane occurs along a specific direction, which subsequently becomes the DW. For each T domain, three S domains exist (see Table 2.1). In consideration of the aforementioned factors, nine possible combinations are possible.

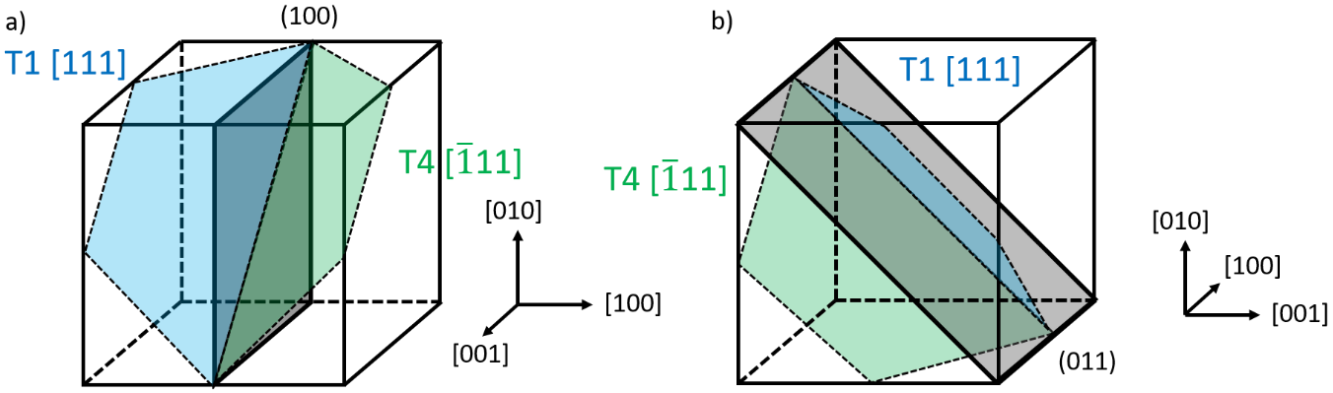

Figure 2.4: Schematic illustration of the two possible orientations of a magnetic transition wall for T1 (blue plane) to T4 (green plane). The transparent black planes represent (100) *and* (011) *planes.*

The selection of the DW plane[27] also encompasses the T domain on both sides of the DW. This is due to the necessity of maintaining the symmetry of the contraction axis through the selected plane. The Figure 2.4 illustrates this point with the example of a magnetic transition from T1 to T4. The two possible DW planes are (100) and (011), as presented on the left and right, respectively. It can be observed that the two T planes are symmetrical with respect to the DW plane. Consequently, only two kinds of magnetic T walls are possible:

- $T_{(100)}$ Wall. This indication unites T walls when the change plane is one of these: (100), (010), or (001). The plane profile of the magnetic Ni cations is that a face-centered cubic (fcc) structure. This particular type of wall has been successfully obtained, see the $T_{(100)}$ wall between T1 and T4.
- $T_{(110)}$ Wall. This indication unites T walls when the change plane is one of these: (110), (101), (011), $(1\bar{1}0)$, $(10\bar{1})$ or $(01\bar{1})$. These directions can be visualized as the two diagonals of a square. The six distinct directions are derived from the premise that a cube is composed of three squares. This particular type of wall has been successfully obtained, see the $T_{(110)}$ wall between T1 and T2.

2.2.4 Construction of domain walls

Domain walls are constructed by the combination of two distinct TS domains among the twelve enumerated in Table 2.1. The two distinct TS domains are generated by implementing the corresponding $\mathcal{H}_{TS}$ Hamiltonian on two sections of a supercell, thereby defining the DW at the interface. Each part corresponds to one side of the DW, and two choices of direction must be made to define $\mathcal{H}_{TS}$:

- A given direction $\mathbf{u_T}$ of the ferromagnetic planes and the rhombohedral contraction (first line of Table 2.1).
- Another direction $\mathbf{u_S}$ of spin easy axis direction within each ferromagnetic plane (one of the three possible S domains for each T domain in Table 2.1) is also given.

The magnetic DW is always situated in the center of the simulation box (the grey plane). For the remaining part of this section, the term "left side of the wall" (TS_L) refers to the portion of the DW with a coordinate value of $x<x_{simu}/2$, while the term "right side of the wall" (TS_R) is defined as the portion with a coordinate value of $x>x_{simu}/2$. Indeed, x_{simu} represents the size of the simulation box. The rectangular simulation box is viewed from a lateral perspective, with x increasing towards the right.

Table 2.3 provides a summary of simulated DWs. The designation of the simulated DW is provided in the first column. The second and third columns, respectively, indicate the crystal orientation in relation to the supercell and the periodic boundary conditions (PBC). The fourth column indicates the DW plane with respect to the supercell. In more precise terms, as $T_{(110)}$ DWs are simulated in a [110] oriented supercell, the (110) supercell plane corresponds to the (100) of the simulation lattice. The final two columns indicate the T-S domain from either side of the DW. It should be noted that all nine T-S combinations have been considered for T walls.

Table 2.3: Summary of simulated DWs with the main parameters indicated.

Domain Walls	Crystal orientation	PBC	DW plane	TS_L	TS_R
S 60° Wall	[100]	No	(100)	T1S3	T1S2
	[010]	Yes			
	[001]	Yes			
S 120° Wall	[100]	No	(100)	T1S3	T1S2
	[010]	Yes			
	[001]	Yes			
$T_{(100)}$ Wall	[100]	No	(100)	T1S1	T4S1
	[010]	Yes		T1S2	T4S2
	[001]	Yes		T1S3	T4S3
$T_{(110)}$ Wall	[110]	No	(110)	T1S1	T2S1
	$[1\bar{1}0]$	Yes		T1S2	T2S2
	[001]	Yes		T1S3	T2S3

A schematic illustration of the construction presented in Table 2.3 is given in Figure 2.5. The upper illustration depicts the S DW. The structure is made of a single T plane, yet the S direction undergoes a transformation throughout the DW. Depending on the direction of rotation, two distinct S-walls can be generated: S 60° and S 120°. The middle and bottom illustrations of Figure 2.5 provide the three S directions corresponding to each of the three T planes. The various orange arrows represent the S directions associated with the T1 plane, while the various yellow arrows represent the S directions associated with the T4 plane. The green arrows illustrate the S directions associated with the T2 plane.

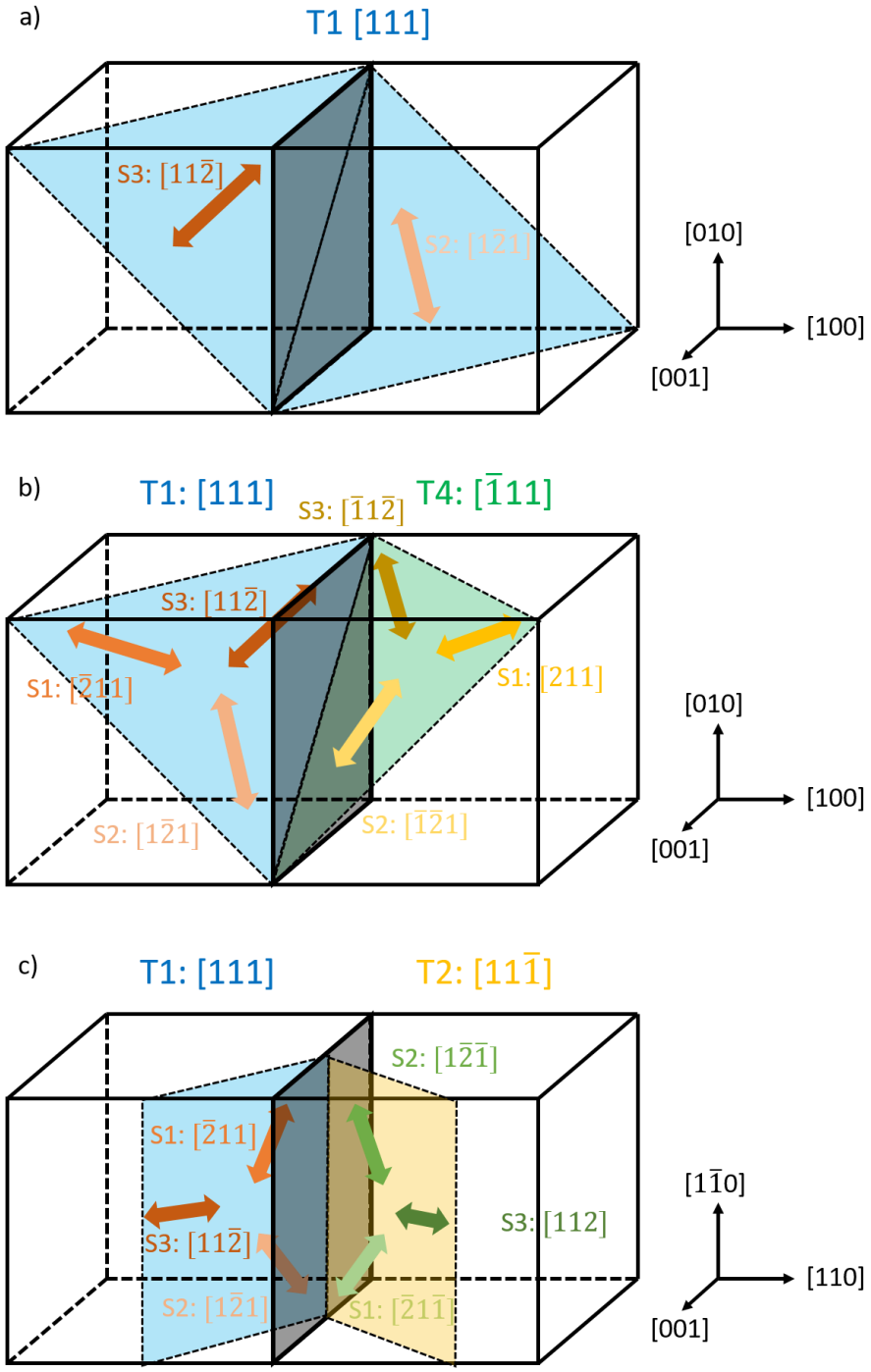

Figure 2.5: Schematic illustration of the DW construction. The top figure represents the construction of S walls, while the two bottom figures depict the construction of $T_{(100)}$ and $T_{(110)}$ DW, respectively.

For each case, specific boundary conditions are applied (see Table 2.3). For instance, the S60° wall T1S3-T1S2 is constructed using cubic supercells oriented along the conventional axis, separated in two sections, left and right. The S60° wall is positioned along the (100) plane with periodic boundary conditions (PBC)

applied in the two other directions, in order to have only one magnetic transition. Without this condition, a secondary DW will be created at x = 0. The T1S3 and T1S2 domains are created on the left and right sides of the supercell, respectively. These are obtained using $\mathcal{H}_{T1S3}$ and $\mathcal{H}_{T1S2}$ by fixing $\mathbf{u_{T1}}$=[111] for the T domain and the contraction direction on both sides of the DW, and $\mathbf{u_{S3}}$ = $[11\bar{2}]$ for the S3 domain on the left side and $\mathbf{u_{S2}}$ = $[1\bar{2}1]$ for the S2 domain on the right side (see Table 2.1).

2.2.5 Symmetry considerations

Some T DWs configurations are equivalent by symmetry. It can be observed in Figure 2.5 that two directions are at an angle of 30° to the common direction at the two T planes, whereas only one direction is at an angle of 90° to the common direction at the two T planes, named "common direction" in the following.

Four distinct spins configurations have been identified by looking at the angle between the S directions and the common direction. They are summarized in Table 2.4. The four distinct configurations are referenced with the angle between the S direction and the common direction, for the two T planes. It can be further detailed by S4 or S5 which indicate the scalar product between the two S directions. The first number is the angle in the T1 plane used as a reference as it is present in the two T wall configurations, while the second number is the angle in the second T plane. For a $T_{(100)}$ wall, the reference 30°-90° signifies an angle of 30° in the T1 plane between the S directions and the common direction $[0\bar{1}1]$, and an angle of 90° between the $[0\bar{1}1]$ direction and the S directions in the T4 plane.

Table 2.4: Summary of the observed symmetry between the different T-S domains for $T_{(100)}$ and $T_{(110)}$ DWs.

$T_{(100)}$ DWs: T1 as TS_L / T4 as TS_R Common direction $[0\bar{1}1]$	T1S1 (90°)	T1S2 (30°)	T1S3 (30°)
T4S1 (90°)	90°-90°	30°-90°	30°-90°
T4S2 (30°)	90°-30°	30°-30° S4	30°-30° S5
T4S3 (30°)	90°-30°	30°-30° S5	30°-30° S4
$T_{(110)}$ DWs: T1 as TS_L / T2 as TS_R Common direction $[\bar{1}10]$	T1S1 (30°)	T1S2 (30°)	T1S3 (90°)
T2S1 (30°)	30°-30° S4	30°-30° S5	90°-30°
T2S2 (30°)	30°-30° S5	30°-30° S4	90°-30°
T2S3 (90°)	30°-90°	30°-90°	90°-90°

2.3 TECHNIQUES FOR DOMAIN WALL ANALYSIS

This section provides an overview of three analytical techniques which will be employed to ascertain the physical properties of DW. The techniques under consideration are stereographic projection, XMLD-PEEM and NVM.

The use of stereographic projections will prove helpful in the analysis of the atomic spin behavior. The XMLD-PEEM calculations will facilitate the measurement of the DW width, while the NVM calculations will enable the measurement of the stray field generated by the DW. It should be noted that this work is composed solely of simulations, and the descriptions of the XMLD-PEEM and NVM techniques are provided exclusively for establishing analogies with the simulation techniques.

2.3.1 Stereographic projection

In order to facilitate the visualization of the spin structure crossing the DW, given the intricate nature of the 3D AF structure, a single plane representation, that is a stereographic projection, can be beneficial. Given that atomic spins lie in T-planes, therefore the selected plane must be one of the two T-planes from either side of the DW.

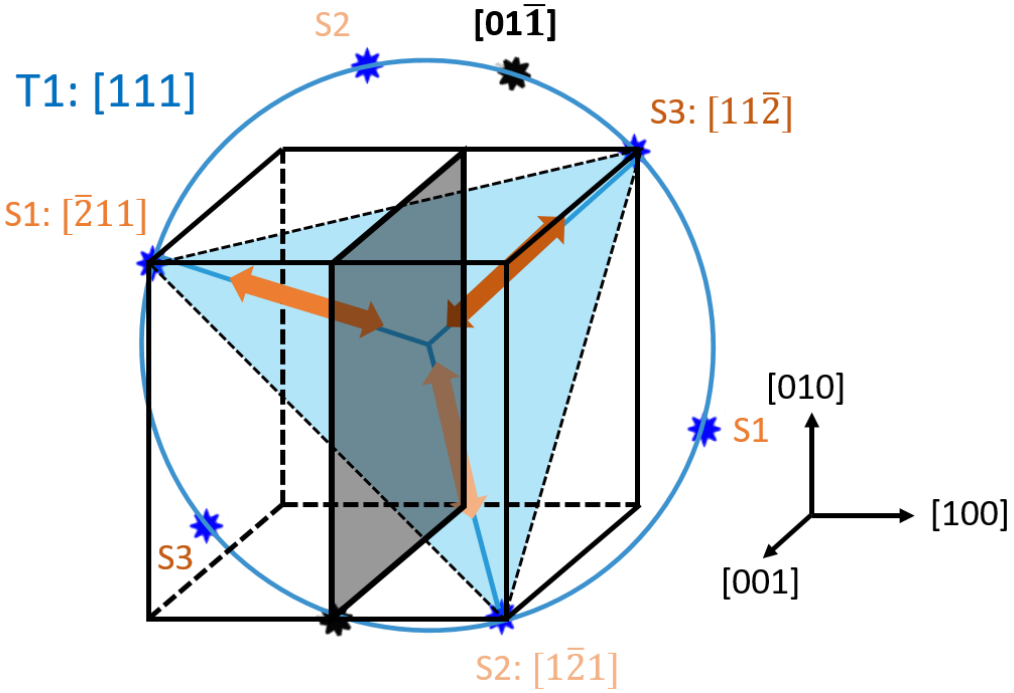

Figure 2.6: Schematic illustration of one stereographic projection in the T1 plane. The distinct S direction are indicated by orange arrows, while the (100) plane is illustrated in grey.

Figure 2.6 illustrates the schematic representation of a stereographic projection construction employing the T1 planes as a reference. T1 planes correspond to the (111) planes. The various S directions are depicted by blue stars. The reference S direction is chosen to be T1S3, which will be indicated by its north position in the stereographic projection. Additionally, the crossing line between the (111) plane and the (100) plane is indicated (i.e $[01\bar{1}]$) by black stars. Given that spins vector norms have by definition a length of 1, points on the radius of the unit circle are projected onto the unit circle itself, while points outside the unit radius circle will be out-plane.

Prior to the application of the stereographic projection, points are reoriented along the (111) axis, with a usual change-base matrix. To illustrate, for a change in (111) orientation, the following matrix is utilized:

$$M_{nb} = \begin{pmatrix} 1/\sqrt{6} & 1/\sqrt{6} & -2/\sqrt{6} \\ 1/\sqrt{2} & -1/\sqrt{2} & 0 \\ 1/\sqrt{3} & 1/\sqrt{3} & 1/\sqrt{3} \end{pmatrix} \qquad (2.4)$$

In this transformation (2.4), if the spin vector is in the (111) plane, the new S_z will be 0. The new S_x and S_y will be respectively the projections on $[11\bar{2}]$ and on $[1\bar{1}0]$, respectively, which are two perpendicular directions between them and 90° away from [111].

A stereographic projection is a polar plot in which the coordinates (r, φ) are calculated in accordance with the following formula:

$$r = \sqrt{S_x^2 + S_y^2}$$
$$\phi = arctan2(S_y, S_x) \qquad (2.5)$$

In Equation (2.5), S_x and S_y represent the spin coordinates in the new base oriented in one of the four [111] directions. The arctan2 function is employed to ensure the identification of an appropriate angle Φ between the x and y coordinates.

Figure 2.7 provides a summary of the main directions for $T_{(100)}$ with T1 and T4 planes, and for $T_{(110)}$ with T1 and T2 planes. Table 2.1 provides a correspondence between names and directions. The reference plane is the T1 plane, which is represented by the gray circle. The main directions are indicated by small stars. The blue stars represent the important directions (principally the three S directions for the two T-domains involved). The blue stars on the gray circle represent S directions of the T1 plane, whereas blue stars inside the gray circle represent S direction of T4 (a) and T2 (b), respectively. These directions form an ellipse due to the fact that T1 and T4 (and T2) are not perpendicular to each other (see Figure 2.1). The black stars indicate the common directions at the two T

planes involved ([0$\bar{1}$1] for T1 and T4 and [$\bar{1}$10] for T1 and T2.). It can be observed that these common directions are at an angle of 60° from one another. The green stars and green squares will represent the direction of the initial and the final states, respectively.

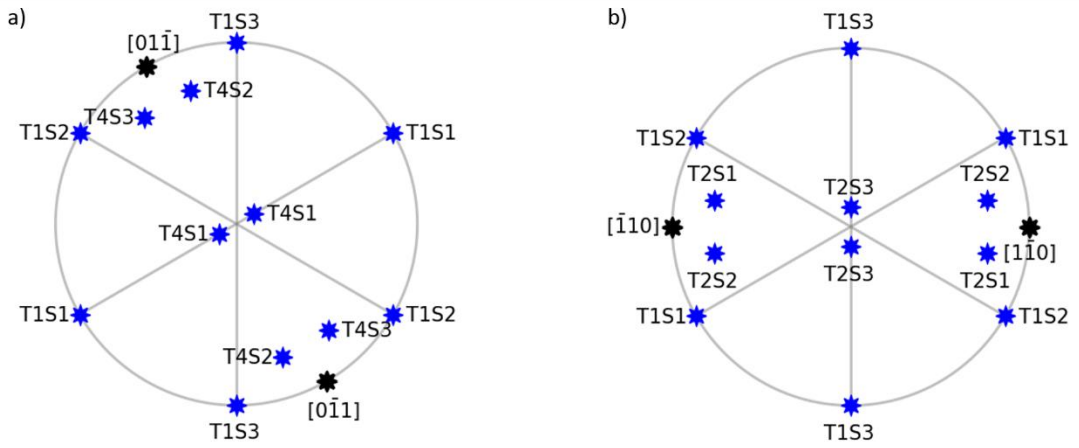

Figure 2.7: Stereographic projection for $T_{(100)}$ (a) and $T_{(110)}$ (b) walls

2.3.2 XMLD-PEEM

The XMLD-PEEM will facilitate the calculation of the DW width through the atomic spin projection on a selected axis.

2.3.2.1 Theoretical considerations

X-ray Magnetic Linear Dichroism (XMLD) and PhotoEmission Electron Microscopy (PEEM) are two commonly employed technics for the study of AF systems[28,29].

In XMLD, linearly polarized x-rays are employed to investigate the anisotropy of the sample, which may originate from the sample structure or magnetism. The principal effect of XMLD is observed at the L edge, where 2p → 3d transitions occur. Consequently, the X-rays are tuned to the L_3 or L_2 edge of the magnetic element. Two local spectra are recorded, one with X-ray linearly s-polarized and one with X-ray linearly p-polarized. The difference between the two spectra is the XMLD spectrum.

As the sample is illuminated with X-rays, some photons are absorbed and electrons are ejected by the photoelectric effect. The electrons are then collected and lead to a PEEM image. Matter has a significant absorption of electrons, only electrons produced by the first nanometers of the sample, near the surface, are ejected and can be collected by the detector. Therefore, PEEM is a surface investigation technique, up to 10 nm in depth.

The XMLD-PEEM technique is a combination of the two aforementioned techniques, which are employed to obtain the AF imaging of a system. Synchrotron sources are employed to illuminate the sample with monochromatic X-rays, resulting in the generation of two images: one with linear left polarization, and one with linear right polarization. The difference between the two recorded images gives a picture of XMLD-PEEM.

In particular, the contrast observed in a XMLD-PEEM picture[29] is linked to:

$$I_{XMLD} = |M^2|(3 - cos^2\,\phi(\boldsymbol{A}, \boldsymbol{E})) \qquad (2.6)$$

In Equation (2.6), I_{XMLD} represents the recorded intensity, M denotes the domain magnetization, and Φ is the angle between the AF axis **A** and the light linear polarization **E**.

By modifying the angle between the surface normal and the incoming polarized light (ω), different contrast can be obtained[30]. The Figure 2.8 represents the contrast variation in function of the ω angle. Knowing the angle between the sample and the light, as well as the possible TS orientations, one can determine the effective orientation of the TS domains.

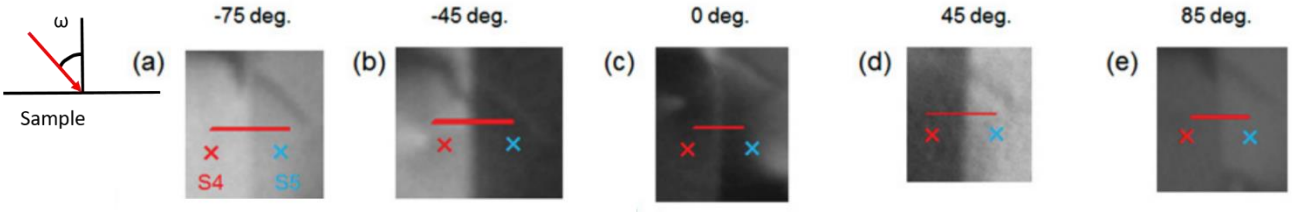

Figure 2.8: XMLD-PEEM contrast variation in function of ω, angle between the surface normal and the incoming polarized light. Adapted from Arai et al.[30].

2.3.2.2 Simulation of XMLD-PEEM

Once the DWs in NiO have been simulated, a pseudo XMLD-PEEM spectrum is generated in order to probe the DW width. The angle between the AF axis and the pseudo-light is adjusted to achieve maximum contrast between the two domains imposed in Vampire simulations.

As an illustration, one may consider the T1S1-T4S2 $T_{(100)}$ DW. In the Vampire simulation, T1S1 is imposed on the left side, thus a projection along T1S1 is used. From the right side of the wall, T4S2 is imposed, thus a second projection along T4S2 is also employed. The contrast difference between the two recorded spectra enables the determination of the DW width. The width is calculated according to:

$$\Pi(x) = \begin{pmatrix} 1 \; if \; I_{L,R}(x) > I_{threshold} \\ 0 \; otherwise \end{pmatrix} \quad (2.7)$$

$$I_{L,R}(x) = \frac{1}{2N_x} \sum_{i=1}^{2N_x} |\boldsymbol{S_i} \cdot \boldsymbol{u_{S_{L,R}}}| \quad (2.8)$$

The function Π(x) defines the DW width. The normalized pseudo XMLD-PEEM intensity in the right and left of the simulation, respectively, is denoted by I_R or I_L. N_x represents the number of atom in a single slice that is parallel to the wall direction. This slice is a (100) slice for $T_{(100)}$ and a (110) slice for $T_{(110)}$. As a projection along the AF axis is made, the pseudo XMLD-PEEM will vary between 1 and -1, as a result of AF order in NiO. In order to study the AF vector, it is necessary to take the absolute value of the projection. In order to record smooth XMLD-PEEM variations in the wall, the mean of two consecutive slices is taken. Consequently, the mean is based on $2N_x$ atoms. The mean of two consecutive slices is the reason for the step-like XMLD-PEEM spectra observed in the graphs of section 2.4. However, this approach ensures a relative smoothing of the XMLD-PEEM signal, which is important in the evaluation of the DW width. Given these conditions, values of $I_{R,L}$ vary between 0 and 1. $I_{threshold}$ is fixed arbitrarily at 98 %. The DW width is defined as the length of Π (x) = 0.

2.3.3 Nitrogen Vacancy Magnetometry

The NVM-like simulations will facilitate the calculation of the stray field generated by the DWs.

2.3.3.1 Theoretical considerations

Nitrogen Vacancy Magnetometry (NVM) is an experimental technic which employs a tip grafted with a diamond engineered to have nitrogen vacancy (NV) defects. A total of more than 100 luminescent defects have been identified in diamonds[31,32]. The one made of single substitutional nitrogen reveals sensitive to small magnetic fields. It displays a pronounced absorption at 637 nm in photoluminescence (PL) spectra, which changes into two absorption peaks in the presence of a magnetic field. The energy difference between the two peaks is correlated with the magnetic field created by the surface, according to the following formula:

$$B = \frac{\Delta E}{2g\mu_B} \quad (2.9)$$

In Equation (2.9), ΔE represents the measured energy difference between the two absorption peaks in PL spectrum. The Landé g-factor, g, and the Bohr magneton, μ_B are included in the denominator.

2.3.3.2 Simulation of NVM

In order to simulate NVM, it is first necessary to choose the observed surface. Given that the AF order is oriented along one of the four [111] directions, along any (100) surface, the surface magnetization is fully compensated. However, if the selected surface is the (111) surface corresponding to the T-domain, a simulated NVM surface measurement can be probed (see Figure 2.9). The signal probed by the simulated tip is the following:

$$\boldsymbol{B}(x,y,d) = \frac{\mu_0}{4\pi}\sum_{i}^{r_i<D}\frac{3(\boldsymbol{S_i}\cdot\boldsymbol{u_i})\boldsymbol{u_i}-\boldsymbol{S_i}}{r_i^3} \qquad (2.10)$$

The magnetic field **B**, as measured by the nanoprobe located at (x,y,d), is the sum of each spin $\mathbf{S_i}$ at position r_i situated in a sphere of radius D. The contribution from each spin $\mathbf{S_i}$ is calculated as the projection along the direction $\mathbf{u_i}$ between its position (of the atomic spin) and the nanoprobe and mitigated by its distance r_i to the nanoprobe. The calculations are performed at a distance d = 400 Å from the sample, which is within the range of the experimental probe-to-sample distance. The sphere of integration with a radius D = 410 Å reveals sufficient to account for the magnetic contribution of spins in close proximity. In the following, B_x, B_y and B_z components of the magnetic field **B** correspond, respectively, to directions perpendicular to DWs (B_x), parallel to DWs (B_y) and normal to the surface (B_z). The Figure 2.9 illustrates the various directions, and the two important distances: the tip to surface distance d and the cutoff distance D.

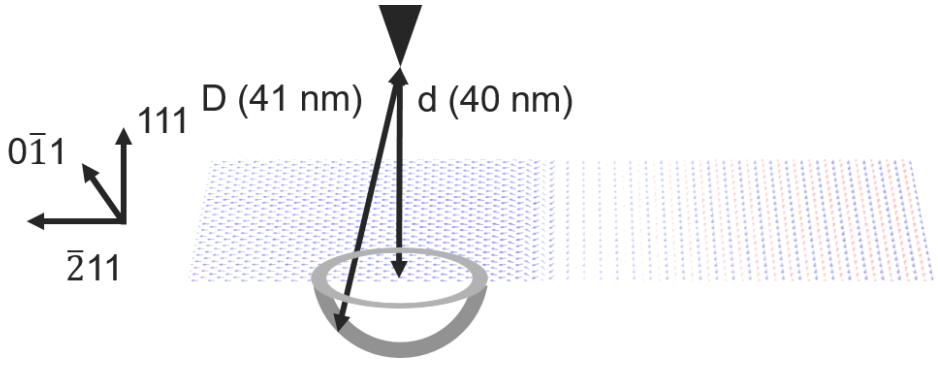

Figure 2.9: Illustration of the simulated NVM setup.

2.4 ATOMIC STRUCTURE OF DOMAIN WALL IN NIO

In this section, the atomic structure at 1 K of each type of DW will be elucidated using the stereographic projections. The results will be presented in a manner that progresses from the relatively simple to the more complex, beginning with the S DWs, then proceeding to the T DWs, and finally examining the geometrical requirement of the splitting zone that appears in T DWs.

2.4.1 Rotation of atomic spins throughout S domain walls

This type of DW is simpler than a T wall, as only one T plane is retained along the DW.

The T1S3-T1S2 DW is constituted by a T1S3 domain on the left side of the wall and a T1S2 domain on the right side of the wall. The general schemes are depicted in Figure 2.10. In each case, the S domains are identical (see Table 2.3), yet the rotation direction differs. For (a), a counterclockwise rotation from left to right across the simulation cell is observed, forming a S 60°. For (b), a clockwise rotation from left to right across the simulation cell is obtained, forming a S 120°.

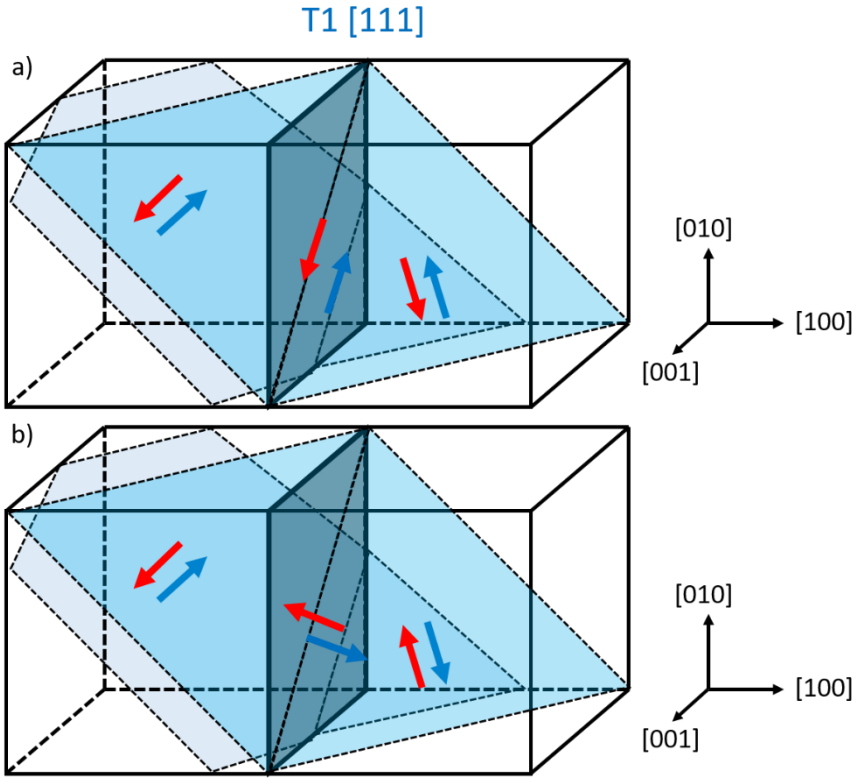

Figure 2.10: a) Schematic representation of a S 60° DW. b) Schematic representation of a S 120° DW. The T1 planes are depicted in cyan, and the red and blue arrows represent the atomic structure of the DW, which is the transparent black plane.

These two S directions are indicated by green disks and green squares, respectively, on the stereographic projections of Figure 2.11. In this projection, one can follow the rotation of spins from the left domain (T1S3) to right domain (T1S2) by utilizing the color scale, which ranges from black to yellow. It is evident that the spins of both ferromagnetic layers in the T1S3 domain rotate in the T1 plane in order to reach the orientation of the T1S2 domain, as all spins remain on the unit-radius circle. It can be observed that the rotations are concomitant in all layers, as the central symmetry is maintained in the stereographic projection. Consequently, all spins maintain their perfect antiferromagnetic alignment between FM layers throughout the DW. The 60° rotations are smooth and occur in the counterclockwise direction. They are designated as R60°. R is used to indicate Rotation and 60° represents the rotation angle (see Table 2.5). It should be noted that the other S 120° DW exhibits rotations of 120°. Consequently, its mechanism is therefore quoted as R120° (see Table 2.5).

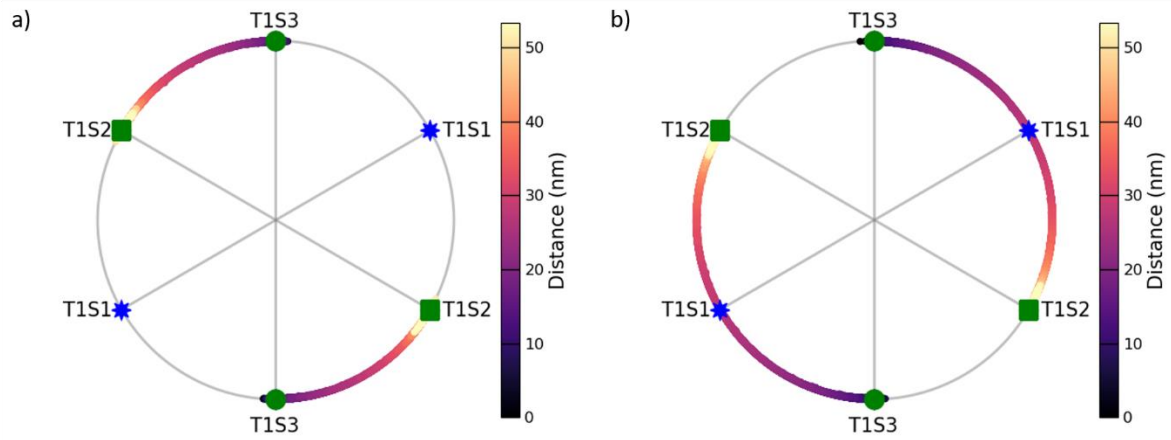

Figure 2.11: Stereographic projection of spins for S 60° (a) and for S 120° (b). 6 $K_u^T = J_2$ is employed in both simulations.

Table 2.5: Mechanisms of spin rotations for S domain walls. The first column present the two TS domains imposed at the right and at the left of the simulation lox. The second column depict the rotation mechanism.

$TS_L \rightarrow TS_R$: Common plane T1 (111)	S DW mechanisms
T1S3→T1S2	R60°
T1S3→T1S2	R120°

2.4.2 Rotation of atomic spins throughout T domain walls

The rotation of spins is more complex for the T1S1-T4S3 $T_{(100)}$ DW as shown in Figure 2.12 (a). Starting from the T1S1 domain, spins of each ferromagnetic layer (the two green circles) first split into two populations when approaching the wall. This results in four different populations of spins, two for each ferromagnetic layer. Such bisections (quoted B in Table 2.6) can be seen as projected spins (purple dots) rotating in both clockwise and counterclockwise directions around green filled circles. Since all spins remain on the unit-radius circle of the stereographic projection, they all rotate in-plane with respect to the T1 domain. In fact, the rotations operate symmetrically (central symmetry on the stereographic projection) and in opposite directions for each subpopulation of a given FM layer. This means that while the spins split and rotate in the T1 plane, they maintain their perfect AF alignments between FM layers. Subsequently, after a rotation of 90° (denoted R90°), all spins gradually join the direction common to both T1 and T4 planes, that is the $[01\bar{1}]$ direction (black stars). The four populations gather together (quoted G) and reduce to two at this very common direction (marked "→" in Table 2.6), one for each ferromagnetic T4 layer.

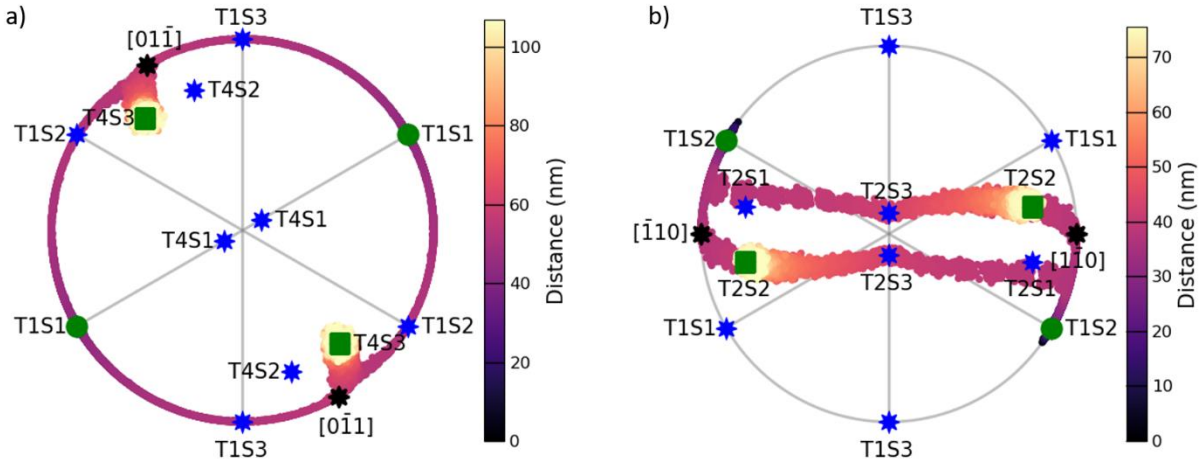

Figure 2.12: Stereographic projection of spins. Figures (a) and (b) correspond, respectively, to $T_{(100)}$ DW (T1S1-T4S3) and to $T_{(110)}$ DW (T1S2-T2S2), which are both viewed from the (111) surface. The anisotropy constant is set at 10 K_u^T = J2. The remaining symbols are identical to those depicted in Figure 2.11.

It should be noted that the bisects (B), rotations (R), and gatherings (G) are geometrically mandatory for spins to reorganize from the T1S1 domain into T4S3. This phenomenon can be observed in Figure 2.14 wherein the spins along two first neighbor lines of nickel atoms are compelled to rotate in opposite directions in order to transition from T1S1 into T4S3. These opposite, in-plane rotations are located in the T1 plane, in close proximity to the DW. Subsequently, following

their convergence at the common direction, the spins emerges from the T1 plane (see Figure 2.12). Their projection thus deviates from the circle. Atomic spins then smoothly reach the directions of the T4S3 domain, with a rotation of 30° (quoted R30°) within the T4 plane.

Such a sequence is shortly quoted: B+R90° $\overset{G}{\rightarrow}$ R30° in Table 2.6. It again means split of the spins (B), then rotation of 90° (R90°) and gathering (G) at the common direction (here $[01\bar{1}]$ and represented by "→") and finally rotation of 30° (R30°). This mechanism can be summarized as a 90°-30° mechanism. The atomic spins begin at 90° of the common direction, gather at the common direction and then undergo a final rotation of 30°.

Table 2.6: Mechanism of spin rotations for T domain walls. The T DWs are classified according to the symmetry considerations of the Table 2.4. The mechanism are divided into two groups. The first group undergoes a total 120° rotation, whereas the other group undergoes an overall 180° rotation.

$T_{(100)}$: Common direction $[0\bar{1}1]$	T DWs and mechanisms
T1S1→T4S3 (90°-30°)	$B + R90° \overset{G}{\rightarrow} R30°$
T1S2→T4S2 (30°-30° S4)	$R60° + B + R90° \overset{G}{\rightarrow} R30°$
T1S2→T4S3 (30°-30° S5)	$R30° \overset{B}{\rightarrow} R90° + G + R60°$
T1S1→T4S1 (90°-90°)	$B + R90° \overset{G}{\rightarrow} R90°$
$T_{(110)}$: Common direction $[\bar{1}10]$	T DWs and mechanisms
T1S3→T2S2 (90°-30°)	$B + R90° \overset{G}{\rightarrow} R30°$
T1S2→T2S2 (30°-30° S4)	$R30° \overset{B}{\rightarrow} R90° + G + R60°$
T1S2→T2S1 (30°-30° S5)	$R60° + B + R90° \overset{G}{\rightarrow} R30°$
T1S3→T2S3 (90°-90°)	$B + R90° \overset{G}{\rightarrow} R90°$

The complexity of the spin rotations increases for the T1S2-T2S2 $T_{(110)}$ DW as can be seen on Figure 2.12 (b), top panel. Initiating the sequence from the T1S2 domain, spins undergo a 30° rotation towards the common direction to the T1 and T2 planes. Subsequently, the spins bisects, separating into four distinct populations and undergo a 90° rotation up to the T2S3 directions, where they gather back in two populations. Finally, they rotate from T2S3 to T2S2. This

sequence is reported as R30° $\overset{B}{\rightarrow}$ R90°+G+R60° in Table 2.6. This type of DW can be summarized as a 30°-30° mechanism. Spins begin at an angle of 30° relative to the common direction, gather at the common direction and end at a direction at an angle of 30° relative to the common direction.

The four examples presented above are representative to all DWs, being S60°, S120°, $T_{(100)}$ and $T_{(110)}$ DWs, as can be seen on Table 2.5 and Table 2.6 . The mechanisms are composed of rotations with various angles. A splitting zone, or alternatively the B+R90°+G mechanism, is systematically present in all T DWs. This splitting zone is geometrically mandatory, as explained in the next section. It should be noted that in the case of the overall 180° rotation, it is not possible to predict the T plane where the splitting zone will occur. The initial configuration presents both sides at 90°, or at 30° of the common direction.

2.4.3 Geometrical requirement of the splitting zone

The most exotic part of these T DWs is the spin splitting that occurs in the middle of the magnetic transition. The geometrical requirement of the splitting zone is illustrated on the Figure 2.13. Atomic spins at the left side of the DW need to be ferromagnetically aligned in the T1 planes. These T1 planes are colored in blue and red to indicate the AF alignment between T1 planes. Without the DW, this alignment will continue along the $[1\bar{1}0]$ diagonal directions. However, at the right side of the DW, these same diagonals exhibit AF alignment of atoms. This is evident by observing the red diagonals across the DW. This create a frustration that the system relieves by adopting a splitting zone.

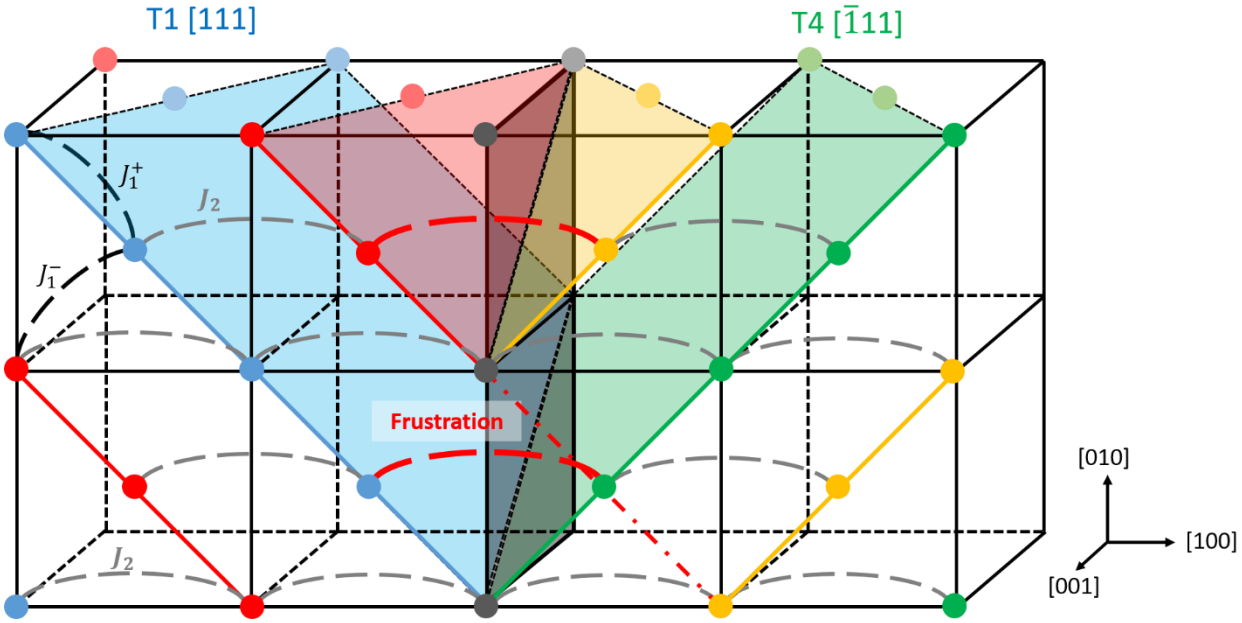

Figure 2.13: Schematic illustration of the geometrical requirement of the splitting zone.

This splitting zone is a balance between two effects:

- Minimizing the angle between the spins in each FM layer, since it is directly related to the super-exchange energy in the Hamiltonian (see (2.1)).
- Minimizing the splitting zone itself to reduce the number of spins with non-zero angles.

Figure 2.14 illustrates the inside of the splitting zone. The atomic positions are represented by small blue and red spheres, and the atomic spins are colored according to their x-axis magnitude. Along the [100] direction, atomic spins are linked through J_2 interactions, while between two lines of atomic spins, the atomic spins are linked with J_1. It can be observed that the two lines of atomic spins turns in two opposite directions, effectively breaking the J_1 interaction, without breaking the J_2 interaction, which is approximately one order of magnitude greater than J_1. This disposition results in the apparition of a deviation angle in T1 planes. It is defined as the angle between two successive atomic spins in the direction of the DW.

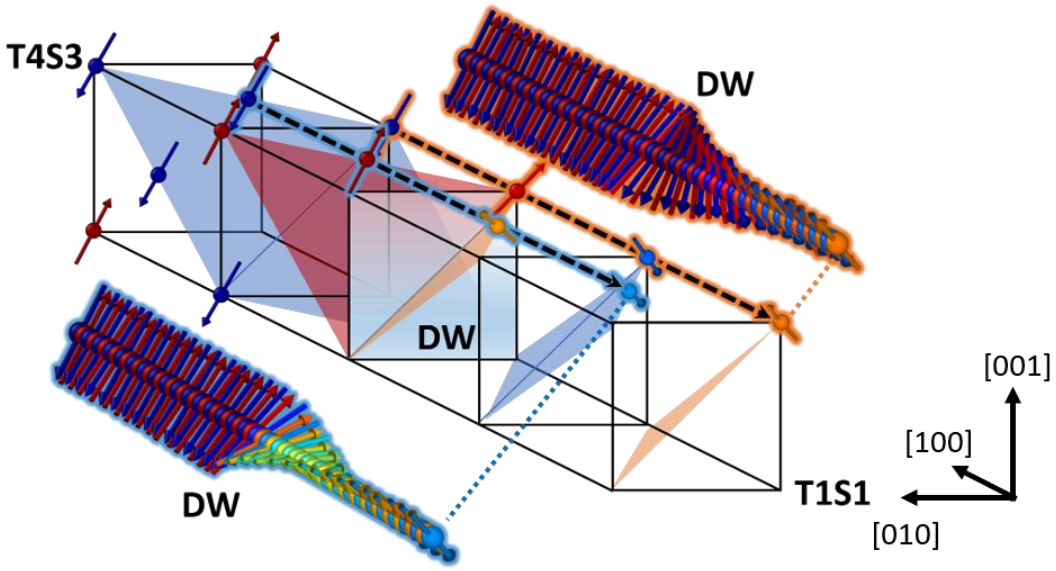

Figure 2.14: Schematic representation of the splitting zone.

The splitting zone is summarized as the mechanisms "B+R90°$\xrightarrow{G}$" in the Table 2.6. Therefore, the splitting zone is defined as a deviation from the ideal in-plane FM alignment, beginning at 90° with respect to the common direction to reach the common direction. Consequently, the rotation angle traversed through the splitting zone is always 90°.

2.5 PHYSICAL PROPERTIES OF DOMAIN WALL IN NIO

This section presents the different physical properties of the various simulated DWs. In the initial section, the results of the simulations of the NVM are presented. In the second part of this section, the widths extracted using the simulated XMLD-PEEM are presented. In order to facilitate a comparison with the experimental width, the extrapolation principle is presented before the comparison with the experimental results.

2.5.1 Simulated domain walls vs stray fields

The stray fields and their components are reported on lower panels of Figure 2.15 for S60° and S120° DWs, and Figure 2.16 for T1S1-T4S3 DW and T1S2-T2S2 DW, respectively. These figures pertains to the surface of observation (111). It should be noted that other surfaces reveal no magnetic field at all.

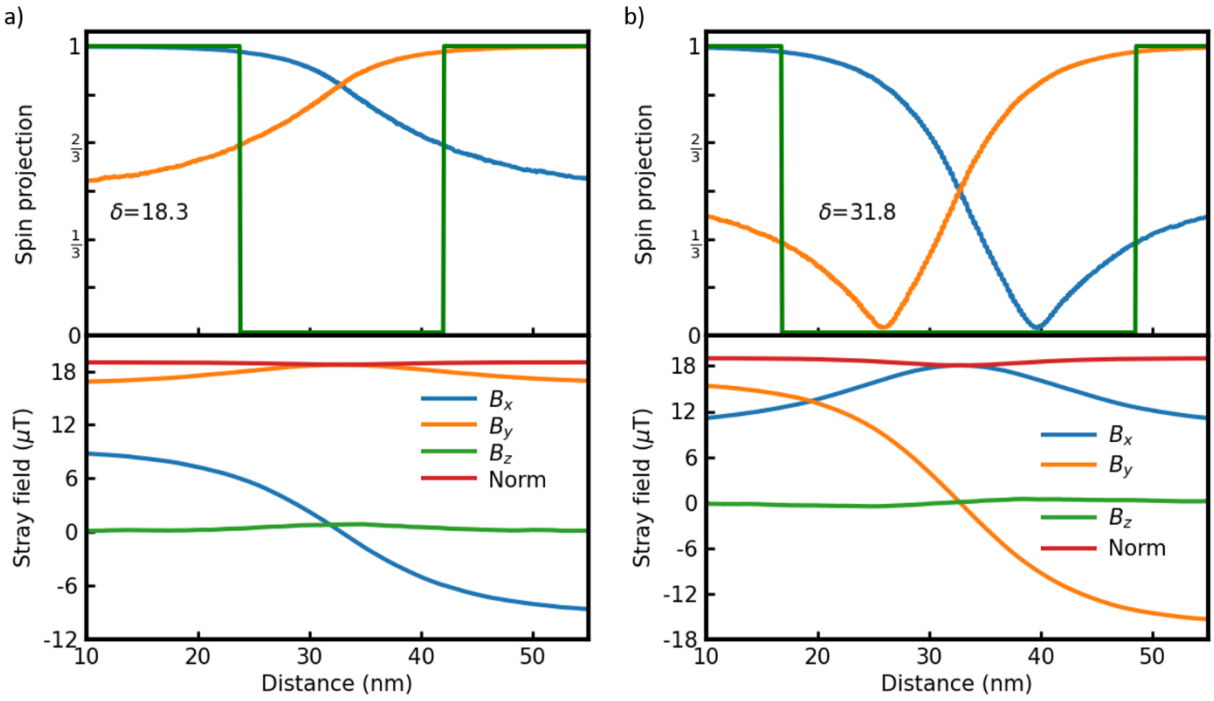

Figure 2.15: Spin projections (upper panel), and stray field (bottom panel) for S 60° DW (T1S3-T1S2) (a) and S 120° DW (T1S3-T1S2) (b), seen from the (1 1 1) surface and plotted as a function of their positions (nm) in the simulation cell with 6 K_u^T = J_2. Normalized intensities of spin projections $I_{L,R}$ are reported for u_{T1S3} (blue line) and u_{T1S2} (orange line) directions. The rectangular function Π (green line) indicates the width δ (nm). The stray field intensity is shown (red line - quoted Norm in μT) with its B_x, B_y, and B_z components (respectively, blue, orange, and green lines).

It is evident that the S DWs has a minimal impact on the magnetic field as it remains constant (red line). In the case of S60°, the B_x component (perpendicular to the DW) shows the most significant change, with positive and then negative values, respectively, on the left and right sides of the wall. In the other case (S120°), it is the B_y component which exhibits the greatest fluctuations. This evolution is analogous to that observed for B_x in the case of S60°.

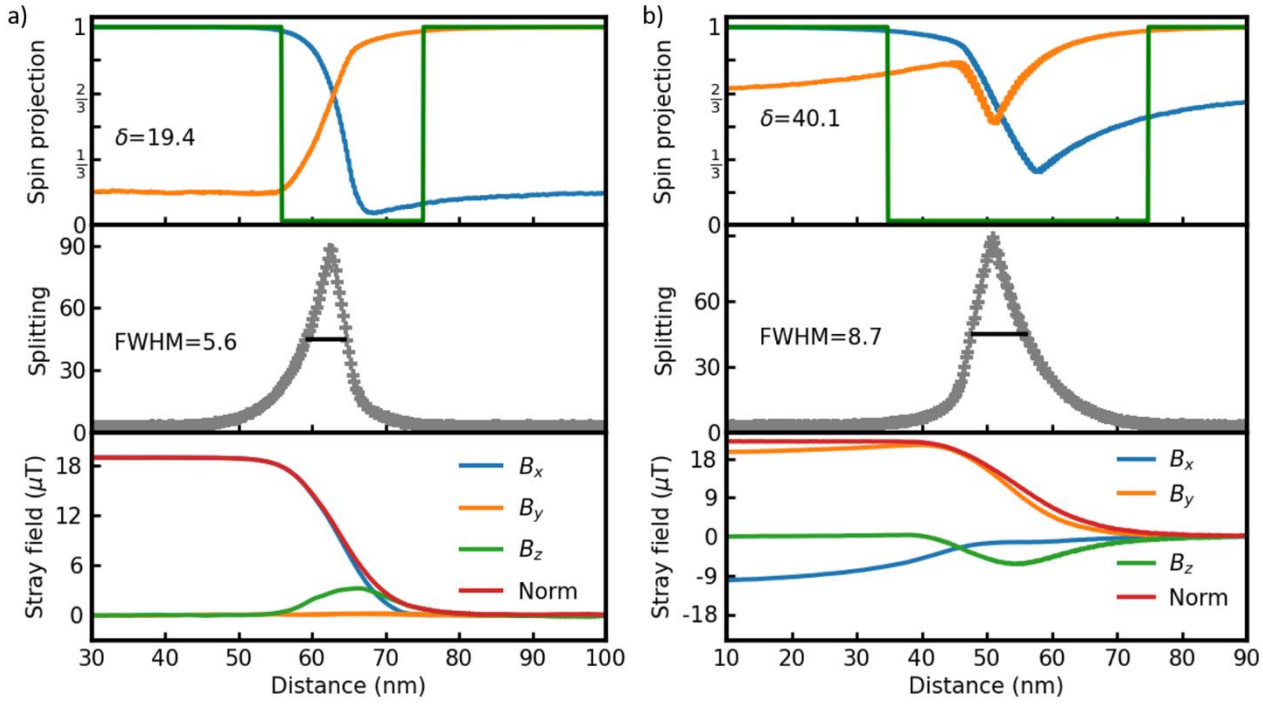

Figure 2.16: First panels illustrate spin projections, second panels present the deviation angle from the optimal AF alignment of spins (quoted splitting, in degrees), and lower panels show the stray field. Figures (a) and (b) pertain, respectively, to $T_{(100)}$ DW (T1S1-T4S3) and to $T_{(110)}$ DW (T1S2-T2S2), which are both viewed from the (111) surface. The anisotropy constant is set at 10 K_u^T = J2. The deviation angles are shown as gray crosses. They are fitted using a Lorentzian function for which the FHWM is reported. The remaining symbols are identical to those depicted in Figure 2.15.

Conversely, both stray fields of the T1S1-T4S3 and the T1S2-T2S2 DWs (red lines in the Figure 2.16, last panels) exhibit strong steps separating constant values of approximatively 20 µT on the left side and zero on the right side. The asymptotic values on either side are related to the FM and AF configurations of spins at the (111) surface, respectively. This phenomenon is observed in all T DWs. As anticipated, the steps in the stray fields are precisely located at the splitting zone, where the spins are not perfectly aligned. Given that the splitting zone is smaller

than the total zone of rotations (*i.e.* the DW width as defined by the projection, see below), the steps are themselves of the same order of magnitude than the splitting zone for all T DWs. In other words, it should be regarded as a Heaviside function for anisotropy constants comparable to those observed in experiments.

2.5.2 Widths of domain walls from XMLD-PEEM

The first investigated DW width is the T1S3-T1S2 DW. The first panel of Figure 2.15 depicts the intensities of spin projections. The two directions $\mathbf{u_{T1S3}}$ and $\mathbf{u_{T1S2}}$ are indeed employed for the spin projections (respectively, the blue and the orange lines), since they correspond to optimal directions on the left and right sides of the DW. It can be observed that the spins projection along $\mathbf{u_{T1S3}}$ exhibits a decrease from a value of one (at the extreme left of the simulation box) as it approaches the DW. The projection smoothly converges toward the asymptotic value of 0.5, which is cos(60°), the angle between spins on the left and the right sides of the DW (see again the top panel). A symmetric behavior is evident in the projection along $\mathbf{u_{T1S2}}$ (orange line). The width of the DW is obtained from the rectangular function (green line) for the (1 1 1) surface. It is calculated to be δ = 18.3 nm for K_u^T = 4.33 meV (see Table 2.7). It should be noted that for K_u^T = 26 meV the width is δ = 7.3 nm, which is considerably smaller and in agreement with expectations as will be recalled below.

Spins projections of $T_{(100)}$ shown in the first panel of Figure 2.16 (a) exhibit markedly disparate shapes. The intensity of the projection on the $\mathbf{u_{T1S1}}$ direction (blue line) declines rapidly to zero, starting from T1S1 domain (extreme left of the simulation box). This phenomenon can be attributed to the 90° rotation between spins at the initial position (green circles, top panel) and the gathering point (black stars). Consequently, the projection is cos (90°) = 0. This decrease to zero is also related the B+R90°+G mechanism mentioned above, wherein spins deviate from their alignment in the T1 plane (see second panel of Figure 2.16 (a)). Subsequently, the intensity rises once more, and converges to the asymptotic value of ⅙, which is the cosine of the angle between $\mathbf{u_{T1S1}}$ and $\mathbf{u_{T4S3}}$ (filled circles and filled squares on top panel of Figure 2.12). The behavior of the intensity projected on the $\mathbf{u_{T4S3}}$ direction (orange line) is not symmetric, in contrast to the observed behavior for S60° or S120° DW. However, starting from T4S3 (extreme right of the simulation box), a pronounce decrease emerges in the same DW region, and the intensity once again converges towards the value of ⅙.

*Table 2.7: Widths of S DWs and T DWs, calculated from atomic spins projections for different domains and for two different surfaces. The column with K_u^T = 0.005 meV reports the widths obtained by extrapolating the simulations (± 10 %). The experimental values are extracted from the work of Arai et al.[30] (see text for details). The behaviors of spins are determined from stereographic projections (see Table 2.5 and Table 2.6). * denotes values obtained by projections.*

S DWs and mechanisms		Widths (nm)							
Common plane T1		Surface (001)				Surface (111)			
$TS_L \rightarrow TS_R$	K_u^T =	26	4.33	0.005	Exp.	26	4.33	0.005	Exp.
T1S3→T1S2	R60°	6.3	14.6	430	-	7.3	18.3	527	-
T1S3→T1S2	R120°	10.5	25.9	775	708	12.9	31.8	949	867*
T DWs and mechanisms		Widths (nm)							
		$T_{(100)}$ DW							
Common direction $[0\bar{1}1]$		Surface (001)				Surface (111)			
$TS_L \rightarrow TS_R$	K_u^T =	26	2.6	0.005	Exp.	26	2.6	0.005	Exp.
T1S1→T4S3	$B + R90° \xrightarrow{G} R30°$	7.9	15.8	272	259	9.4	19.4	333	317*
T1S2→T4S2	$R60° + B + R90° \xrightarrow{G} R30°$	9.8	23.6			11.9	29.1		
T1S2→T4S3	$R30° \xrightarrow{B} R90° + G + R60°$	10.4	25.9	514	555	12.5	31.6	629	680*
T1S1→T4S1	$B + R90° \xrightarrow{G} R90°$	11.7	28.0			14.2	33.6		
		$T_{(110)}$ DW							
Common direction $[\bar{1}10]$		Surface $(\bar{1}10)$				Surface (111)			
$TS_L \rightarrow TS_R$	K_u^T =	26	2.6	0.005	Exp.	26	2.6	0.005	Exp.
T1S3→T2S2	$B + R90° \xrightarrow{G} R30°$	7.8	15.5	265	409	13.3	26.7	459	708*
T1S2→T2S2	$R30° \xrightarrow{B} R90° + G + R60°$	9.8	23.2			17.1	40.1		
T1S2→T2S1	$R60° + B + R90° \xrightarrow{G} R30°$	9.8	25.6	511	728*	17.5	44.6	885	1261*
T1S3→T2S3	$B + R90° \xrightarrow{G} R90°$	11.4	27.8			19.8	47.7		

The intensities of spins projections of $T_{(110)}$ (see first panel of Figure 2.16 (b)) show some similarities with those of the T1S1-T4S3 DW. The intensities decrease once more in the splitting zone, where spins deviate from their AF alignments in the T2 plane (see second panel). It should be noted that the drop does not reach zero (blue line) because the angle between the spins in T1S1 and T2S3 is not 90°. The asymptotic value is ⅔ (the cosine of the angle between $\mathbf{u_{T1S1}}$ and $\mathbf{u_{T2S1}}$).

The calculated widths for T1S1-T4S3 and T1S2-T2S2 are δ = 19.4 nm and δ = 40.1 nm respectively for K_u^T = 2.6 meV (see surface (111) in Table 2.7). These two cases are quite distinct, and it is important to emphasize that it this is due to the distinct behaviors of two different contributions. One of these contributions is related to the splitting zone, while the other is related to the travelled angles of spins.

Regarding first the splitting zone, it can be observed that its width is between 5 and 10 nm for both T1S1-T4S3 and T1S2-T2S2 DWs. This is evidenced by the FWHM of the deviation angle from the optimal AF alignment of spins reported in second panels of Figure 2.16. This splitting zone is the result an optimization process of the spins configurations with respect to the total energy. Since the splitting is geometrically mandatory, the system faces two opposite constraints: firstly, the angles between spins in each FM layer must be minimized, as this is directly related to the energy of super-exchange in the Hamiltonian (see Equation (2.1)). Secondly, the splitting zone itself must be minimized in order to reduce the number of spins with non-zero angles.

The second contribution to the widths is the travelled angles of spins rotations. For instance, the traveled angles of T1S2-T2S2 are longer than the one of T1S1-T4S3 DW. The former configuration (T1S2-T2S2) totals rotations of 90° (the sum of R30° and R60°) apart from the splitting zone, while the latter shows a smaller angle of 30° only. Consequently, the calculated widths (for each K_u^T) are higher for T1S2-T2S2 DW compared to T1S1-T4S3 DW.

This trend can be corroborated in all DWs, including the S DW. This relationship between the traveled angles and widths is nearly bijective. The calculated widths are very similar to each other for a given traveled angles. This is demonstrated for both $T_{(100)}$ and $T_{(110)}$ DWs. Three of them (gathered lines in Table 2.7) show comparable widths at both constants of anisotropy K_u^T with mechanisms comprising by B+R90°+G and traveled angles of 90°. In contrast, the cases following B+R90°+G and traveled angles of 30° stand out.

It is therefore relevant to gather T DWs according to their mechanisms of rotation, and consequently according to their widths. Thus, out of the four $T_{(100)}$ DWs independent by symmetry (see Table 2.4), two distinct mechanisms and thicknesses can be distinguished. One corresponds to a singlet of DWs, and the

other to a triplet of DWs. A comparable distinction can be made regarding the $T_{(110)}$ DWs. The two groups of singlets and triplets are T1S1-T4S3 and (T1S1-T4S1, T1S2-T4S2, T1S2-T4S3) for $T_{(100)}$ DWs and T1S3-T2S2 and (T1S3-T2S3, T1S2-T2S2, T1S2-T2S1) for $T_{(110)}$ DWs (see Table 2.7 for the calculated widths and Table 2.4 for the symmetry equivalence).

2.5.3 Extrapolation of simulated domain walls

As evidenced in Table 2.7, the widths presented are markedly smaller (on the order of tens of nanometers) than those observed in experiments, which ranged from 200 nm up to 1 µm [30,33]. This discrepancy originates from the choice of both the K_u^T and the K_u^S anisotropy constants for the simulations.

It should be noted that high values (ranging from $K_u^T = J_2$ down to 10 $K_u^T = J_2$) are required to afford calculations in tractable supercells, which typically comprise millions of magnetic atoms. The realistic values of anisotropy constants are orders of magnitude lower, approximatively 5 µeV[30,34]. Nevertheless, it is well established that the width of DWs, δ, is related to the constant of anisotropy K[35]:

$$\delta \propto \frac{1}{\sqrt{K}} \qquad (2.11)$$

In order to extrapolate the results of our simulations to describe macroscopic situations, an investigation was conducted regarding the evolution of the widths of DWs as a function of the anisotropy constants. The super-exchange constants J_2, J_1^+ and J_1^- were maintained at fixed values. The ratio of 100 between K_u^T and K_u^S was also retained. Figure 2.17 presents the evolution of widths for S60° and S120° DWs, $T_{(100)}$ and $T_{(110)}$ DWs, respectively, across the first, second, and third panels.

It is evident that variations in widths are consistent with the predictions of Equation (2.11), thereby strengthening the calculations. It also evident that the slopes of different DWs mechanism vary, which conforms to the known angular dependence of the widths with the rotation of spins throughout the DWs [35]. Furthermore, the singlets and triplets of T DWs previously discussed are easily discerned by the blue and red symbols, respectively, in the middle and bottom panels of Figure 2.17. S60° and S120°, and the singlet and the triplet of each $T_{(100)}$ and $T_{(110)}$ DWs are fitted independently (see red/blue lines). In order to extrapolate the widths of the calculated DWs and to compare with experimental data, K_u^T is set at 5 µeV (and indeed K_u^S at 0.05 µeV), in the range of the experimental values[1].

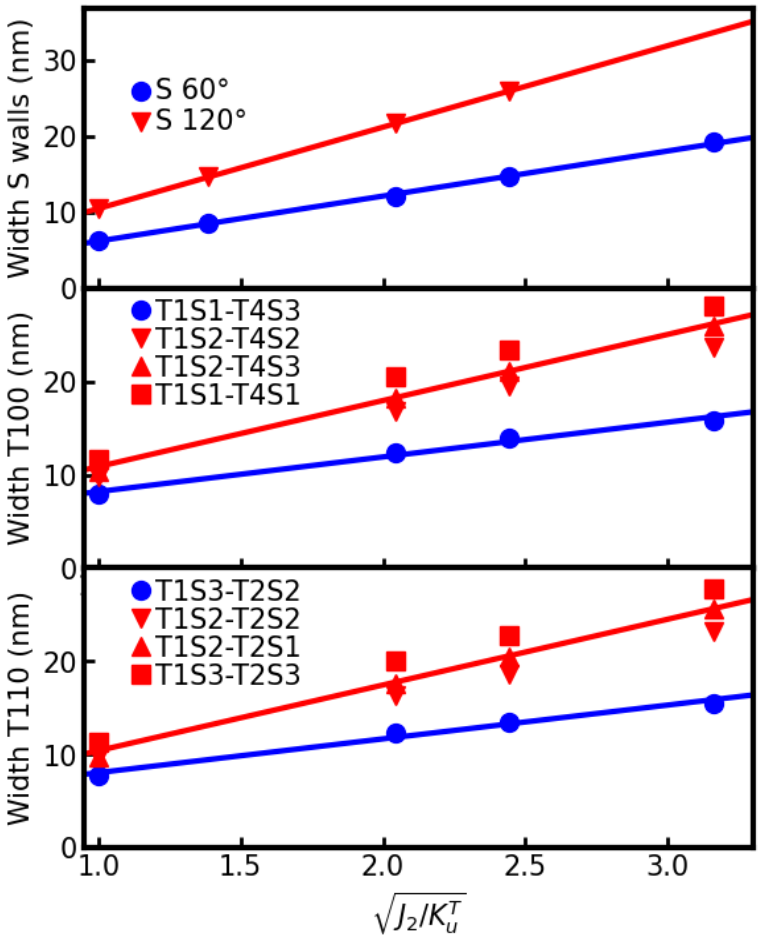

Figure 2.17: Evolution of the widths (in nm) of S60° and S120°, $T_{(100)}$ and $T_{(110)}$ DWs as a function of K_u^T calculated from spins projections. The super-exchange constants were maintained at a fixed value.

The results are reported in Table 2.7. The widths of S DWs were found to be 527 nm and 949 nm, respectively, for S60° and S120°. The latter value is in close agreement to the experimental value of 867 nm[30]. With regards to T DWs, two distinct widths are observed for each type, one for the singlets and another one for the triplets. The $T_{(100)}$ and $T_{(110)}$ widths are strikingly similar. The singlet present a value of 272 and 265 nm for $T_{(100)}$ and $T_{(110)}$ widths, respectively. The triplet value is 514 and 511 nm for $T_{(100)}$ and $T_{(110)}$ widths, respectively.

2.5.4 Comparison of simulated domain walls with experiment

It is noteworthy that the experimental measurements reported by Arai et al[30] for $T_{(001)}$ and $T_{(011)}$ DWs show a bimodal distribution of the widths (see Figure 2.18 (b) and (c)). In the light of the aforementioned simulations, each bimodal distribution is fitted using two Gaussian functions, with ratio of three between their areas, corresponding to the ratio between the triplets and the singlets. The results of the fitting process are illustrated in Figure 2.18.

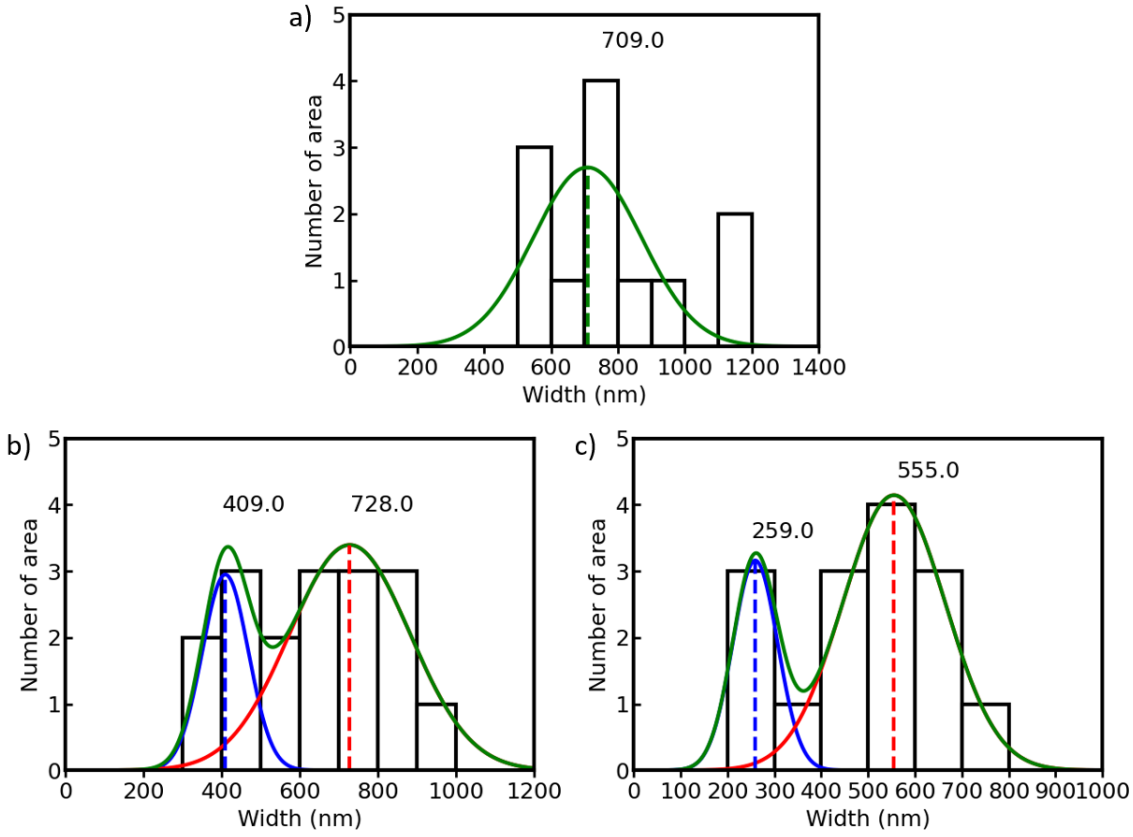

Figure 2.18: Widths (in nm) of DWs measured by Arai[30] using XMLD-PEEM images (histogram in black) and fitting (green lines) using one Gaussian function for S120° DW (a) and two Gaussian functions (blue and red lines) for each T DW ($T_{(011)}$ for (b) and $T_{(001)}$ for (c)).

It is notable that the experimental widths extracted by these two Gaussian functions and the ones extrapolated from simulations are strikingly similar for $T_{(100)}$ (see Table 2.7). The extrapolated widths for $T_{(100)}$ on the (001) surface are 272 nm for the singlet and 514 nm for the triplet, respectively. These values are to be compared with the experimental widths of 259 nm and 555 nm, respectively. The discrepancy is greater for $T_{(110)}$, with the extrapolated singlet width at 265 nm to be compared with the experimental value of 409 nm and the triplet width at 511 nm for to be compared with 728 nm. This disagreement may be attributed to the deviation of the DW plane from 90° angle with respect to the surface in the experimental setting.

2.6 CONCLUSIONS

In this Chapter, atomistic spin simulations have been employed to provide insights on the internal structures of Domain Walls (DWs) in NiO. All T DWs and two S DWs have been considered using high anisotropy constants, thus allowing for a reasonable numerical simulation to be conducted. The orientations of spins throughout the DWs have been carefully analyzed. The mechanisms observed give a strong basis to understand the experimental XMLD-PEEM images, which have been emulated by calculations of spins projections. Additionally, they offer insights into the anticipated experimental NVM signals, which have been simulated from calculations of stray fields.

The detailed analysis of the simulations indicates that the spins adopt mechanisms of reorientation throughout the DWs, which involve only two specific characteristics. The first one is common to all DWs. Spins accommodate the difference in orientations of bordering domains by rotations with various angles. They always keep their AF alignments between FM layers and transit to common directions when two different T planes are involved, *i.e.* in the cases T DWs. The second characteristic does appear only in T DWs. Spins break their FM alignments in each T plane, still keeping their AF alignments between previously FM layers. This break or splitting zone is geometrically necessary.

Calculations of the widths of DWs from spins projections exhibit various values depending on the type of wall and on the constants of anisotropy. In fact, the change of widths is related to the travelled angles of spins throughout DWs, with an almost bijective relation between both. The higher the travelled angles – apart from the splitting zone - the higher the width of the DW.

Incidentally, the mechanism/width couple reveals a relevant criterion to distinguish T DWs. It allows to separate the four DWs of each $T_{(100)}$ and $T_{(110)}$ wall that are independent by symmetry into a singlet and a triplet. This separation as singlet/triplet was not done in experiments by Arai *et al.*[30] for their estimations of widths.

Calculations also show that widths change with the constant of anisotropy and are proportionnal to $1/\sqrt{K_u^T}$. This indeed strengthens the calculations. More interestingly, it opens the possibility to extrapolate calculated widths at experimental values of constants of anisotropy. Doing so, widths close to the experimental ones refitted with singlets and triplets were obtained.

Finally, atomic spins simulations confirm that stray fields are null for all surfaces of observation where spins are AF at the surface. Indeed, surfaces (111) show finite values (of around 20 µT at a probe-to-surface distance of 40 nm) when a FM

surface is exposed. As a consequence, only steps in the magnetic field are generated by DWs for this surface. This step can likely be seen as a Heaviside function in experiments.

2.7 BIBLIOGRAPHY

(1) Hutchings, M. T.; Samuelsen, E. J. Measurement of Spin-Wave Dispersion in NiO by Inelastic Neutron Scattering and Its Relation to Magnetic Properties. *Phys. Rev. B* **1972**, *6* (9), 3447–3461. https://doi.org/10.1103/PhysRevB.6.3447.

(2) Uchida, E.; Fukuoka, N.; Kondoh, H.; Takeda, T.; Nakazumi, Y.; Nagamiya, T. Magnetic Anisotropy of Single Crystals of NiO and MnO. *J. Phys. Soc. Jpn.* **1967**, *23* (6), 1197–1203. https://doi.org/10.1143/JPSJ.23.1197.

(3) Srinivasan, G.; Seehra, M. S. Magnetic Susceptibilities, Their Temperature Variation, and Exchange Constants of NiO. *Phys. Rev. B* **1984**, *29* (11), 6295–6298. https://doi.org/10.1103/PhysRevB.29.6295.

(4) Slack, G. A. Crystallography and Domain Walls in Antiferromagnetic NiO Crystals. *Journal of Applied Physics* **1960**, *31* (9), 1571–1582. https://doi.org/10.1063/1.1735895.

(5) Yamada, T.; Saito, S.; Shimomura, Y. Magnetic Anisotropy, Magnetostriction, and Magnetic Domain Walls in NiO. II. Experiment. *J. Phys. Soc. Jpn.* **1966**, *21* (4), 672–680. https://doi.org/10.1143/JPSJ.21.672.

(6) Evans, R. F. L.; Atxitia, U.; Chantrell, R. W. Quantitative Simulation of Temperature-Dependent Magnetization Dynamics and Equilibrium Properties of Elemental Ferromagnets. *Phys. Rev. B* **2015**, *91* (14), 144425. https://doi.org/10.1103/PhysRevB.91.144425.

(7) Evans, R. F. L.; Fan, W. J.; Chureemart, P.; Ostler, T. A.; Ellis, M. O. A.; Chantrell, R. W. Atomistic Spin Model Simulations of Magnetic Nanomaterials. *J. Phys.: Condens. Matter* **2014**, *26* (10), 103202. https://doi.org/10.1088/0953-8984/26/10/103202.

(8) Yamada, T. Spin Configuration in Antiferromagnetic Domain Walls of the NiO-Type Crystals. *J. Phys. Soc. Jpn.* **1966**, *21* (4), 650–664. https://doi.org/10.1143/JPSJ.21.650.

(9) Ködderitzsch, D.; Hergert, W.; Temmerman, W. M.; Szotek, Z.; Ernst, A.; Winter, H. Exchange Interactions in NiO and at the NiO(100) Surface. *Phys. Rev. B* **2002**, *66* (6), 064434. https://doi.org/10.1103/PhysRevB.66.064434.

(10) Nakahigashi, K. Crystal Structure of Antiferromagnetic NiO Determinded by X Ray Topography. *Journal of the physical Society of Japan* **1975**.

(11) Li, Y.-Y. Magnetic Moment Arrangements and Magnetocrystalline Deformations in Antiferromagnetic Compounds. *Phys. Rev.* **1955**, *100* (2), 627–631. https://doi.org/10.1103/PhysRev.100.627.

(12) Chirac, T.; Chauleau, J.-Y.; Thibaudeau, P.; Gomonay, O.; Viret, M. Ultrafast Antiferromagnetic Switching in NiO Induced by Spin Transfer Torques. *Phys. Rev. B* **2020**, *102* (13), 134415. https://doi.org/10.1103/PhysRevB.102.134415.

(13) Dietz, R. E.; Parisot, G. I.; Meixner, A. E. Infrared Absorption and Raman

Scattering by Two-Magnon Processes in NiO. *Phys. Rev. B* **1971**, *4* (7), 2302–2310. https://doi.org/10.1103/PhysRevB.4.2302.

(14) Shanker, R.; Singh, R. A. Analysis of the Exchange Parameters and Magnetic Properties of NiO. *Phys. Rev. B* **1973**, *7* (11), 5000–5005. https://doi.org/10.1103/PhysRevB.7.5000.

(15) Betto, D.; Peng, Y. Y.; Porter, S. B.; Berti, G.; Calloni, A.; Ghiringhelli, G.; Brookes, N. B. Three-Dimensional Dispersion of Spin Waves Measured in NiO by Resonant Inelastic x-Ray Scattering. *Phys. Rev. B* **2017**, *96* (2), 020409. https://doi.org/10.1103/PhysRevB.96.020409.

(16) Liu, C.-Y.; Ruotsalainen, K.; Bauer, K.; Decker, R.; Pietzsch, A.; Föhlisch, A. Excited-State Exchange Interaction in NiO Determined by High-Resolution Resonant Inelastic x-Ray Scattering at the Ni M 2 , 3 Edges. *Phys. Rev. B* **2022**, *106* (3), 035104. https://doi.org/10.1103/PhysRevB.106.035104.

(17) de Graaf, C.; Broer, R.; Nieuwpoort, W. C. Comparison of the Superexchange Interaction in NiO and in a NiO[100] Surface. *Chemical Physics Letters* **1997**, *271* (4–6), 372–376. https://doi.org/10.1016/S0009-2614(97)00457-0.

(18) De P. R. Moreira, I.; Illas, F.; Martin, R. L. Effect of Fock Exchange on the Electronic Structure and Magnetic Coupling in NiO. *Phys. Rev. B* **2002**, *65* (15), 155102. https://doi.org/10.1103/PhysRevB.65.155102.

(19) Luo, W.; Zhang, P.; Cohen, M. L. Splitting of the Zone-Center Phonon in MnO and NiO. *Solid State Communications* **2007**, *142* (9), 504–508. https://doi.org/10.1016/j.ssc.2007.03.047.

(20) Gambino, D.; Malyi, O. I.; Wang, Z.; Alling, B.; Zunger, A. Density Functional Description of Spin, Lattice, and Spin-Lattice Dynamics in Antiferromagnetic and Paramagnetic Phases at Finite Temperatures. *Phys. Rev. B* **2022**, *106* (13), 134406. https://doi.org/10.1103/PhysRevB.106.134406.

(21) Pokhilko, P.; Zgid, D. Broken-Symmetry Self-Consistent GW Approach: Degree of Spin Contamination and Evaluation of Effective Exchange Couplings in Solid Antiferromagnets. *The Journal of Chemical Physics* **2022**, *157* (14), 144101. https://doi.org/10.1063/5.0114080.

(22) Archer, T.; Pemmaraju, C. D.; Sanvito, S.; Franchini, C.; He, J.; Filippetti, A.; Delugas, P.; Puggioni, D.; Fiorentini, V.; Tiwari, R.; Majumdar, P. Exchange Interactions and Magnetic Phases of Transition Metal Oxides: Benchmarking Advanced *Ab Initio* Methods. *Phys. Rev. B* **2011**, *84* (11), 115114. https://doi.org/10.1103/PhysRevB.84.115114.

(23) Anderson, P. W. New Approach to the Theory of Superexchange Interactions. *Phys. Rev.* **1959**, *115* (1), 2–13. https://doi.org/10.1103/PhysRev.115.2.

(24) Gvozdikova, M. V.; Melchy, P.-E.; Zhitomirsky, M. E. Magnetic Phase Diagrams of Classical Triangular and Kagome Antiferromagnets. *J. Phys.: Condens. Matter* **2011**, *23* (16), 164209. https://doi.org/10.1088/0953-8984/23/16/164209.

(25) Keffer, F.; O'Sullivan, W. Problem of Spin Arrangements in MnO and Similar

Antiferromagnets. *Phys. Rev.* **1957**, *108* (3), 637–644. https://doi.org/10.1103/PhysRev.108.637.

(26) He, G.; Zhang, H.; Ni, J.; Liu, B.; Xu, C.; Xiang, H. Microscopic Magnetic Origin of Rhombohedral Distortion in NiO. *Chinese Phys. Lett.* **2022**, *39* (6), 067501. https://doi.org/10.1088/0256-307X/39/6/067501.

(27) Blech, I. A.; Meieran, E. S. X-Ray Topography of Single Crystal NiO. *Philosophical Magazine* **1966**, *14* (128), 275–288. https://doi.org/10.1080/14786436608219011.

(28) Folven, E.; Takamura, Y.; Grepstad, J. K. X-PEEM Study of Antiferromagnetic Domain Patterns in LaFeO3 Thin Films and Embedded Nanostructures. *Journal of Electron Spectroscopy and Related Phenomena* **2012**, *185* (10), 381–388. https://doi.org/10.1016/j.elspec.2012.07.001.

(29) Scholl, A.; Ohldag, H.; Nolting, F.; Stöhr, J. X-Ray Photoemission Electron Microscopy, a Tool for the Investigation of Complex Magnetic Structures.

(30) Arai, K.; Okuda, T.; Tanaka, A.; Kotsugi, M.; Fukumoto, K.; Ohkochi, T.; Nakamura, T.; Matsushita, T.; Muro, T.; Oura, M.; Senba, Y.; Ohashi, H.; Kakizaki, A.; Mitsumata, C.; Kinoshita, T. Three-Dimensional Spin Orientation in Antiferromagnetic Domain Walls of NiO Studied by x-Ray Magnetic Linear Dichroism Photoemission Electron Microscopy. *Phys. Rev. B* **2012**, *85* (10), 104418. https://doi.org/10.1103/PhysRevB.85.104418.

(31) Jelezko, F.; Wrachtrup, J. Single Defect Centres in Diamond: A Review. *physica status solidi (a)* **2006**, *203* (13), 3207–3225. https://doi.org/10.1002/pssa.200671403.

(32) Rondin, L.; Tetienne, J.-P.; Hingant, T.; Roch, J.-F.; Maletinsky, P.; Jacques, V. Magnetometry with Nitrogen-Vacancy Defects in Diamond. *Rep. Prog. Phys.* **2014**, *77* (5), 056503. https://doi.org/10.1088/0034-4885/77/5/056503.

(33) Arai, K.; Okuda, T.; Tanaka, A.; Kotsugi, M.; Fukumoto, K.; Oura, M.; Senba, Y.; Ohashi, H.; Nakamura, T.; Matsushita, T.; Muro, T.; Kakizaki, A.; Kinoshita, T. Complete Assignment of Spin Domains in Antiferromagnetic NiO(100) by Photoemission Electron Microscopy and Cluster Model Calculation. *J. Phys. Soc. Jpn.* **2010**, *79* (1), 013703. https://doi.org/10.1143/JPSJ.79.013703.

(34) Schrön, A.; Rödl, C.; Bechstedt, F. Crystalline and Magnetic Anisotropy of the 3 d -Transition Metal Monoxides MnO, FeO, CoO, and NiO. *Phys. Rev. B* **2012**, *86* (11), 115134. https://doi.org/10.1103/PhysRevB.86.115134.

(35) Mitsumata, C.; Sakuma, A. Generalized Model of Antiferromagnetic Domain Wall. *IEEE Transactions on Magnetics* **2011**, *47* (10), 3501–3504. https://doi.org/10.1109/TMAG.2011.2158523.

3 EXPERIMENTAL TECHNIQUES AND SIMULATION METHODS

The experimental techniques and simulation methods employed for the characterization of the $Fe_{\alpha}Ni_{\beta}Cr_{\gamma}O_4$ spinel thin films are provided in this chapter. The growth technique (OA-MBE) is first presented, along with structural (RHEED, XRR, XRD), chemical (XPS), and magnetic (VSM) characterizations. Additionally, two synchrotron based experimental methods dedicated to the fine structure investigation are presented: X-ray magnetic circular dichroism (XMCD) and Resonant X-ray diffraction (RXD). These two methods require theoretical model spectra for a quantitative analysis. The theoretical basis of spectrum calculations are then outlined.

3.1 EPITAXIAL GROWTH BY OXYGEN-ASSISTED MOLECULAR BEAM EPITAXY

In order to investigate the crystallographic structure and physical properties of the $Fe_\alpha Ni_\beta Cr_\gamma O_4$ spinel system, it is necessary to elaborate thin films of varying stoichiometry in α, β, and γ. The growth method chosen must allow to obtain high crystalline quality thin films, be versatile (in order to access a multitude of compositions), and be precise in terms of composition.

The Oxygen-plasma Assisted Molecular Beam Epitaxy (OA-MBE) method has been selected[1]. Samples produced by OA-MBE exhibit high crystalline quality[2,3]. The compositions can be modified by adjusting the temperature of the cells in which the metals are evaporated (Knudsen effusion cells), in contrast to another well-known technique for the oxide growth: the Pulsed Laser Deposition (PLD) technique. In this case, the growth of thin films with different compositions and/or a fine doping involves the use of multiple targets with the required stoichiometry.

Figure 3.1 provides a schematic illustration of an OA-MBE apparatus. The fundamental principle of molecular beam epitaxy (MBE) is the generation of a molecular or atomic beam activated by thermal energy. The atomic or molecular beams are then directed on a substrate, wherein an epitaxy can occur in agreement with the crystalline structure of the selected substrate. The term "epitaxy" is used to describe the crystalline coherence between the substrate and the film, which is related to the crystalline structure and lattice parameter of the substrate and the film.

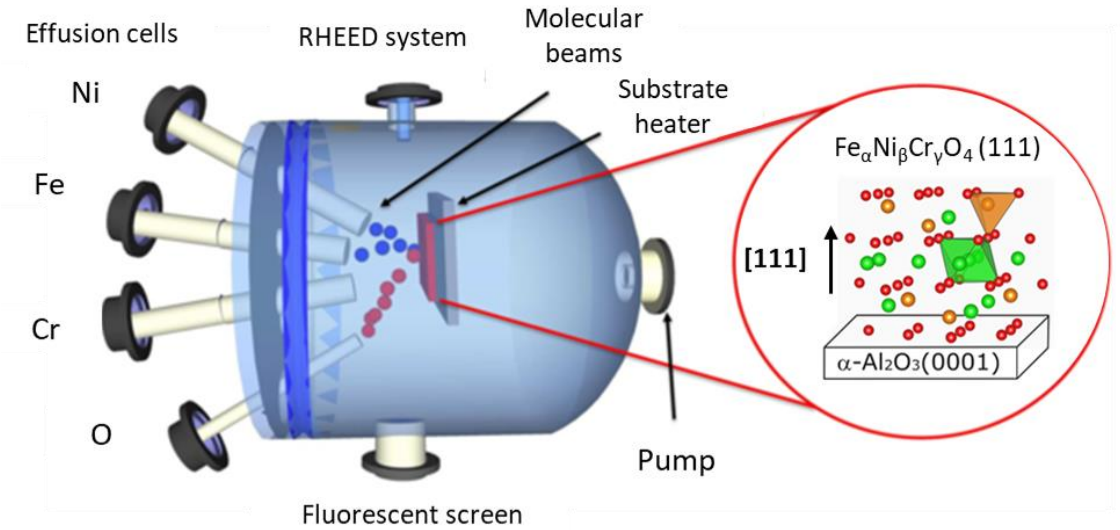

Figure 3.1: Schematic illustration of the AO-MBE apparatus. Adapted from Vila-Fungueiriño et al.[4].

In order to reduce surface defects and ensure a high crystalline quality, it is generally essential to maintain a low evaporation rate. In practice, the optimal growth rate is in the range of a few to tens Å. min^{-1}. At these growth rates, the atoms have sufficient time to migrate on the surface, thereby reducing the defects in the growing film. Additionally, mechanical shutters are employed to control the beginning and end of the deposition, thus enabling the growth of multilayers. Figure 3.2 presents the specific AO-MBE setup developed in CEA-SPEC and used in this work.

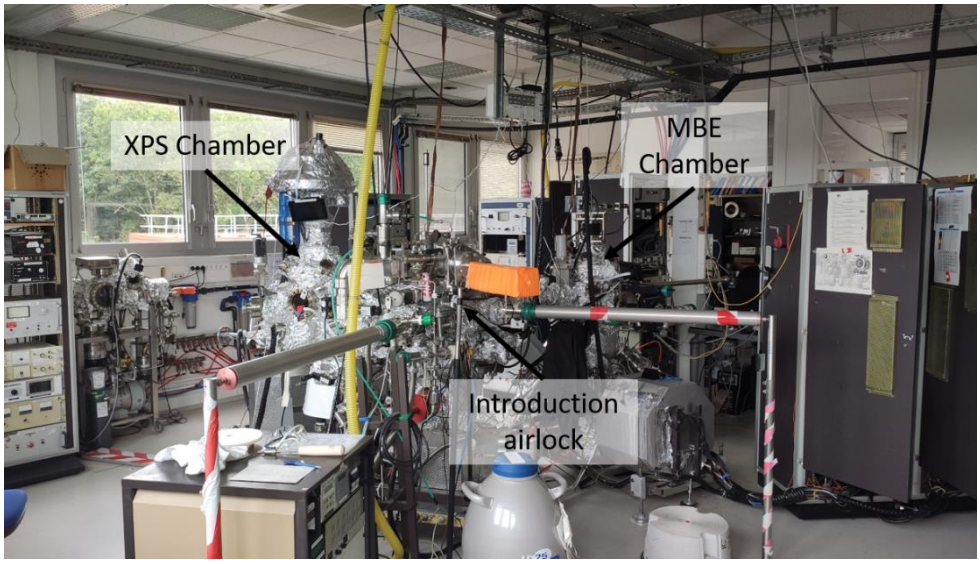

Figure 3.2: The OA-MBE setup developed in CEA-SPEC.

The MBE growth of the samples is performed under ultra-high vacuum (UHV) conditions. The pumping system of the MBE setup, comprising turbomolecular, ionic, and titanium sublimation pumps, is used to maintain a partial pressure of 10^{-10} mbar. These conditions minimize the contaminations due to external pollutants (H_2O, C, etc…), and allow the use of the Reflection High-Energy Electron Diffraction (RHEED) technique to record *in situ* and in real-time the growth of the layers. This technique gives information on the crystallographic properties of the surface and also on the growth mode (2D *vs* 3D) of the sample (*cf.* section 3.2).

For an Oxygen-plasma assisted set-up, the oxygen flux is introduced into the MBE chamber via an atomic oxygen radio-frequency plasma source. The plasma source is comprised of a water-cooled quartz cavity. A constant oxygen pressure (PO_2) is introduced into the quartz cavity ($0.1 < PO_2 < 0.5$ Torr) via a molecular oxygen (O_2) gas bottle. Once within the cavity, an electrical discharge or RF power (Pf) varying between 250 and 450 W generates the atomic oxygen plasma. This discharge results in the dissociation of some molecular oxygen species into atomic oxygen via electronic dissociation. The atomic oxygen is finally introduced

into the chamber via an effusion hole with a diameter of 200 µm. This oxygen species serves as the primary oxidizing agent. The quantity of atomic oxygen introduced is of course a key point for the metallic oxidation states and the crystalline quality of the oxide.

The metallic fluxes of nickel, iron, and chromium are controlled by the temperature of each Knudsen effusion cell. An initial value of the deposition rate is obtained by using a quartz balance. However, these measurements are done at room temperature and in the absence of oxygen plasma, whereas the deposition is made on a hot substrate with the oxygen plasma. These measurements are therefore purely indicative. It will be necessary to check the film thickness, stoichiometry and structure by using different techniques as detailed below.

The growth conditions result in the thermodynamic equilibrium not being reached. Consequently, MBE can be defined as a kinetic process. The MBE growth process comprises four primary steps[1]. The initial stage of the process is the adsorption of atoms on the surface. Subsequently, the atoms migrate, then incorporate into the substrate or growing layer. Finally, the atoms that are not incorporated undergo thermal desorption.

The growth mechanisms are governed by the kinetics of the surface reaction between the incoming atomic beams and the growing layer. Three general modes of crystal growth on surface (see also Figure 3.3) can be distinguished[1]:

- The layer-by-layer mode (Frank-van der Merwe mode). The atoms are strongly bonded to the surface, forming a complete monolayer.
- The island mode (Volmer-Weber mode) is characterized by the formation of discrete islands of crystals on the surface. The atoms exhibit a preference for binding between themselves over binding at the surface. The formation of small clusters of the growth materials at the surface then leads to their growth into islands of the desired materials.
- The layer plus island mode (Stanski-Krastanov mode). After the formation of the first monolayers and their covering of the surface, atoms have an energetic preference for forming clusters, which will evolve into islands. This mode is a combination of the two previous modes. It begins at a layer-by-layer mode and evolves into an island mode.

As a process governed by kinetics, the substrate is usually submitted to high temperatures in order to obtain the desired phase. In the MBE configuration, a heater is located close to the sample holder. The heater is heating by Joule effect and the temperature is recorded by a thermocouple situated in the immediate vicinity of the sample holder.

It should be noted that the MBE apparatus is also equipped with an *in situ* XPS (see below), to determine preliminary elemental composition without any organic pollutant.

The objectives of this study is to synthesize $Fe_{\alpha}Ni_{\beta}Cr_{\gamma}O_4$ thin films in a large composition range for a comprehensive investigation of their physicochemical properties with the metallic content. Each desired composition should be therefore the result of a delicate compromise between UHV conditions, deposition time, temperatures of the Knudsen cells and of the substrate.

3.2 STRUCTURAL CHARACTERIZATION OF THIN FILMS

This section presents an overview of the structural characterization techniques used in this work. The section begins with a description of Reflection High Energy Electron Diffraction (RHEED), and concludes with a presentation of two X-ray methods: X-Ray Reflectivity (XRR), and X-Ray Diffraction (XRD).

3.2.1 Reflection High Energy Electron Diffraction

Reflection High Energy Electron Diffraction (RHEED) is a widely used technique for the observation in real-time and *in situ* of the film growth modes and the crystalline structure during the deposition. In the RHEED gun, a high-energy electron beam (U = 30 kV and I_f ~ 1.7 A) is directed towards the substrate at a grazing incident angle ($\theta < 4°$). The emission current (I_e) is near 10 mA. The diffracted electrons from the surface are collected on a fluorescent screen and the resulting diffraction pattern is recorded by a CCD camera with the KSA 400 software.

The spatial resolution in RHEED analysis for a well-collimated electron beam is typically in the range of 100 nm. In the case of two-dimensional materials, the observations made on the screen originate from the intersection of the rods of the reciprocal space with the Ewald sphere.

Two directions are systematically probed: $[1\bar{1}00]$ (or called D1 in the following) and $[1\bar{2}10]$ (or called D2 in the following) for the sapphire substrate (α-Al_2O_3 (0001). The number and position of streaks represent the reciprocal lattice of the surface along the direction perpendicular to the electron beam. The crystallographic structure of the growing layer is thus deduced from the RHEED patterns.

Figure 3.3 illustrates the typical RHEED patterns that can be observed according to the growth mode. If the atomic terraces in the probed plane exceed the beam coherence (Figure 3.3 (a)), bright spots will be visible on the screen. In the case of well-ordered two-dimensional materials, such as the sapphire substrates used in this experiment, the observation of bright lines emanating from the spot is indicative of the presence of Kikuchi lines, which are a consequence of inelastic scattering processes. In instances where the atomic terrace sizes are close to that of the electron beam, it is possible to distinguish the presence of fine streaks, as illustrated in Figure 3.3 (b). These streaks are associated with the broadening of the points due to the presence of small out-of-phase domains, with a characteristic length scale which is approximately the electron beam coherence length. The width of the streaks is inversely proportional to the average domain size.

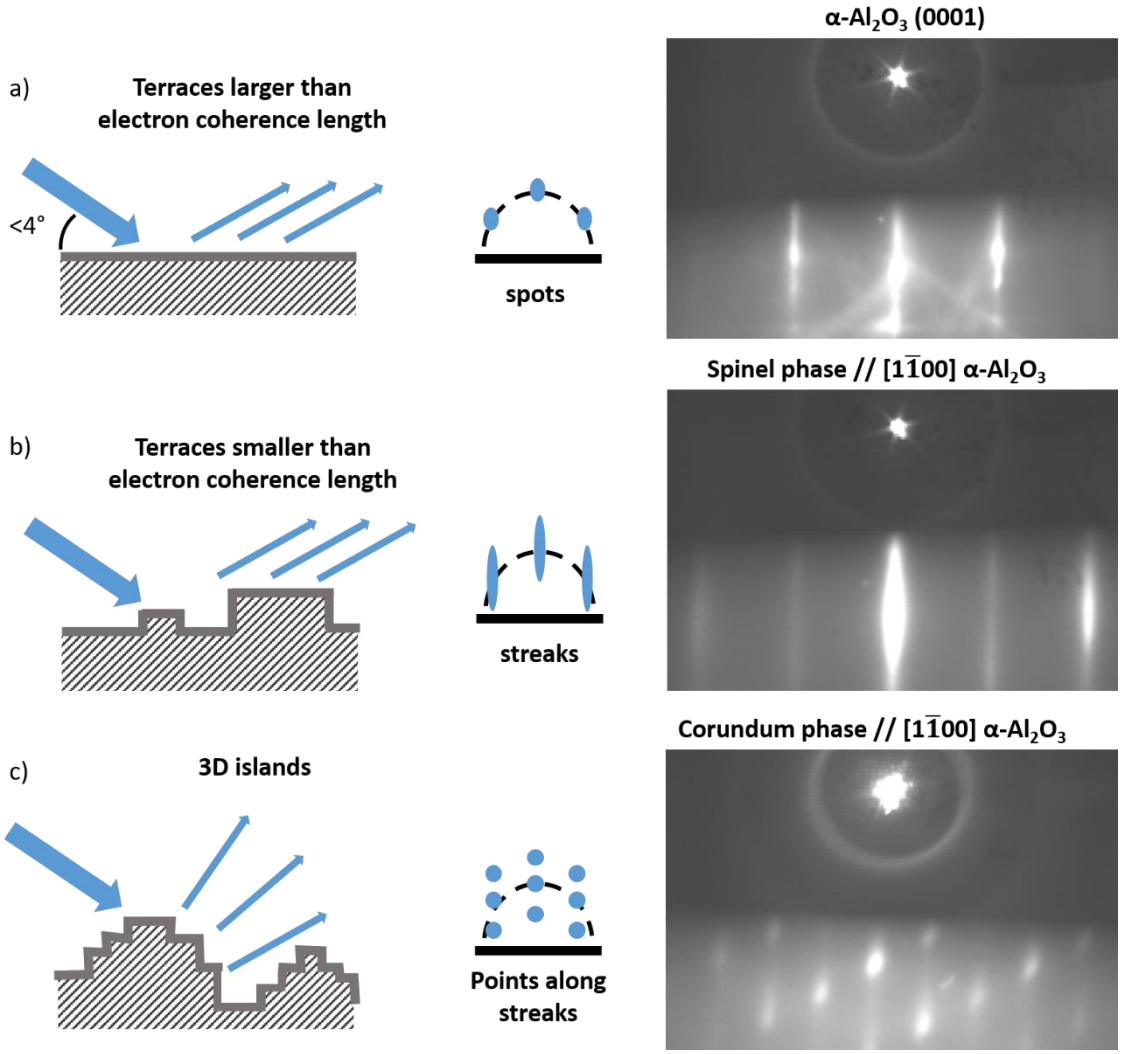

Figure 3.3: Schematic illustration of RHEED patterns for different surface morphologies. The first column depicts a schematic illustration of the growing layer, the second illustrates the expected RHEED pattern and the third column presents one experimental example.

When the growth conditions are not optimized, the presence of spots along the streaks can be observed, as illustrated by Figure 3.3 (c). This is indicative of a three-dimensional (3D) growth mode. In order to gain insight into this particular RHEED pattern, it is necessary to revisit the concept of layer-by-layer deposition. As the roughness of the domain increases, intensity modulation along the streaks is observed. This modulation is the result of interference between the various terraces, which exhibit different heights and widths. If the aforementioned trend persists, only points along the streaks will be observed, behavior which is characteristic of a 3D growth mode. In this work, the objective is to elaborate thin layers with a very low roughness, *i.e* to obtained b) patterns.

As said previously, the RHEED patterns were recorded in two distinct directions according to α-Al_2O_3 substrates: [$1\bar{1}00$] (or D1) and [$1\bar{2}10$] (or D2). Different information can be extracted from the RHEED patterns:

- The crystalline quality and the growth mode of the layer. The RHEED pattern allows for the identification of whether the growth mode is layer-by-layer or 3D islands (see Figure 3.3).
- The evolution of the in-plane lattice parameter can be monitored by using the substrate as a reference. The distance between streaks in the reciprocal space, is inversely proportional to the atoms spacing in the real space. By measuring the distance between the streaks of the substrate and between the streaks of the film, it is possible to determine the in-plane lattice parameter. However, this method is not accurate. The streaks have a notable width, which presents a challenge in identifying the maximum. This analysis can be partially corrected by selecting a large area in the image and by averaging the profile.
- The crystalline structure. Indeed, different structures in the ternary oxide system can crystallize, such as corundum-type (*e.g.* α-Cr_2O_3, α-Fe_2O_3), halite-type (FeO) or spinel-type (Fe_3O_4) structures. The RHEED patterns of these structures are different. In the case of an α-Cr_2O_3 (0001) layer grown on top of α-Al_2O_3 (0001) sapphire, the space group remains unchanged, and only a broadening of the bright spots of the α-Al_2O_3 substrate in fine streaks is observed as the layer is growing. In the case of a spinel-type structure, due to the epitaxial relationship between the substrate and the spinel phase, an evolution of the RHEED patterns is observed along the [$1\bar{1}00$] and [$11\bar{2}$] directions. This is evidenced by the apparition of additional streaks associated to the spinel phase. Along the D1 direction, the spinel streaks apparition is combined with the disappearance of two streaks of the sapphire (see chapter 4). In the D2 direction, only two additional streaks associated to the spinel phase appear without any disappearance of sapphire streaks.

3.2.2 X-ray methods and thin film specifications

This subsection will describe two distinct types of X-ray experiments: X-Ray Reflectivity (XRR)[5,6] and X-Ray Diffraction (XRD)[6,7], which will be used for the access to the film thickness, roughness and the crystalline structure of the $Fe_\alpha Ni_\beta Cr_\gamma O_4$ thin films.

The X-ray diffractometer is defined by five distinct components: the X-ray source, the incident optics, the goniometer, the receiving optics, and the detector. Figure 3.4 illustrates the location of each component.

The X-ray source is a compact tube comprising two electrodes. The electrons are generated by a tungsten cathode. These electrons are then accelerated through the application of a high voltage, typically in the range of 10 kV, and subsequently collide with an anode comprising a variety of materials. The most commonly material used is the copper, for which both Kα and Kβ radiations are well-known (λ= 1.54059 Å for $K\alpha_1$ λ= 1.54443 Å for $K\alpha_2$ and λ= 1.39223 Å for Kβ). Note that the selection of anodes with a shorter wavelength enables the analysis of a larger area in the reciprocal space.

The incident and receiving optics can be used in two distinct configurations: Bragg Brentano geometry for powder diffraction and parallel beam geometry for thin film diffraction.

The goniometer is a fundamental part of the diffractometer. It is used to control the different angles, as detailed in Figure 3.4. ω is the angle between the incident X-ray beam and the Bragg planes (*i.e.* the planes for which diffraction occurs). θ is the angle between the reflected beam and the Bragg plane. 2θ is the angle between the reflected beam (*i.e.* the detector) and the incident beam. The tilting angle, ψ, is the angle associated to the rotation of the Bragg planes around the horizontal plane. This angle is generally used for pole figures. The azimuth angle, Φ, is the angle of rotation in a horizontal position. Additionally, another angle, χ, can be defined by the following relationship: $\chi = 90° - \psi$. Such setups are commonly defined as four-axis diffractometers, related to the four angles (ω, θ, ψ and Φ).

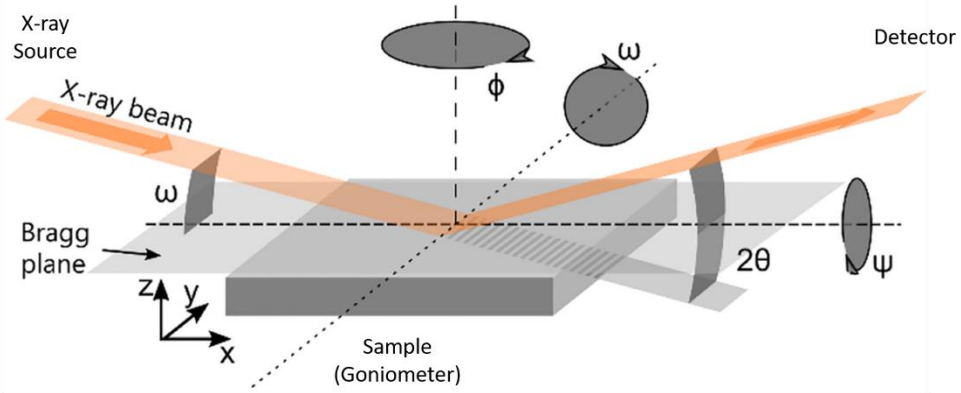

Figure 3.4: Schematic illustration of the various angles employed in a thin film diffractometer, from Harrington et al.[7]

The final component of the diffractometer is the detector. The detector is utilized to transform X-ray radiation into an electrical signal. The nomenclature of detectors is based on their dimensionality, which can be classified as a point detector (0D), line detector (1D), or area detector (2D). In function of the incoming

X-rays, attenuators may be necessary in order to reduce the incoming signal, to prevent non-linearity, and accelerated ageing. The maximum count is usually in the range of 10^4 to 10^6 counts per second (cps). In the spinel layers grown on top of α-Al_2O_3 (0001) substrates, an intensity of around 10^6 cps are observed for the (0006) peak of the sapphire.

3.2.3 X-ray Reflectivity of thin films

In the case of X-Ray Reflectivity (XRR), the thickness and the roughness will be probed. The X-ray beam arrives at an angle close to the critical angle. Below the critical angle, the X-ray intensity is totally reflected on the surface, and the curve displays a flat signal. At the critical angle, the X-ray begins to probe the film, and thus the reflected intensity begins to decrease. Above the critical angle, the interferences between the X-ray beams reflected at the surface of the sample and at the surface of the substrate induce oscillations in the signal. The XRR measurement is a purely optical measurement due to the difference of refractive indexes (n) between the layer and the substrate.

The refractive index n of the material is determined to be:

$$n = 1 - \delta - i\beta \tag{3.1}$$

$$\delta = \left(\frac{r_e \lambda^2}{2\pi}\right) N_0 \rho \frac{\sum_i x_i (Z_i + f_i')}{\sum_i x_i M_i} \tag{3.2}$$

$$\beta = \left(\frac{r_e \lambda^2}{2\pi}\right) N_0 \rho \frac{\sum_i x_i (Z_i + f_i'')}{\sum_i x_i M_i} \tag{3.3}$$

δ and β represent the real and imaginary part of the refractive index (n), respectively. r_e is the classical radius of an electron. N_0 is the Avogadro number. λ is the X-ray wavelength. ρ represents the density in g/cm^3. Z_i denotes the atomic number of the i^{th} atom. M_i signifies the atomic weight of the i^{th} atom. x_i is the atomic ratio of the i^{th} atom, and f'i et f''i are respectively the real and imaginary atomic scattering factors of the i^{th} atom. The critical angle θ_c is directly proportional to δ by the given formula:

$$\theta_c = \sqrt{2\,\delta} \tag{3.4}$$

Given that δ is proportional to the density of the film, it follows that the critical angle is proportional to the square root of the film density.

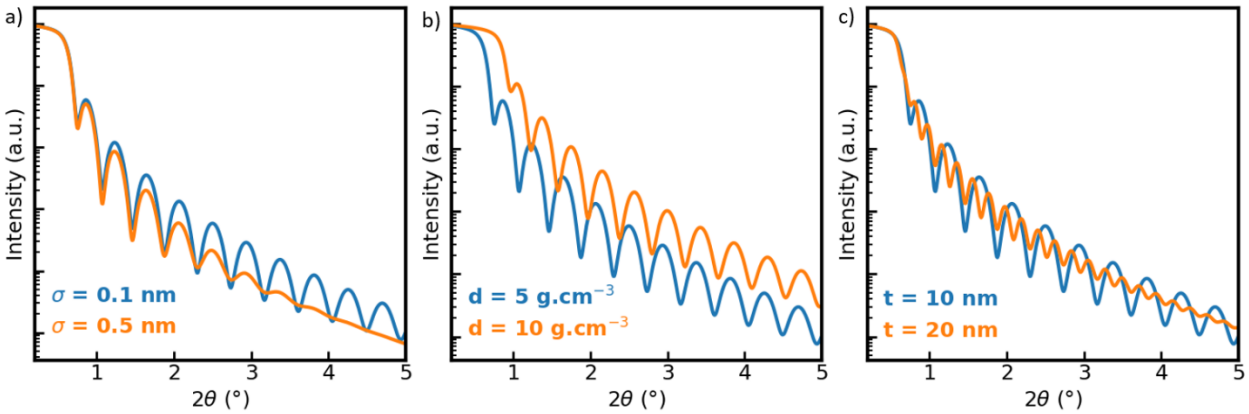

Figure 3.5: Effect of roughness variation (a), density variation (b), and thickness variation (c) on the resulting signal in XRR.

The fitting of the XRR curves by using REFLEX[8] or SimulReflec software, allows to extract three parameters such as: film thickness (t), roughness (σ_{RMS}), and density (ρ). All these parameters and their impact on the XRR signal are shown in Figure 3.5. The blue curve is the same between the three subfigures, and parameters used to generate this curve are the following. The thickness has been fixed at 10 nm, roughness at 0.1 nm, density at 5 g.cm^{-3}, f' at 100 fm and f'' at 10 fm, which is close to the magnetite values of 5.85 g.cm^{-3}, 108 fm and 9.7 fm for density, f' and f'' respectively.

- Density. The critical angle is a direct indication of the material density. An increase of the density generates a more important critical angle.
- Thickness. The interferences from the X-rays reflected at the surface of the sample and the X-rays reflected at the surface of the substrate exhibit oscillations depending both on the sample thickness and δ index, as defined in equations (3.1) and (3.2). Thicker the film, more important is the oscillation frequency.
- Roughness. The magnitude of oscillations are related to the surface roughness. It has been observed that the rougher the interface, the less intense the amplitude of the oscillations.

3.2.4 X-ray Diffraction of thin films

In the case of X-ray Diffraction (XRD), the thickness, the crystalline quality and the lattice parameter will be probed. The X-ray wavelength is of the same order of magnitude as the interatomic distances in a thin film. This phenomenon will result in constructive or destructive interferences between the reflected beams on the different atomic planes. The Bragg law describes the inter-planar distance:

$$n\lambda = 2d_{hkl}sin\theta_B \qquad (3.5)$$

n represents the order of the reflection, λ denotes the X-ray wavelength, d_{hkl} is the interatomic planar spacing in which h k l subscript refers to the Miller indices associated to the (h k l) plane and θ_B is the Bragg angle between the incident X-rays and the atomic plane. The interatomic d spacing calculated in the cubic and hexagonal structures are respectively:

$$d_{hkl}^{cubic} = \frac{a_{cubic}}{\sqrt{h^2 + k^2 + l^2}} \tag{3.6}$$

$$d_{hkl}^{hexagonal} = \frac{1}{\sqrt{\frac{4}{3}\frac{h^2 + k^2 + hk}{a_{hexagonal}^2} + \frac{l^2}{c_{hexagonal}^2}}} \tag{3.7}$$

The a and c denote the lattice parameters in the two different systems: cubic and hexagonal. These two structures can be used for spinel oxides considered in this thesis due to the [111] growth orientation of the spinel layer on sapphire.

Usually, the spinel structure is described by a cubic lattice ($a_{cubic} = b_{cubic} = c_{cubic}$). However, due to the strain induced by the [111] growth orientation on sapphire , it adopts a hexagonal lattice ($a_{hexagonal} = b_{hexagonal} \neq c_{hexagonal}$). These two lattices are related by the following relations:

$$\begin{aligned} a_{hexagonal} &= {}^{a_{cubic}}/_{\sqrt{2}} \\ c_{hexagonal} &= \sqrt{3}\, a_{cubic} \end{aligned} \tag{3.8}$$

Different measurements were done on each sample: 2θ/ω and rocking curves (RC). The 2θ/ω measurement is the thin film equivalent of the 2θ/θ measurement for powder diffraction. In a 2θ/ω scan, the incident angle (ω) is maintained at half the scattering angle (2θ). The Bragg plane is maintained in parallel with the surface of the sample. Consequently, the Bragg condition (see equation (3.5)) is only fulfilled for (h k l) planes parallel to the sample surface. In our case, the spinel phase grows on the [111] crystallographic orientation on the (0001) plane of the sapphire substrate. Consequently, only the out-of-plane lattice parameter can be probed here. In-plane lattice parameters measurement requires an alternative configuration of the diffractometer, with a distinct variation of diffractometer angle (2θ/ϕ).

A Gaussian function is employed to fit the film peaks, thereby extracting both the position and full width at half maximum (FWHM) values of each peak. The peak position will be used to determine the lattice parameter (see equations (3.5) and (3.6)). The FWHM can be used as a preliminary estimation of the thickness of the layer, according to the Scherrer law:

$$t = \frac{0.89 * \lambda}{FWHM * cos\,\theta} \quad (3.9)$$

t represents the crystallite size, λ the wavelength of the X-ray source, FWHM the full width at half maximum (in radians) of the peak, and θ the position of the peak (in radians). In the case of 2D growth mode, the crystallite size probed by the Scherrer law is the size in the direction normal to the surface sample, *i.e.* the layer thickness.

A rocking curve (RC) is defined as the variation of the incident angle ω around the center Bragg angle 2θ (which is kept constant). This process aligns planes that are not parallel with the surface sample in the Bragg plane. The result is a Gaussian curve, which provides insight into the distribution of planes as a function of surface tilt. The full width at half maximum (FWHM) is influenced by factors such as mosaic spread, dislocation, and substrate curvature. A smaller FWHM value indicates a higher crystalline quality of the grown phase.

The XRR and XRD measurements were done at room temperature on a Rigaku SmartLab diffractometer available in the SPEC/LNO laboratory. The wavelength was a monochromatic Cu Kα radiation (λ = 1.54186 Å). The sample is initially moved in the z-direction to ensure that the X-ray intensity is divided by two. It is then aligned to guarantee that the normal to the diffractometer goniometer is also the normal to the surface of the sample. Subsequently, the XRR measurement is done, and the resulting XRR curve is fitted. Subsequently, an XRD measurement is done with 2θ/ω varying between 35° and 42° for the sapphire substrate. A Gaussian function was employed to obtain position and FWHM of the (222) substrate peak, whereas a pseudo-Voigt function was employed for the (0006) substrate peak. In addition, some in-plane lattice measurements were performed.

3.3 CHEMICAL CHARACTERIZATION OF THIN FILMS

This section presents an overview of X-ray Photoemission Spectroscopy (XPS), outlining its underlying principles and key features, and providing insights into the determination of the chemical composition of our samples.

3.3.1 Theoretical considerations

The XPS method is a surface analytical technique in which the surface of the sample is excited by soft X-rays[9], resulting in the emission of electrons through photoelectric effect. These electrons are then analyzed to obtain information regarding the elemental composition, elemental oxidation state or crystal field surrounding atoms.

The two most commonly utilized sources of soft X-rays in a commercial XPS setup are Mg Kα (1253.6 eV) and Al Kα (1486.6 eV). Once the photons are created, they interact with the surface region of the sample, providing energy to the surface atoms and thus causing some electrons to be emitted via the photoelectric effect. The energy of the photoemitted electrons is described by energy conservation law:

$$KE = h\nu - BE - \varphi \qquad (3.10)$$

hν represents the energy of the incident X-ray photons, BE is the binding energy of the atomic orbital from which the electrons are emitted, and φ is the work function of the spectrometer. The binding energy can be regarded as the difference between the initial and final states of an electron. In the initial state, the electron is located within the electronic cloud and thus the atom is in a neutral state A^0. In the final state, the electron leaves the electronic cloud, resulting in the creation of a cation A^+.

Each element has a unique set of binding energy values for these electronic levels, enabling surface elements to be identified. The elemental concentration can be determined by analyzing the area below the respective elemental peak (*cf.* section 3.3.2). In the case of transition metals (Fe, Ni and Cr), the quantification is generally achieved with *2p* core levels. These levels exhibit the greatest intensity (greater excitation probability). In addition to the quantification, according to fluctuations in the core levels binding energies, resulting from factors such as chemical potential, oxidation state or bond character, the BE can serve as an indicator of the chemical state of an element.

The XPS *2p* core levels spectra of transition metal oxide are particularly complex to interpret for various reasons[10–13]. Firstly, the *p*, *d*, and *f* orbitals undergo a

splitting phenomenon at the stage of ionization, consequence of the spin-orbit coupling. Secondly, some additional satellite peaks can be observed. In the case of transition metals, the phenomenon is attributed to a shake-up process. When an excitation and ejection of a core level electron occurs, energy can be transferred to other electrons. This phenomenon promotes the electrons to higher energy levels. This transition leads to a loss of energy of the main photoelectron. Satellite peaks can be then observed at higher binding energy sides. Finally, spectral asymmetry and peak broadening are also observed in transition metals oxides due to coupling between the core-hole and the unpaired electrons in the *3d* outer shell. This effect is referred as intra-atomic multiplet coupling[11,14]. This complex interpretation of *2p* core levels spectrum is illustrated in Figure 3.6 for Fe-2p core levels spectra of various iron compounds. Broad peak are observed due to the multiplet coupling. The chemical state of iron (Fe^{2+} or Fe^{3+}) will result in the appearance of different satellite peaks, which can provide preliminary insights into the charge of iron. Indeed, in α-Fe_2O_3, when all the iron atoms are only in the oxidation state +3, a satellite peak is observed at 8 eV after the main Fe $2p_{3/2}$ peak. In contrast, in pure Fe^{2+} compounds such Fe_2SiO_4, the satellite peak appears at 4 eV after the main Fe $2p_{3/2}$ peak.

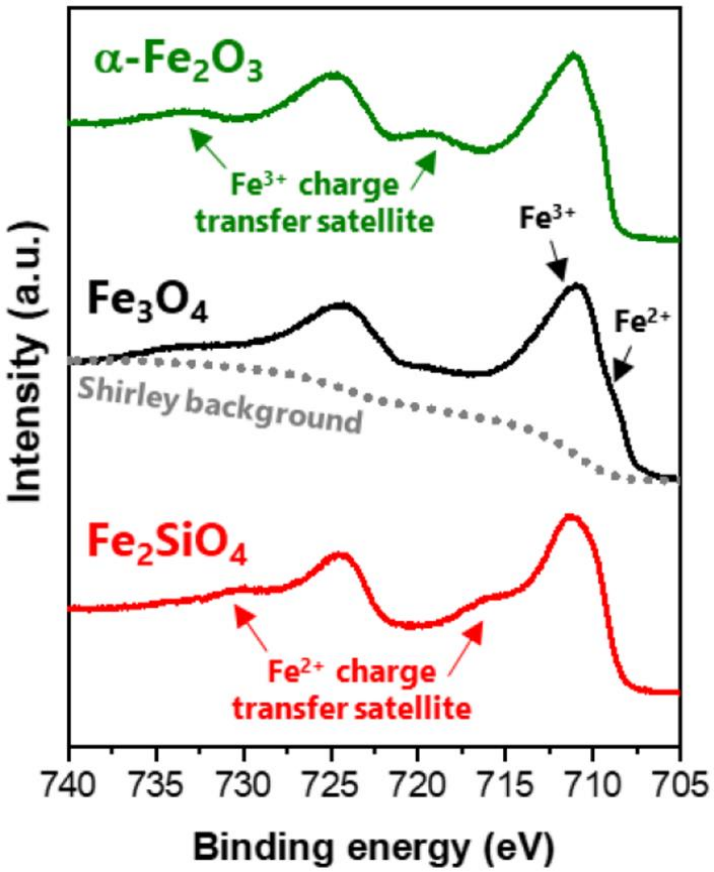

Figure 3.6: XPS Fe-2p core levels spectra for different reference iron oxides[15].

In addition, the photoemission process can also lead to the emission of Auger electrons. These electrons are emitted due to the energy given by the relaxation of an electrons in the hole created by photoemission process.

Once an electron has been created, it must leave the sample in order to be detected by the spectrometer. However, the probability of an electron interacting with matter is significantly higher than that of a photon interacting with matter. A photon exhibit mean free path of few micrometers, and thus the ionization process described above arrives in the initial micrometers of the sample. In contrast to photons, electrons can leave the sample without losing energy due to interactions with matter within the first 10 nm of the surface.

3.3.2 Quantification of the stoichiometry of the thin films

In this work, the XPS measurements are performed mainly to estimate the thin film compositions (α, β and γ). The number of photoelectrons per second received by the detector for a given peak and for a homogeneous sample is given by the following equation:

$$I = nf\sigma\theta y\lambda AT \tag{3.11}$$

In equation (3.11), I represents the number of photoelectrons per second, n represents the number of atoms of the element per cm^3 of the sample, f represents the X-ray flux (in photons.cm^{-2}.s^{-1}). The photoelectric cross-section, σ, for the atomic orbital under study is expressed in cm^2, while the angular efficiency factor, θ, represents the instrumental arrangement. y represents the efficiency of the photoelectric process. The mean free path of the photoelectrons in the sample is represented by λ. The irratiated area of the sample is represented by A, while the detection efficiency is represented by T. The value of interest is n, which represents the number of atoms of the studied element. The equation (3.11) can be reorganized as follows:

$$n = \frac{I}{f\sigma\theta y\lambda AT} \tag{3.12}$$

The denominator can be considered as an atomic sensitivity factor, S. Finally, a general expression can be formulated for the determination of the atomic fraction C_x of a constituent in a given sample:

$$C_x = \frac{n_x}{\sum n_i} = \frac{I_x/S_x}{\sum I_i/S_i} \tag{3.13}$$

In equation (3.13), the fraction of each constituent x (C_x) is therefore the fraction of the corresponding area, normalized by its sensitivity factor S_x on the sum of areas of other constituents i, normalized by their respective sensitivity factors S_i.

Once the area has been measured and given that the atomic sensitivity factor is known, the atomic stoichiometry can be determined. In this case, the Scofield sensitivity factor is used[15].

The area of each spectrum region is determined through a three-step process. Initially, a Shirley background is generated and subtracted from the signal[15]. Subsequently, the overall area of the region is determined. Ultimately, each area is divided by the corresponding Scofield factor, thereby yielding the sample stoichiometry in terms of metallic cations.

This study employs both *in situ* (within the MBE apparatus) and *ex situ* XPS setups. The *in situ* XPS is situated at the SPEC/LNO, while the *ex situ* XPS is located at the S2CM/LECA. The *in situ* XPS can use both Mg and Al Kα sources, whereas the ex situ XPS uses only Al Kα. However, this source is monochromated, which enables a better energy resolution. The *in situ* XPS is used just after the growth in order to obtain preliminary elemental composition data and is realized with the Mg Kα anode. The definitive composition is determined with the *ex situ* XPS (Al Kα anode), which possesses superior energy resolution and is equipped with a flood gun. The flood gun is employed for the purpose of fixing charge effects. It is used for less conductive samples when necessary. High-resolution spectra are done at room temperature in the *ex situ* apparatus. The binding energies are corrected by fixing the *1s* line of carbon at 285.0 eV. The carbon originates from organic contamination. The spectra are adjusted by using the commercial "AVANTAGE" or "CASAXPS"[16] software. The resulting chemical composition have uncertainties of approximately 10 %.

3.4 FINE STRUCTURE CHARACTERIZATION OF THIN FILMS

The fine structure characterization aims at the determination of the cationic site distribution. In this work, synchrotron-based methods for probing this fine structure will be explored: X-ray Absorption Spectroscopy (XAS), X-ray Magnetic Circular Dichroism (XMCD) and Resonant X-ray Diffraction (RXD). This section will describe the principles and key features of these techniques.

3.4.1 X-ray Absorption Spectroscopy and X-Ray magnetic circular dichroism

X-Ray Absorption Spectroscopy (XAS)[17] refers to a wide range of different synchrotron-based techniques. Depending on the photons energy (or studied transitions), XAS techniques have many designations. For example, X-ray absorption near edge spectroscopy (XANES), Extended X-ray Absorption Fine Structure (EXAFS) or Resonant X-ray Diffraction (RXD, technique that combines XAS and XRD) study the K edge of the element (*1s* → continuum transition). These two techniques have been employed in various spinel systems to determine the oxidation state, cationic distribution, or coordination number[18–23]. In order to investigate the fine structure of the $Fe_\alpha Ni_\beta Cr_\gamma O_4$ spinel thin films, XAS and XMCD analyses have been done.

The following section will examine the $L_{2,3}$ edge of nickel, chromium, and iron. The XAS signal in spinel oxides is primarily described by the *2p→3d* transition, which occurs through electron dipole transition ($2p^6 3d^n \rightarrow 2p^5 3d^{n+1}$). One of the most significant applications of the $L_{2,3}$ edges XAS experiment is the use of polarized X-rays to assess local magnetic properties in ferromagnetic or ferrimagnetic systems. More detailed information can be found in literature[17,24–26]. The dichroism signal originates from the difference in X-ray absorption. Indeed, the X-rays absorption in ferromagnetic or ferrimagnetic systems differs according to the X-ray polarization (right or left circular polarization, or even horizontal or vertical polarization). This discrepancy can be attributed to the different populations of electrons that are probed and the allowed transitions within the *3d* states. If left or right circular polarization is used, the technique is called X-ray Magnetic Circular Dichroism (XMCD). If horizontal or vertical polarization is used, the technique is called X-ray Magnetic Linear Dichroism (XMLD). The latter technique is employed to study AF systems, as detailed in Chapter 2.

The fundamental principle underlying this technique is the measurement of the energy-dependent fine structure of the X-ray absorption coefficient (μ(E)) of a specific element, near the absorption edge. The probability that X-rays will be absorbed is described by the Beer-Lambert's Law:

$$I_{sample} = I_0 e^{-\mu t} \quad (3.14)$$

$$\mu \approx \frac{\rho Z^4}{AE^3} \quad (3.15)$$

I_{sample} represents the intensity of the X-ray transmitted through the sample, I_0 denotes the X-ray intensity incident to the sample, μ is the absorption coefficient and t represents the sample thickness. The value of μ is significantly influenced by the energy (E) and atomic number (Z) according to the formula presented in Equation (3.15), where ρ represents the sample density and A denotes the atomic mass of the studied element.

In this process, a core electron is excited into an empty state. Therefore, a significant increase in absorption is observed when the incident X-ray has the same energy as the Binding Energy (BE) of a core electron. This intense peak is referred as the absorption edge. In the case of $L_{2,3}$ edges, the *2p* electrons are excited into the *3d* state. Similar to the XPS technique, the position and shape of XAS signal is sensitive to the electronic structure and the local environment. Given that the excited electrons are in a *3d* state, the obtained signal is very sensitive to the crystal field (*i.e.* octahedral or tetrahedral sites) surrounding the absorbing atoms. The incident X-rays are tuned to the energy $L_{2,3}$ edges of one of the three elements: iron, nickel, or chromium. As a result, this technique is chemically and orbitally selective. In the particular case of iron, the slight deviation in position between Fe(II) and Fe(III), as well as between octahedral and tetrahedral sites, permits the decomposition of all the entire iron contribution, as the XMCD signal is a linear combination of all individual sites.

In the case of XMCD technique, a magnetic field is applied in the same direction as the wave vector of incident photons in order to align atomic spins. Two spectra are recorded, one with right circular polarization (σ^+) and one with left circular polarization (σ^-). The XMCD intensity is thus given by:

$$I_{XMCD} = \sigma^+ - \sigma^- \quad (3.16)$$

Figure 3.7 describes the two-steps process of the XMCD experiment. Primarily, an electron is excited through left or right circularly polarized X-rays (yellow arrows). A portion of the angular momentum carried by photons is converted into spin via spin-orbit coupling. The acquired spin moment is dependent on the polarization orientation and spin-orbit coupling (l + s in L_3 edge and l - s at the L_2 edge). Subsequently, the second step is the spin-conservative transition (black arrows) into the *3d* valence band, whereby a spin-up electron is prevented from entering the down valence band. As the samples exhibit magnetic ordering, the spin down valence band is not symmetric with respect to the spin up valence band. This

asymmetry results in a non-zero signal in XMCD. In addition to the previously discussed chemical and orbital selectivity, XMCD also probes the magnetic moment of an element.

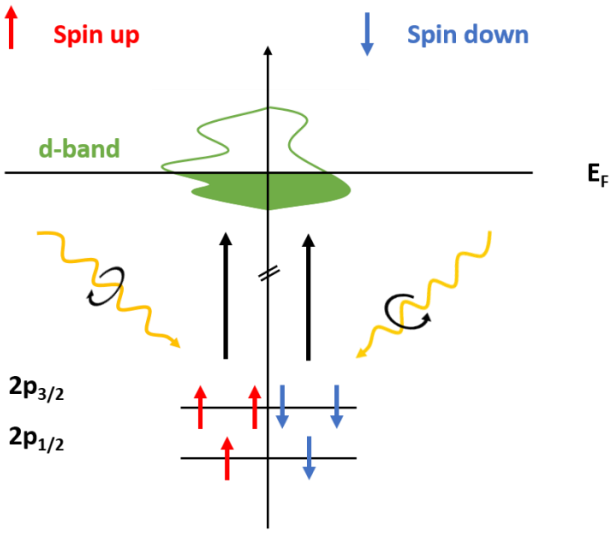

Figure 3.7: Schematic illustration of a XMCD experiment. The left circular X-rays probe spin-up electrons, while the right circular X-rays probe spin-down electrons.

The XMCD technique can also be used to record magnetic hysteresis loops associated with the distinct magnetic species. In the case of iron spinel, two geometries (T_d and O_h) and two cationic species (Fe^{2+} and Fe^{3+}) can be present in the material. In contrast to XMCD spectra, magnetic hysteresis are obtained by varying the magnetic field at a given energy. The selection of this energy allows for the separation and the determination of the magnetic contribution of each iron species.

In this study, XAS and XMCD experiments were performed on the $L_{2,3}$ edge for iron, nickel and chromium. The measurements were done at the DEIMOS beamline of Synchrotron Soleil, in collaboration with Dr. Philippe OHRESSER, Dr. Edwige OTERO, and Dr. Antoine BARBIER, and at the ESRF ID 32 beamline, in collaboration with Dr. Pamela VASCONCELLOS. The two end stations of the DEIMOS beamline, CroMag and MagneTwo, were used, in the initial and the subsequent runs. The CroMag station permits the utilization of a magnetic field strength up to 7 Tesla, in contrast to the 2 Tesla limit of the MagneTwo station. The samples were subjected to a magnetic field of ± 2 Tesla (up to ± 4 Tesla, for the samples studied in the CroMag station and at ESRF), oriented parallel to the wave vectors of the incident photons. Spectra were obtained at 300 K for all samples, and for some samples at low temperatures (T= 4 K, 20 K or 107 K). In the majority, the angle between the beam and the sample surface was 35°, but some

experiments were performed at 90°. The signal was recorded in Total Electron Yield (TEY). As the emitted electrons are strongly absorbed, the probed electrons are coming from a depth of around 2-5 nm. All experiments were carried out in an ultra-high vacuum, with a partial pressure of approximately 10^{-10} mbar. Two information were deduced from the XAS/XMCD spectra:

- The cationic site distribution. As previously said, the XMCD spectrum is a linear combination of all the individual contributions. The decomposition of the spectrum allows the quantification of each cationic contribution.
- The magnetic hysteresis loops of individual species. The recording of magnetic hysteresis allows to analyze the contribution of each individual species on the magnetic properties.

3.4.2 Resonant X-ray diffraction

Resonant X-ray Diffraction (RXD) is an experimental technique combining X-ray diffraction (XRD) with X-ray Absorption Spectroscopy (XAS). The RXD technique is defined as the study of diffraction peaks in the vicinity of an absorption edge. It was pioneered by different authors[27] in the 90s. This technique combines the elemental selectivity allowed by the XAS technique and the structural sensibility of the XRD technique, and therefore is a perfect tool for fine structure investigations.

The XRD signal is generated by the long-range order of a crystal, with some atomic planes leading to the constructive interference of X-ray in accordance with the Bragg law (see equation (3.5)). The diffraction peaks intensity is directly proportional to the structure factor by the following relation:

$$I_{hkl} = |F_{hkl}|^2 \cdot M_{hkl} \cdot LP(\theta) \cdot TF(\theta) \qquad (3.17)$$

The peak intensity of a given atomic plane of Miller indices (h k l) is denoted by I_{hkl}. The aforementioned intensity is affected by a number of factors: the structure factor F_{hkl}; the multiplicity of plane factor M_{hkl}; the Lorentzian and polarization factor LP(θ); and the temperature factor TF(θ). The final two factors are linked with the experimental conditions, while the first two terms are linked to the crystallographic structure of the materials. The structure factor is given by:

$$F_{hkl} = \sum_i f_i(\boldsymbol{Q}, E) * exp\left(-j2\pi(hx_i + ky_i + lz_i)\right) \qquad (3.18)$$

f_i represents the atomic scattering factor for the i^{th} atom, depending on both **Q**, the wave vector transfer and the energy E. h, k and l denote the Miller indices of the (h k l) plane of reflection, and x_i, y_i and z_i signify the fractional coordinates of

the i^{th} atom in the crystal lattice. Consequently, one part is related to the chemical composition of the sample (f_i), while the second part is related to the crystallographic structure ((h k l) plane). In the spinel structure, peaks such as (622) or (222) are sensitive only to the O_h cations, while peaks such as (202) or (602) are sensitive only to the T_d cations. Some peaks can also show a contribution from both sites ((531) or (400)).

In the case of transition metals, the atomic scattering factors f_i are close, as it is approximately proportional to Z, the atomic number. Consequently, the direct XRD experiment does not permit the discrimination between the contributions of iron, nickel, and chromium species. Conversely, the RXD experiment, through the chemical selectivity allowed by the energy selection, can discriminate between the distinct metallic cation, because the atomic scattering factor is dependent on the X-ray energy. In the vicinity of a transition, the atomic scattering factor f_i can be decomposed into three contributions:

$$f_i(\boldsymbol{Q}, E) = f_{i,0}(\boldsymbol{Q}) + f_i'(E) + jf_i''(E) \qquad (3.19)$$

The first term in equation (3.19) is independent of energy (but dependent on the wave vector transfer **Q**), and the second and third terms, respectively, denote the real and imaginary parts of the anomalous factor of the atom i, dependent of the energy. These two terms become significant in the vicinity of an absorption edge. Figure 3.8 presents the variation of the real part and the imaginary part of the anomalous factor for the iron K edge (7120 eV, black dotted line). The real part displays a deep well, while the imaginary part exhibits a step-like variation at the K edge. Consequently, by studying the energetic variations of a peak and by tuning the X-ray energy to the desired elemental K edge, it is possible to obtain signals where one of the contributing factors is the presence of the probed element in O_h or T_d sites.

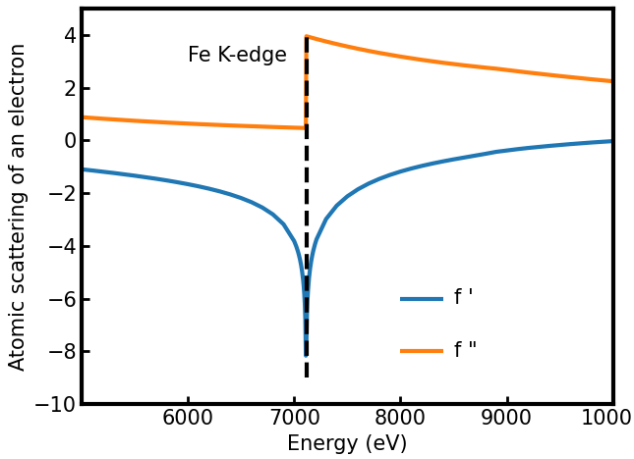

Figure 3.8: Energy variation of the two terms of the anomalous scattering in the case of iron, in multiple of scattering of one electron ($2.82e^{-15}$ m).

The RXD technique was performed at the beamline SiXS at the synchrotron Soleil. Experimental station 2 (open-air, without deposition apparatus) was selected, with a beryllium dome with inert N_2 atmosphere to protect samples from the deposition of pollutants. The local contact was Dr. Alina VLAD, in collaboration with Dr. Antoine BARBIER. This beamline has an X-ray range of 5 keV to 20 keV. Experiments in Grazing Incidence X-ray Diffraction (GIXD) were performed at 15 keV, which permits a comprehensive exploration of the reciprocal space and the choice of the peaks to perform RXD. The RXD experiments on the K-edge were performed for two elements: iron (7120 eV) and nickel (8300 eV). The chromium RXD experiment was not accomplished due to the limitations of the beamline. The chromium K-edge is localized at 6 keV, which is close to the limit for the beamline (5 keV). Consequently, a significant decrease in signal results from this close proximity with the limit. The GIXD and RXD experiments allow the extraction of two principal information:

- The epitaxial relationship between the substrate and the film. The GIXD experiment allow a complete assessment of the reciprocal space, and therefore the epitaxial relationship between the substrate and the film.
- Partial site distribution for iron and nickel species. The RXD experiment is not very sensitive to the cationic charge, but can distinguish between T_d or O_h occupancy.

3.5 SIMULATION OF XMCD AND RXD SPECTRA

In order to extract the cationic site distribution of our $Fe_\alpha Ni_\beta Cr_\gamma O_4$ spinel thin films from the XMCD and RXD spectra, simulations of these spectra are necessary. The following section will provide a description of the software developed to calculate the XMCD spectra (Quanty), and the software used to calculate the RXD spectra (FDMNES).

3.5.1 Quanty simulation of XMCD spectra

In order to extract the local structure of Ni, Fe and Cr cations from $L_{2,3}$ edge XMCD spectra, it is necessary to perform simulations of the different reference spectra. The underlying principle governing the simulation of XMCD spectra is the Fermi golden rule:

$$\Gamma_{i\to f} = \frac{2\pi}{\hbar}\left|\langle\Phi_f|T|\Phi_i\rangle\right|^2 \delta_{E_f - E_i - h\nu} \qquad (3.20)$$

$\Gamma_{i\to f}$ represents the transition probability per unit of time, $\langle\Phi_g|T|\Phi_i\rangle$ denotes the transition matrix between the final state Φ_f and the initial state Φ_i. The Dirac operator $\delta_{E_f - E_i - h\nu}$ guarantees the conservation of energy by ensuring that the final energy (E_f) is equal to the initial energy (E_i) plus the transition energy. The transition matrix T incorporates the selection rule of photoexcitation and the polarization. The initial and final state wave functions (Φ_i and Φ_f), which are unknown, necessitate the use of approximation by the calculation software. The methodology for making these approximations is discussed elsewhere in the literature[17].

In this study, Quanty[28–30] was chosen as the simulation tool to generate the theoretical curves. The Quanty simulation uses a localized approach based on atomic multiplet theory in order to describe many-body effects. This approach is referred to as crystal field multiplet (CFM). In this context, an atomic Hamiltonian describes the interaction with the absorbing atom (H_{atom}). The crystal field Hamiltonian (H_{CF}) encompasses symmetry aspects of the solid, and a Zeeman Hamiltonian (H_{Zeeman}) describes the interaction between the atoms and the magnetic field. These three contributions are summarized in the following equation:

$$H_{CFM} = H_{atom} + H_{CF} + H_{Zeeman} \qquad (3.21)$$

The first part of a Quanty simulation is the simulation of the initial and final states multiplet (Φ_i and Φ_f). A multielectronic state is described with quantum mechanics with the following Hamiltonian:

$$H_{atom} = H_{Kin} + H_{e/N} + H_{e/e} + H_{SO} \quad (3.22)$$

H_{Kin} represents the kinetic energy of electrons, $H_{e/N}$ denotes the nucleus-electron coulombic attraction, $H_{e/e}$ signifies the coulombic repulsion between electron-electron pairs, and the final term H_{SO} represents the spin-orbit coupling of each electron.

The second phase of the Quanty simulation involves the incorporation of solid-state effect (H_{CF}). A transition metal situated within a crystalline structure will undergo a splitting of its five-fold degenerate *3d* orbitals, which will occur according to the repartition of anions surrounding the transition metal cation. This splitting is commonly referred as Δ, the crystal field parameter. Two distinct anionic environment are possible in a spinel structure: octahedral (O_h) or tetrahedral (T_d), as illustrated in Figure 3.9. In the case of O_h symmetry, the six-fold coordinated anions are positioned along the three axes of the Cartesian symmetry, with two anions positioned along each axis. Therefore, when the anions approach the metallic cation, the *3d* cation orbitals pointing in the Cartesian directions are destabilized ($3d_{x^2-y^2}$ and $3d_{z^2}$), while the remaining three are stabilized, as their orbitals do not point in the direction of the anions ($3d_{xy}$, $3d_{xz}$, $3d_{yz}$). The group of orbitals formed with increased energy is described as 'e_g' group, while the other group is designated as the 't_{2g}' group. The crystal field splitting term is subsequently designated as Δ_O or 10 D_q, which is employed to describe the energy difference between these two groups of orbitals.

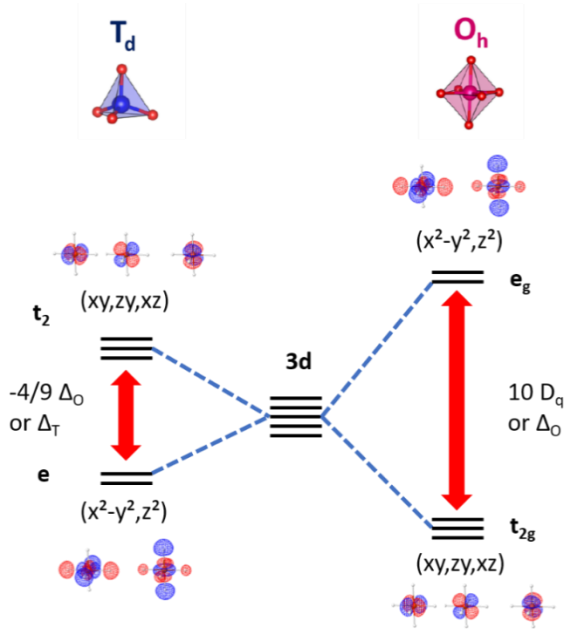

Figure 3.9: Energy level diagram illustrating the 3d orbitals splitting for an O_h anionic arrangement and a T_d anionic arrangement. Energy between orbitals is given in terms of crystal field parameters.

In the case of tetrahedral symmetry, the anions are situated on the alternate vertices of a cube with the cation in the center. In this instance, the stabilized orbitals are now the orbitals pointing in the Cartesian directions (*i.e.* $3d_{x^2-y^2}$ and $3d_{z^2}$; *e* symmetry), while the destabilized orbitals are the three remaining ones ($3d_{xy}$, $3d_{xz}$, $3d_{yz}$, t_2 symmetry). The crystal field splitting term is then referred to as Δ_T. In the case of identical cation-anion distance, the octahedral and tetrahedral parameters are linked with the following relation: $\Delta_T = -4/9*\Delta_O$. The negative sign indicates the inversion of the two orbitals groups.

The final term in the crystal field multiplet Hamiltonian is the interaction with the applied magnetic field (H_{Zeeman}). In a XMCD experiment a magnetic field (B_{app}) is applied to aligned atomic spins. This Hamiltonian is composed of two parts, one incorporating the local mean exchange field created by neighboring atoms (B_{exc}) and the orbital part interacting with the applied field (B_{app}).

$$H_{Zeeman} = \mu_B \gamma B_{exc} S_z + \mu_B B_{app} L_z \qquad (3.23)$$

The term μ_B represents the Bohr magnetron, while γ denotes the gyromagnetic ratio. The assumption is made that B_{exc} has the same direction as B_{app}. Given that B_{app} is applied in the z direction, only the z contribution of atomic spin moment S_z and orbital angular momentum L_z are employed.

All of these parameters are included in the Quanty simulation. The last step is the effective calculation of the resulting spectra. The code uses second quantization and Lanczos recursion method to calculate the spectra under the form of a Green function (G(ω)), thus avoiding the final state calculation.

3.5.2 FDMNES simulations of RXD spectra

The selected simulation software for predicting RXD behaviors is FDMNES (for Finite Difference Method Near-Edge Structure) package, developed by Joly *et al.* at ESRF[31]. This a free, ab initio and open source package. FDMNES is able to generate both the crystallography and the X-ray absorption in the same calculation. When a periodic system is created within the code, FDMNES generates a cluster around the absorbing atom. The FDMNES model of the anomalous factors (f′ and f′′ of Equation (3.19)) is defined as follows:

$$f_j^*(\omega) = \frac{m_e}{\hbar^2} \sum_{f,g} \frac{\left(E - E_g^{(j)}\right)^2 \left\langle \psi_g^{(j)} \middle| \hat{O}_{out}^* \middle| \psi_f \right\rangle \left\langle \psi_f \middle| \hat{O}_{in} \middle| \psi_g^{(j)} \right\rangle}{\hbar\omega - \left(E - E_g^{(j)}\right) + \frac{i}{2}\Gamma_f(E)} \qquad (3.24)$$

The superscript * of $f_j^*(\omega)$ denotes the real or imaginary part of the anomalous factor for atom j. m_e represents the electron mass, $\hbar\omega$ denotes the photon energy,

E_g and E signify respectively the energies of the ground state $\psi_g^{(j)}$ and the photo-excited state ψ_f. X-ray absorption necessitates a core localized level as a ground state, thus the index j describes one atom in the unit cell. The summation over j in the structure factor (see equation (3.18)) adds the contributions of all the atoms in the unit cell. The final state ψ_f is an unoccupied state of the continuum, thus its j index is omitted. The quantity Γ_f is the sum of the inverse of the final state and the core hole lifetimes, and thus depends on the chemical type of the absorber. The $\hat{O}_{in}$ and $\hat{O}_{out}^*$ terms represent, respectively, the incoming photon field and the outgoing one. The subscripts of the sum denote the ground state (g) and the final, photo-excited state (f).

The electron-photon interaction is described classically by means of a field operator Ô. In the X-ray regime, the magnetic part of the electromagnetic field can be neglected, and a satisfactory development comprises the first two terms of the multipolar expansion. The first term is the excitation of the electric dipole, while the second term is the excitation of the electric quadrupole.

The calculations are accomplished following the following steps. The initial step is to perform a self-consistent atomic calculation in order to get the initial level ψ_g for the absorber and the atomic densities for the atoms in the cluster. To calculate the absorption signal, an excited electronic configuration for the absorbing atom is assumed, *i.e.* the core electron is placed on the first available unoccupied level. The atomic densities are then superposed to get the charge density of the cluster and the Poisson equation is solved to get the Coulomb potential. Once the potential has been constructed, the Schrödinger-like equation (SE) is solved to obtain the final states ψ_f (r) (or some related quantities). Subsequently, the matrix elements featured in equation (3.24) are calculated. Finally, the sum over the states in equation (3.24) and the convolution are performed (with a Lorentzian function to account for the broadening due to the core hole lifetime $\Gamma_f(E)$).

FDMNES features two ways of calculating the ψ_f (r) state: the finite difference method (FDM) and the multiple scattering theory (MST), within the limits of the muffin-tin approximation (MT). The first method assumes a crystal potential that has spherical symmetry around atoms (the muffin-tin spheres) and is constant in the remaining space. The second method use a full potential and consist of constructing a space grid and discretizing the SE on the points of this grid. No approximation is needed with this second method, providing a more accurate but more time-consuming description of the phenomenon.

3.6 MAGNETIC CHARACTERIZATION OF THIN FILMS

The spinel oxides studied are usually ferrimagnetic. Ferrimagnetic materials exhibit a non-zero magnetic moment below the Curie temperature. The following section presents the magnetic characterization of the samples by the Vibrating Sample Magnetometry (VSM) technique.

In our VSM setup, two distinct experiments can be performed. (i) The evolution of the magnetization (M) as a function of temperature (T) or M (T) curves in order to access to the Curie temperature. (ii) The evolution of the magnetization as a function of the magnetic field (H) (or M (H) curves) in order to access to the magnetic hysteresis loops. By these loops measurements, we can define the coercive field (H_C), the remanence (M_R) and the magnetization at saturation (M_S) (see Figure 3.10).

The fundamental principle of a VSM experiment is the measurement of the voltage (V) induced in the detection coils when a magnetic sample vibrates periodically in the presence of a magnetic field ($\mu_0 H_{ext}$). The measured voltage is the time derivative of the induced flux ($V = -d\phi/dt$), which is related to the magnetic moment of the sample (μ, in $A.m^2$) with the following equation:

$$\phi = \left(\frac{B}{I}\right) * \mu \qquad (3.25)$$

ϕ is the magnetic induced flux, B the magnetic field produced by the current I flowing in the detection coils. Combining the detected voltage with equation $\phi = \left(\frac{B}{I}\right) * \mu$ (3.25), it is possible to measure μ as a function of $\mu_0 H_{ext}$.

The hysteresis loops is recorded in a PPMS-VSM magnetometer setup from Quantum Design in our laboratory (SPEC/LNO). Hysteresis loops are performed at three temperatures (T = 10 K, 100 K, and 300 K) for all samples, and with a magnetic field varying from +1 T to -1 T at 300 K, and from +1.5 T to -1.5 T at lower temperatures in order to reach the magnetic saturation. The sample is fixed with a double-edge adhesive and a protective film of Teflon. The magnetic field can be aligned along the $[11\bar{2}0]$ or $[1\bar{1}00]$ axes of sapphire substrates, the [010] or [100] axes of (001)-oriented $MgAl_2O_4$, the $[11\bar{2}]$ or $[1\bar{1}0]$ axes of (111)-oriented $MgAl_2O_4$. However, the samples do not exhibit in-plane magnetic anisotropy. Consequently, the direction of the applied magnetic field does not influence the magnetic signal of the thin film.

The data analysis involves the removal of the diamagnetic contribution from the substrate (α-Al_2O_3 or $MgAl_2O_4$). This is achieved by subtracting a linear fit obtained at high field. As the magnetic moment μ ($A.m^2$) is proportional to the

measured magnetic volume (V), a second treatment consists in the normalization of the signal by the volume in order to access to the magnetization M (in $A.m^{-1}$). Therefore, the film thickness is obtained from the XRR reflectivity measurements (see section 3.2.3) and the surface is used. Figure 3.10 illustrates the treatment and the three magnetic parameters, which can be deduced from these measurements:

- Saturation magnetization (M_S). The saturation magnetization is the value obtained when the magnetic moments are aligned with the external magnetic field. M_S is measured at the beginning of the initial branch (M_{S1}) and at the beginning of the return branch (M_{S2}) through the mean of the hundred first values of each hysteresis branch. The presented values are the average signal (in $kA.m^{-1}$) between the M_{S1} and - M_{S2} values.
- Remanent magnetization (M_R). The remanent magnetization is the residual magnetization that persists when an external magnetic field is no longer present, following an initial saturation process. The remanent magnetization values are determined by measuring the intersection between the hysteresis loop and the vertical line ($\mu_0 H = 0$ T), which is obtained through interpolation of the hysteresis curve. The M_R values are also measured two times for the back and forth of the hysteresis loop, in the same manner as the M_S values. The presented values are the average signal (in $kA.m^{-1}$) between the M_{R1} and - M_{R2} values.
- Coercive field (H_C). The coercive field is defined as the point of intersection between the hysteresis loop and the horizontal line (M = 0) through the interpolation of the hysteresis curve. High value of coercive field can be as large as 4 T (for $SmCo_5$ permanent magnet[32]). Such materials are called "magnetically hard". Materials with low coercive field are called "magnetically soft". Additionally, the H_C value is determined twice, and the subsequent values represent the average value (in Oe) between the $-H_{C1}$ and H_{C2} values.

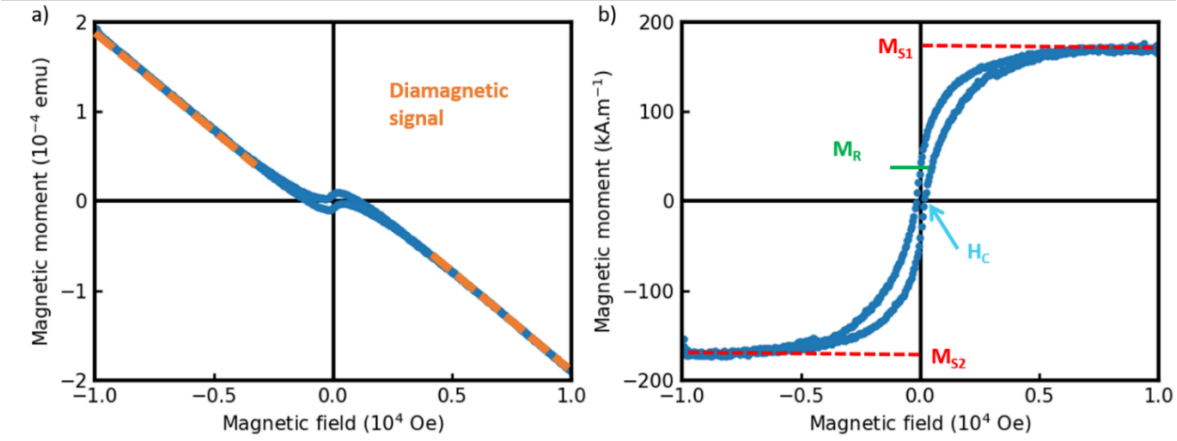

Figure 3.10: Hysteresis loop of a spinel sample before (a) and after (b) the subtraction of the linear diamagnetic contribution (which is

indicated in orange) and normalization.

3.7 BIBLIOGRAPHY

(1) Herman, M. A.; Sitter, H. *Molecular Beam Epitaxy: Fundamentals and Current Status*; Gonser, U., Osgood, R. M., Panish, M. B., Sakaki, H., Lotsch, H. K. V., Series Eds.; Springer Series in Materials Science; Springer: Berlin, Heidelberg, 1996; Vol. 7. https://doi.org/10.1007/978-3-642-80060-3.

(2) Gota, S.; Moussy, J.-B.; Henriot, M.; Guittet, M.-J.; Gautier-Soyer, M. Atomic-Oxygen-Assisted MBE Growth of Fe3O4 (1 1 1) on α-Al2O3 (0 0 0 1). *Surface Science* **2001**, *482–485*, 809–816. https://doi.org/10.1016/S0039-6028(00)01066-9.

(3) Gota, S.; Guiot, E.; Henriot, M.; Gautier-Soyer, M. Atomic-Oxygen-Assisted MBE Growth of α − F e 2 O 3 on α − A l 2 O 3 (0001): Metastable FeO(111)-like Phase at Subnanometer Thicknesses. *Phys. Rev. B* **1999**, *60* (20), 14387–14395. https://doi.org/10.1103/PhysRevB.60.14387.

(4) Vila-Fungueiriño, J. M.; Bachelet, R.; Saint-Girons, G.; Gendry, M.; Gich, M.; Gazquez, J.; Ferain, E.; Rivadulla, F.; Rodriguez-Carvajal, J.; Mestres, N.; Carretero-Genevrier, A. Integration of Functional Complex Oxide Nanomaterials on Silicon. *Front. Phys.* **2015**, *3*. https://doi.org/10.3389/fphy.2015.00038.

(5) Yasaka, M. X-Ray Thin-FIlm Measurement Techniques. **2010**.

(6) Segmüller, A.; Noyan, I. C.; Speriosu, V. S. X-Ray Diffraction Studies of Thin Films and Multilayer Structures. *Progress in Crystal Growth and Characterization* **1989**, *18*, 21–66. https://doi.org/10.1016/0146-3535(89)90024-5.

(7) Harrington, G. F.; Santiso, J. Back-to-Basics Tutorial: X-Ray Diffraction of Thin Films. *J Electroceram* **2021**, *47* (4), 141–163. https://doi.org/10.1007/s10832-021-00263-6.

(8) Vignaud, G.; Gibaud, A. REFLEX: A Program for the Analysis of Specular X-Ray and Neutron Reflectivity Data. *J Appl Cryst* **2019**, *52* (1), 201–213. https://doi.org/10.1107/S1600576718018186.

(9) Chastain, J. *Handbook of X-Ray Photoelectron Spectroscopy*; Perkin-Elmer Corporation, 1992; Vol. 40.

(10) Vasconcelos Borges Pinho, P.; Chartier, A.; Moussy, J.-B.; Menut, D.; Miserque, F. Crystal Field Effects on the Photoemission Spectra in Cr2O3 Thin Films: From Multiplet Splitting Features to the Local Structure. *Materialia* **2020**, *12*, 100753. https://doi.org/10.1016/j.mtla.2020.100753.

(11) Grosvenor, A. P.; Biesinger, M. C.; Smart, R. St. C.; McIntyre, N. S. New Interpretations of XPS Spectra of Nickel Metal and Oxides. *Surface Science* **2006**, *600* (9), 1771–1779. https://doi.org/10.1016/j.susc.2006.01.041.

(12) Biesinger, M. C.; Brown, C.; Mycroft, J. R.; Davidson, R. D.; McIntyre, N. S. X-Ray Photoelectron Spectroscopy Studies of Chromium Compounds. *Surface and Interface Analysis* **2004**, *36* (12), 1550–1563.

https://doi.org/10.1002/sia.1983.

(13) Biesinger, M. C.; Payne, B. P.; Grosvenor, A. P.; Lau, L. W. M.; Gerson, A. R.; Smart, R. St. C. Resolving Surface Chemical States in XPS Analysis of First Row Transition Metals, Oxides and Hydroxides: Cr, Mn, Fe, Co and Ni. *Applied Surface Science* **2011**, *257* (7), 2717–2730. https://doi.org/10.1016/j.apsusc.2010.10.051.

(14) Hermsmeier, B.; Fadley, C. S.; Krause, M. O.; Jimenez-Mier, J.; Gerard, P.; Manson, S. T. Direct Evidence from Gas-Phase Atomic Spectra for an Unscreened Intra-Atomic Origin of Outer-Core Multiplet Splittings in Solid Manganese Compounds. *Phys. Rev. Lett.* **1988**, *61* (22), 2592–2595. https://doi.org/10.1103/PhysRevLett.61.2592.

(15) Scofield, J. H. Hartree-Slater Subshell Photoionization Cross-Sections at 1254 and 1487 eV. *Journal of Electron Spectroscopy and Related Phenomena* **1976**, *8* (2), 129–137. https://doi.org/10.1016/0368-2048(76)80015-1.

(16) Fairley, N.; Fernandez, V.; Richard-Plouet, M.; Guillot-Deudon, C.; Walton, J.; Smith, E.; Flahaut, D.; Greiner, M.; Biesinger, M.; Tougaard, S.; Morgan, D.; Baltrusaitis, J. Systematic and Collaborative Approach to Problem Solving Using X-Ray Photoelectron Spectroscopy. *Applied Surface Science Advances* **2021**, *5*, 100112. https://doi.org/10.1016/j.apsadv.2021.100112.

(17) Groot, F. de. *High-Resolution X-ray Emission and X-ray Absorption Spectroscopy*. ACS Publications. https://doi.org/10.1021/cr9900681.

(18) Neuville, D. R.; Ligny, D. de; Cormier, L.; Henderson, G. S.; Roux, J.; Flank, A.-M.; Lagarde, P. The Crystal and Melt Structure of Spinel and Alumina at High Temperature: An *in-Situ* XANES Study at the Al and Mg K-Edge. *Geochimica et Cosmochimica Acta* **2009**, *73* (11), 3410–3422. https://doi.org/10.1016/j.gca.2009.02.033.

(19) Figueroa, S. J. A.; Stewart, S. J. First XANES Evidence of a Disorder–Order Transition in a Spinel Ferrite Compound: Nanocrystalline ZnFe2O4. *J Synchrotron Rad* **2009**, *16* (1), 63–68. https://doi.org/10.1107/S0909049508032433.

(20) F. Marco, J.; Ramón Gancedo, J.; Gracia, M.; Luis Gautier, J.; I. Ríos, E.; M. Palmer, H.; Greaves, C.; J. Berry, F. Cation Distribution and Magnetic Structure of the Ferrimagnetic Spinel NiCo2O4. *Journal of Materials Chemistry* **2001**, *11* (12), 3087–3093. https://doi.org/10.1039/B103135J.

(21) Wei, C.; Feng, Z.; Baisariyev, M.; Yu, L.; Zeng, L.; Wu, T.; Zhao, H.; Huang, Y.; Bedzyk, M. J.; Sritharan, T.; Xu, Z. J. Valence Change Ability and Geometrical Occupation of Substitution Cations Determine the Pseudocapacitance of Spinel Ferrite XFe2O4 (X = Mn, Co, Ni, Fe). *Chem. Mater.* **2016**, *28* (12), 4129–4133. https://doi.org/10.1021/acs.chemmater.6b00713.

(22) Pinho, P. V. B. Experimental and Theoretical Study on Fe-Cr-O Thin Films: From Fine Structure to Macroscopic Behavior. phdthesis, Université Paris-Saclay, 2022. https://theses.hal.science/tel-03917144 (accessed 2024-04-

19).

(23) Pinho, P. V. B.; Chartier, A.; Menut, D.; Barbier, A.; Hunault, M. O. J. Y.; Ohresser, P.; Marcelot, C.; Warot-Fonrose, B.; Miserque, F.; Moussy, J.-B. Stoichiometry Driven Tuning of Physical Properties in Epitaxial Fe3-xCrxO4 Thin Films. *Applied Surface Science* **2023**, *615*, 156354. https://doi.org/10.1016/j.apsusc.2023.156354.

(24) Carra, P.; Thole, B. T.; Altarelli, M.; Wang, X. X-Ray Circular Dichroism and Local Magnetic Fields. *Phys. Rev. Lett.* **1993**, *70* (5), 694–697. https://doi.org/10.1103/PhysRevLett.70.694.

(25) Funk, T.; Deb, A.; George, S. J.; Wang, H.; Cramer, S. P. X-Ray Magnetic Circular Dichroism—a High Energy Probe of Magnetic Properties. *Coordination Chemistry Reviews* **2005**, *249* (1), 3–30. https://doi.org/10.1016/j.ccr.2004.05.017.

(26) O'Brien, C. J.; Rák, Z.; Brenner, D. W. Free Energies of (Co, Fe, Ni, Zn)Fe2O4 Spinels and Oxides in Water at High Temperatures and Pressure from Density Functional Theory: Results for Stoichiometric NiO and NiFe2O4 Surfaces. *J. Phys.: Condens. Matter* **2013**, *25* (44), 445008. https://doi.org/10.1088/0953-8984/25/44/445008.

(27) Pickering, I. J.; Sansone, M.; Marsch, J.; George, G. N. Diffraction Anomalous Fine Structure: A New Technique for Probing Local Atomic Environment.

(28) Haverkort, M. W.; Sangiovanni, G.; Hansmann, P.; Toschi, A.; Lu, Y.; Macke, S. Bands, Resonances, Edge Singularities and Excitons in Core Level Spectroscopy Investigated within the Dynamical Mean-Field Theory. *EPL* **2014**, *108* (5), 57004. https://doi.org/10.1209/0295-5075/108/57004.

(29) Haverkort, M. W.; Zwierzycki, M.; Andersen, O. K. Multiplet Ligand-Field Theory Using Wannier Orbitals. *Phys. Rev. B* **2012**, *85* (16), 165113. https://doi.org/10.1103/PhysRevB.85.165113.

(30) Lu, Y.; Höppner, M.; Gunnarsson, O.; Haverkort, M. W. Efficient Real-Frequency Solver for Dynamical Mean-Field Theory. *Phys. Rev. B* **2014**, *90* (8), 085102. https://doi.org/10.1103/PhysRevB.90.085102.

(31) Bunău, O.; Joly, Y. Self-Consistent Aspects of x-Ray Absorption Calculations. *J. Phys.: Condens. Matter* **2009**, *21* (34), 345501. https://doi.org/10.1088/0953-8984/21/34/345501.

(32) de Campos, M. F.; Landgraf, F. J. G.; Saito, N. H.; Romero, S. A.; Neiva, A. C.; Missell, F. P.; de Morais, E.; Gama, S.; Obrucheva, E. V.; Jalnin, B. V. Chemical Composition and Coercivity of SmCo5 Magnets. *Journal of Applied Physics* **1998**, *84* (1), 368–373. https://doi.org/10.1063/1.368075.

4 CRYSTALLINE GROWTH, STRUCTURE AND MAGNETIC PROPERTIES OF SPINEL THIN FILMS

The second part of this PhD. thesis is a comprehensive study on the structural and physical properties of high crystalline quality epitaxial $Fe_{\alpha}Ni_{\beta}Cr_{\gamma}O_4$ thin films. The experimental conditions used to grow $Fe_{\alpha}Ni_{\beta}Cr_{\gamma}O_4$ thin films are given. Thereafter, the film stoichiometry and crystalline structure are determined. The structural quality is probed by X-ray and electrons diffraction while the stoichiometry is obtained through X-ray photoemission spectroscopy. Finally, the magnetic properties of each spinel films are investigated by magnetometry.

4 CRYSTALLINE GROWTH, STRUCTURE AND MAGNETIC PROPERTIES OF SPINEL THIN FILMS

4.1 OA-MBE GROWTH OF SPINEL THIN FILMS

This first section will present the epitaxial growth of $Fe_\alpha Ni_\beta Cr_\gamma O_4$ thin films. The choice of different substrates is initially discussed. Then, the growth conditions and the fine control of the stoichiometry (*i.e.* Fe, Ni and Cr contents) are described.

4.1.1 Substrates choice and preparation

The spinel oxide thin films ($Fe_\alpha Ni_\beta Cr_\gamma O_4$) are grown on monocrystalline α-Al_2O_3 (0001) (c-plane) sapphire substrates due to the experience of our laboratory (SPEC/LNO) in the crystalline growth of spinel oxides on this substrate[1–3]. Sapphire α-Al_2O_3 crystallizes in a hexagonal structure (space group 166[4]) with lattice parameters: a = b = 4.76 Å and c = 12.99 Å[5].

For Cr-rich samples, the films exhibit a tendency to grow in the corundum phase[6], typical of sapphire (α-Al_2O_3). Consequently, for some stoichiometries (*e.g.* $NiCr_2O_4$), the decision has been made to elaborate the films on the well-known spinel $MgAl_2O_4$ substrate. Two orientations for this substrate have been selected: (111) and (001). $MgAl_2O_4$ crystallizes in a cubic structure (space group 227[4]) with lattice parameters: a = b = c = 8.08 Å[7].

Two distinct methods have been developed for the preparation of the substrates. For sapphire, a well-known cleaning process, as described in the litterature[1,2], is used, involving a 5 minutes mixing period in an aqueous solution prepared from 100 ml of distilled water, 1 ml of H_2O_2 and 1 ml of NH_4OH. H_2O_2 and NH_4OH serve to remove any organic pollutants due to transportation or manipulation. Then, the substrate is dried trough a N_2 gas flow to remove any residual liquid. The sapphire substrate is then introduced in the OA-MBE chamber and exposed to the oxygen plasma for 10 to 20 minutes at the growth temperature (around 450 °C).

In the case of the spinel-type $MgAl_2O_4$ substrate, another preparation method is used. Different cleaning procedures have been published, as in this reference[8]. Several modifications have been done in this work. Our cleaning procedure involves the use of the two organic solvents, with a 2-minute stirring in acetone, drying in an N_2 flow, and another 2-minute stirring in isopropanol and a final drying in an N_2 flow without annealing at high temperature. Prior to deposition, the substrate is exposed to oxygen plasma for 10 to 20 minutes to eliminate residual organic pollutants at the growth temperature (around 450 °C).

4.1.2 Exploratory strategies in a quaternary system

A rigorous investigation of the quaternary (Fe-Ni-Cr-O) spinel phase diagram is complex from an experimental point of view. Consequently, numerous $Fe_{\alpha}Ni_{\beta}Cr_{\gamma}O_4$ samples with different stoichiometries (various α, β, and γ) have been elaborated to explore the phase diagram (see Chapter 1). Several growth strategies have been adopted.

The initial challenge is to obtain a reference sample with optimal structural and chemical properties. Once this reference sample synthesized, one of the three temperatures of the effusion cells (Ni, Fe or Cr) has been modified. For example in order to obtain a sample with an increasing nickel content, the temperature of the nickel cell has been increased. This process has been reiterated until the RHEED signal is no longer indicative of a high quality sample with the expected spinel structure. The same process is done for the synthesis of chromium-enriched samples, with the temperature of the chromium cell as the controlling parameter. This strategy permits the exploration along a line of composition in the quaternary phase diagram.

In order to explore compositions near Fe_3O_4 with minimal Ni and/or Cr doping quantities, it has been decided to select a high iron flux and to reduce the chromium and nickel fluxes to a minimum.

4.1.3 Epitaxial growth of $Fe_{\alpha}Ni_{\beta}Cr_{\gamma}O_4$ spinel thin films

Once the chemical cleaning process finished, the substrate is fixed to a sample holder and is transferred into the OA-MBE chamber. The sample holder is heated by the heater to the adequate temperature (see Table 4.1). Then, the atomic oxygen plasma is created for a second cleaning process. The oxygen plasma is usually created with a RF power of 350 W and a PO_2 = 0.42 Torr regulated with a baratron. This plasma cleaning is accomplished at the growth temperature while the effusion cells are heating. The synthesis begins by the removal of the mechanical shutters of the desired cells. The sample is therefore synthesized under a coevaporation of two or three molecular beams, with the atomic oxygen plasma. The growth conditions are summarized in Table 4.1.

The initial five samples have been produced using distinct iron and nickel effusion cells from those employed for the remainder of this study. This is the reason why the temperature of the cells is a little bit different.

Another important point to mention here is the problem encountered with our oxygen plasma source (Addon). Due to problems with the oxidation efficiency two other plasma sources has been used during this PhD. thesis called “Oxford”

and "Soleil". According to the source selected, the RF power and the PO_2 can be changed. However, the majority of the samples have been synthesized with a RF power of 350 W and a Baratron tuned to 4.2 (*i.e.* PO_2 = 0.42 Torr).

Table 4.1: Summary of the growth conditions of samples selected in this thesis manuscript.

Sample	Substrate	Substrate T (°C)	Fe cell T (°C)	Ni cell T (°C)	Cr cell T (°C)	Source	PO_2 (Torr)
1	Al_2O_3 (0001)	548	1294	1345		Addon	0.40
2	Al_2O_3 (0001)	550	1239	1348		Addon	0.40
3	Al_2O_3 (0001)	548	1231	1347		Addon	0.40
4	Al_2O_3 (0001)	543	1284	1348		Addon	0.40
5	Al_2O_3 (0001)	547	1234	1340	1279	Addon	0.35
6	Al_2O_3 (0001)	736	1054	1263	1316	Addon	0.35
7	Al_2O_3 (0001)	738	1052	1262	1334	Addon	0.35
8	Al_2O_3 (0001)	728	917	1280	1315	Addon	0.42
9	Al_2O_3 (0001)	772	917	1281	1297	Addon	0.42
10	Al_2O_3 (0001)	731	917	1269	1297	Addon	0.42
11	Al_2O_3 (0001)	758	916	1248	1296	Addon	0.42
12	Al_2O_3 (0001)	738	918	1246	1272	Addon	0.42
13	Al_2O_3 (0001)	730	888	1270	1312	Addon	0.42
14	Al_2O_3 (0001)	733	917	1224	1295	Addon	0.42
15	Al_2O_3 (0001)	725	866	1256	1314	Addon	0.42
16	MAO (100)	688		1239	1328	Oxford	0.20
17	MAO (111)	666		1240	1340	Addon	0.50
18	Al_2O_3 (0001)	677	838	1220	1278	Soleil	0.42
19	Al_2O_3 (0001)	686	850	1227	1316	Soleil	0.42
20	Al_2O_3 (0001)	683	857	1265	1340	Soleil	0.42
21	Al_2O_3 (0001)	684	852	1265	1355	Soleil	0.42
22	Al_2O_3 (0001)	687	852	1265	1376	Soleil	0.42

4.2 MONITORING THE FILM GROWTH WITH RHEED MEASUREMENTS

The thin film growth is followed in real-time by RHEED diffraction. The evolution of the RHEED images provides insights into the crystallographic structure and growth mode. The following section presents a summary of information extracted from RHEED patterns.

The samples grown on sapphire (0001) and on $MgAl_2O_4$ (MAO), with two orientations: (001) and (111), induce distinct RHEED patterns. The RHEED images of the three substrates followed by the evolution of the RHEED images during the layer growth are shown below.

4.2.1 RHEED images of the substrates

Figure 4.1 illustrates the RHEED patterns observed for a MAO (001) substrate along two appropriate crystallographic orientations. A spinel layer grown on this substrate should have the same (001) crystallographic structure. Therefore, during the deposition of a spinel film, the patterns should be maintained with an elongation of the points into streaks or a multitude of points, according to the growth mode (see Chapter 3).

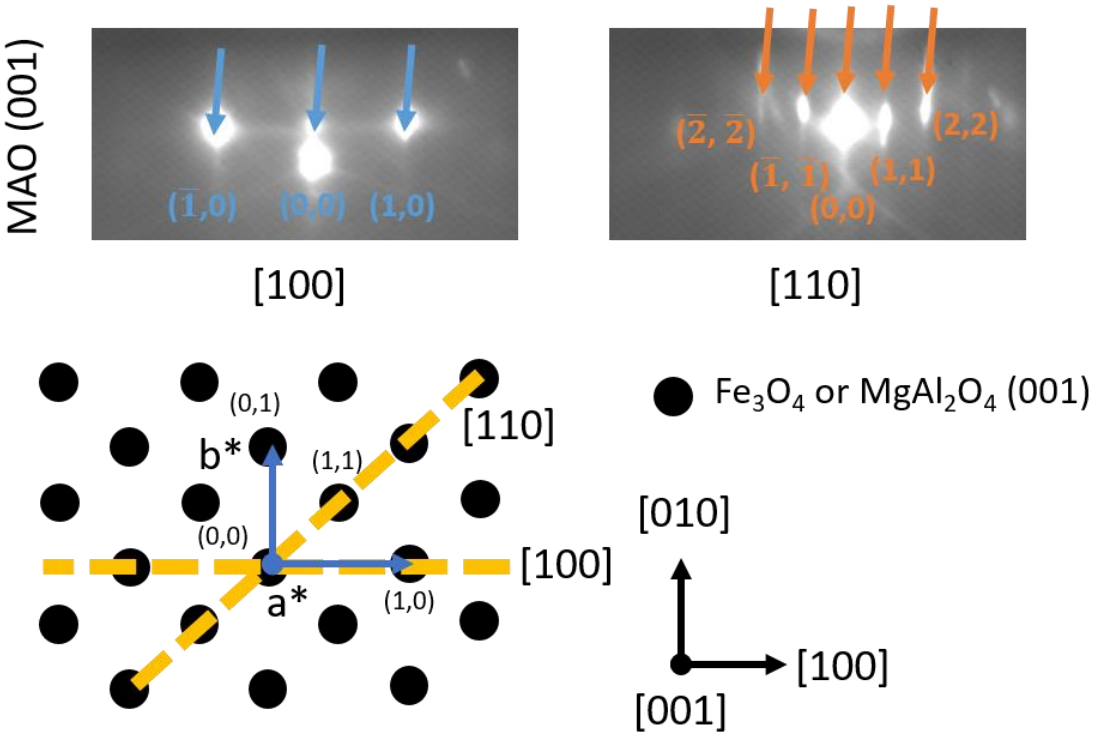

Figure 4.1: RHEED patterns of an $MgAl_2O_4$ (001) (or MAO) substrate. A schematic illustration of the reciprocal space with the two crystallographic directions of observation is shown.

Figure 4.2 illustrates the RHEED patterns of MAO(111) and α-Al_2O_3 (0001) substrates. A schematic illustration of the reciprocal space is provided. The FeO pattern is also provided because it represents the oxygen sublattice common to the three different iron oxides (FeO, Fe_3O_4 and α-Fe_2O_3). With regard to the [1$\bar{1}$0] direction (equivalent to [1$\bar{1}$00] for sapphire), the patterns observed for MAO (111) and α-Al_2O_3 (0001) are comparable. Similarly, the patterns observed in the [11$\bar{2}$] direction (equivalent to [11$\bar{2}$0] for sapphire) are also similar. From the illustration of the reciprocal space, it can be expected that the formation of a spinel layer on a MAO (111) substrate will result in comparable RHEED patterns, because no reorientation of the reciprocal space is observed. However, on α-Al_2O_3 (0001), the two directions will be inverted, due to a 30° reorientation of the reciprocal space passing from sapphire to spinel struture. In both cases, elongation of the points into streaks or multiple points, in accordance with the growth mode is expected.

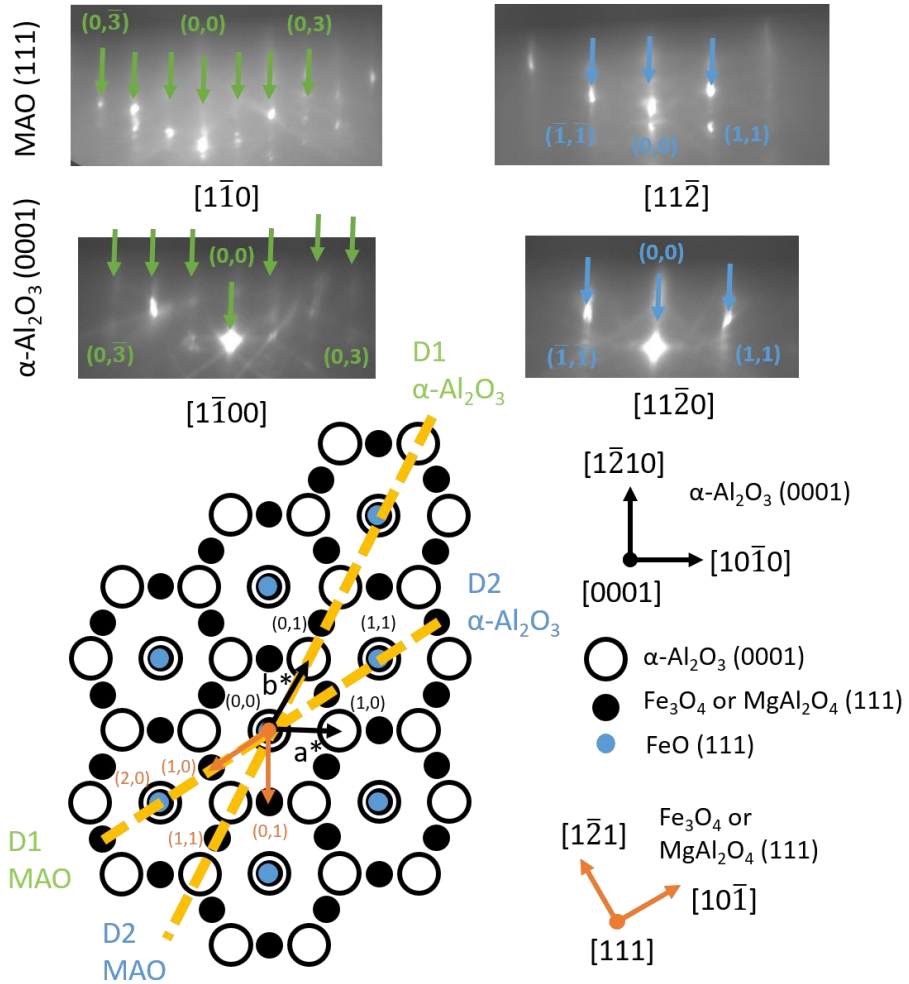

Figure 4.2: RHEED patterns of MAO (111) and α-Al_2O_3 (0001) substrates. The black and orange arrows refer, respectively, to α-Al_2O_3 and MAO orientation of the reciprocal space. The green and blue arrows refers to [1$\bar{1}$0] *and* [11$\bar{2}$] *directions, with a reorientation of the reciprocal space of 30° between the sapphire and the MAO structures.*

4.2.2 Evolution of the RHEED images during growth

This section will first describe the spinel growth on MAO and then on sapphire substrates.

The growth on MAO substrates is depicted in Figure 4.3. The RHEED patterns remain unchanged throughout the synthesis on both orientations ((001) and (111)). Consequently, the growing phase exhibits the crystallographic structure of a spinel. At the beginning of the deposition, some points with Kikuchi lines are discernible, which are characteristic of a monocrystalline surface. At the end of the synthesis, these points have evolved into streaks. In the case of MAO (001), the intensity along the streak is irregular and exhibits some points. It is characteristic of a 2D/3D growth mode. In contrast, on MAO (111), the streaks are regular, which is characteristic of a 2D growth mode.

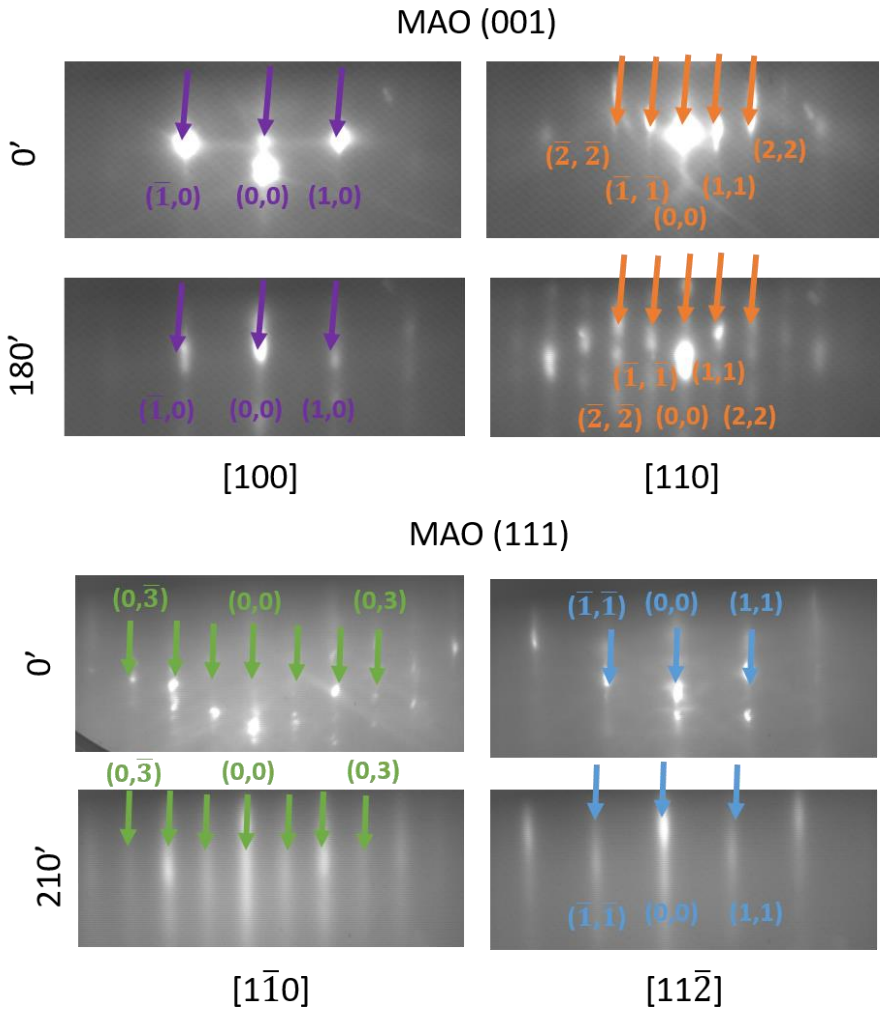

Figure 4.3: RHEED patterns recording during the growth of a spinel sample on MAO (001) (up) and MA0 (111) (down).

The evolution of the RHEED patterns of the growing spinel phase on sapphire substrates is more complex. The Figure 4.4 shows the typical evolution of RHEED patterns during the growth of a spinel oxide with a schematic illustration of the reciprocal space for sapphire and various iron oxides. Note that the blue circles (*i.e.* (0,3) and (1,1) streaks and equivalents) correspond to FeO (111) and to the oxygen sublattice common to all these oxides. The vectors of the reciprocal space (a* and b*) and some streaks coordinates are indicated in black for α-Al_2O_3 and in orange for the spinel phase.

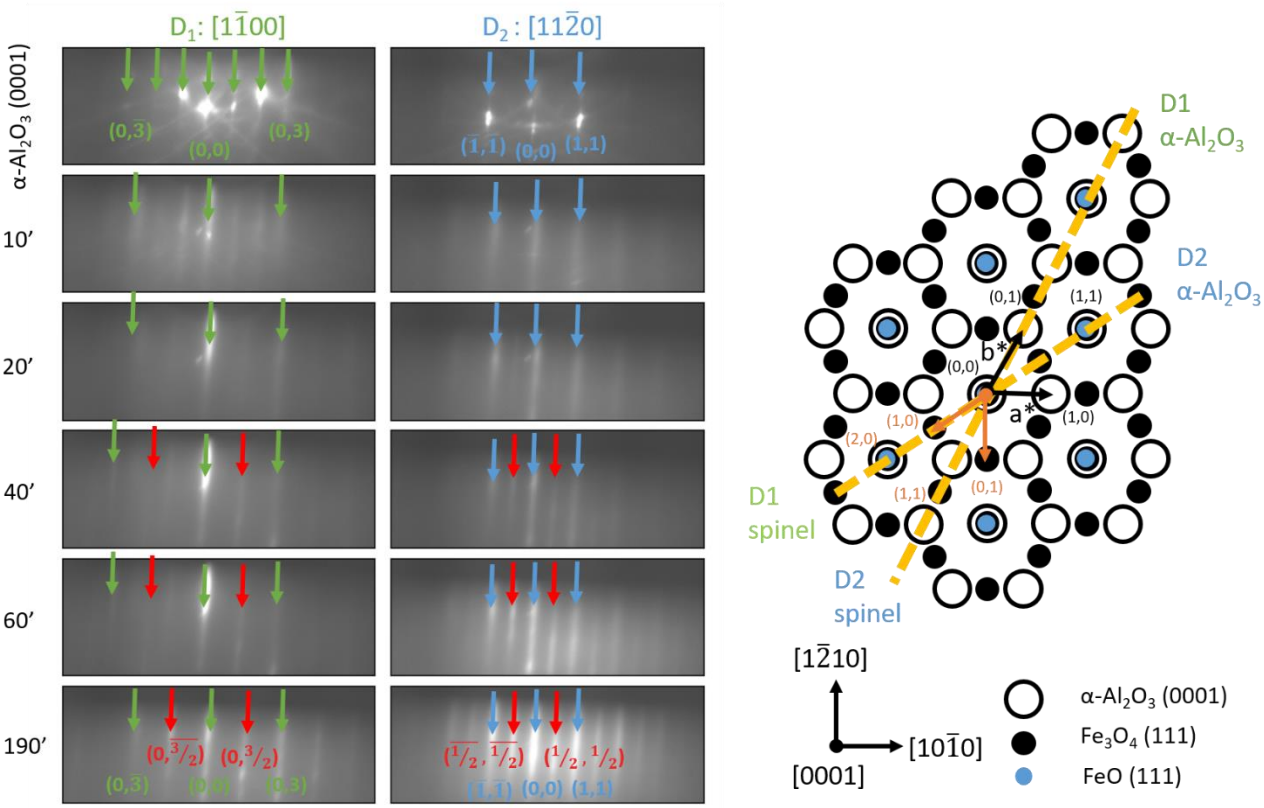

Figure 4.4: RHEED patterns recorded during the growth of the spinel sample 19 on α-Al_2O_3 (0001).

The first images are typical for a monocrystalline sapphire substrate with Kikuchi lines. In the [1$\bar{1}$00] (D1) direction, a central point (0,0) is observed, along with three satellite points on the left and right sides ((0,1),(0,2) and (0,3) for right side). The other direction [11$\bar{2}$0] (D2) exhibits a single point on the left and on the right sides (($\bar{1}$,$\bar{1}$) and (1,1)) of the central point (0,0). During the growth, on the D1 direction, the rods with indices (0,1) and (0,2) disappear, whereas the (0,3) rod persists at 10 and 20 minutes of growth duration. The structure evolves from a [1$\bar{1}$00] direction (sapphire substrate) to a [1$\bar{2}$1] direction of the spinel structure. At 20 minutes the two sapphire streaks have completely disappear and a new streak (0,$^3/_2$), characteristic of the spinel [1$\bar{2}$1] appears (red arrows). After 40

minutes, the new streak is fully visible, situated between the two previous ones. On the D2 direction, an alternative mechanism is observed. No streaks disappear, and a new streak (½,½) appears between the sapphire streaks ((0,0) and (1,1)). At 30 minutes (not shown here), the streak is fully visible. This streak is characteristic of the [$1\bar{1}0$] direction of the spinel phase. At 40 minutes, the characteristic streaks of the spinel phase. (black circles on the schematic illustration and red arrows on the left of Figure 4.4) are fully discernible in both directions. The points of the beginning become fine and homogenous along the two directions, starting at 10 minutes of growth. This indicates a 2D growth mode of the film.

The other samples, also grown on sapphire substrates, exhibit a similar RHEED pattern evolution along the two directions, with the appearance of the spinel streaks within the first hour of growth. Therefore, the patterns are characteristic of a 2D growth mode, for the majority of samples. It can be established that the spinel phase grows on the sapphire substrate with a reorientation of the crystallographic structure of 30°. This reorientation is necessary to adapt to the crystallographic structure of the substrate.

Note, that for some compositions, samples can exhibit slight modulations along the streaks, indicating the beginning of 3D growth mode. This is mainly the case for samples enriched in chromium as previously described elsewhere[6].

4.2.3 In-plane lattice parameter determination

The last information which can be extracted from the RHEED images is the distance between streaks, which is proportional to d*, the distance in the reciprocal space. The evolution of the in-plane lattice parameter can be monitored with the KSA RHEED software in real-time.

The intensity profile is obtained by taking a rectangular region within the sapphire RHEED image. The coordinates of the sapphire points are recorded and the distance is measured in pixel. The scale of the RHEED image can be calculated by dividing d* (of the sapphire) by the measured pixel distance. In the case of the [$1\bar{1}00$] direction (D1) in the Figure 4.4, 160 pixels are measured between the central point and the third point. This pixel distance corresponds to d_{330} = 0.79 Å. With a conversion in terms of d*, the value is d^*_{330} = 7.95 $Å^{-1}$. Accordingly, the scale of the RHEED image is 0.05 $Å^{-1}.pxl^{-1}$. The scale is used to quantify the reciprocal distance between spinel streaks. The value is then converted back in terms of real space distance by taking the inverse of the measured d*.

In the literature, the most common method of presentation is to present $d_{phase}/d_{sapphire}$. For illustrative purposes, one example is shown in Figure 4.5 for the

RHEED images of the Figure 4.4. From the sapphire distance, a first increase up to 1.09 is observed for the initial hour of deposition in the case of the d1 direction, and only for 30 minutes for the D2 direction. The D2 direction exhibits a faster decrease than the D1 direction. After two hours, the two directions have a ratio of approximately 1.07, which is similar to the observed ratio for the magnetite film (approximately 1.08)[2]. This lattice mismatch of 6% to 8 % between the two lattices is important and will influence the crystallographic properties. In the field of epitaxial growth[1], the lattice mismatch is usually less than 1 %.

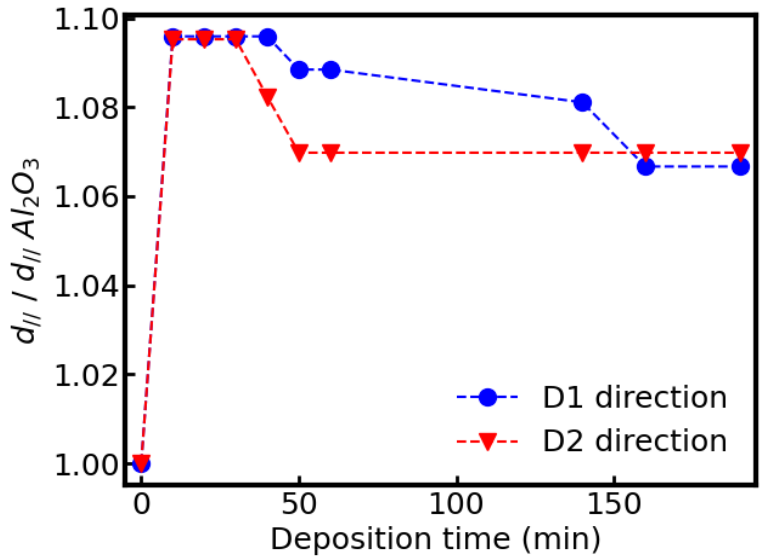

Figure 4.5 Evolution of the in-plane interreticular distance in the two RHEED directions.

The measured distance can be converted into an in-plane lattice parameter through usual formulae (see chapter 3 for hexagonal convention). The lattice parameter of sapphire is 4.76 Å, and increases to 5.86 Å and 5.88 Å for the D1 and D2 directions of the spinel phase, respectively.

In conclusion, the RHEED diffraction patterns indicate that the growth mode is 2D for the different spinel oxide layers. Nevertheless, the presence of chromium in the samples reduces the quality of the RHEED images, which is one of the reasons why an $MgAl_2O_4$ substrate has been selected for high chromium contents.

4.3 CHEMICAL COMPOSITION DETERMINATION

After the thin films growth, the stoichiometry of the samples are determined using XPS spectroscopy. The following section will address the challenges associated to the quantification of $Fe_\alpha Ni_\beta Cr_\gamma O_4$ thin films. The evolution of the XPS spectra in relationships to the α, β, and γ stoichiometry is then detailed.

4.3.1 Quantification challenges for $Fe_\alpha Ni_\beta Cr_\gamma O_4$ thin films

XPS analysis has been performed using two distinct types of setups (see chapter 3). In the XPS located in the SPEC laboratory, an non monochromatic Mg Kα X-ray source is used, whereas in the S2CM laboratory, a monochromatic Al Kα X-ray source is selected. These two X-ray sources present some advantages and disadvantages for the access to the composition.

In the case of the Mg Kα X-ray source, the O KLL Auger peak is situated close to the Fe *2p* core level peaks. Therefore, the background is significantly disrupted by the presence of this peak, changing the area of the signal in the Fe 2p region. The iron stoichiometry is thus overestimated. This analysis is therefore discarded.

In the case of Al Kα X-ray source, Figure 4.6 displays a detailed illustration of the Fe 2p region. It can be observed that the Ni LMM Auger peak occurs between 690 and 750 eV, which coincides with the region of the Fe *2p* core levels. The presence of this peak in the region of Fe 2p will result in an overestimation of the iron composition.

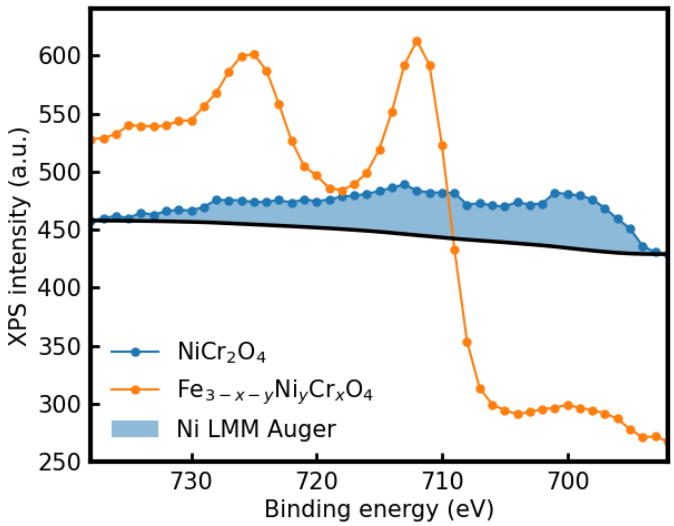

Figure 4.6: Fe 2p core levels spectra obtained with a Al Kα X-ray source. The blue curve represents a spectrum without iron ($NiCr_2O_4$), while the orange curve depicts a sample with iron.

This overestimation is corrected by subtracting an estimated Auger Ni LMM area. The estimation of this Auger Ni LMM peak is obtained using an area ratio between the Ni 2p and Ni LMM contributions using $NiCr_2O_4$ and NiO samples. The area ratio is supposed constant for all compounds. The *3p* core levels can be also probed as shown on the Figure 4.7. The *3p* regions of each cation are close to each other and no Auger line interference is present in this region. However, the *3p* transition is of low intensity and the acquisition time may be significant, especially for elements at low content. A comparison between the aforementioned Ni auger area subtraction methodology (relative quantification = 48 at. % Fe, 15 at. % Ni and 37 at. % Cr) and a quantification performed on the 3p core levels region (relative quantification= 47 at. % Fe, 16 at. % Ni and 37 at. % Cr) yielded highly similar quantitative results. Thus, the *2p* core levels have been used for the quantification in this work.

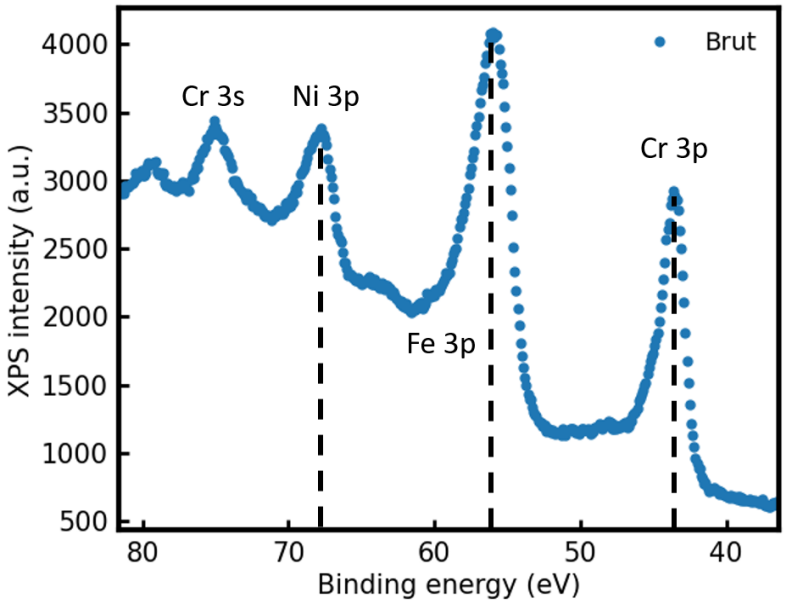

Figure 4.7: XPS 3p core levels spectrum on a spinel oxide layer recorded with a X-ray Al Kα source.

4.3.2 Chemical composition deduced from XPS

The chemical composition obtained is summarized in Table 4.2. The different layers have a composition with $0 < \gamma < 2.12$ and $0.15 < \beta < 1$.

Table 4.2: Composition of studied $Fe_\alpha Ni_\beta Cr_\gamma O_4$ samples.

Sample	Metal relative quantification			Corresponding stoichiometry
	Fe (at.%)	Ni (at.%)	Cr (at.%)	
1	74	26	0	$Fe_{2.22}Ni_{0.78}O_4$
2	94	6	0	$Fe_{2.82}Ni_{0.18}O_4$
3	88	12	0	$Fe_{2.64}Ni_{0.36}O_4$
4	95	5	0	$Fe_{2.85}Ni_{0.15}O_4$
5	81	7	12	$Fe_{2.43}Ni_{0.21}Cr_{0.36}O_4$
6	57	19	24	$Fe_{1.71}Ni_{0.57}Cr_{0.72}O_4$
7	48	15	37	$Fe_{1.44}Ni_{0.45}Cr_{1.11}O_4$
8	50	30	20	$Fe_{1.50}Ni_{0.90}Cr_{0.60}O_4$
9	51	34	15	$Fe_{1.53}Ni_{1.02}Cr_{0.45}O_4$
10	60	23	17	$Fe_{1.80}Ni_{0.69}Cr_{0.51}O_4$
11	69	13	18	$Fe_{2.07}Ni_{0.39}Cr_{0.54}O_4$
12	74	14	12	$Fe_{2.22}Ni_{0.42}Cr_{0.36}O_4$
13	42	32	26	$Fe_{1.26}Ni_{0.96}Cr_{0.78}O_4$
14	75	7	18	$Fe_{2.25}Ni_{0.21}Cr_{0.54}O_4$
15	32	31	37	$Fe_{0.96}Ni_{0.93}Cr_{1.11}O_4$
16	0	29.2	70.8	$Ni_{0.88}Cr_{2.12}O_4$
17	0	33.2	66.8	$NiCr_2O_4$
18	77	5	18	$Fe_{2.31}Ni_{0.15}Cr_{0.54}O_4$
19	62	5	33	$Fe_{1.86}Ni_{0.15}Cr_{0.99}O_4$
20	54	11	35	$Fe_{1.62}Ni_{0.33}Cr_{1.05}O_4$
21	48	9	43	$Fe_{1.44}Ni_{0.27}Cr_{1.29}O_4$
22	40	8	52	$Fe_{1.20}Ni_{0.24}Cr_{1.56}O_4$

Note that the samples with a high content of chromium (*i.e.* $Ni_{0.88}Cr_{2.12}O_4$ and $NiCr_2O_4$) have been elaborated on MAO (001) and MAO (111) respectively.

Figure 4.8 summarizes the composition of the different samples in a quaternary phase diagram. The right side and the center of the phase diagram are well explored, with a significant number of samples. Nevertheless, the top right corner and the center left should require further investigations in order to enhance the precision of our analyses. It is clear that the region close to $NiCr_2O_4$ remains unexplored. As explained before, this is due to the difficulty to elaborate crystalline oxide layers in this stoichiometry range.

A limitation of this work is the absence of cross-validation with alternative experimental techniques for the XPS composition. Nevertheless, from the previous work accomplished on the $Fe_{3-\gamma}Cr_{\gamma}O_4$ series[9] (in red in the Figure 4.8), electron energy-loss spectroscopy (EELS) and energy dispersive X-ray (EDX) have yielded similar results to the XPS quantification.

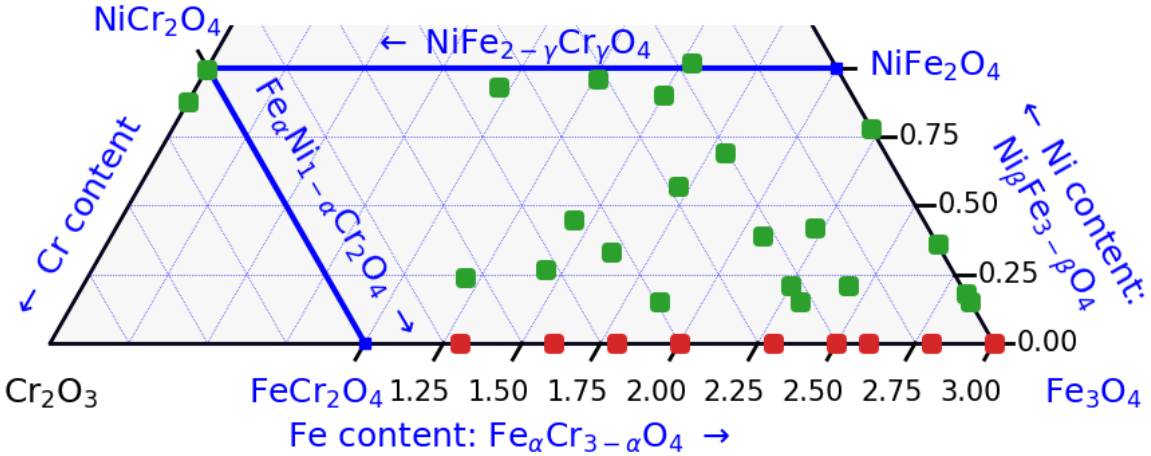

Figure 4.8: Chemical composition of thin films obtained by XPS measurements represented in a quaternary phase diagram. The red squares represent the $Fe_{3-\gamma}Cr_{\gamma}O_4$ samples synthesized in a previous PhD. work[9].

4.3.3 Evolution in the XPS spectra according to the stoichiometry

Figure 4.9 displays the evolution of the normalized XPS Fe *2p* core levels spectra according to the stoichiometries of $Ni_{\beta}Fe_{3-\beta}O_4$.

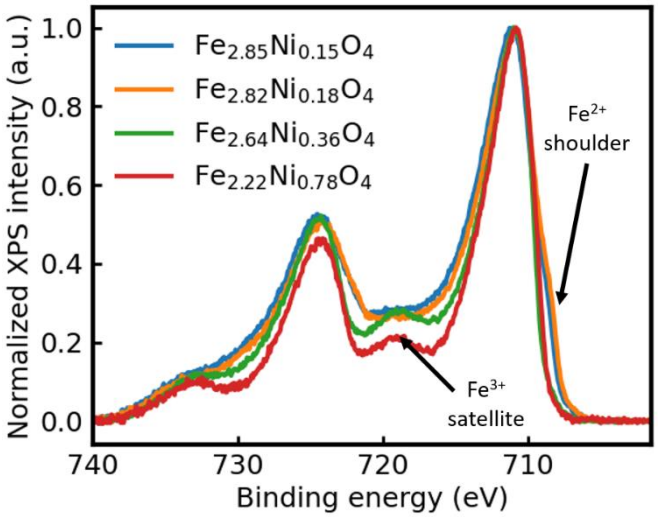

Figure 4.9: Normalized and Shirley background subtracted XPS Fe 2p core levels spectra for $Ni_{\beta}Fe_{3-\beta}O_4$ thin film series.

On the Fe *2p*$_{3/2}$ peak, a slight Fe^{2+} shoulder is observed at 708.3 eV in samples with low nickel content (blue and orange curves). These samples exhibited nickel stoichiometries below 0.18. Samples exhibiting more nickel do not have this shoulder. However, one satellite *2p*$_{3/2}$ peak appears at 719 eV. This peak are related to iron at oxidation state +3. These observations indicates that the nickel cations replace the Fe^{2+} cations leading to the presence of only iron in oxidation state 3+.

The effect of the chromium doping on the Fe *2p* core levels spectra is presented in Figure 4.10. At a fixed nickel concentration (left), the chromium introduction results in a decrease of the Fe^{3+} satellite peak, and to the apparition of the Fe^{2+} shoulder in the Fe *2p*$_{3/2}$ peak. The Fe^{2+} proportion had increased. At fixed chromium concentration (right), the nickel introduction has the opposite effect, as already observed for $Ni_\beta Fe_{3-\beta}O_4$ series. The Fe^{2+} shoulder disappears, and the Fe^{3+} satellite peak appears. The Fe^{3+} proportion had increased. From these Fe *2p* core levels spectra, it can be hypothesized that Cr^{3+} and Ni^{2+} are the main cations.

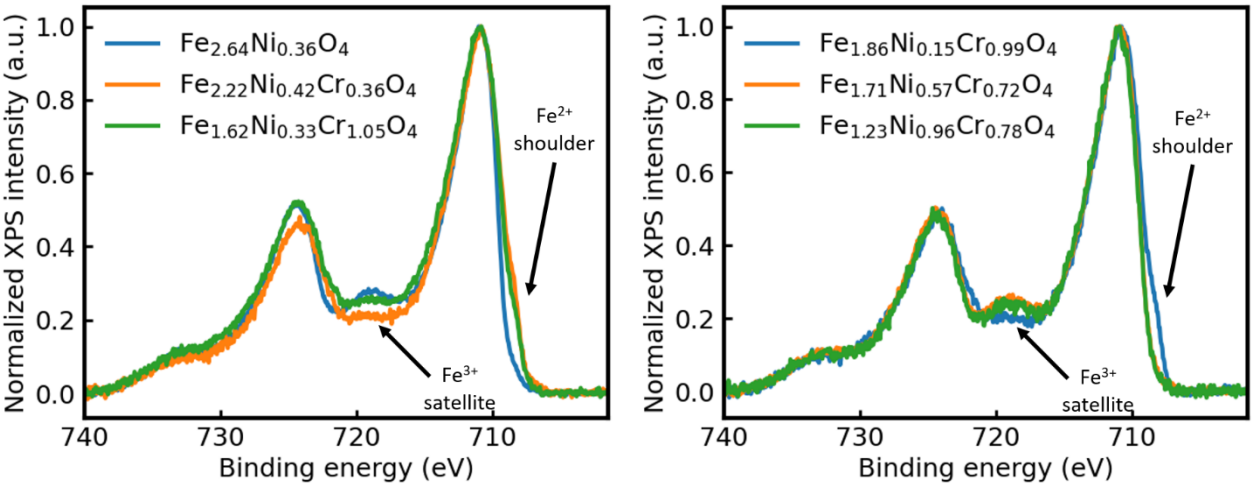

Figure 4.10: Normalized and Shirley background subtracted XPS Fe 2p core levels spectra for $Fe_{2.60-\gamma}Ni_{0.40}Cr_\gamma O_4$ (left) and $Fe_{2.20-\beta}Ni_\beta Cr_{0.80}O_4$ (right) series.

Figure 4.11 illustrates the Ni *2p* core levels spectra for the $Ni_\beta Fe_{3-\beta}O_4$ series and some samples with β = 1. The $Ni_\beta Fe_{3-\beta}O_4$ series (left side) exhibit few variations. The nickel species remains at the same oxidation levels, and in the same crystallographic site. According to the literature for bulk compounds[10], the nickel is Ni^{2+} and in O_h sites. In particular, the *2p*$_{3/2}$ peak is located at 855 eV. With the introduction of chromium in the structure (at β = 1, right side), the 2p$_{3/2}$ peak position shifts to the left of the spectra with the decrease of iron stoichiometry. The samples exhibiting the $NiCr_2O_4$ stoichiometry (Ni^{2+} in T_d sites for bulk samples) display a distinctive shape compared to the previous ones. The *2p*$_{3/2}$

peak is now located at 856.2 eV and 856 eV for red and purple curves, respectively, and a pronounced shoulder is now discernible at 854.2 eV. For samples enriched in nickel and chromium (orange and green curves), the spectral shape appears as a mixture between the two previously described extremes, with a progressive shift in peak position, from 855 eV towards 856 eV.

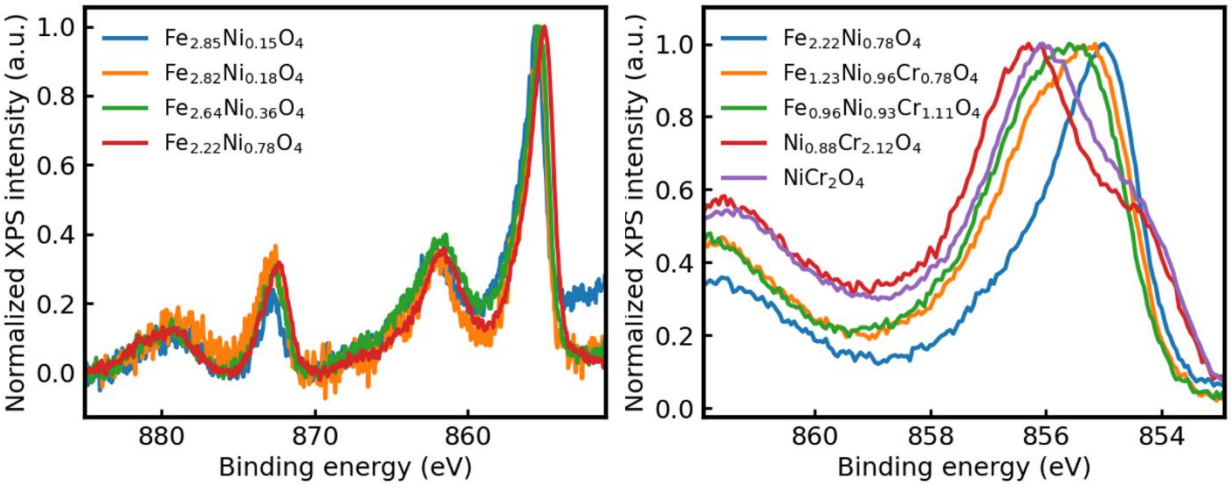

Figure 4.11: Normalized and Shirley subtracted background XPS Ni 2p core levels spectra for $Ni_{\beta}Fe_{3-\beta}O_4$ series (left) and zoom on the $2p_{3/2}$ peak for samples for $Fe_{2-\gamma}Ni_1Cr_{\gamma}O_4$ series (right).

In the literature[11], the calculated XPS Ni^{2+} *2p* spectra at a T_d site shows a displacement of the $2p_{3/2}$ peak position (856 eV) compared to a O_h site (855 eV). The spectra of the $Ni_{\beta}Fe_{3-\beta}O_4$ series are in agreement with that of $NiFe_2O_4$[12], whereas some features are distinct compared to NiO[13]. Reference spectra for $NiCr_2O_4$[14] do not exhibit a shoulder at 855 eV. Two hypotheses can be formulated to take into account this shape evolution. The first is an increased presence of Ni^{2+} in T_d sites, while the second suggests an increasing deformation of the crystallographic site. A combination of these two hypotheses could be also a possible explanation. The first hypothesis can be addressed through fine structure investigations (XMCD or RXD), while the second can be addressed through XRD.

The Cr *2p* core levels spectra are depicted in Figure 4.12. For samples grown on sapphire, we can observe multiplet peaks on the $2p_{3/2}$ Cr core level as already observed. It has been shown that the relative amplitude of these peaks is mainly related to the strain in the layer in Cr_2O_3[9]. In opposition, the $NiCr_2O_4$ and $Ni_{0.88}Cr_{2.12}O_4$ samples (red and purple curves) exhibit a slightly different peak shape. It can be attributed to the nature of the substrate, and the presence of a different strain in the layer. The $2p_{3/2}$ peak positions among the samples remain at the same binding energy (576.5 eV). This indicate that the chromium remains at the oxidation state (Cr^{3+}).

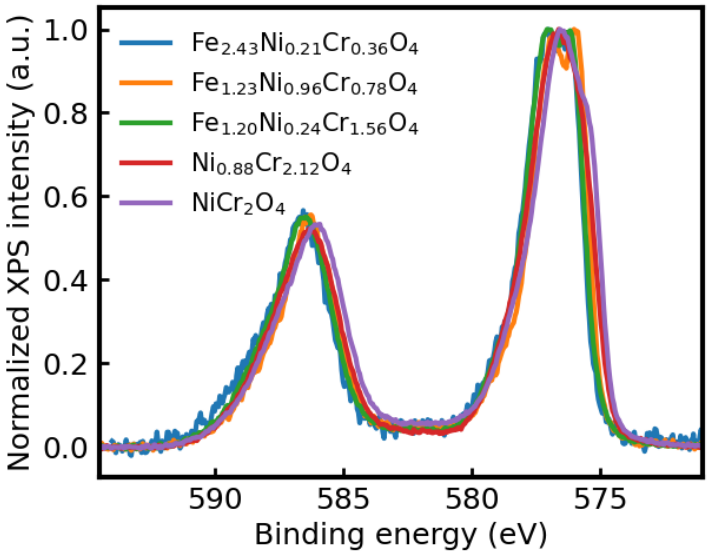

Figure 4.12: Normalized and Shirley subtracted XPS Cr 2p core levels spectra.

In conclusion, XPS measurements of the *2p* core levels (for Fe, Ni and Cr) have been systematically performed on the different layers. The quantification of the different peaks presents several challenges according to the choice of the X-ray source (Mg Kα or Al Kα) or in the background subtraction (overlapping of Auger/XPS peaks). Nevertheless, the chemical composition of the samples can be extracted from these measurements. Some evolutions have been discerned:

- The Fe *2p* core levels XPS spectra exhibit few variations with the stoichiometry. A slight shoulder at 708.3 eV can be attributed to Fe^{2+} in the samples containing a low amount of nickel without any chromium. This shoulder is also observed when chromium is introduced (at fixed nickel concentration) and when nickel content decreases (at a fixed chromium concentration). The Fe^{3+} satellite peak exhibits the opposite variation.
- Similarly, the XPS Cr *2p* core levels spectra show minimal variations, thus indicating that the chromium remains in the same oxidation state.
- Conversely, the XPS Ni *2p* core levels spectra exhibit larger variations. The $2p_{3/2}$ peak shifts to a higher energy. It can be due to a progressive displacement of Ni atoms from O_h site into T_d site, or a deformation of the O_h site. The shoulder at 855 eV of the $NiCr_2O_4$ spectra may be explained by this second hypothesis. The CFM calculation of the Ni *2p* core levels spectrum can be helpful in the understanding and quantitative analysis of this spectrum.

4.4 STRUCTURAL INVESTIGATIONS OF SPINEL THIN FILMS

The chemical composition of the layers being determined, it is now crucial to probe the crystalline structure of thin films as a function of the Ni, Fe and Cr content The following section will describe XRR analyses (film thickness, roughness, density) and XRD measurements (in-plane and out-of-plane lattice parameters, crystallographic structure, rocking curve, etc…).

4.4.1 Sample thickness investigations with XRR

The thickness of the layers has been systematically measured by X-ray Reflectivity (XRR). Several XRR curves associated to typical compositions are shown in Figure 4.13 and a summary of the results is provided in Table 4.3. By fitting the XRR oscillations, the film thickness (t, in nm), density (ρ in g.cm^{-3}) and root-mean-square roughness (σ_{RMS}, in nm) of the samples can be extracted. The fitted parameters are indicated in the inset of the graphs and in Table 4.3. The film thickness can vary between the samples (5 nm< t < 25 nm) due to the variation of the deposition time but also of the metallic fluxes for defining the different compositions.

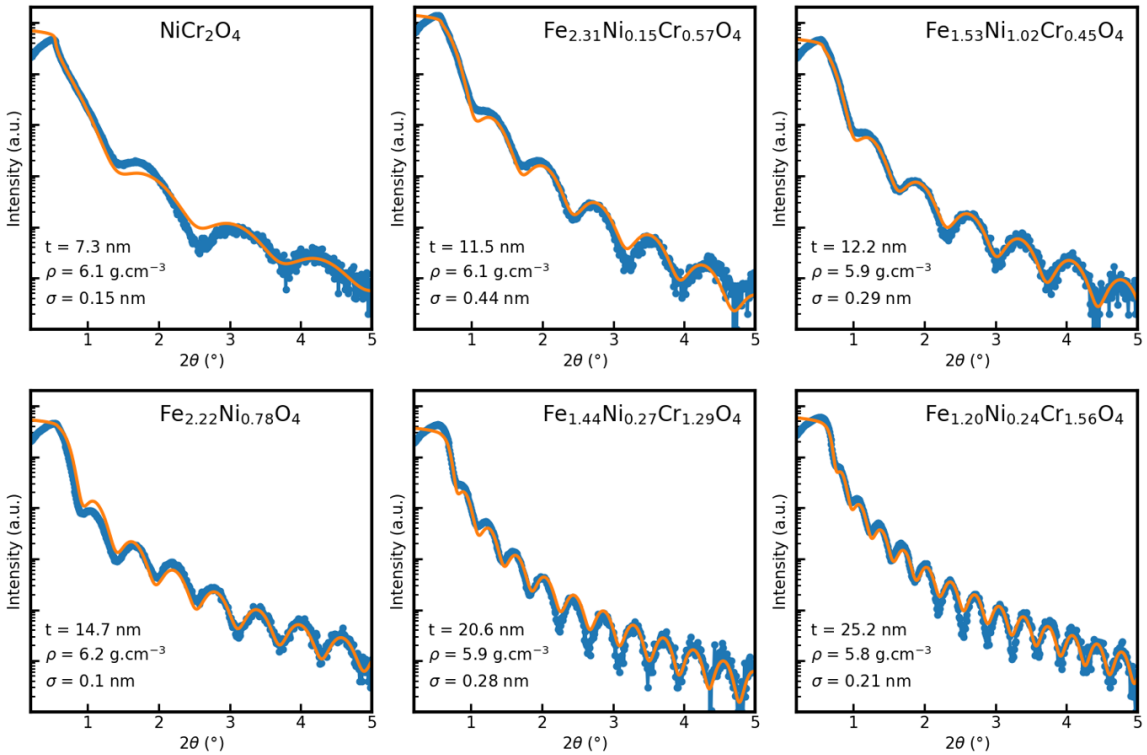

Figure 4.13: X-ray reflectivity curves for different samples. The experimental curves are represented by the blue lines, while the fitted curves are depicted by the orange curves.

*Table 4.3: Structural information extracted from XRR. * and ** indicate MAO (001) and MAO (111) substrate. For *, the Scherrer thickness (S) is indicated.*

Sample	Stoichiometry	t (nm)	ρ (g.cm^{-3})	σ_{RMS} (nm)
1	$Fe_{2.22}Ni_{0.78}O_4$	14.7	6.2	0.1
2	$Fe_{2.82}Ni_{0.18}O_4$	12.1	6.0	0.34
3	$Fe_{2.64}Ni_{0.36}O_4$	8.7	6.9	0.78
4	$Fe_{2.85}Ni_{0.15}O_4$	15.8	5.8	0.27
5	$Fe_{2.43}Ni_{0.21}Cr_{0.36}O_4$	13.7	6.0	0.24
6	$Fe_{1.71}Ni_{0.57}Cr_{0.72}O_4$	11.3	6.2	0.32
7	$Fe_{1.44}Ni_{0.45}Cr_{1.11}O_4$	12.3	5.9	0.32
8	$Fe_{1.50}Ni_{0.90}Cr_{0.60}O_4$	14.3	6.0	0.40
9	$Fe_{1.53}Ni_{1.02}Cr_{0.45}O_4$	12.2	5.9	0.29
10	$Fe_{1.80}Ni_{0.69}Cr_{0.51}O_4$	10.9	6.5	0.28
11	$Fe_{2.07}Ni_{0.39}Cr_{0.54}O_4$	10.0	6.1	0.21
12	$Fe_{2.22}Ni_{0.42}Cr_{0.36}O_4$	9.7	6.1	0.18
13	$Fe_{1.23}Ni_{0.96}Cr_{0.78}O_4$	8.1	6.3	0.17
14	$Fe_{2.25}Ni_{0.21}Cr_{0.54}O_4$	9.3	6.3	0.22
15	$Fe_{0.96}Ni_{0.93}Cr_{1.11}O_4$	7.2	6.2	0.39
16*	$Ni_{0.88}Cr_{2.12}O_4$	4.8 (S)		
17**	$NiCr_2O_4$	7.3	6.1	0.15
18	$Fe_{2.31}Ni_{0.15}Cr_{0.57}O_4$	11.5	6.1	0.44
19	$Fe_{1.86}Ni_{0.15}Cr_{0.99}O_4$	15.7	5.2	0.19
20	$Fe_{1.62}Ni_{0.33}Cr_{1.05}O_4$	17.9	5.8	0.34
21	$Fe_{1.44}Ni_{0.30}Cr_{1.29}O_4$	20.6	5.9	0.28
22	$Fe_{1.20}Ni_{0.24}Cr_{1.56}O_4$	25.2	5.8	0.21

The σ_{RMS} roughnesses are weak whatever the samples composition and the film thickness, varying mainly from σ= 0.1 to 0.45 nm. The low roughnesses observed in the samples is indicative of 2D materials, which is the initial objective.

4.4.2 Lattice parameters and crystalline quality analysis via XRD

This section will present the lattice parameters obtained by XRD diffraction as function of composition. At first, we will present the out-of-plane measurements (and the access to the c parameter), followed by rocking curve (RC) measurements on specific peaks (222). We will use of the Scherrer formula to access to the crystalline quality. Subsequently, in-plane measurements will be done for the determination of the in plane lattice parameters. Finally, in addition to the previous RHEED analyses, the epitaxial relationships between the substrate and the spinel obtained from these in-plane measurements will be detailed.

4.4.2.1 Out-of-plane lattice parameter determination

A typical example of an out-of-plane XRD measurement of one spinel oxide thin film is shown in Figure 4.14. The sample has been grown on an α-Al_2O_3 (0001) substrate. The (0006) peak position of the substrate is at 2θ = 41.69°, which corresponds to an out-of-plane lattice parameter of c= 12.999 Å. In the overall spectrum, only (h h h) peaks are present for the spinel phase. The (222) peak, even if its intensity is rather low in spinel phases, is the most intense peak which is selected for complementary analyses. A Gaussian function (orange curve) is used to fit the peak and to define precisely its position and full width at half maximum (FWHM). By determining these two parameters, the lattice parameter (Bragg law) and the crystalline thickness (Scherrer law) can be determined. Similarly, the RC measurement on the (222) peak is fitted with a Gaussian function (see inset of Figure 3.26). The FWHM can be related the crystalline disorientation of the grains along the c axis and therefore provides information on the crystalline quality of the film.

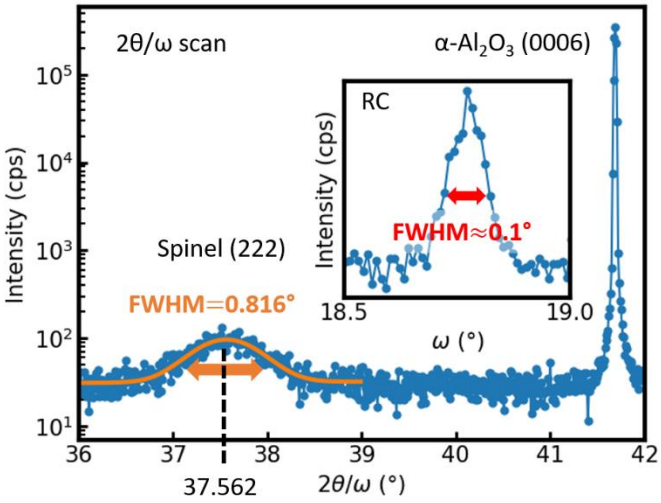

Figure 4.14: X-ray diffraction in out-of-plane configuration for the sample $Fe_{1.44}Ni_{0.45}Cr_{1.11}O_4$. The blue curve represents the XRD data. In inset: the rocking curve for the (222) peak.

The out-of-plane measurements are summarized in Table 4.4. Two notations are used for the lattice parameter according to the hexagonal or cubic convention. As the spinel phase grows in the [111] direction, the sapphire substrate induces some deformations on the growing layer, which is better described by a hexagonal lattice. For comparison with the literature, the cubic convention will be also used (*cf.* section 3.2.4). . All lattice parameters in the cubic convention are within the range of a spinel phase comprising II-III ions[15].

*Table 4.4: Summary of the structural information obtained with XRD measurements. * and ** indicate MAO (001) and MAO (111) substrates.*

Sample Stoichiometry	$c_{hexagonal}$ (Å)	c_{cubic} (Å)	Scherrer thickness (nm)	FWHM RC (°)
$Fe_{2.22}Ni_{0.78}O_4$	14.455	8.346	15.9	0.098
$Fe_{2.82}Ni_{0.18}O_4$	14.559	8.406	12.3	0.093
$Fe_{2.64}Ni_{0.36}O_4$	14.545	8.398	7.3	0.097
$Fe_{2.85}Ni_{0.15}O_4$	14.498	8.370	16.2	0.096
$Fe_{2.43}Ni_{0.21}Cr_{0.36}O_4$	14.475	8.357	14.3	0.095
$Fe_{1.71}Ni_{0.57}Cr_{0.72}O_4$	14.372	8.298	11.2	0.101
$Fe_{1.44}Ni_{0.45}Cr_{1.11}O_4$	14.365	8.294	10.2	0.095
$Fe_{1.50}Ni_{0.90}Cr_{0.60}O_4$	14.421	8.326	14.7	0.097
$Fe_{1.53}Ni_{1.02}Cr_{0.45}O_4$	14.419	8.325	12.8	0.099
$Fe_{1.80}Ni_{0.69}Cr_{0.51}O_4$	14.436	8.335	11.8	0.093
$Fe_{2.07}Ni_{0.39}Cr_{0.54}O_4$	14.486	8.364	10.6	0.099
$Fe_{2.22}Ni_{0.42}Cr_{0.36}O_4$	14.453	8.344	10.1	0.097
$Fe_{1.23}Ni_{0.96}Cr_{0.78}O_4$	14.389	8.307	7.0	0.098
$Fe_{2.25}Ni_{0.21}Cr_{0.54}O_4$	14.496	8.369	9.7	0.094
$Fe_{0.96}Ni_{0.93}Cr_{1.11}O_4$	14.377	8.300	7.2	0.094
$Fe_{2.31}Ni_{0.15}Cr_{0.57}O_4$	14.411	8.320	12.4	0.095
$Fe_{1.86}Ni_{0.15}Cr_{0.99}O_4$	14.462	8.350	15.8	0.093
$Fe_{1.62}Ni_{0.33}Cr_{1.05}O_4$	14.446	8.341	18.7	0.091
$Fe_{1.44}Ni_{0.30}Cr_{1.29}O_4$	14.399	8.313	19.4	0.091
$Fe_{1.20}Ni_{0.24}Cr_{1.56}O_4$	14.418	8.324	24.6	0.088
$Ni_{0.88}Cr_{2.12}O_4$ *	*	8.545	4.8	0.095
$NiCr_2O_4$ **	14.315	8.265	7.2	0.113

The out-of-plane lattice parameter (in hexagonal convention) as a function of the composition is plotted in Figure 4.15.

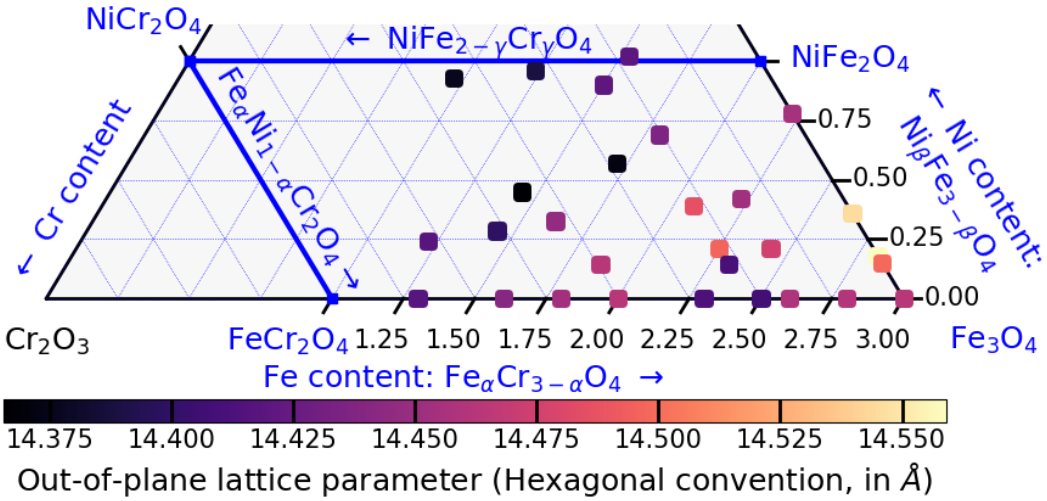

Figure 4.15: Out-of-plane lattice parameters in hexagonal convention (in Å) indicated in the quaternary diagram.

Some trends can be drawn. The highest lattice parameter is obtained for $Fe_{2.82}Ni_{0.18}O_4$. The nickel insertion in the stoichiometry results in lower lattice parameters. Increasing the chromium concentration (at a constant nickel concentration) results in a first increase of the lattice parameter, then decrease and increase again. This shape remains until β = 0.50. After this boundary, the nickel and chromium concentration increase results in a decrease of the lattice parameter. To analyze further these variations, the fine structure is required (see Chapter 6).

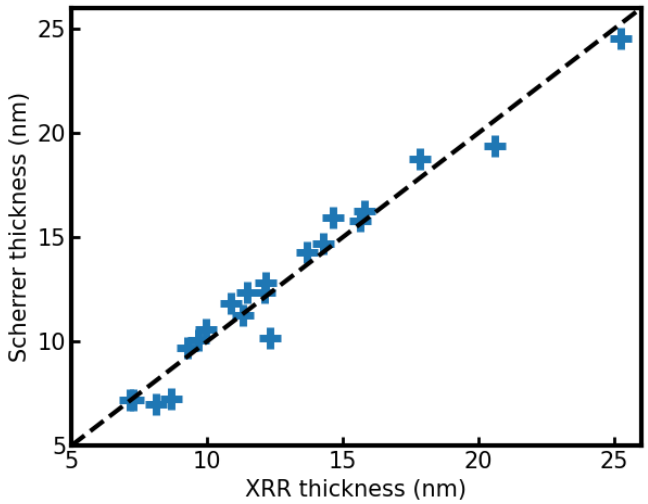

Figure 4.16: Comparison between the XRR thickness and the Scherrer thickness. The blue crosses represent the different samples.

The Scherrer law can be used to determine the thickness of the crystalline layer via the FWHM of the (h h h) peak. The film thickness having previously determined by XRR (or "optical" thickness), a comparison between the two methods is shown in Figure 4.16. The relationship is excellent, showing that the optical thickness probed by XRR is equivalent to the thickness of the crystalline phase probed by the Scherrer law and thus indicating the excellent crystalline quality of the films

The rocking curves exhibited FWHM values of approximately 0.1°, which indicate the high crystalline quality of the thin film synthetized (see Figure 4.14). The minimum value obtained is 0.088°, while the maximum is 0.113°. The mean value is 0.096°.

4.4.2.2 In-plane lattice parameter determination

In order to access to the in-plane lattice (a) parameter, in-plane XRD measurements have been done on several samples grown on sapphire substrates or MAO substrates.

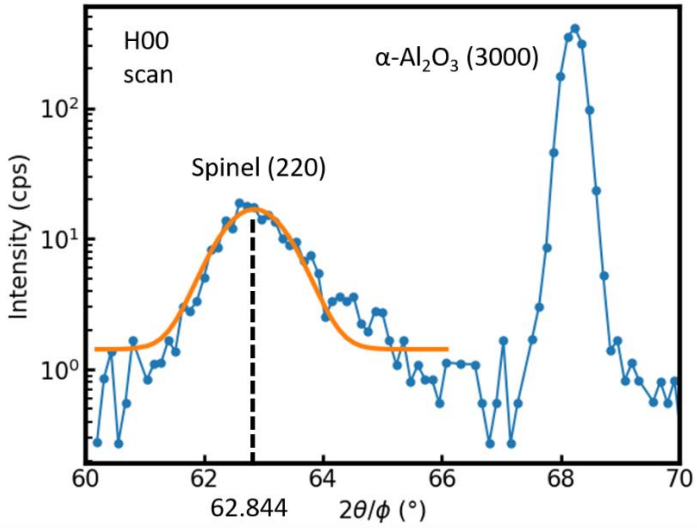

Figure 4.17: In-plane XRD measurement (H00 scan) for the sample $Fe_{1.20}Ni_{0.24}Cr_{1.56}O_4$. The blue curve represents the XRD data, and the orange curve depicts the Gaussian fit.

Figure 4.17 shows a (h00) scan of $Fe_{1.20}Ni_{0.24}Cr_{1.56}O_4$ sample. In this geometry, the peak of the substrate is identified as (3000), whereas the peak of the spinel layer observed is identified to (220) in the hexagonal convention (equivalent to (440) in the cubic convention). If an in-plane lattice parameter of 5.91 Å for hexagonal convention is considered, the interreticular distances are 1.4775 Å and 1.7061 Å for (220) and (300) peaks, respectively (see chapter 3). With the Bragg law, the obtained distance is 1.479 Å, which corresponds to the (220) peak.

*Table 4.5: Summary of the in-plane lattice parameter measurements. * and ** indicate MAO (001) and MAO (111) substrates.*

Sample Stoichiometry	d (Å)	$a_{hexagonal}$ (Å)	a_{cubic} (Å)
$Fe_{2.43}Ni_{0.21}Cr_{0.36}O_4$	1.48	5.92	8.37
$Fe_{1.71}Ni_{0.57}Cr_{0.72}O_4$	1.48	5.91	8.37
$Fe_{1.44}Ni_{0.45}Cr_{1.11}O_4$	1.48	5.91	8.36
$Fe_{0.96}Ni_{0.93}Cr_{1.11}O_4$	1.47	5.88	8.32
$Fe_{1.20}Ni_{0.24}Cr_{1.56}O_4$	1.48	5.91	8.37
$Ni_{0.88}Cr_{2.12}O_4$ *	2.04	*	8.16
$NiCr_2O_4$ **	1.46	5.82	8.24

The results of the in-plane lattice parameter (a) measurements as a function of the composition are presented in in Table 4.5 and in Figure 4.18. Concerning the growth on sapphire substrates, the in-plane lattice parameter for the majority of samples is comprised between 5.909 Å and 5.917 Å. One sample exhibits a slightly smaller lattice parameter of 5.883 Å. This sample has a stoichiometry close to the equimolar composition $FeNiCrO_4$. Some additional deformations may result from this composition but as illustrated in Figure 4.18, this region has not been sufficiently explored.

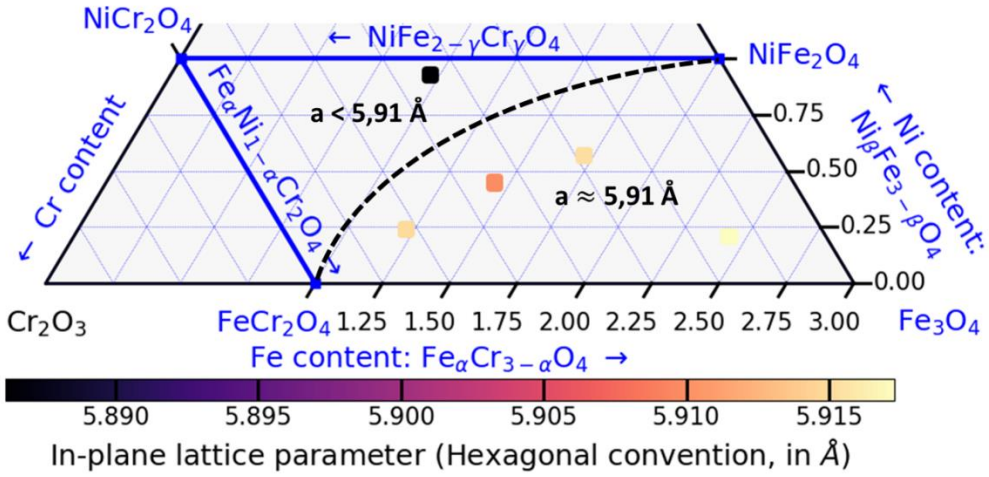

Figure 4.18: In-plane lattice parameter in hexagonal convention (in Å) indicated in the quaternary diagram.

An attempt is made to divide the area into two zones, one with an in-plane lattice parameter of approximately 5.91 Å and one with a value below this. With regard to the MAO substrates, the substrate peak gives a substrate lattice parameter of 8.076 Å and 7.995 Å for the (001) and (111) orientations, respectively. The lattice parameter for the (111) orientation is surprising given the 8.08 Å lattice parameter observed for the bulk material. The two layers of $NiCr_2O_4$ exhibited lattice parameter significantly lower than the previous samples, with values of 8.161 Å and 8.235 Å for the (001) and (111) orientations, respectively.

4.4.2.3 Epitaxial relationships between the spinel thin film and the substrates

With these out-of-plane and in-plane measurements on oxides layers grown on three types of substrates, it is possible to determine their epitaxial relationship, which is defined as the manner in which the spinel layer grows on each substrate. The epitaxial relationships for the MAO (001), MAO (111), and α-Al_2O_3 (0001) substrates are indicated by the equations (4.1), (4.2), and (4.3), respectively.

$$\begin{aligned} [100]_{spinel} &\parallel [100]_{MAO\ (001)} \\ [010]_{spinel} &\parallel [010]_{MAO\ (001)} \\ [001]_{spinel} &\parallel [001]_{MAO\ (001)} \end{aligned} \quad (4.1)$$

$$\begin{aligned} [11\bar{2}]_{spinel} &\parallel [11\bar{2}]_{MAO\ (111)} \\ [1\bar{1}0]_{spinel} &\parallel [1\bar{1}0]_{MAO\ (111)} \\ [111]_{spinel} &\parallel [111]_{MAO\ (111)} \end{aligned} \quad (4.2)$$

$$\begin{aligned} [11\bar{2}]_{spinel} &\parallel [1100]_{sapphire\ (0001)} \\ [1\bar{1}0]_{spinel} &\parallel [3000]_{sapphire\ (0001)} \\ [111]_{spinel} &\parallel [0001]_{sapphire\ (0001)} \end{aligned} \quad (4.3)$$

The epitaxial relationships for the MAO substrates are in good agreement with the RHEED analyses. Concerning the sapphire substrate, the spinel phase exhibits a 30° reorientation of the lattice. This reorientation is necessary to adapt to the crystallographic structure of the substrate. For example, an in-plane lattice parameter of 5.91 Å for the spinel phase gives an interreticular distance of 1.48 Å and 1.71 Å for the (220) and the (300) peaks, respectively. The (3000) sapphire peak corresponds to a distance of 1.37 Å. Consequently, the in-plane lattice mismatch ($(d_{spinel}-d_{sapphire})/d_{sapphire}$) is 7.5 % for the (220) peak and 24.2 % for the (300) peak, respectively. The reorientation of the spinel lattice by 30° has reduced the lattice mismatch of 16.7 % (69 % when considering 24.2 % as the starting point, which is significant).

4.5 MAGNETIC INVESTIGATION

The magnetic behavior of the samples has been probed by VSM magnetometry (see chapter 3) at different temperatures (T= 10 K, 100 K and 300 K). Figure 4.19 shows the magnetic hysteresis loops obtained for the $Fe_{1.53}Ni_{1.02}Cr_{0.45}O_4$ layer at different temperatures. The loop obtained at 300 K is almost closed, but for lower temperatures, the hysteresis loops are open. At T= 10 K, the magnetic hysteresis loop shows a pronounced shoulder at around - 2500 Oe. Many hypotheses have been advanced to explain this shoulder. The most common ones are the presence of a second magnetic phase like FeO[16] or the presence of antiphase boundaries (APBs) within the crystallographic structure.

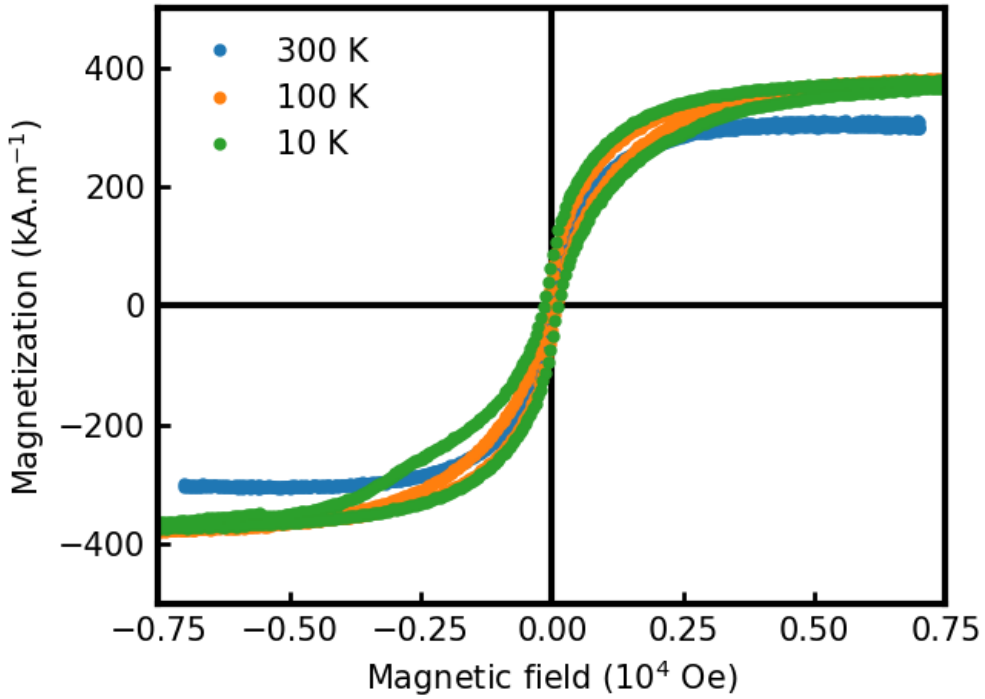

Figure 4.19: Magnetic hysteresis loops obtained at three temperatures for $Fe_{2.07}Ni_{0.39}Cr_{0.54}O_4$.

The results of the magnetic characterization are plotted in Table 4.6. Some trends can be drawn from these measurements. However, for a more accurate description of the variations of these magnetic properties, the fine structure is required (see Chapter 5).

*Table 4.6: Summary of the magnetic parameters for all samples extracted from VSM measurements. M_S, M_R and H_C are noted in kA.m^{-1}. * and ** indicate samples grown on MAO (001) and MAO (111) substrates.*

Sample Stoichiometry	10 K			100 K			300 K		
	M_S	M_R	H_C	M_S	M_R	H_C	M_S	M_R	H_C
$Fe_{2.22}Ni_{0.78}O_4$	159	69	47	147	43	31	141	9	6
$Fe_{2.82}Ni_{0.18}O_4$	770	225	30	735	158	18	600	68	7
$Fe_{2.64}Ni_{0.36}O_4$	540	130	27	520	54	10	424	27	5
$Fe_{2.85}Ni_{0.15}O_4$	260	130	83	230	95	48	190	32	17
$Fe_{2.43}Ni_{0.21}Cr_{0.36}O_4$	640	255	35	600	165	18	490	85	8
$Fe_{1.71}Ni_{0.57}Cr_{0.72}O_4$	67	22	41	71	12	11	51	5	4
$Fe_{1.44}Ni_{0.45}Cr_{1.11}O_4$	120	48	56	79	20	14	172	7	2
$Fe_{1.50}Ni_{0.90}Cr_{0.60}O_4$	138	59	74	118	33	26	86	9	4
$Fe_{1.53}Ni_{1.02}Cr_{0.45}O_4$	1022	130	11	786	87	7	692	67	5
$Fe_{1.80}Ni_{0.69}Cr_{0.51}O_4$	383	68	11	355	43	7	300	18	2
$Fe_{2.07}Ni_{0.39}Cr_{0.54}O_4$	426	69	6	399	47	6	451	23	3
$Fe_{2.22}Ni_{0.42}Cr_{0.36}O_4$	548	73	7	555	58	5	562	38	3
$Fe_{1.23}Ni_{0.96}Cr_{0.78}O_4$	219	82	52	178	66	35	138	24	9
$Fe_{2.25}Ni_{0.21}Cr_{0.54}O_4$	86	12	8	66	9	6	64	7	4
$Fe_{0.96}Ni_{0.93}Cr_{1.11}O_4$	267	106	69	222	67	33	186	25	11
$Fe_{2.31}Ni_{0.15}Cr_{0.57}O_4$	133	36	34	118	27	17	101	12	5
$Fe_{1.86}Ni_{0.15}Cr_{0.99}O_4$	84	21	32	73	15	16	65	8	6
$Fe_{1.62}Ni_{0.33}Cr_{1.05}O_4$	68	15	18	78	13	10	95	10	5
$Fe_{1.44}Ni_{0.30}Cr_{1.29}O_4$	45	8	12	42	8	11	49	6	6
$Fe_{1.20}Ni_{0.24}Cr_{1.56}O_4$	276	80	25	248	52	12	237	36	8
$Ni_{0.88}Cr_{2.12}O_4$ *	490	102	21	404	74	13	390	58	10
$NiCr_2O_4$ **	159	69	47	147	43	31	141	9	6

These M_S, M_R and H_C results are also summarized in the following phase diagrams (Figure 4.20, Figure 4.21, and Figure 4.22, respectively) for each temperature.

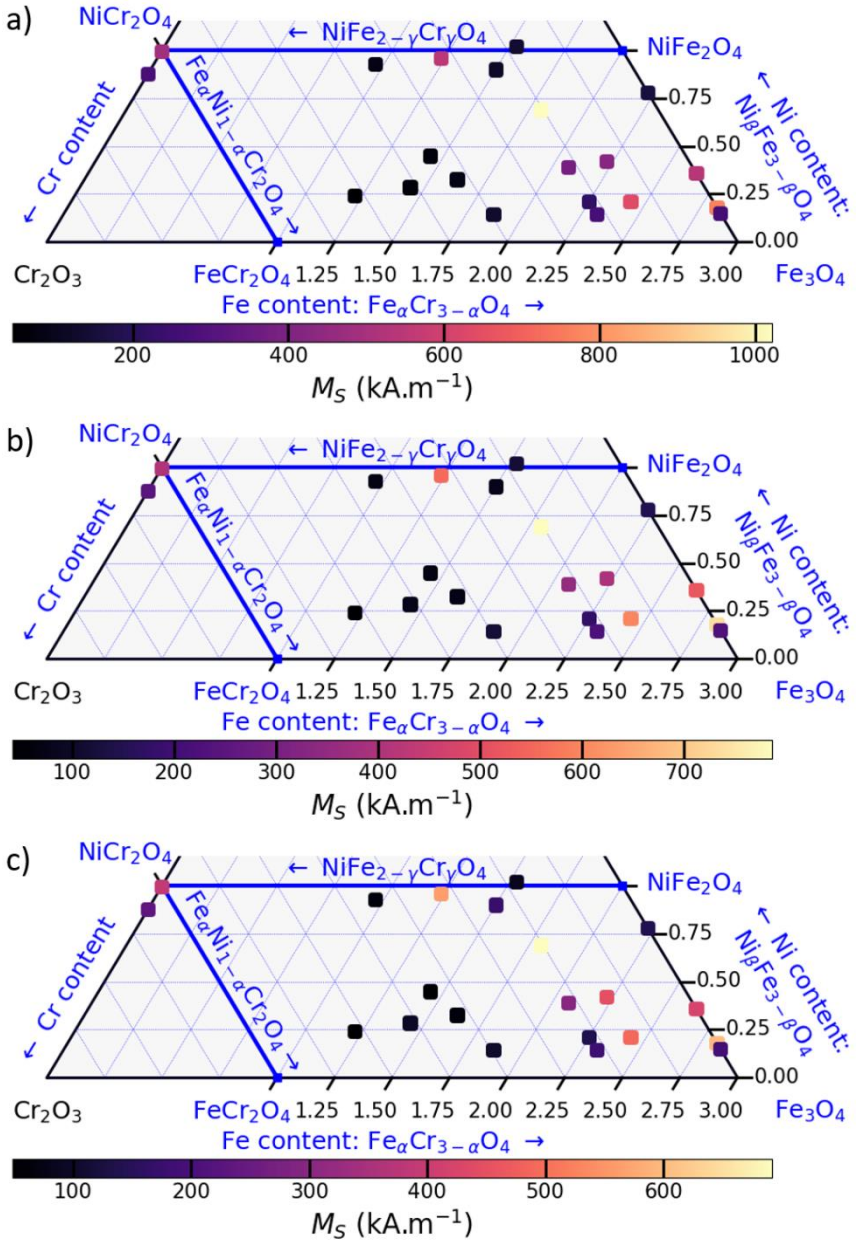

Figure 4.20: M_S at 10 K (a), 100 K (b) and 300 K (c) for each sample composition.

As the Cr stoichiometry is increasing, the M_S displays a notable decreasing at the exception of the two $NiCr_2O_4$ samples. Concerning the Ni stoichiometry, samples between β = 0.25 and β = 0.50 with 2.25 to 2.50 iron content possess the highest M_S. Note that one sample exhibits a markedly elevated M_S. This anomalous behavior can be attributed to a substantial substrate contribution, which is considerably more pronounced than in the other samples. Fe_3O_4 exhibits M_S value of 430-510 kA.m^{-1} in single crystal[17], while $NiFe_2O_4$ exhibits M_S values of 270 kA.m^{-1} in bulk[18]. These values are in agreement with the values of our samples.

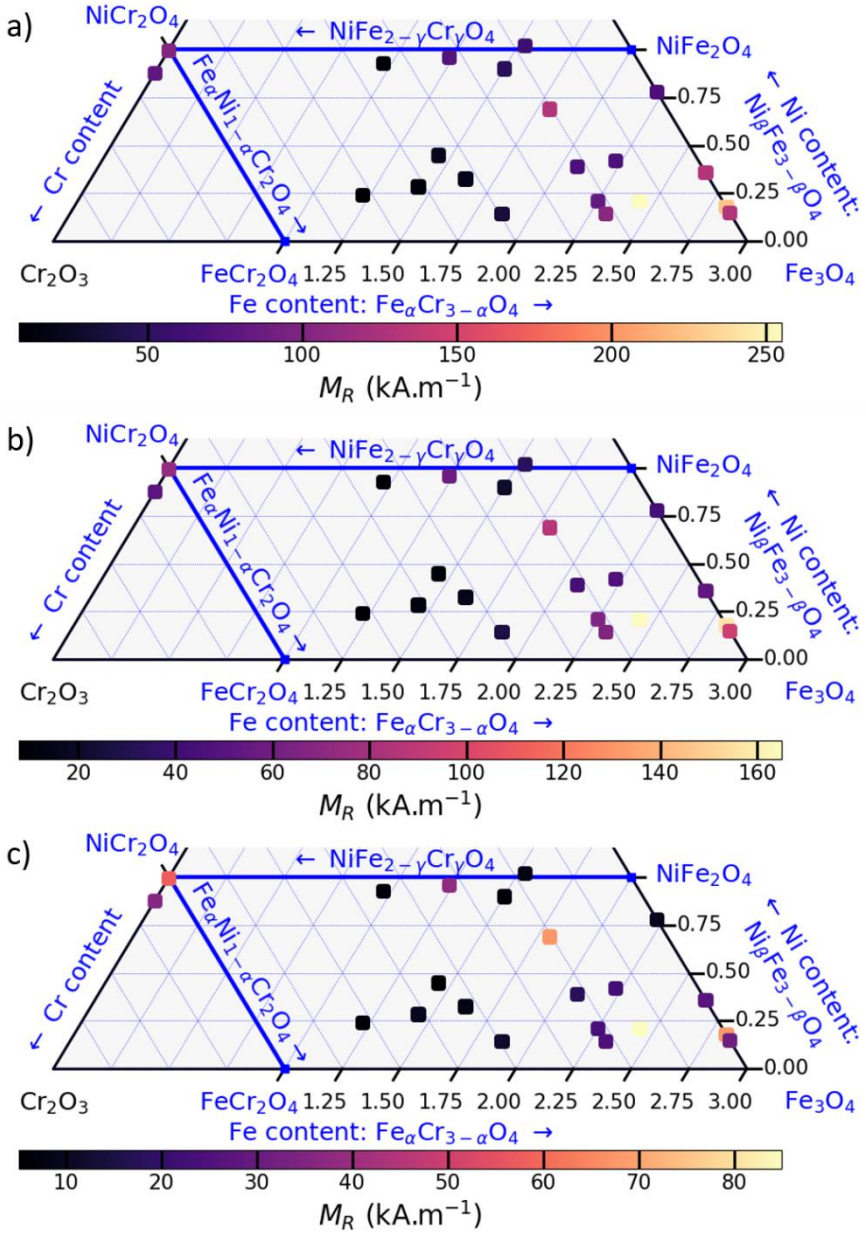

Figure 4.21: M_R at 10 K (a), 100 K (b) and 300 K (c) for each sample composition.

M_R variations exhibit analogous characteristics to those observed in M_S variations. Introducing Ni and Cr within the structure results in lower M_R, at the exception of the sample at β = 0.75 and α = 1.75. This sample is the sample with markedly high M_S. Another sample has a high M_R at α = 2.50 and β = 0.25. The reported values of M_R are lower than the reported values at room temperature for $NiFe_2O_4$[19] and Fe_3O_4[20], which is 107 $kA.m^{-1}$ and 200 $kA.m^{-1}$, respectively. It can be explained by the thin film form of our samples. In nanodevices, the magnetic proterties are highly dependant of the size of the studied sample[6].

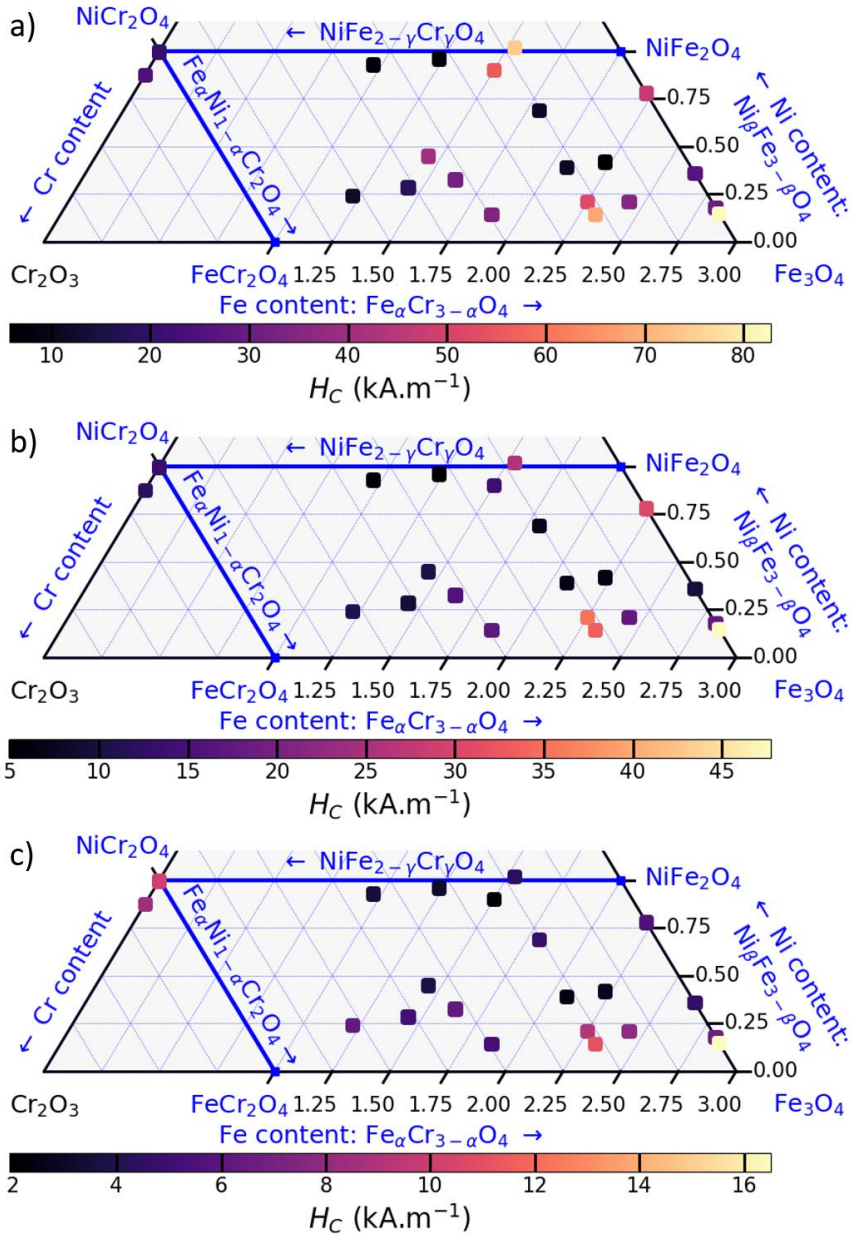

Figure 4.22: H_C at 10 K (a), 100 K (b) and 300 K (c) for each sample composition.

H_C variations do not exhibit the same patterns as those observed in M_S and M_R. The values range from 100 Oe to 1000 Oe at 10 K. The weakest H_C values are located at the top of the quaternary diagram (high Ni content). At fixed Ni content, the increasing of Cr content induces a decreasing of the value of H_C. The reported values of H_C for Fe_3O_4[20] is between 100 Oe to 300 Oe ,while for $NiFe_2O_4$[21] it is 200 Oe. The reported values for our samples are below the literature values. As for M_R values, it may be due to the thin film form of our samples. In nanodevices, the magnetic proterties are highly dependant of the size of the studied sample[6].

A final observation concerns the magnetic behavior of $NiCr_2O_4$ samples (samples located in the upper left quadrant of the blue spinel zone; the sample grown on (111) $MgAl_2O_4$ is located just above the sample grown on (001) $MgAl_2O_4$). In the literature, these samples are reported to exhibit a Curie temperature at approximately 80 K[22]. However, VSM measurements at T= 300 K, present an open magnetic hysteresis loop as shown in Figure 4.23. The sample grown on the $MgAl_2O_4$ (111) surface exhibits a higher magnetization than the sample grown on the (001) surface. The surprising ferrimagnetic behavior at 300 K is perhaps due to magnetic inhomogeneity in the layer, or due to a strain effect (weak thickness these two samples: 4.8 and 7.29 nm for $Ni_{0.88}Cr_{2.12}O_4$ and $NiCr_2O_4$, respectively).

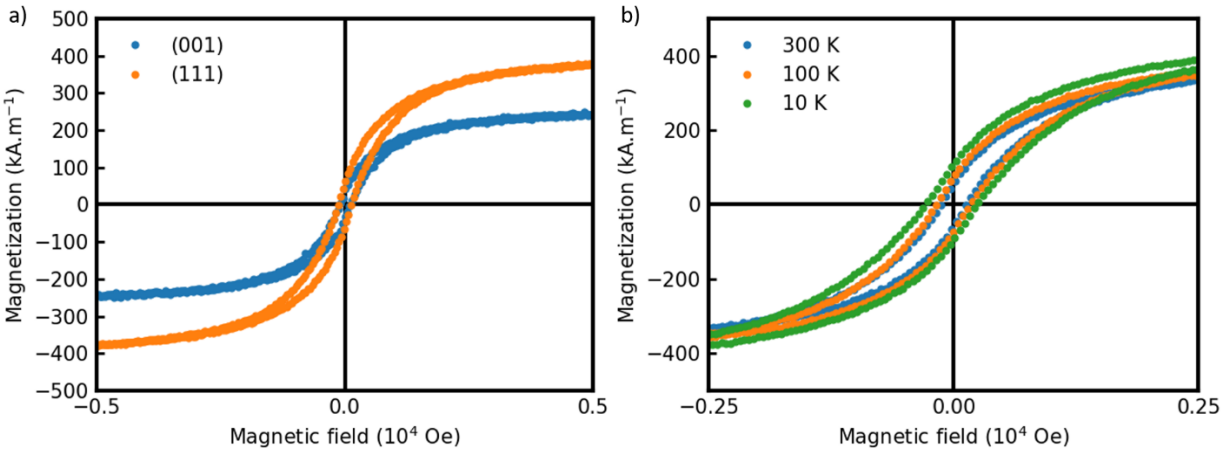

Figure 4.23: a) Hysteresis loops at T= 300 K for $NiCr_2O_4$ (001) and (111) samples. b) Hysteresis loops at 300 K, 100 K and 10 K for (111) sample.

4.6 CONCLUSIONS

Spinel $Fe_\alpha Ni_\beta Cr_\gamma O_4$ thin films have been grown successfully on the c-plane (0001) of sapphire substrates by AO-MBE. *In situ* RHEED acquisitions demonstrated the high crystalline quality of the elaborated thin films, confirming the (111) spinel structure with a low roughness. Increasing the chromium content induces nevertheless a deterioration of the growth mode from 2D to 3D.

The stoichiometry of the films have been assessed by using XPS measurements. A large range of composition of the (Fe-Ni-Cr-O) quaternary phase diagram has been explored. A composition area (*i.e.* Fe-doped $NiCr_2O_4$) is nevertheless hard to access due to the difficulties to obtain crystalline layers for this high Cr content. Indeed, Cr_2O_3 exhibits the same hexagonal corundum structure as the sapphire substrate, and samples with a significant content in chromium tend to mimic this structure[9]. To avoid this corundum structure, thin films with compositions close to $NiCr_2O_4$ have been obtained by changing the nature of the substrate. The spinel-type $MgAl_2O_4$ (001) and (111) substrates allowed to elaborate spinel thin films with a high chromium content.

X-ray diffraction (XRD) measurements confirmed the high crystalline quality of the thin films. No secondary phase is observed, and only the (h h h) peak is observed in the 2θ/ω curves. The rocking curves exhibit a FWHM around 0.1°, which confirmed the crystalline quality of the different layers. The relationship between the XRR and the Scherrer thickness is linear, confirming the absence of amorphous phases in thin films. In addition, some in-plane measurements have been performed, and the combination of out-of-plane and in-plane data yields the complete epitaxial relationship between the spinel phase and the three different substrates selected.

The VSM measurements indicated a significant decrease of magnetic properties (M_S, M_R) with the increasing chromium and nickel contents. However, it is possible to identify an optimal composition in nickel and chromium which allow to optimize the magnetic properties (zone around $\beta = 0.25$ and $0.25 < \gamma < 0.50$ and $2.25 < \alpha < 2.50$).

In order to correlate the structure (lattice parameter) and the magnetic properties (M_S, M_R and H_C) of the different spinel layers with the composition, it is now necessary to determine the cationic site distribution (*i.e.* the fine structure) as we will describe now.

4.7 BIBLIOGRAPHY

(1) Gota, S.; Guiot, E.; Henriot, M.; Gautier-Soyer, M. Atomic-Oxygen-Assisted MBE Growth of α − F e 2 O 3 on α − A l 2 O 3 (0001): Metastable FeO(111)-like Phase at Subnanometer Thicknesses. *Phys. Rev. B* **1999**, *60* (20), 14387–14395. https://doi.org/10.1103/PhysRevB.60.14387.

(2) Gota, S.; Moussy, J.-B.; Henriot, M.; Guittet, M.-J.; Gautier-Soyer, M. Atomic-Oxygen-Assisted MBE Growth of Fe3O4 (1 1 1) on α-Al2O3 (0 0 0 1). *Surf. Sci.* **2001**, *482–485*, 809–816. https://doi.org/10.1016/S0039-6028(00)01066-9.

(3) Moussy, J.-B.; Gota, S.; Bataille, A.; Guittet, M.-J.; Gautier-Soyer, M.; Delille, F.; Dieny, B.; Ott, F.; Doan, T. D.; Warin, P.; Bayle-Guillemaud, P.; Gatel, C.; Snoeck, E. Thickness Dependence of Anomalous Magnetic Behavior in Epitaxial ${\mathrm{Fe}}_{3}{\mathrm{O}}_{4}(111)$ Thin Films: Effect of Density of Antiphase Boundaries. *Phys. Rev. B* **2004**, *70* (17), 174448. https://doi.org/10.1103/PhysRevB.70.174448.

(4) *International Tables for Crystallography*, 2016th ed.; Vol. A.

(5) Mega, N.; Wibowo, S.; Nada, N.; Ogasawara, K. Comparative Study on R-Line and U-Band Energies of Ruby Estimated from One-Electron and Many-Electron First-Principles Approaches. *J. Phys. Conf. Ser.* **2019**, *1179*, 012104. https://doi.org/10.1088/1742-6596/1179/1/012104.

(6) Pinho, P. V. B.; Chartier, A.; Menut, D.; Barbier, A.; Hunault, M. O. J. Y.; Ohresser, P.; Marcelot, C.; Warot-Fonrose, B.; Miserque, F.; Moussy, J.-B. Stoichiometry Driven Tuning of Physical Properties in Epitaxial Fe3-xCrxO4 Thin Films. *Appl. Surf. Sci.* **2023**, *615*, 156354. https://doi.org/10.1016/j.apsusc.2023.156354.

(7) Jing, S.; Li-Bin, L.; Ning-Kang, H.; Jin, Z.; Yong, L. Investigation on Lattice Constants of Mg-Al Spinels. *J. Mater. Sci. Lett. - J MATER SCI LETT* **2000**, *19*, 225–227. https://doi.org/10.1023/A:1006710808718.

(8) Kim, J. H.; Kim, B.; Andeen, D.; Lange, F. F. Seeded Epitaxial Growth of ZnO Thin Films on $MgAl_2O_4$ Substrates Using the Chemical Solution Deposition Method. *J. Mater. Res.* **2007**, *22* (4), 943–949. https://doi.org/10.1557/jmr.2007.0109.

(9) Pinho, P. V. B. Experimental and Theoretical Study on Fe-Cr-O Thin Films: From Fine Structure to Macroscopic Behavior. phdthesis, Université Paris-Saclay, 2022. https://theses.hal.science/tel-03917144 (accessed 2024-04-19).

(10) Sawatzky, G. A.; Van Der Woude, F.; Morrish, A. H. Mössbauer Study of Several Ferrimagnetic Spinels. *Phys. Rev.* **1969**, *187* (2), 747–757. https://doi.org/10.1103/PhysRev.187.747.

(11) Kochur, A. G.; Kozakov, A. T.; Googlev, K. A.; Mikheykin, A. S.; Torgashev, V. I.; Bush, A. A.; Nikolskii, A. V. Chemical Bonding and Valence State of 3d-Metal Ions in Ni1−xCoxCr2O4 Spinels from X-Ray Diffraction and X-Ray

Photoelectron Spectroscopy Data. *J. Electron Spectrosc. Relat. Phenom.* **2014**, *195*, 208–219. https://doi.org/10.1016/j.elspec.2014.07.010.

(12) Yadav, R. S.; Kuřitka, I.; Vilcakova, J.; Havlica, J.; Masilko, J.; Kalina, L.; Tkacz, J.; Enev, V.; Hajdúchová, M. Structural, Magnetic, Dielectric, and Electrical Properties of NiFe2O4 Spinel Ferrite Nanoparticles Prepared by Honey-Mediated Sol-Gel Combustion. *J. Phys. Chem. Solids* **2017**, *107*, 150–161. https://doi.org/10.1016/j.jpcs.2017.04.004.

(13) Uhlenbrock, S.; Scharfschwerdt, C.; Neumann, M.; Illing, G.; Freund, H.-J. The Influence of Defects on the Ni 2p and O 1s XPS of NiO. *J. Phys. Condens. Matter* **1992**, *4* (40), 7973. https://doi.org/10.1088/0953-8984/4/40/009.

(14) Lenglet, M.; d'Huysser, A.; Arsene, J.; Bonnelle, J. P.; Jorgensen, C. K. XANES, X-Ray Photo-Electron and Optical Spectra of Divalent Nickel at the Crystallographic Transition in NiCr2O4 and the Ni1-xCuxCr2O4 System: Correlation with the Jahn-Teller Effect. *J. Phys. C Solid State Phys.* **1986**, *19* (17), L363. https://doi.org/10.1088/0022-3719/19/17/003.

(15) Sickafus, K. E.; Wills, J. M.; Grimes, N. W. Structure of Spinel. *J. Am. Ceram. Soc.* **1999**, *82* (12), 3279–3292. https://doi.org/10.1111/j.1151-2916.1999.tb02241.x.

(16) Wasilewski, P.; Virgo, D.; Ulmer, G. C.; Schwerer, F. C. Magnetochemical Characterization of Fe(FexCr2−x)O4 Spinels. *Geochim. Cosmochim. Acta* **1975**, *39* (6), 889–902. https://doi.org/10.1016/0016-7037(75)90035-6.

(17) Paul, K. Magnetic and Transport Properties of monocrystallineFe 3 O 4. *Open Phys.* **2005**, *3* (1), 115–126. https://doi.org/10.2478/BF02476510.

(18) Alarifi, A.; Deraz, N. M.; Shaban, S. Structural, Morphological and Magnetic Properties of NiFe2O4 Nano-Particles. *J. Alloys Compd.* **2009**, *486* (1), 501–506. https://doi.org/10.1016/j.jallcom.2009.06.192.

(19) Tomitaka, A.; Kobayashi, H.; Yamada, T.; Jeun, M.; Bae, S.; Takemura, Y. Magnetization and Self-Heating Temperature of $NiFe_2O_4$ Nanoparticles Measured by Applying Ac Magnetic Field. *J. Phys. Conf. Ser.* **2010**, *200* (12), 122010. https://doi.org/10.1088/1742-6596/200/12/122010.

(20) Nagahama, T.; Matsuda, Y.; Tate, K.; Kawai, T.; Takahashi, N.; Hiratani, S.; Watanabe, Y.; Yanase, T.; Shimada, T. Magnetic Properties of Epitaxial Fe3O4 Films with Various Crystal Orientations and Tunnel Magnetoresistance Effect at Room Temperature. *Appl. Phys. Lett.* **2014**, *105* (10), 102410. https://doi.org/10.1063/1.4894575.

(21) Chand Verma, K.; Pratap Singh, V.; Ram, M.; Shah, J.; Kotnala, R. K. Structural, Microstructural and Magnetic Properties of NiFe2O4, CoFe2O4 and MnFe2O4 Nanoferrite Thin Films. *J. Magn. Magn. Mater.* **2011**, *323* (24), 3271–3275. https://doi.org/10.1016/j.jmmm.2011.07.029.

(22) Tomiyasu, K.; Kagomiya, I. Magnetic Structure of $NiCr_2O_4$ Studied by Neutron Scattering and Magnetization Measurements. *J. Phys. Soc. Jpn.* **2004**, *73* (9), 2539–2542. https://doi.org/10.1143/JPSJ.73.2539.

5 FINE STRUCTURE INVESTIGATION

This chapter will present two synchrotron based methods allowing the study of the fine structure of the ternary spinel oxides. The first part presents the X-ray Magnetic Circular Dichroism (XMCD) results, which will be used for exploring the cationic ordering and magnetic properties. Secondly, the results obtained by Resonant X-ray Diffraction (RXD) are analyzed. The information extracted from this technique, will allow to probe also the cationic site distribution as a function of the stoichiometry of the layers. The fine structure and the inversion parameter deduced from these two different experiments will be discussed in association with theoretical models.

5 FINE STRUCTURE INVESTIGATION

5.1 X-RAY MAGNETIC CIRCULAR DICHROISM FINE STRUCTURE INVESTIGATION

XAS/XMCD experiments have been performed in order to access to the cationic site distribution as a function of the composition. These measurements need to be simulated with the Quanty simulation code in order to extract the cationic distribution.

5.1.1 Experimental conditions

The XAS/XMCD measurements have been done on two different beamlines at different temperatures (T=300 K, 107 K, 20 K, 4 K), magnetic fields (μ_0H= 2 Tesla, 4 Tesla) or incident angle (θ= 30°, 35°, 90°). The experimental parameters used for these XAS/XMCD experiments are summarized in Table 5.1.

Table 5.1: Experimental conditions for XAS/XMCD acquisitions on spinel oxide layers.

Thin films	Beamline	Tp (K)	Field (T)	θ (°)	Low Tp (K)	Field (T)	θ (°)
$Fe_{2.22}Ni_{0.78}O_4$	Deimos Cromag	300	4	35		No	
$Fe_{2.82}Ni_{0.18}O_4$	Deimos Cromag	300	4	35		No	
$Fe_{2.43}Ni_{0.21}Cr_{0.36}O_4$	Deimos Cromag	300	4	35		No	
$Fe_{1.71}Ni_{0.57}Cr_{0.72}O_4$	Deimos Cromag	300	4	35	4	4	35
$Fe_{1.44}Ni_{0.45}Cr_{1.11}O_4$	Deimos Cromag	300	4	35	4	4	35
$Fe_{2.64}Ni_{0.36}O_4$	ESRF ID 32	300	3	35		No	
$Fe_{2.85}Ni_{0.15}O_4$	ESRF ID 32	300	3	35		No	
$Fe_{2.43}Ni_{0.21}Cr_{0.36}O_4$	ESRF ID 32	300	3	35	20	3	35
$Fe_{2.22}Ni_{0.42}Cr_{0.36}O_4$	ESRF ID 32	300	4	35	4	4	35
$Fe_{2.25}Ni_{0.21}Cr_{0.54}O_4$	ESRF ID 32	300	4	35/90	4	4	35/90
$Fe_{0.96}Ni_{0.93}Cr_{1.11}O_4$	ESRF ID 32	300	4	35	4	4	35
$Fe_{1.50}Ni_{0.90}Cr_{0.60}O_4$	Deimos MagneTwo	300	2	90		No	
$Fe_{1.53}Ni_{1.02}Cr_{0.45}O_4$	Deimos MagneTwo	300	2	90		No	
$Fe_{1.80}Ni_{0.69}Cr_{0.51}O_4$	Deimos MagneTwo	300	2	90		No	
$Fe_{2.07}Ni_{0.39}Cr_{0.54}O_4$	Deimos MagneTwo	300	2	90		No	
$Fe_{1.86}Ni_{0.15}Cr_{0.99}O_4$	Deimos MagneTwo	300	2	90		No	
$Fe_{1.62}Ni_{0.33}Cr_{1.05}O_4$	Deimos MagneTwo	300	2	90		No	
$Fe_{1.44}Ni_{0.27}Cr_{1.29}O_4$	Deimos MagneTwo	300	2	90	107	±2	30/90
$Fe_{1.20}Ni_{0.24}Cr_{1.56}O_4$	Deimos MagneTwo	300	2	90		No	

5.1.2 Theoretical curves calculations with Quanty

Theoretical contributions for each species (II and III species, located in both the T_d and O_h sites) are required to extract the fine structure of the oxide layer.

From the octahedral site preference, we claim that chromium will only occupy O_h sites[1,2]. The nickel will exhibit a slight preference for O_h sites (less than chromium) whereas the iron will not exhibit such a preference. From these considerations, a total of seven theoretical XMCD curves must be calculated: $Fe_{T_d}^{3+}$, $Fe_{T_d}^{2+}$, $Fe_{O_h}^{3+}$, $Fe_{O_h}^{2+}$, $Ni_{O_h}^{2+}$, $Ni_{T_d}^{2+}$, and $Cr_{O_h}^{3+}$. The theoretical contribution for each species is calculated with the code Quanty[3–5] (see chapter 3), through the graphical user interface Crispy[6].

The Quanty code has already been used in our laboratory for $Fe_{3-x}Cr_xO_4$ series[7] or Cr_2O_3 thin films. This code introduces different parameters. The F_k, G_k (employed to reduce electron-electron interaction and to simulate effects such covalency and charge transfer) and ζ parameters (spin-orbit interaction, causing the separation of the *2p* edge into $2p_{3/2}$ and $2p_{1/2}$) affect the initial and final Hamiltonians. The experimental conditions (applied magnetic field, temperature), the crystal field parameters, and convolution parameters (Lorentzian and Gaussian choice) can also be added. In the case of T_d or O_h sites, only the D_q parameter is relevant for the crystal field. But in less symmetrical environments, additional parameters may be needed, such as D_σ and D_τ in the C_{3v} case.

For a comprehensive description of the Hamiltonian parameters and their role on the resulting signal, the reader can refer to the previous thesis[8]. The major trends are recalled. Increasing F_k and G_k values shift the features towards higher energies, while increasing Δ values change the intensity ratio between features of L_2 and L_3 edges. The ζ parameter allows to control the separation between the L_3 and L_2 edges. For the others parameters, their modification does not change the shape of the signal, but just its intensity. Subsequently, the temperature was fixed at 10 K and the magnetic field at 2 Tesla. It was observed that the convolution parameters do not influence the position of the resulting peaks; but only affect the value of the full-width at half-maximum (FWHM). A higher value of Gaussian convolution results in a broader peak.

The complete set of parameters used for each curve is summarized in Table 5.2. These parameters for the iron species are identical to those fitted previously by Pinho[8]. New sets of parameters were tested, notably a crystal field description with C_{3v} symmetry. However, no significant improvements have been observed.

Table 5.2: Parameters used in Quanty simulations.

Parameters	$Fe_{T_d}^{3+}$	$Fe_{T_d}^{2+}$	$Fe_{O_h}^{3+}$	$Fe_{O_h}^{2+}$	$Ni_{O_h}^{2+}$	$Ni_{T_d}^{2+}$	$Cr_{O_h}^{3+}$
F_k	0.6	0.6	0.6	0.6	0.8	0.8	0.8
G_k	0.6	0.6	0.6	0.6	0.8	0.8	0.8
ζ	1	1	1	1	1	1	1
Δ	0.67	0.62	1.5	1.4	1.5	0.67	2.2
Magnetic field (T)	-2	-2	2	2	2	-2	2
Temperature (K)	10	10	10	10	10	10	10
Lorentzian	0.6 / 0.6	0.6 / 0.6	0.6 / 0.6	0.6 / 0.6	0.6 / 0.6	0.6 / 0.6	0.4 / 0.4
Gaussian	0.3	0.3	0.3	0.3	0.3	0.3	0.3

In regard to the iron species, the curves have been calculated with identical reduction parameters and ζ. Furthermore, the temperature and convolutions parameters are identical. The difference lies into the crystal field parameter Δ and the magnetic field. The crystal field parameter Δ_t of tetrahedral sites is fixed at 4/9 of the value of the crystal field parameter Δ_O of octahedral sites. The sign of magnetic field is used to have calculated curves pointing towards the positive values (negative value of the field) or the negative values (positive value of the field). This is linked to the minus sign in the Zeeman Hamiltonian in the crystal field multiplet Hamiltonian. Concerning the nickel species, the ratio of 4/9 has been applied to calculate the T_d contribution compared to the O_h one, and a negative magnetic field has also been applied (calculated curve pointing towards positive values).

The different simulated contributions are shown in Figure 5.1, along with the main features. The Cr L_3 edge displays three negative peaks (a, b and c), followed by one significant positive peak (d), while the Cr L_2 edge shows one negative peak (f) in the middle of two positive peaks (e and g). In the iron $L_{2,3}$ edge, four distinct peaks appear in the experimental spectra, which are related to a specific cation in a specific site. The $Fe_{T_d}^{3+}$ contribution (c) has a significant peak close to $Fe_{O_h}^{3+}$ (d) peak, which has repercussions in the distribution of these two species. Indeed, an increase of $Fe_{T_d}^{3+}$ contribution results in an expansion of the area in question, which in turn conceals a portion of the contribution from $Fe_{O_h}^{3+}$. Concerning the nickel $L_{2,3}$ edges, the $Ni_{T_d}^{2+}$ (a) contribution is less intense than the $Ni_{O_h}^{2+}$ (b and c), which will induce some difficulties for the identification of $Ni_{T_d}^{2+}$.

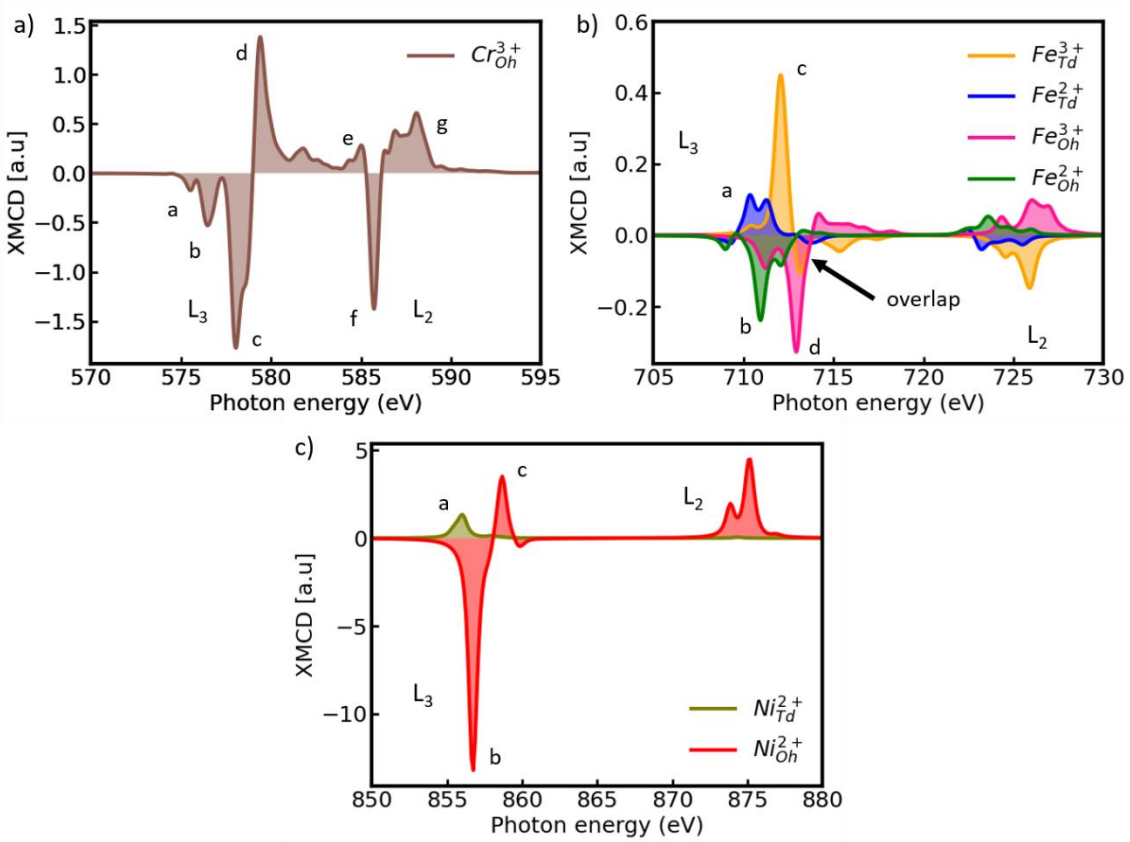

Figure 5.1: Calculated XMCD spectra of chromium (a), iron (b), and nickel (c) species with parameters described in Table 5.2.

5.1.3 Considerations on the fitting of XMCD spectra

In order to obtain the contribution of each atomic species, the final step in the exploitation of XMCD data is the linear fitting of the experimental data (L_3 edge for nickel and iron and $L_{2,3}$ edges for chromium), with the sum of the theoretical curves established above. The different contributions are obtained through a two-steps fitting. First, a fitting "least squares" algorithm is applied. Prior to this algorithm, the theoretical curves are adjusted in energy to ensure that the simulated peak aligns with the corresponding experimental peak. The algorithm optimizes the entire selected area of the spectrum, and the resulting fitting curves are frequently below the experimental curves at the principal peak, $Fe_{T_d}^{3+}$ peak in the case of iron L_3 edge and $Ni_{O_h}^{2+}$ for nickel L_3 edge. Consequently, a second step is required in which the automatic fitting is manually adjusted. In this step, the objective is to optimize the peak height for each contribution, thereby ensuring a high degree of correlation between the sum of contribution and the experimental XMCD at each peak. However, this approach may result in a slight reduction in the precision of the fitting outside of the peaks. The resulting fit is presented in Figure 5.2.

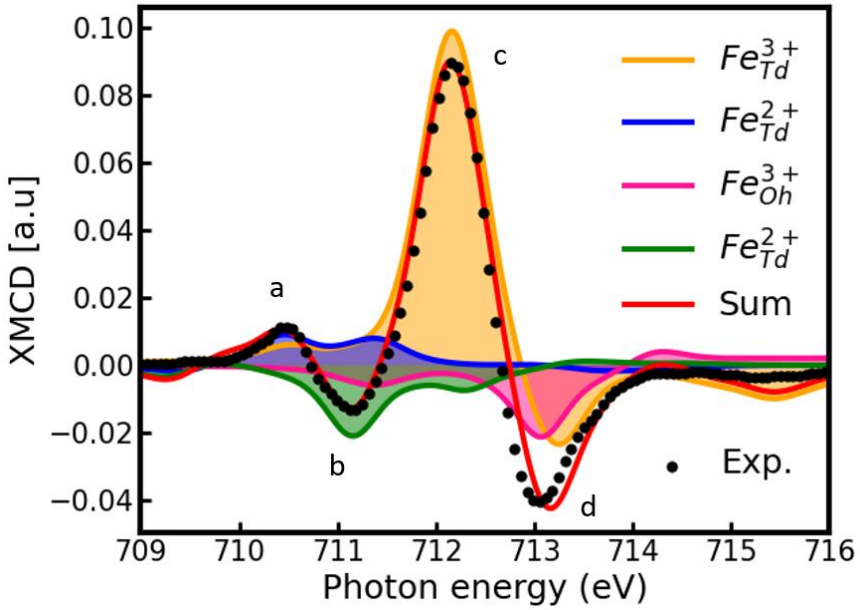

Figure 5.2: Fe L_3 edge XMCD spectrum of $Fe_{1.44}Ni_{0.45}Cr_{1.11}O_4$ sample at 300 K, adjusted manually. The color curve are identical to the Figure 5.1.

The XMCD fit methodology is first employed individually for each present elements (chromium (5.1.4), nickel (5.1.5) and iron (5.1.6 and 5.1.7)). A model of cationic occupancies (5.1.8) is subsequently presented to extract the inversion parameter and to verify the coherence of the iron fits.

Once the coefficients for each contribution obtained, they are transformed to express the percentage of each atomic species. This is achieved by dividing the appropriate coefficient by the sum of all coefficients (see equation (5.1) for the example of $\%Fe^{3+}_{T_d}$). Then, these percentages are converted into an occupancy value by multiplying by the stoichiometric number of iron (α). As an illustration, the occupancy value of the T_d and O_h species is given by equation (5.2), and the occupancy, in percentages, of the T_d and O_h species are given by equations (5.3) and (5.4). The spinel formula, Fe_3O_4, comprising three cations, with one T_d site for two O_h sites, explains the division by two in the occupancy percentage formula of the O_h site.

$$\%\mathrm{Fe}^{3+}_{\mathrm{Td}} = \frac{coefficient\left(\mathrm{Fe}^{3+}_{\mathrm{Td}}\right)}{\sum iron\ coefficients} \qquad (5.1)$$

$$Occupancy\ (site)\ (absolute\ value) = \%\ species * \alpha \qquad (5.2)$$

$$Occupancy\ (T_d)\ (\%) = \%species_{T_d} * \alpha \qquad (5.3)$$

$$Occupancy\ (O_h)\ (\%) = \%species_{O_h} * \alpha/2 \qquad (5.4)$$

5.1.4 Chromium $L_{2,3}$ edges XMCD spectra

First of all, the chromium $L_{2,3}$ edges XMCD spectra have been analyzed to ascertain their ordering in T_d or O_h sites.

Figure 5.3 shows a selected subset of normalized XMCD spectra at T = 300 K for the chromium $L_{2,3}$ edges. The spectra exhibit similar shape. The presence of three peaks in the L_3 edge (at 577.5 eV, 578.6 eV and 580.2 eV for a, b and c) and one at the L_2 edge (588 eV, f) is characteristic of $Cr_{O_h}^{3+}$, as shown with the theoretical curve.

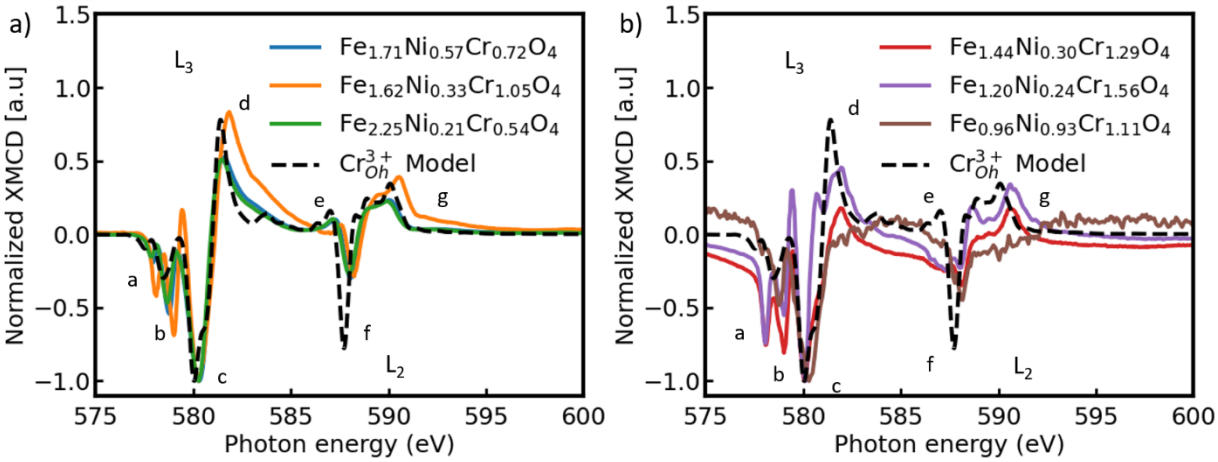

Figure 5.3: XMCD spectra at the chromium $L_{2,3}$ edges, at T = 300 K, for low-to-medium chromium content (a) and high chromium content (b).

The samples with the highest Cr content present experimental challenges due to the insulating behavior of the samples. A comparison of their XMCD spectra is provided in Figure 5.3 (b). The three-peaks structure observed at the L_3 edge (a, b and c) and the decreasing peak at the L_2 edge (f) are evident in all samples. The purple curve demonstrates a sudden decline in the L_2 edge structure (absence of e peak), which is associated with a signal jump in one of the recorded spectra. This phenomenon is deemed to be unphysical. The brown curve exhibits the greatest number of discrepancies. No peak d was observed at 582 eV, and the structure of the L_2 was found to be markedly different (no e or g peaks). The signal is also the most noisy, which can explain the discrepancy in the L_2 edge and the absence of the 582 eV peak. Consequently, despite the noisy signal, these signals can be attributed to $Cr_{O_h}^{3+}$, with some reserves on the $Fe_{0.96}Ni_{0.93}Cr_{1.11}O_4$ composition (brown curve).

At the exception of $Fe_{0.96}Ni_{0.93}Cr_{1.11}O_4$ composition, all experimental $L_{2,3}$ edges XMCD spectra are related to Cr^{3+} in O_h sites.

5.1.5 Nickel $L_{2,3}$ edges XMCD spectra

Concerning the Ni cations distribution, the Ni $L_{2,3}$ edges XMCD spectra for some selected samples is presented in Figure 5.4 (a). In order to compare the shape of the curves, all curves are divided by their respective minimum, and shifted in order to have the L_3 peak at 856.6 eV. The curves are highly similar, and related to $Ni_{O_h}^{2+}$, as indicated by the theoretical model.

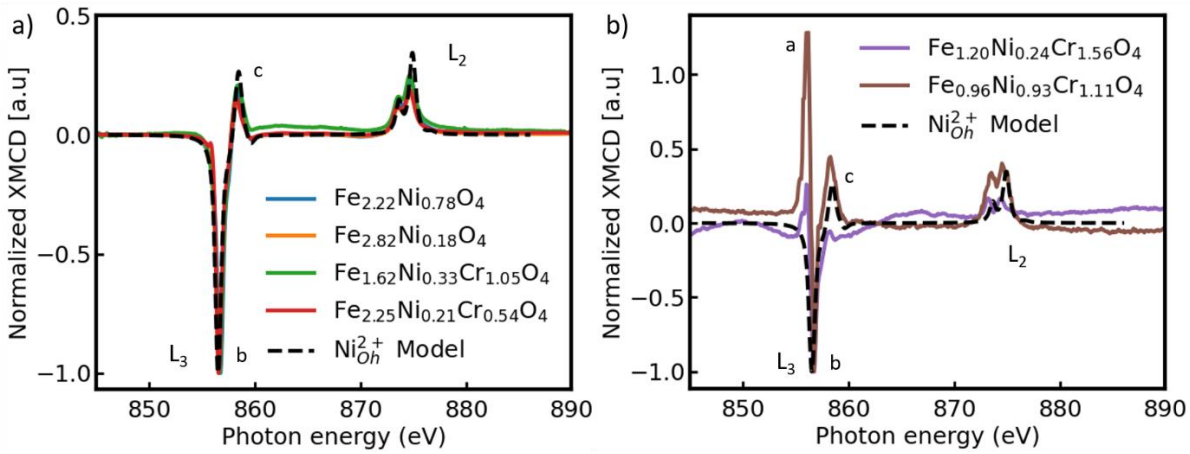

Figure 5.4: XMCD spectra at the nickel $L_{2,3}$ edges, at T = 300 K, for low-to-medium chromium content (a) and high chromium content (b).

Two compositions deserve a particular attention with regard to the Ni $L_{2,3}$ edges, as illustrated in Figure 5.4 (b). The first distinction between this samples set and the theoretical curve is the pre-L_3 edge peak (a) observed at 856.0 eV. This supplementary peak may have two potential origins. It is possible that this peak is a consequence of the charge effect as these two samples exhibit a high insulating behavior. But it may be also a contribution from $Ni_{T_d}^{2+}$. This second hypothesis seems more likely, as the Ni *2p* XPS spectra for $Fe_{0.96}Ni_{0.93}Cr_{1.11}O_4$ and $Fe_{1.20}Ni_{0.24}Cr_{1.56}O_4$ were different from the XPS spectrum for $Fe_{2.22}Ni_{0.78}O_4$.

Simulations indicate that the contribution of $Ni_{T_d}^{2+}$ is very weak (one tenth of the $Ni_{O_h}^{2+}$ contribution). Fitting the XMCD spectra results in Ni^{2+} cations occupying mainly the T_d sites. For example, a fit for the $Fe_{1.20}Ni_{0.24}Cr_{1.56}O_4$ composition is shown in Figure 5.5. The fitting results for the two samples with high chromium content are presented in Table 5.3. The result for $Fe_{0.96}Ni_{0.93}Cr_{1.11}O_4$ is unphysical as iron also occupied T_d sites, which gives a species presence in T_d sites $\gg 1$.

Table 5.3: Information extracted from the nickel L_3 edge XMCD fits.

Sample($Fe_\alpha Ni_\beta Cr_\gamma O_4$)	$Ni_{T_d}^{2+}$	$Ni_{O_h}^{2+}$
$Fe_{1.20}Ni_{0.24}Cr_{1.56}O_4$	0.19	0.05
$Fe_{0.96}Ni_{0.93}Cr_{1.11}O_4$	0.85	0.08

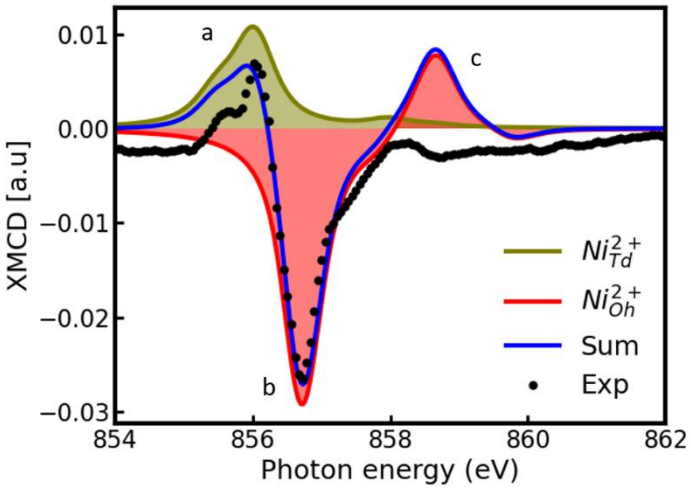

Figure 5.5: XMCD Ni L_3 edge fit for $Fe_{1.20}Ni_{0.24}Cr_{1.56}O_4$ at 300 K.

In conclusion, all samples present Ni^{2+} in O_h sites, with the exception of two compositions. In the case of these two samples ($Fe_{1.20}Ni_{0.24}Cr_{1.56}O_4$ and $Fe_{0.96}Ni_{0.93}Cr_{1.11}O_4$), the XPS spectrum exhibited a resemblance to that of $NiCr_2O_4$ samples (Ni^{2+} solely on T_d sites). The fit of these XMCD spectra results in Ni^{2+} predominantly localized at T_d sites.

5.1.6 Iron $L_{2,3}$ edges XMCD spectra

Concerning the iron $L_{2,3}$ edges XMCD spectra, Figure 5.6 present a selected subset of normalized (at Fe^{3+}_{Td} peak) iron L_3 edge XMCD spectra. The Fe^{3+}_{Td} peak (c) is slightly shifted in energy and the intensity of the three other peaks vary significantly. In some samples, the Fe^{2+}_{Td} peak (a) disappears (blue and green curves).

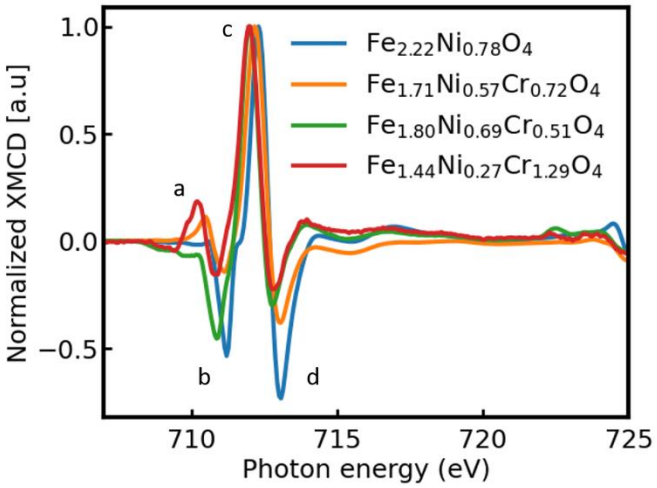

Figure 5.6: Iron L_3 edge XMCD spectra at T = 300 K for selected samples.

The overall results of the iron L_3 edge XMCD spectra fits are indicated in the Table 5.4. The sample stoichiometry is provided, with the occupancy in absolute value and δ, the inversion parameter ($\delta = \frac{Fe_{T_d}^{3+}}{\sum Fe_{Td}}$, see 5.1.8 for explanations). In light of the sole occupation of O_h sites by Cr^{3+} and Ni^{2+}, the fit should provide values of $\Sigma\, Fe_{T_d}$ close to unity for all samples. This objective is accomplished for all samples, at the exception of the four last samples exhibiting $\Sigma\, Fe_{T_d} > 1$ or $\Sigma\, Fe_{T_d} < 0.90$. These samples exhibit the highest Cr content in their stoichiometry.

*Table 5.4: Iron cationic distribution and inversion parameter obtained from the iron L_3 edge XMCD fits, at T =300 K. (E) indicates ESRF experiments. * indicates a $Ni_{T_d}^{2+}$ contribution.*

Sample($Fe_\alpha Ni_\beta Cr_\gamma O_4$)	Cationic distribution $(T_d)[O_h]_2O_4$	δ
$Fe_{2.22}Ni_{0.78}O_4$	$(Fe_{0.95}^{3+})[Fe_{0.63}^{3+}Fe_{0.63}^{2+}Ni_{0.78}^{2+}]O_4$	1.00
$Fe_{2.82}Ni_{0.18}O_4$	$(Fe_{0.94}^{3+})[Fe_{0.85}^{3+}Fe_{1.03}^{2+}Ni_{0.18}^{2+}]O_4$	1.00
$Fe_{2.64}Ni_{0.36}O_4$ (E)	$(Fe_{0.99}^{3+})[Fe_{0.92}^{3+}Fe_{0.73}^{2+}Ni_{0.36}^{2+}]O_4$	1.00
$Fe_{2.85}Ni_{0.15}O_4$ (E)	$(Fe_{0.96}^{3+})[Fe_{0.97}^{3+}Fe_{0.97}^{2+}Ni_{0.15}^{2+}]O_4$	1.00
$Fe_{2.43}Ni_{0.21}Cr_{0.36}O_4$	$(Fe_{0.98}^{3+})[Fe_{0.47}^{3+}Fe_{0.98}^{2+}Ni_{0.21}^{2+}Cr_{0.36}^{3+}]O_4$	1.00
$Fe_{2.43}Ni_{0.21}Cr_{0.36}O_4$ (E)	$(Fe_{0.99}^{3+})[Fe_{0.57}^{3+}Fe_{0.86}^{2+}Ni_{0.21}^{2+}Cr_{0.36}^{3+}]O_4$	1.00
$Fe_{1.71}Ni_{0.57}Cr_{0.72}O_4$	$(Fe_{0.89}^{3+}Fe_{0.27}^{2+})[Fe_{0.20}^{3+}Fe_{0.35}^{2+}Ni_{0.57}^{2+}Cr_{0.72}^{3+}]O_4$	0.77
$Fe_{1.44}Ni_{0.45}Cr_{1.11}O_4$	$(Fe_{0.70}^{3+}Fe_{0.25}^{2+})[Fe_{0.21}^{3+}Fe_{0.28}^{2+}Ni_{0.45}^{2+}Cr_{1.11}^{3+}]O_4$	0.73
$Fe_{1.50}Ni_{0.90}Cr_{0.60}O_4$	$(Fe_{0.74}^{3+}Fe_{0.24}^{2+})[Fe_{0.11}^{3+}Fe_{0.40}^{2+}Ni_{0.90}^{2+}Cr_{0.60}^{3+}]O_4$	0.75
$Fe_{1.53}Ni_{1.02}Cr_{0.45}O_4$	$(Fe_{0.78}^{3+}Fe_{0.23}^{2+})[Fe_{0.13}^{3+}Fe_{0.39}^{2+}Ni_{1.02}^{2+}Cr_{0.45}^{3+}]O_4$	0.77
$Fe_{1.80}Ni_{0.69}Cr_{0.51}O_4$	$(Fe_{0.93}^{3+})[Fe_{0.14}^{3+}Fe_{0.74}^{2+}Ni_{0.69}^{2+}Cr_{0.51}^{3+}]O_4$	1.00
$Fe_{2.07}Ni_{0.39}Cr_{0.54}O_4$	$(Fe_{1.0}^{3+})[Fe_{0.19}^{3+}Fe_{0.88}^{2+}Ni_{0.39}^{2+}Cr_{0.54}^{3+}]O_4$	1.00
$Fe_{2.22}Ni_{0.42}Cr_{0.36}O_4$ (E)	$(Fe_{0.98}^{3+})[Fe_{0.46}^{3+}Fe_{0.78}^{2+}Ni_{0.42}^{2+}Cr_{0.36}^{3+}]O_4$	1.00
$Fe_{2.25}Ni_{0.21}Cr_{0.54}O_4$ (E)	$(Fe_{0.98}^{3+})[Fe_{0.38}^{3+}Fe_{0.89}^{2+}Ni_{0.21}^{2+}Cr_{0.54}^{3+}]O_4$	1.00
$Fe_{0.96}Ni_{0.93}Cr_{1.11}O_4$ (E)	$*(Fe_{0.64}^{3+}Fe_{0.32}^{2+}Ni_{0.85}^{2+})[Ni_{0.08}^{2+}Cr_{1.11}^{3+}]O_4$	0.67
$Fe_{1.86}Ni_{0.15}Cr_{0.99}O_4$	$(Fe_{0.58}^{3+}Fe_{0.77}^{2+})[Fe_{0.20}^{3+}Fe_{0.31}^{2+}Ni_{0.14}^{2+}Cr_{1.01}^{3+}]O_4$	0.43
$Fe_{1.62}Ni_{0.33}Cr_{1.05}O_4$	$(Fe_{0.48}^{3+}Fe_{0.74}^{2+})[Fe_{0.17}^{3+}Fe_{0.23}^{2+}Ni_{0.33}^{2+}Cr_{1.07}^{3+}]O_4$	0.39
$Fe_{1.44}Ni_{0.27}Cr_{1.29}O_4$	$(Fe_{0.63}^{3+}Fe_{0.42}^{2+})[Fe_{0.38}^{2+}Ni_{0.27}^{2+}Cr_{1.29}^{3+}]O_4$	0.60
$Fe_{1.20}Ni_{0.24}Cr_{1.56}O_4$	$*(Fe_{0.52}^{3+}Fe_{0.37}^{2+}Ni_{0.19}^{2+})[Fe_{0.32}^{2+}Ni_{0.05}^{2+}Cr_{1.56}^{3+}]O_4$	0.58

In certain samples, some peaks are absent, indicating the absence of one of the cationic species of iron. The cationic species most frequently absent is $Fe_{T_d}^{2+}$. Indeed, this species is absent in all instances where α > 2 in the stoichiometry. In these cases, the T_d site is solely occupied by Fe^{3+} species. Three other samples deserve a peculiar attention ($Fe_{1.44}Ni_{0.30}Cr_{1.29}O_4$, $Fe_{1.20}Ni_{0.24}Cr_{1.56}O_4$, and

$Fe_{0.96}Ni_{0.93}Cr_{1.11}O_4$). Two of them exhibit the higher chromium content, while the other one approaches a 1:1:1 ratio. For the former, only a limited number of iron species exist in the III oxidation state. The remaining O_h sites are occupied by Fe^{2+}, while all Fe^{3+} are located on the T_d sites. For the latter, the composition of β+ γ is close to 2, inducing no O_h sites for iron species. Consequently, the iron species occupy only the T_d sites.

Figure 5.7 illustrates the occupancy (in absolute value) of each iron species in their respective site. In the lower right corner, Fe^{3+} occupies the T_d site exclusively. This is consistent given that no contribution of $Fe_{T_d}^{2+}$ is discernible in this part. By moving upward and leftward in the diagram, the occupancy of the T_d site by Fe^{3+} decreases with the increasing presence of Fe^{2+} within the structure. Thus, despite the increasing representation of $Fe_{T_d}^{3+}$ among the iron species, the occupancy of Fe^{3+} in T_d site tends to decrease. In particular, moving leftward in the diagram indicates an increase in Cr^{3+} concentration, which results in significantly decreasing the Fe^{3+} contribution.

The remaining iron species (Fe^{2+} and Fe^{3+} at O_h sites) are predominantly located in the bottom right corner. The doping of Fe_3O_4 with nickel and chromium species results in the progressive abandonment of the O_h sites by iron species, which is manifested by a decreasing occupancy, moving upward and leftward. The $Fe_{O_h}^{3+}$ species is almost entirely absent at the β = 1 blue line, in contrast to the $Fe_{O_h}^{2+}$, which remains present in a low occupancy proportion (0 to 0.40). Given that the nickel species is 2+ charged, this is an unusual occurrence. This discrepancy can be partially explained by the non-zero contribution of $Fe_{T_d}^{3+}$ in the peak of $Fe_{O_h}^{3+}$, leading to an underestimation of $Fe_{O_h}^{3+}$.

The total occupancy exhibited by the two samples having $Ni_{T_d}^{2+}$ contribution is presented in Table 5.5. In the case of the $Fe_{0.96}Ni_{0.93}Cr_{1.11}O_4$ sample, the occupancy of the T_d site is significantly higher than 1, which question the pertinence of the methodology for this sample. The second sample ($Fe_{1.20}Ni_{0.24}Cr_{1.56}O_4$) exhibit a total T_d occupancy of 1.08. Consequently, the presence of $Ni_{T_d}^{2+}$ is more plausible than in the other sample.

Table 5.5: Total occupancy of the two samples exhibiting $Ni_{T_d}^{2+}$.

Sample($Fe_\alpha Ni_\beta Cr_\gamma O_4$)	T_d Occupancy			O_h Occupancy			
	$Fe_{T_d}^{3+}$	$Fe_{T_d}^{2+}$	$Ni_{T_d}^{2+}$	$Fe_{O_h}^{3+}$	$Fe_{O_h}^{2+}$	$Ni_{O_h}^{2+}$	$Cr_{O_h}^{3+}$
$Fe_{0.96}Ni_{0.93}Cr_{1.11}O_4$ (E)	0.64	0.32	0.85	0.0	0.0	0.08	1.11
$Fe_{1.20}Ni_{0.24}Cr_{1.56}O_4$	0.52	0.37	0.19	0.0	0.32	0.05	1.56

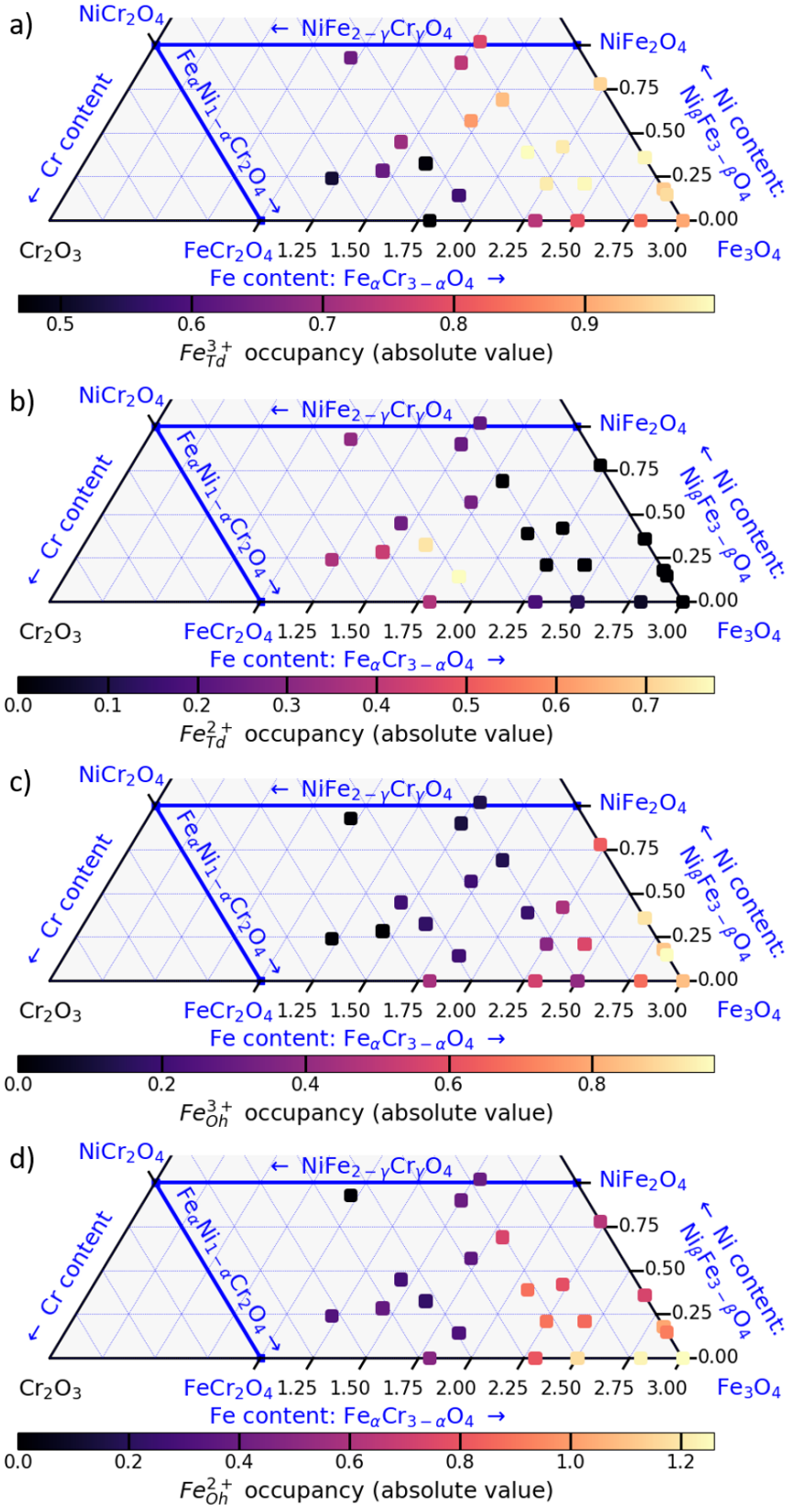

Figure 5.7: Quaternary plot of the occupancy (in absolute value) of all iron species. The results concerning $Fe^{3+}_{T_d}$, $Fe^{2+}_{T_d}$, $Fe^{3+}_{O_h}$, and $Fe^{2+}_{O_h}$ are illustrated in a), b), c) and d), respectively.

5.1.7 Trends in specific series

It is possible to draw some tendencies from these results. In the $Ni_{\beta}Fe_{3-\beta}O_4$ series, the $Fe_{T_d}^{3+}$ remains constant at 1 and $Fe_{T_d}^{2+}$ at 0. The two other contributions decrease with β increasing.

In the $Ni_{\beta}Fe_{2.50-\beta}Cr_{0.50}O_4$ series, the $Fe_{T_d}^{3+}$, $Fe_{T_d}^{2+}$, $Fe_{O_h}^{3+}$ and $Fe_{O_h}^{2+}$ contributions starts at 0.85, 0.05 0.40 and 1 respectively. The $Fe_{T_d}^{2+}$ remains near 0, before increasing to 0.25 at β = 1.0. The $Fe_{T_d}^{2+}$ increase until β = 0.50, before decreasing to 0.8 at β =1.0. The $Fe_{O_h}^{2+}$ contribution decreases from 1 to 0.40, while the $Fe_{O_h}^{3+}$ decreases from 0.40 to 0.20 until β = 0.50, and remains constant at 0.20 with the increase of β to 1.

In the $Fe_{3-\gamma}Cr_{\gamma}O_4$ series, the $Fe_{T_d}^{3+}$, $Fe_{T_d}^{2+}$, $Fe_{O_h}^{3+}$ and $Fe_{O_h}^{2+}$ starts respectively at 1, 0, 0.8 and 1.2 at γ = 0. The $Fe_{T_d}^{2+}$ increases gradually, while $Fe_{T_d}^{3+}$ and $Fe_{O_h}^{2+}$ decreases gradually. The $Fe_{O_h}^{3+}$ decreases until γ = 0.50 (α = 2.50) and increases between γ = 0.50 and γ = 0.75 (α = 2.25). It ends by a decreases after γ = 0.75.

5.1.8 Theoretical model for species distribution

The inversion parameter δ can be derived from the cationic distribution, with the help of a theoretical model for species distribution. The inversion parameter δ is defined as the total occupancy of O_h sites by cations in valence state II (Ni^{2+} or Fe^{2+}).

The following theoretical model is derived from the observation that chromium cations are only in O_h sites at valence state III (thus, $Cr_{O_h}^{3+}$ = γ), while nickel cations can be on both sites, at valence state II (thus, $Ni_{T_d}^{2+} + Ni_{O_h}^{2+}$ = β). The model equations are written in the following:

$$\begin{gathered}\sum Cations^{2+} = Fe_{T_d}^{2+} + Fe_{O_h}^{2+} + Ni_{T_d}^{2+} + Ni_{O_h}^{2+} = 1 \\ \sum Cations^{3+} = Fe_{T_d}^{3+} + Fe_{O_h}^{3+} + Cr_{O_h}^{3+} = 2 \\ \sum Site_{Oh} = Fe_{O_h}^{2+} + Fe_{O_h}^{3+} + Ni_{O_h}^{2+} + Cr_{O_h}^{3+} = 2 \\ \sum Site_{Td} = Fe_{T_d}^{2+} + Fe_{T_d}^{3+} + Ni_{T_d}^{2+} = 1 \\ \alpha + \beta + \gamma = 3\end{gathered} \tag{5.5}$$

Given four independent equations and six unknowns, it is straightforward that two parameters are required to fully describe the solution. The parameters selected to express the remaining variables are $Fe_{T_d}^{2+}$ and $Ni_{T_d}^{2+}$, as their values are most of the time zero. The resulting model are presented in the following:

$$\begin{aligned} Fe_{T_d}^{3+} &= 1 - Fe_{T_d}^{2+} - Ni_{T_d}^{2+} \\ Fe_{O_h}^{3+} &= 1 - \gamma + Fe_{T_d}^{2+} + Ni_{T_d}^{2+} \\ Fe_{O_h}^{2+} &= 1 - \beta - Fe_{T_d}^{2+} \\ Ni_{O_h}^{2+} &= \beta - Ni_{T_d}^{2+} \end{aligned} \tag{5.6}$$

The δ definition is given by $\delta = Fe_{O_h}^{2+} + Ni_{O_h}^{2+}$. The variables can be expressed as a function of δ and $Ni_{T_d}^{2+}$. The outcomes are presented in the following:

$$\begin{aligned} Fe_{T_d}^{3+} &= \delta \\ Fe_{T_d}^{2+} &= 1 - \delta - Ni_{T_d}^{2+} \\ Fe_{O_h}^{3+} &= 2 - \gamma - \delta \\ Fe_{O_h}^{2+} &= \delta - \beta + Ni_{T_d}^{2+} \\ Ni_{O_h}^{2+} &= \beta - Ni_{T_d}^{2+} \end{aligned} \tag{5.7}$$

The inversion parameter is therefore equal to the value of $Fe_{T_d}^{3+}$ occupancy.

This model can be utilized as a guideline for the XMCD fit, as the quantity of nickel and chromium is known. However, given that the system cannot be solved without one or two additional constraints, it cannot be employed as a definitive standard. It is worth mentioning that constraints can be introduced in the fitting process in order to ensure that the linear coefficients of each contribution follow the model developed. The fitting result is illustrated in Figure 5.8. The two primary discrepancies originate from the O_h contributions, with the $Fe_{O_h}^{2+}$ contribution being underestimated and the $Fe_{O_h}^{3+}$ contribution being overestimated. This "constrained" fit process can be used as a tool to study more accurately the crystal field around iron species, by the introduction of other geometries, such as C_{3v}. However, in regards to the discrepancies with the experimental curve, this approach has not been pushed forward.

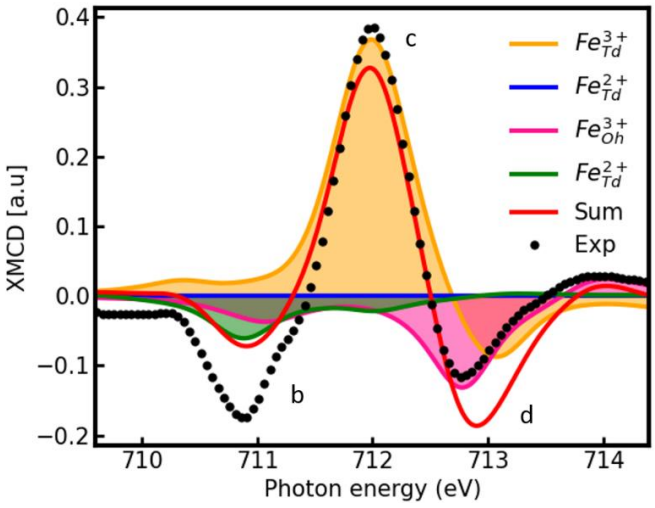

Figure 5.8: Fitted XMCD iron L_3 edge spectra at T = 300 K with constraints. The sample has $Fe_{1.80}Ni_{0.69}Cr_{0.51}O_4$ stoichiometry.

In the light of this model, the inversion parameter δ corresponds to the occupancy of $Fe_{T_d}^{3+}$ (see equation (5.7)). Given that some samples have sums of Fe_{Td} species in excess to one, the definition of δ that has been adopted is as follows:

$$\delta = \frac{Fe_{T_d}^{3+}}{\sum Fe_{Td}} \qquad (5.8)$$

In order to normalize and therefore obtain inversion parameter values of one when only $Fe_{T_d}^{3+}$ is observed, $Fe_{T_d}^{3+}$ is divided by $\sum Fe_{Td}$ in equation (5.8). The aforementioned definition of δ is presented on a quaternary diagram in Figure 5.9. The two samples with $\sum Fe_{Td}$ > 1.2 have the lowest inversion parameter. In the lower right corner, all the samples exhibit an inverse spinel structure, with the exception of the right of the bottom line. The inverse spinel structure is defined by the exclusive occupation of T_d sites by III cations, inserting Ni or Cr in the stoichiometry results in a decreasing δ.

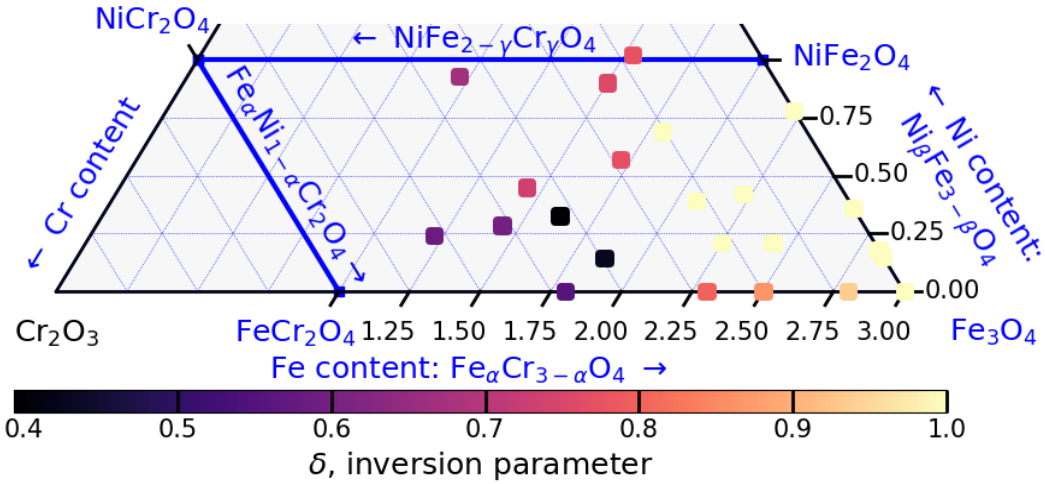

Figure 5.9: Quaternary plot of δ, the inversion parameter.

5.1.9 Low temperatures XMCD spectra

In the spinel oxides studied, different magnetic and/or structural transitions may occur. For example in Fe_3O_4, a structural transition associated with the inhibition of electron hopping between II and III cations located in O_h sites is present: the Verwey transition, which occurs around T = 120 K[9]. In $FeCr_2O_4$, the magnetic transition and its Curie temperature (T_c) is located approximatively at 80 K. Therefore, in order to investigate these magnetic and/or structural transitions, XAS and XMCD spectra were also recorded at low temperatures.

5.1.9.1 Chromium $L_{2,3}$ edges

Figure 5.10 depicts the normalized XMCD spectra at the Cr $L_{2,3}$ edges for room temperature (300 K, red curve) and low temperature (4 K or 107 K, blue curve). In the first row of spectra, a significant reduction in the intensity of the c peak of the L_3 edge is observed in all the spectra at low temperature. The overall curve shape stays similar to an unique contribution of $Cr_{O_h}^{3+}$. Two of the three samples that were not in accordance with the $Cr_{O_h}^{3+}$ model (see Figure 5.3 (b)) have been studied at low temperatures. They are presented in the second row of graphs. The resulting XMCD spectra exhibit a curve shape more similar to a $Cr_{O_h}^{3+}$ contribution than was observed at T = 300 K. This confirms the hypothesis that $Cr_{O_h}^{3+}$ is the unique species of chromium present in these samples.

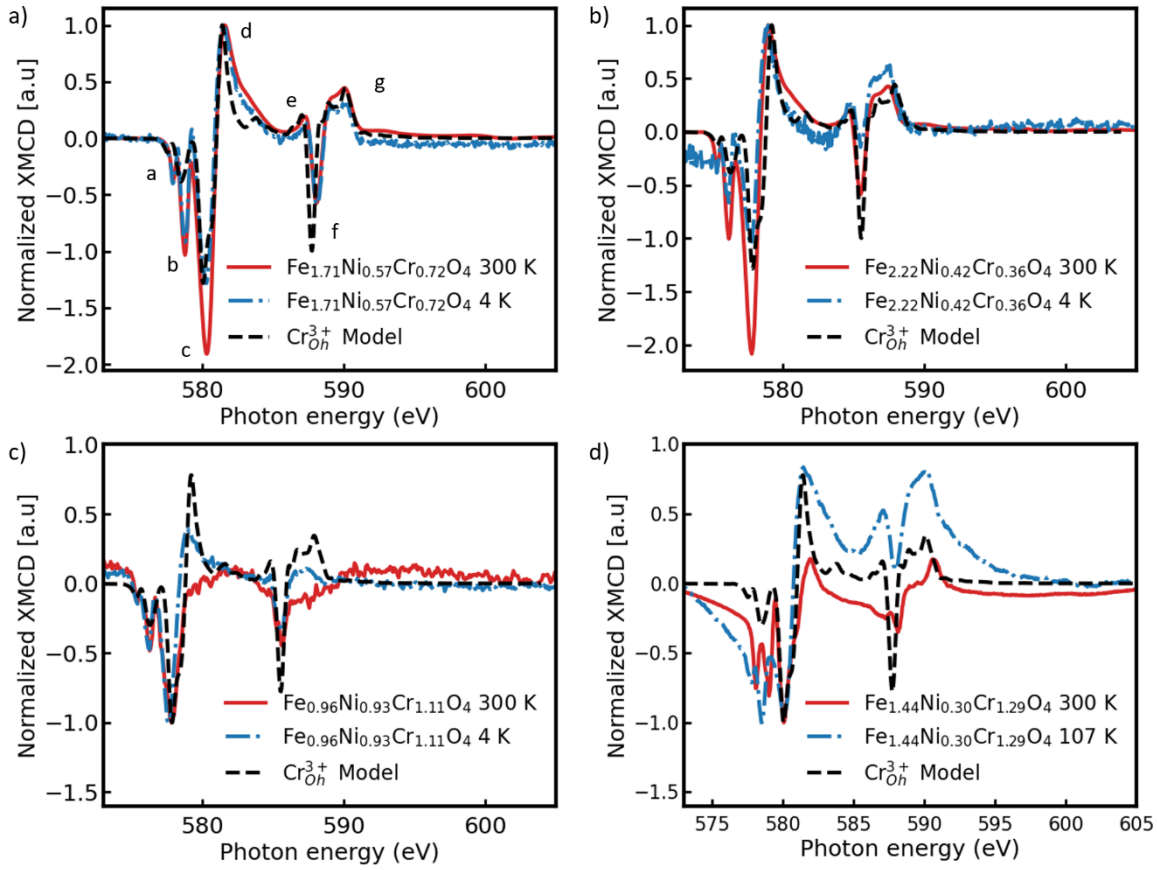

Figure 5.10: Comparison of normalized Cr $L_{2,3}$ edges XMCD spectra at T = 300 K and low temperatures (T = 4 K or 107 K). The normalization is done by the maximum for (a) and (b), and by the minimum for (c) and (d).

5.1.9.2 Nickel $L_{2,3}$ edges

Figure 5.11 presents the normalized Ni $L_{2,3}$ edges XMCD spectra for two selected samples at room temperature (300 K) and low temperature (4 K) . On Figure 5.11 (a), the XMCD spectra at both temperature exhibit a similar shape, in good agreement with the $Ni_{O_h}^{2+}$ model spectrum.

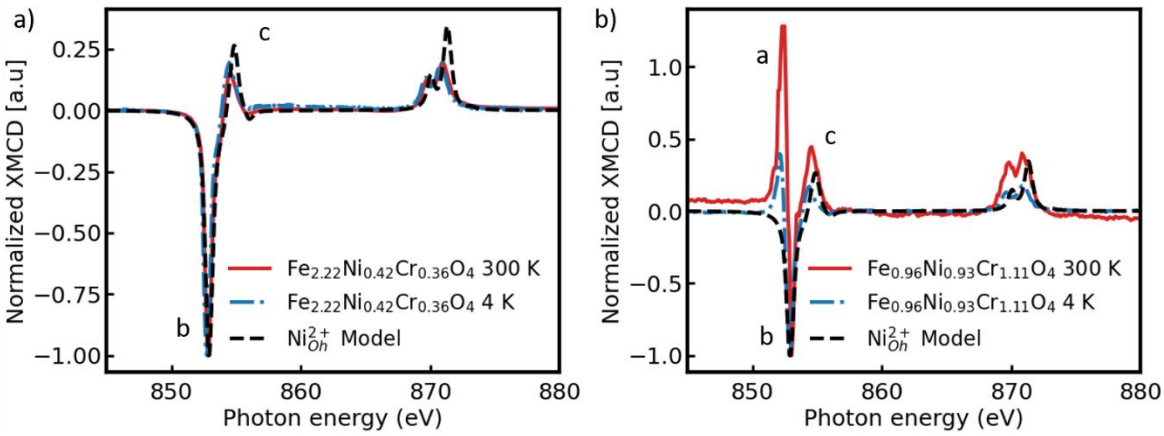

Figure 5.11: Comparison of normalized XMCD spectra at 300 K and low temperatures at the Ni $L_{2,3}$ edges.

One of the two samples depicted in Figure 5.4 (b), exhibiting the presence of the $Ni_{T_d}^{2+}$ peak (a), is shown on Figure 5.11 (b). It displays an XMCD spectra at T = 4 K that exhibits a tendency towards $Ni_{O_h}^{2+}$ with the decrease of the peak a. This lends further support to the hypothesis that the anomalous signal observed at 300 K was associated with weak magnetic properties at that temperature, rather than a substantial contribution from $Ni_{T_d}^{2+}$. Unfortunately, the second sample exhibiting potential $Ni_{T_d}^{2+}$ contribution ($Fe_{1.20}Ni_{0.24}Cr_{1.56}O_4$) has not been studied at low temperatures. The occupancies extracted from nickel L_3 edge XMCD fits at low temperatures are presented in Table 5.6. This variation is in the error bar (around 0.10). The cationic distribution has been reported to vary with temperature due to thermal diffusion[1-2]. These observations are seen at high temperatures, at the opposite of our experiments.

Table 5.6: Occupancies extracted from the nickel L_3 edge XMCD fits, at T = 300 K and 4K.

Sample ($Fe_{0.96}Ni_{0.93}Cr_{1.11}O_4$)	$Ni_{T_d}^{2+}$	$Ni_{O_h}^{2+}$
300 K (E)	0.85	0.08
4 K (E)	0.78	0.16

5.1.9.3 Iron $L_{2,3}$ edges

Figure 5.12 illustrates the normalized XMCD at the Fe $L_{2,3}$ edges spectra at room temperature and low temperatures. Some samples exhibit identical normalized XMCD spectra between 300 K and low temperatures. These samples are not shown here. The three first spectra shown on Figure 5.12 exhibit a significant increase in the two peaks corresponding to the Fe species in O_h sites (peaks b and d). The sample displays in the (d) subfigure has a 1:1:1 ratio stoichiometry. In comparison to the signal at 300 K, which is limited to the iron peaks in T_d sites (peaks upwards), the XMCD signal becomes more refined, and the contributions of the other Fe species become apparent. The discrepancy between the signals at 300 K and 4 K can be attributed to the relatively weak magnetic signal resulting from this sample. As the temperature decreases, the saturation magnetization increases, resulting in a higher XMCD signal.

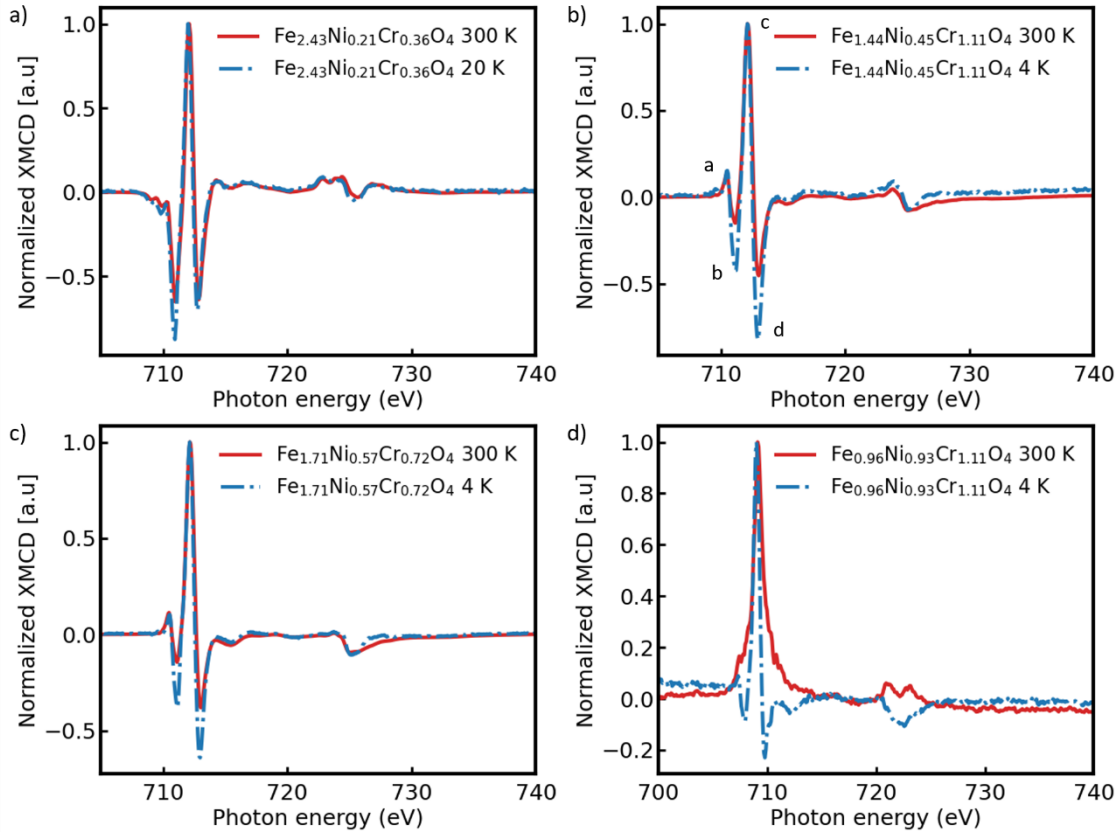

Figure 5.12 Comparison of normalized Fe $L_{2,3}$ edges XMCD spectra at 300 K and low temperature (T = 4 K or 20 K).

The occupancies extracted from iron L_3 edge XMCD fits at low temperatures are presented in Table 5.7.

– The samples with minor changes in the shape of the spectra are the $Fe_{2.43}Ni_{0.21}Cr_{0.36}O_4$ (Figure 5.12 (a)), $Fe_{2.22}Ni_{0.42}Cr_{0.36}O_4$, and $Fe_{2.25}Ni_{0.21}Cr_{0.54}O_4$

samples (with α > 2). The percentages of $Fe_{T_d}^{3+}$ exhibit no modification (peak c), while the two remaining species (b and d peaks) exhibit variation around 5 %, which is the uncertainty of the measurement.

- The two samples, $Fe_{1.44}Ni_{0.45}Cr_{1.11}O_4$ and $Fe_{1.71}Ni_{0.57}Cr_{0.72}O_4$ (Figure 5.12 (b) and (c), respectively), show important decrease in the percentage of $Fe_{T_d}^{3+}$ (c peak), linked to the presence of $Fe_{O_h}^{2+}$ and $Fe_{O_h}^{3+}$ (b and d peaks) in a nearly identical proportion, which is reflected in the inversion parameter (-0.1 compared to the room temperature).
- The 1:1:1 stoichiometry sample displays an overall percentage of $Fe_{T_d}^{3+}$ (c peak) that remains identical between the two temperatures, but the $Fe_{T_d}^{2+}$ (a peak) contribution has nearly disappeared. The two remaining contributions appear (b and d peaks). The Σ Fe_{T_d} exhibit a significant decrease (of 0.3), but with the diminution of the overall $Fe_{T_d}^{2+}$ (a peak), the inversion parameter increases from 0.67 at 300 K to nearly 1 at 4 K.
- The $Fe_{1.44}Ni_{0.27}Cr_{1.29}O_4$ sample is the only sample exhibiting a marked increase in the percentage of $Fe_{T_d}^{3+}$ (c peak). The 5 % increase principally came from the $Fe_{T_d}^{2+}$ (a peak), and a small contribution of $Fe_{O_h}^{3+}$ (d peak) is observed at 107 K, which was not present at 300 K. The increase in the $Fe_{T_d}^{3+}$ contribution and the decrease in $Fe_{T_d}^{2+}$ results in an increase of the inversion parameter.

Table 5.7: Occupancies extracted from the iron L_3 edge XMCD fits, at low temperatures.

Sample ($Fe_\alpha Ni_\beta Cr_\gamma O_4$)	Tp (K)	$Fe_{T_d}^{3+}$	$Fe_{T_d}^{2+}$	$Fe_{O_h}^{3+}$	$Fe_{O_h}^{2+}$	δ
$Fe_{2.43}Ni_{0.21}Cr_{0.36}O_4$	300	0.98	0.00	0.47	0.98	1.00
	300 (E)	0.99	0.00	0.57	0.86	1.00
	20 (E)	0.93	0.00	0.47	1.04	1.00
$Fe_{2.22}Ni_{0.42}Cr_{0.36}O_4$	300 (E)	0.98	0.00	0.46	0.78	1.00
	4 (E)	0.96	0.00	0.51	0.74	1.00
$Fe_{2.25}Ni_{0.21}Cr_{0.54}O_4$	300 (E)	0.98	0.00	0.38	0.89	1.00
	4 (E)	1.00	0.00	0.30	0.95	1.00
$Fe_{1.71}Ni_{0.57}Cr_{0.72}O_4$	300	0.87	0.24	0.25	0.35	0.78
	4	0.65	0.29	0.34	0.43	0.69
$Fe_{1.44}Ni_{0.45}Cr_{1.11}O_4$	300	0.70	0.25	0.21	0.28	0.73
	4	0.48	0.28	0.32	0.36	0.63
$Fe_{0.96}Ni_{0.93}Cr_{1.11}O_4$	300 (E)	0.64	0.32	0.00	0.00	0.67
	4 (E)	0.65	0.01	0.07	0.22	0.98
$Fe_{1.44}Ni_{0.27}Cr_{1.29}O_4$	300	0.63	0.43	0.00	0.38	0.60
	107	0.70	0.35	0.05	0.33	0.67

5.1.10 XMCD Hysteresis loops

By varying the magnetic field at a fixed energy position, it is possible to record the magnetic hysteresis loop for each species. The hysteresis curves recorded in grazing incidence at 4 K by using the fluorescence yield (TFY) are presented in Figure 5.13.

The introduction of chromium induces a notable reduction in magnitude of the hysteresis loops, especially for the loops at the Ni L_3 edge. The $Fe_{T_d}^{3+}$ hysteresis is inverted compared to the $Cr_{O_h}^{3+}$ hysteresis. This is due to the ferrimagnetism of spinel, wherein the T_d cations are aligned antiferromagnetically with the O_h cations. A surprising behavior is the reversal of the $Ni_{O_h}^{2+}$ hysteresis loop. The green and blue curves exhibits the same directionality than the $Fe_{T_d}^{3+}$ curve, while the orange is at the opposite. This reversal is an artefact. In electron yield (TEY), the Ni hysteresis exhibits the same directionality as the Cr cations, for all samples. The TEY is not displayed here, due to additionnal measure artefacts, which renders the treatment of TCY data more difficult than that of TFY data.

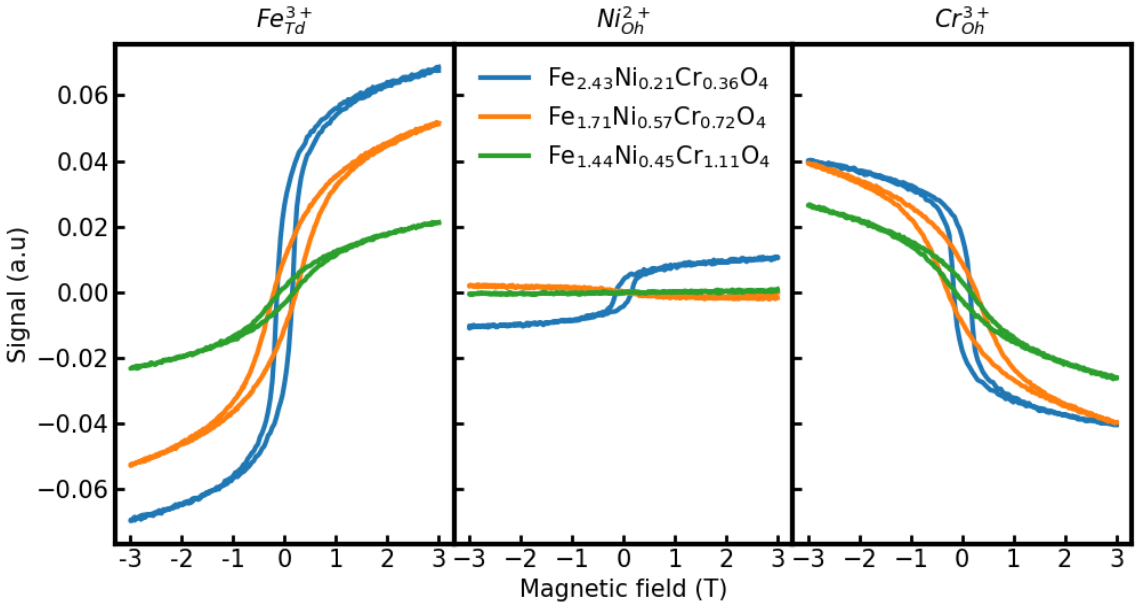

Figure 5.13 Magnetic XMCD hysteresis loops of different samples for each species at T = 300 K.

These XMCD magnetic hysteresis loops can be discussed in relation with the macroscopic VSM magnetic loops shown in the chapter 4. In fact, The VSM curves show the magnetic response of the entire sample, whereas a XMCD hysteresis loop is chemically selective and probes preferentially the magnetic order for one species. The M_S and M_R can not be quantified with XMCD, as the signal is a difference of two spectra.

Table 5.8: Coercive fields (H_C) at 300 K, in kA.m^{-1}, extracted from the XMCD hysteresis loops.

Sample	$Fe_{T_d}^{3+}$	$Ni_{O_h}^{2+}$	$Cr_{O_h}^{3+}$	VSM
$Fe_{2.43}Ni_{0.21}Cr_{0.36}O_4$	119	115	127	8
$Fe_{1.71}Ni_{0.57}Cr_{0.72}O_4$	163	119	223	
$Fe_{1.44}Ni_{0.45}Cr_{1.11}O_4$	95	24	103	4

The H_C parameter extracted from these hysteresis loops are shown in Table 5.8. The measured H_C by VSM magnetometry is two orders of magnitude lower than the value measured by XMCD. The VSM measurement probe the overall magnetic behavior while the XMCD probes the magnetic order for each species, which can explain the differences observed.

5.2 RESONANT X-RAY DIFFRACTION FINE STRUCTURE INVESTIGATION

The following sections will discuss the challenges for probing the cationic site distribution by RXD measurements and the procedures developed for the treatment of the data. Then, simulations will help in the comprehension of the data analysis. Finally, the cationic ordering in the different sites (T_d and O_h) will be discussed as a function of the composition of the spinel oxide layers.

5.2.1 Exploitation of RXD to obtain the fine structure

The theoretical basis for RXD has been developed in chapter 3. This section will explain how to obtain fine structure information from the RXD experiments.

The intensity of a X-ray diffraction experiment is proportional to the square of $|F_{hkl}|$. F_{hkl} is the structure factor of the (h k l) plane defined by:

$$F_{hkl} = \sum_i f_i(E) * \exp\left(-j2\pi(hx_i + ky_i + lz_i)\right) \quad (5.9)$$

$$with\ f_i(\boldsymbol{Q}, E) = f_{i,0}(\boldsymbol{Q}) + f_i'(E) + jf_i''(E) \quad (5.10)$$

The atomic scattering factors is decomposed in three contributions. The first term is independent of energy (but dependent on the wave vector transfer **Q**), and the second and third terms, respectively, denote the real part and imaginary parts of the anomalous factor of the atom. f_i''(E) is proportional to the X-ray absorption cross section σ_i (E), and f_i'(E) and f_i''(E) are mutually related by their Kramers-Kronig relation. It is also recalled that F_{hkl} definition induces that in the spinel structure, peaks such as (622) or (222) are sensitive only to the O_h cations, while peaks such as (202) or (602) are sensitive only to the T_d cations. By combining (5.9) and (5.10), the diffracted peak intensity is proportional to:

$$\begin{aligned} |F|^2 = (A^2 + B^2) + 2(A\alpha + B\beta)f'(E) + \\ 2(B\alpha - A\beta)f"(E) + (\alpha^2 + \beta^2)(f'(E)^2 + f"(E)^2) \end{aligned} \quad (5.11)$$

$$with: \quad A = \sum_i f_{0,i} cos\ (2\pi(hx_i + ky_i + lz_i)$$

$$B = \sum_i f_{0,i} sin\ (2\pi(hx_i + ky_i + lz_i)$$

$$\alpha = \sum_i cos\ (2\pi(hx_i + ky_i + lz_i)$$

$$\beta = \sum_i sin\ (2\pi(hx_i + ky_i + lz_i)$$

A and B represent, respectively, the real and imaginary parts of the structure factor in the absence of anomalous effects, and are energy independent. The terms α and β denotes the sums of cosines and sines of the anomalous effect. They are also energy independent. Therefore, the structure factor of the diffraction peaks can be separated into a real part, A, and an imaginary part, B: F = A + *j*B. To go further, the structure factor (in the case of the spinel space group) can be written as a sum of contributions coming from the T_d and O_h sites:

$$F_{hkl} = A_{O_h} + A_{T_d} + i\,(B_{O_h} + B_{T_d}) \tag{5.12}$$

$$with: \begin{cases} A_{O_h} = \sum_{O_h\ sites} f_{0,O_h} cos\ (2\pi(hx_i + ky_i + lz_i) \\ A_{T_d} = \sum_{T_d\ sites} f_{0,T_d} cos\ (2\pi(hx_i + ky_i + lz_i) \\ B_{O_h} = \sum_{O_h\ sites} f_{0,O_h} sin\ (2\pi(hx_i + ky_i + lz_i) \\ B_{T_d} = \sum_{T_d\ sites} f_{0,T_d} sin\ (2\pi(hx_i + ky_i + lz_i) \end{cases}$$

The terms A_{O_h}, A_{T_d}, B_{O_h} and B_{T_d} denote, respectively, the real part of the O_h contribution, the real part of the T_d contribution, the imaginary part of the O_h contribution and the imaginary part of the T_d contribution. For the sake of simplicity, the structure factor is not squared, and only the energy independent components f_0 are written.

By studying the variations of peaks containing a mix between O_h and T_d contributions and by tuning the X-ray energy to the desired elemental K edge, it is possible to obtain signals where the presence of the element (in both sites) will modulate the intensity and the form of the signal.

5.2.2 SiXS indexation of the reciprocal space and implications

In our experiments on the SiXS beamline, the sapphire substrate (space group 167) is used as reference in the reciprocal space. As shown before with RHEED patterns, the samples grow on the sapphire substrate with an angular rotation of 30°. The principal observation of the D1 (H00) and D2 (HH0) RHEED patterns is the transformation of the D1 streaks of the sapphire into D2 streaks for the spinel phase in hexagonal convention (space group $R\bar{3}m$, 166[10]). Conversely, the D2 streaks of the sapphire is transformed into D1 streaks for the spinel phase in hexagonal convention 166.

The RXD measurements are done with the following methodology. The energy is initially set at a value below a K edge (Ni or Fe). A rocking curve (RC or ω scan) is performed at this energy. Then, the energy is shifted through the edge and another RC scan is recorded. A total of 60 energy points are generated at each diffraction peak.

Table 5.9 summarized the peaks of the RXD experiment and the A and B calculated for these peaks. In addition, the equivalences in the three space groups are indicated. To calculate the resulting real and imaginary parts of each diffraction peak, the spinel cubic convention (space group 227) is used. The atomic scattering coefficient f_0 was set to one to simplify. Unfortunately, no peaks exhibiting solely the T_d contribution has been scanned, because of the complex epitaxial relationship between the substrate and the spinel phase. On the (440) diffraction peak, the ratio 2 O_h for 1 T_d sites is seen on the A contribution. Given that the RXD signal is proportional to the square of the structure factor, the (511) and (311) should give similar signals, while the (531) peak should display distinct shapes in function of the ratio between T_d and O_h sites.

Table 5.9 Peaks of the RXD experiment. The three lattice conventions are indicated.

Sapphire Space group 167 (SiXS setup)			Spinel Space group 166 (Hexagonal)			Spinel Space group 227 (Cubic)			Real part A (227)		Imaginary part B (227)	
H	K	L	H	K	L	H	K	L	O_h	T_d	O_h	T_d
2.78	0	0	2	2	0	4	4	0	3072	1536	0	0
2.78	0	5.56	2	2	6	6	2	2	0	0	3072	0
2.78	0	2.78	2	2	3	5	3	1	-1086	768	-1086	768
1.39	1.39	2.78	3	0	3	5	1	1	1086	768	-1086	-768
1.39	0	2.78	1	1	3	3	1	1	1086	768	1086	768

In the following section, the space group 227 convention will be maintained. This is particularly advantageous as the positioning of the O_h and T_d sites in the 227 space group gives rise to supplementary conditions in hkl (see equation (5.9)) where only one of the two contributions is visible (for example, (622) for O_h and (602) for T_d). These supplementary conditions are lost by passing to the subgroup 166.

A summary of the completed RXD experiment is shown in Table 5.10. Due to a lack of beam time, the last sample was less extensively examined than the two preceding samples, particularly at the iron K edge.

Table 5.10 Summary of the RXD experiments conducted.

Samples	Diffraction Peaks (227)			Ni K edge	Fe K edge
$Fe_{2.43}Ni_{0.21}Cr_{0.36}O_4$	4	4	0	Yes	Yes
	6	2	2	Yes	No
	5	3	1	Yes	Yes
	5	1	1	Yes	Yes
	3	1	1	Yes	Yes
$Fe_{1.71}Ni_{0.57}Cr_{0.72}O_4$	4	4	0	Yes	Yes
	6	2	2	Yes	No
	5	3	1	Yes	Yes
	5	1	1	Yes	Yes
	3	1	1	Yes	Yes
$Fe_{1.44}Ni_{0.45}Cr_{1.11}O_4$	4	4	0	Yes	Yes
	6	2	2	Yes	No
	5	3	1	Yes	No
	5	1	1	Yes	No
	3	1	1	Yes	Yes

5.2.3 Data analysis

A three-dimensional representation of the data is shown in Figure 5.14, for the sample with the stoichiometry $Fe_{1.71}Ni_{0.57}Cr_{0.72}O_4$ at the Ni K edge on the (622) peak. The surface plot represents the distinct RC scan at each energy. The x-axis, y-axis and z-axis represent, respectively, the omega angle, the energy of the scan and the X-ray signal. Three distinct graphs can be extracted from this representation. On the bottom side, a cartography (ω-E) is shown. On the right side, the different RC scan are presented, with different colors. A slight deviation to the left (*i.e.*, a weaker ω angle) is observed with the increasing energy. The data that will be analyzed in this section are the data presented on the left side of the graph. It presents the signal as a function of energy.

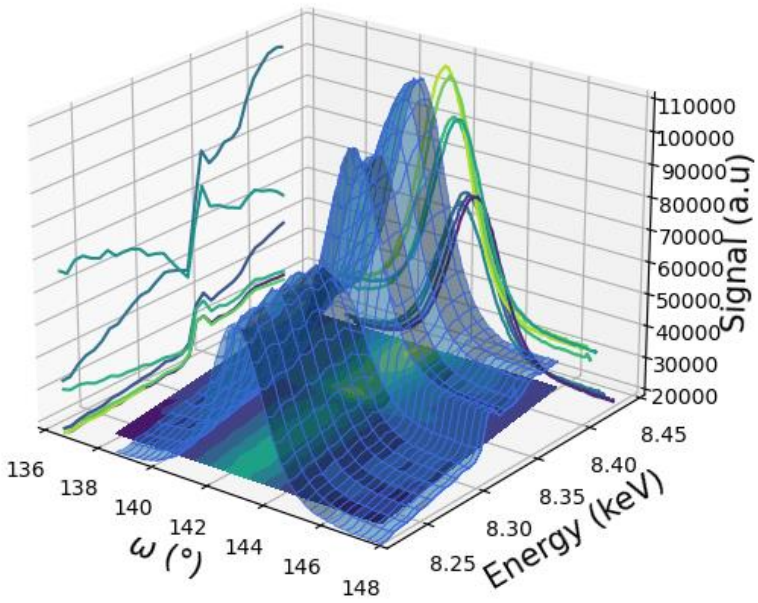

Figure 5.14: Three-dimensional representation of the (622) peak at the Ni K edge for the $Fe_{1.71}Ni_{0.57}Cr_{0.72}O_4$ sample.

Figure 5.15 shows the associated cartography (ω, E). The cartography is slightly in diagonal, as the ω angle definition varies with the energy as the energy is increasing. Two regions can be distinguished on the image: the center of the image where the signal is maximum and the sides of the image where the signal is minimum (background). However, an increase of the intensity is observed at approximately E = 8.327 keV: the K edge of nickel. This background exhibits the same curve shape as a XAS performed on the nickel K edge.

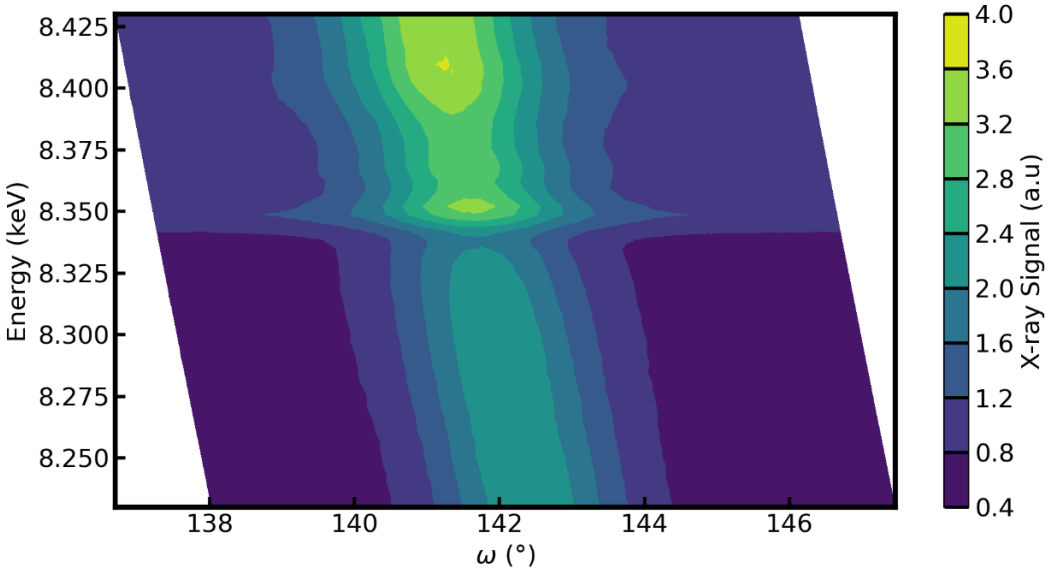

Figure 5.15: Cartography (ω, E) of a RXD experiment.

The principal challenge for the treatment of the RXD raw data arises from the variable background (bk) with energy. Indeed, the background exhibits a significant increase after the K edge. Figure 5.16 shows an example of the background removal. If the signal is directly extracted from the RC scans (blue curve), an important signal is observed, which resembles a XAS spectrum at the K edge. The background (green curve) looks also like a K edge XAS spectrum. It is removed in the curve displayed in orange. The orange signal is considerably weaker compared to the blue curve (raw data).

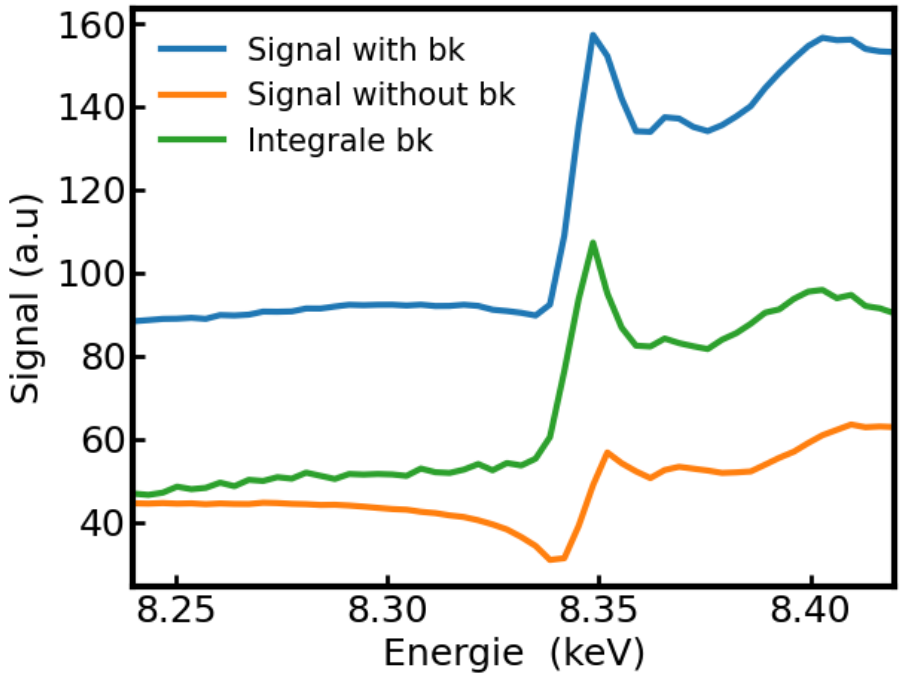

Figure 5.16: Example of background (bk) removal for data of Figure 5.14.

The methodology developed to treat the RXD raw data use the different RC curves. The resulting data is a Gaussian curve, above a certain quantity of background (see right side of Figure 5.14). In order to subtract the background, the mean of the first five points and the mean of the final five point are registered. These two means are employed to fit a linear curve. The integral of this linear fit is registered as the background, and the linear fit is subtracted from the raw data. Subsequently, the subtracted signal is fitted with a Gaussian curve and integrated in order to limit the noise. This integral is registered at the corresponding energy as the RXD signal. The next points are obtained following the same methodology. This method enables the registration of the background and the RXD signal in a simultaneous way.

5.2.4 Understanding parameters with FDMNES simulations

FDMNES accepts as input the crystalline structure with various parameters, including the lattice parameter, the cation site occupancy or the radius of the aggregates where the Schrödinger equation (SE) is solved.

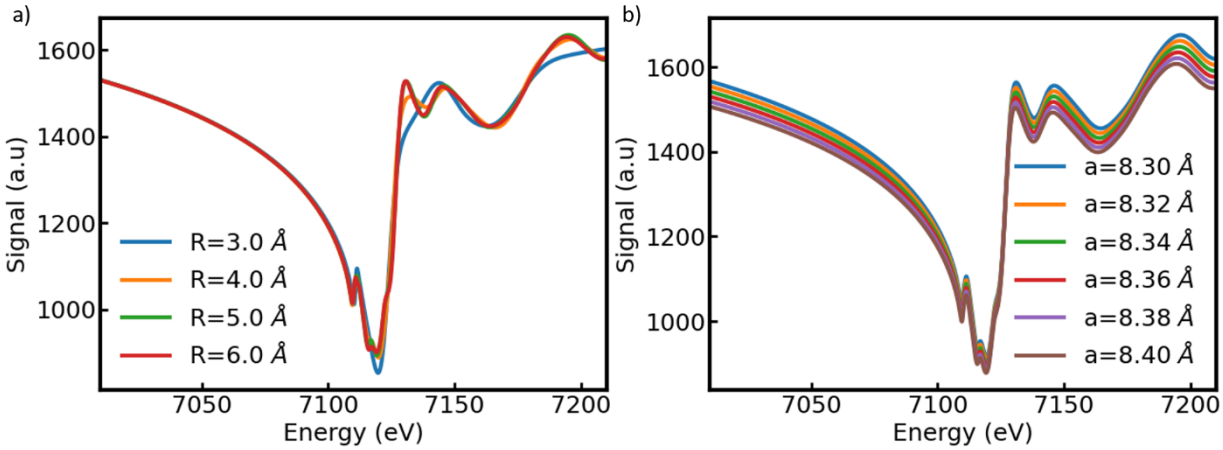

Figure 5.17: Simulated RXD signal as a function of the aggregate radius (a) and as a function of the in-plane lattice parameter (b). The aggregate radius is R = 5.0 Å for (b).

The aggregate radius (R) can be modified. Figure 5.17 (a) shows the evolution of the simulations for a magnetite sample (Fe_3O_4) at the iron K edge for the (311) diffraction peak as a function of this parameter. A small radius, e.g. R=3.0 Å (blue curve) induces an inappropriate description of the fine structure. This is particularly evident for the peak following the K edge. For a larger radius, the shape of the curves is better. Therefore the radius aggregate was chosen at the value of R= 5.0 Å.

Figure 5.17 (b) illustrates the simulated signals as a function of the in-plane lattice parameter. The data exhibit no significant changes. The only discernible effect is the slight reduction in the offset due to the increase of the lattice parameter. The post K edge is not significantly modified, and thus the in-plane lattice parameter will be set at a= 8.36 Å.

Figure 5.18 displays the last parameter which can be studied: the influence of the cationic site (T_d and O_h) on the XRD signal. Three simulations were done. The first one is a mix of iron in T_d and O_h sites (*e.g.* (Fe)[Fe_2]O_4, blue curve). The second is a structure with iron only in T_d sites (*e.g.* (Fe)[Cr_2]O_4, green curve). The third is a structure with iron only in O_h sites and chromium in T_d sites (*e.g.* (Cr)[Fe_2]O_4, orange curve).

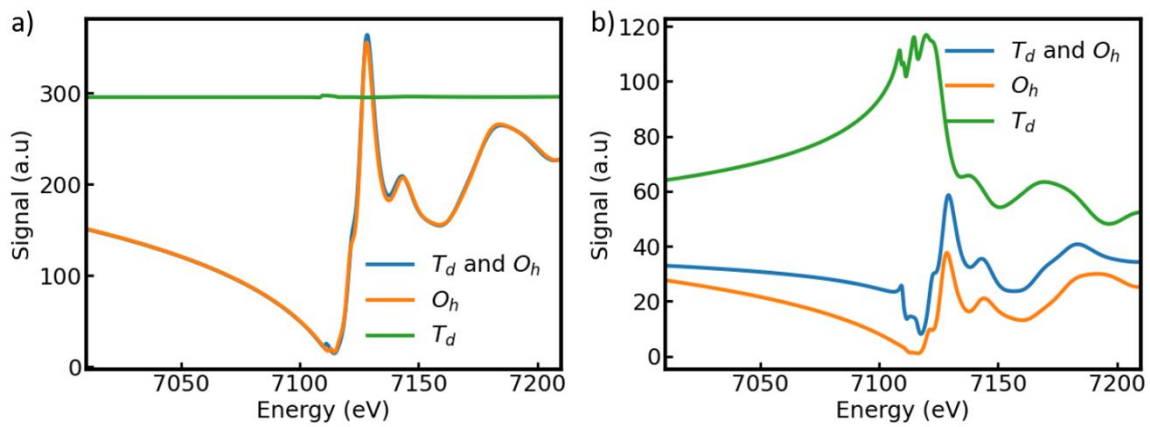

Figure 5.18: Simulated RXD signal at the iron K edge for the (622) peak (a) and the (531) peak (b) as a function of the cationic site of iron.

The (622) peak does not exhibit an absorption dip in the green curve, as the T_d contribution is zero for this peak. Concerning the (531) peak, the O_h signal shows an absorption dip, while the T_d contribution exhibits an absorption peak. The resulting signal of a sample containing iron on both sites appears as a mix between the two other curves.

5.2.5 Comparisons of RXD data with FDMNES simulations

The experimental RXD signals will be interpreted using the FDMNES simulations for the Ni and the Fe K edges for each sample.

5.2.5.1 Supplementary data treatment

The RXD signals for the five diffraction peaks analyzed for the Ni K edge are shown in Figure 5.19 (a). To facilitate the comparison with FDMNES simulations, firstly, a linear background is removed for all peaks. Secondly, the signal is divided by its minimum. Consequently, the absorption edge is set to a value of -1. The resulting normalized RXD signals are shown in Figure 5.19 (b).

Note that the three features in the fine structure outlined in Figure 5.19 (b) are found in all the RXD signals, at the exception of the 8354 eV peak in the (440) signal. The resulting RXD for the (531) peak is noisy, in contrast to the other peaks. This elevated noise level can be attributed to the little difference between the RC integration and the integration of the linear portion (background) of the RC. This phenomenon is shown in Figure 5.16. The pre-edge absorption peak at 8300 eV for the (311) peak is consistently identified as a measure artifact.

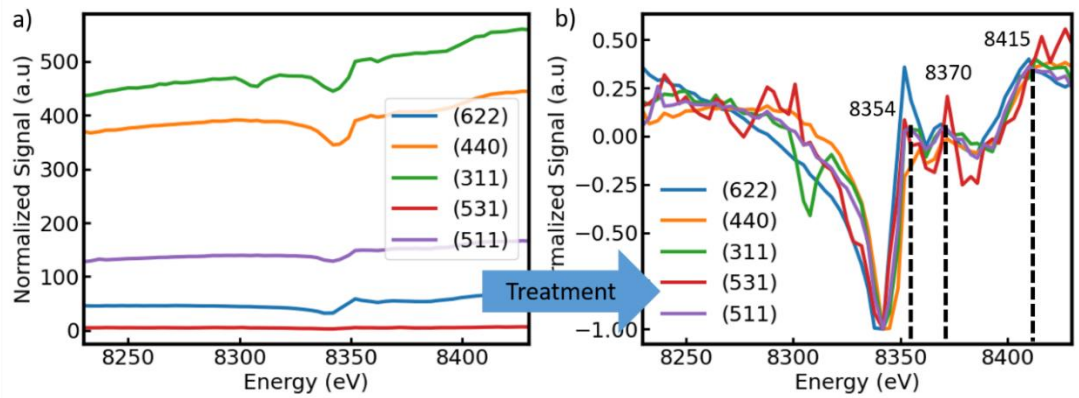

Figure 5.19: Raw data obtained for RXD signals at the Ni K edge of $Fe_{1.71}Ni_{0.57}Cr_{0.72}O_4$ (a) and the resulting treatment (b).

The FDMNES calculations were performed with parameters described above. For the Fe and Ni K edges, a Gaussian convolution with a width of 10eV and 5 eV, respectively, was employed. As the experimental data are noisy and have limited sampling (60 energy points for a range of 200 eV), convolutions with high widths are necessary to compare calculations and experimental signals. The cationic distribution provided to FDMNES is indicated in Table 5.11. No Ni or Cr cations were placed in T_d sites, and the stoichiometry was approximated (to treat only the second significant digit in the composition) as follows: $Fe_{1.71}Ni_{0.57}Cr_{0.72}O_4$ stoichiometry into $Fe_{1.65}Ni_{0.60}Cr_{0.75}O_4$, $Fe_{2.43}Ni_{0.21}Cr_{0.36}O_4$ stoichiometry into $Fe_{2.40}Ni_{0.24}Cr_{0.36}O_4$ and $Fe_{1.44}Ni_{0.45}Cr_{1.11}O_4$ stoichiometry into $Fe_{1.50}Ni_{0.45}Cr_{1.05}O_4$.

Table 5.11: Cationic repartition used for the FDMNES calculations (in fractional site occupancy).

Sample	Fe T_d	Ni T_d	Cr T_d	Fe O_h	Ni O_h	Cr O_h
$Fe_{2.43}Ni_{0.21}Cr_{0.36}O_4$	1	0	0	0.700	0.120	0.180
$Fe_{1.71}Ni_{0.57}Cr_{0.72}O_4$	1	0	0	0.325	0.300	0.375
$Fe_{1.44}Ni_{0.45}Cr_{1.11}O_4$	1	0	0	0.250	0.225	0.525

5.2.5.2 Ni K edge

Figure 5.20 presents the comparison between the experimental RXD signal at the Ni K edge, treated with the procedure mentioned above, and the FDMNES calculations for the $Fe_{1.71}Ni_{0.57}Cr_{0.72}O_4$ sample. A good overall agreement is observed. Two discrepancies are evident. In the pre edge region, the absorption well is more pronounced for calculations compared to the experimental signal. The post-edge structure is noisy in the experimental signal, even if the main features are visible.

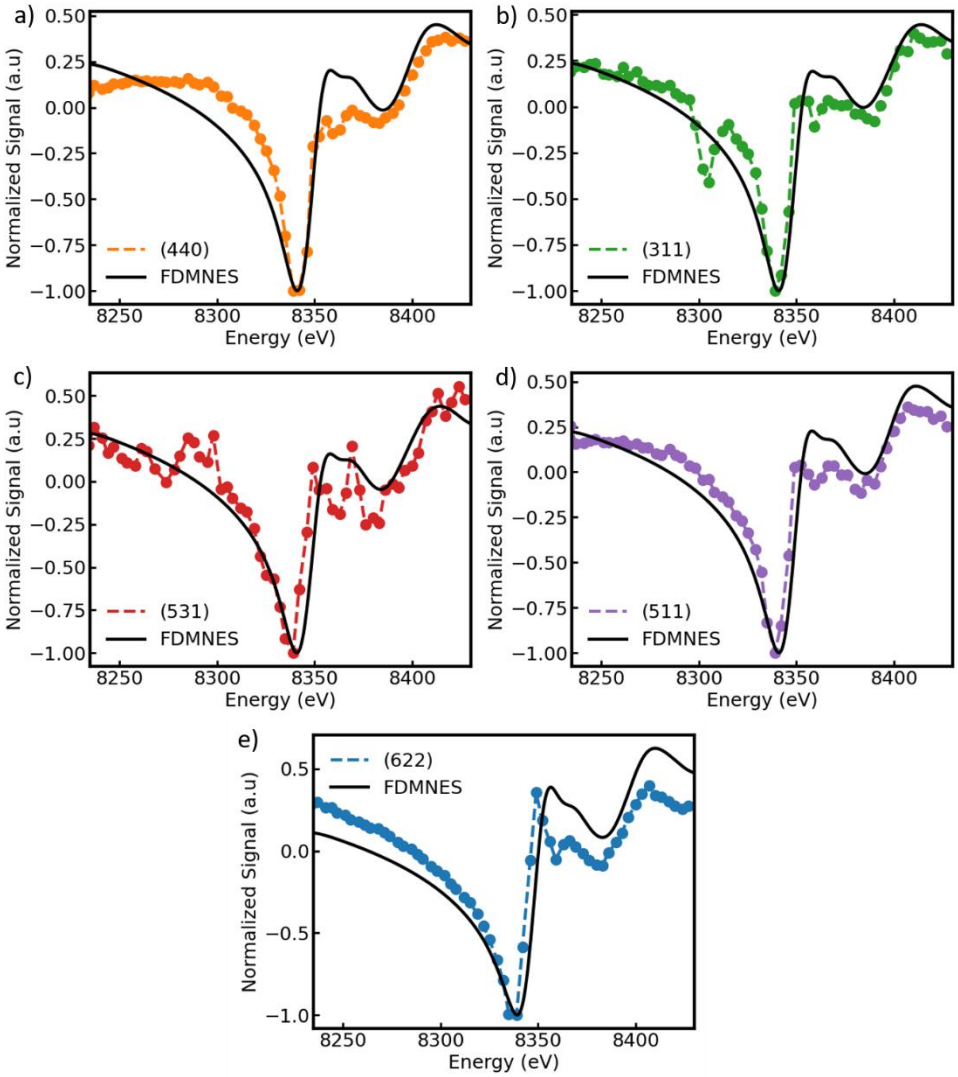

Figure 5.20: Normalized experimental and simulated RXD signals at the Ni K edge for the $Fe_{1.71}Ni_{0.57}Cr_{0.72}O_4$ sample.

The results for $Fe_{2.43}Ni_{0.21}Cr_{0.36}O_4$ and $Fe_{1.44}Ni_{0.45}Cr_{1.11}O_4$ samples at the Ni K edge are similar. The (440) and (311) RXD signals for the $Fe_{2.43}Ni_{0.21}Cr_{0.36}O_4$ sample exhibit considerable noise, and deviating significantly compared to the simulations. The remaining RXD signals, despite the presence of noise, exhibit a close alignment with the calculated curves. Similarly, the observations made regarding $Fe_{1.71}Ni_{0.57}Cr_{0.72}O_4$ sample can be extended to $Fe_{1.44}Ni_{0.45}Cr_{1.11}O_4$ sample. The (531) signal in $Fe_{1.44}Ni_{0.45}Cr_{1.11}O_4$ is of lower quality and is less closely aligned with the calculated curve.

The FDMNES calculations are in good agreement with the RXD experimental signal at the Ni K edge for all peaks. This signifies that the hypothesized cationic distribution (*i.e.* Ni^{2+} only in O_h sites) is true.

5.2.5.3 Fe K edge

The results for the Fe K edge for $Fe_{1.71}Ni_{0.57}Cr_{0.72}O_4$, $Fe_{2.43}Ni_{0.21}Cr_{0.36}O_4$ and $Fe_{1.44}Ni_{0.45}Cr_{1.11}O_4$ samples are presented in Figure 5.21, Figure 5.22, and Figure 5.23, respectively. The $Fe_{1.71}Ni_{0.57}Cr_{0.72}O_4$ sample (Figure 5.21) exhibits a high degree of similarity with the simulations in the case of the (511) and (311) signals. The (440) data set does not yield a particularly strong fit. The pre-edge is more flat, and the slope into the absorption well is more intense. Of particular interest is the formation of an absorption peak by the experimental signal in the (531) case. The post-edge structure in this signal is not accurately reproduced. The origin of the observed absorption peak can be attributed to the overrepresentation of the T_d site in comparison to the O_h site, as evidenced in Table 5.9 and in Table 5.11.

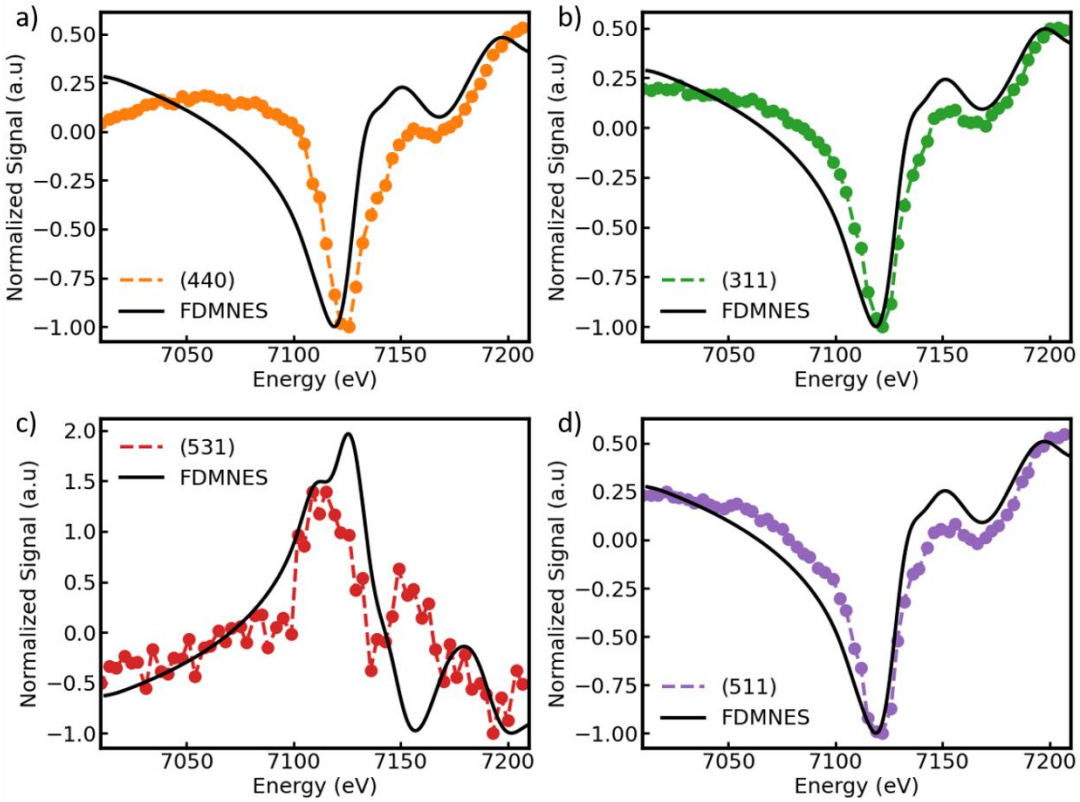

Figure 5.21: Normalized experimental and simulated RXD signals at the Fe K edge for the $Fe_{1.71}Ni_{0.57}Cr_{0.72}O_4$ sample. The diffraction peaks (440), (311), (531), and (511) are represented in (a), (b), (c), and (d), respectively.

The results for $Fe_{2.43}Ni_{0.21}Cr_{0.36}O_4$ sample (Figure 5.22) are analogous to those observed for $Fe_{1.71}Ni_{0.57}Cr_{0.72}O_4$ sample. The (311) and (511) signals are reproduced with a relatively high degree of fidelity by the calculations. The (440) exhibits the same defects as observed in $Fe_{1.71}Ni_{0.57}Cr_{0.72}O_4$ sample. The most

noteworthy aspect of this is the stark contrast in the shape of the (531) curve. In contrast to the single major peak observed in sample $Fe_{1.71}Ni_{0.57}Cr_{0.72}O_4$, two distinct absorption wells and one absorption peak are now evident. The signal is also accurately reproduced by the simulation, even in the post-edge structure. This markedly different shape can be attributed to the disparate ratio between the O_h and T_d sites.

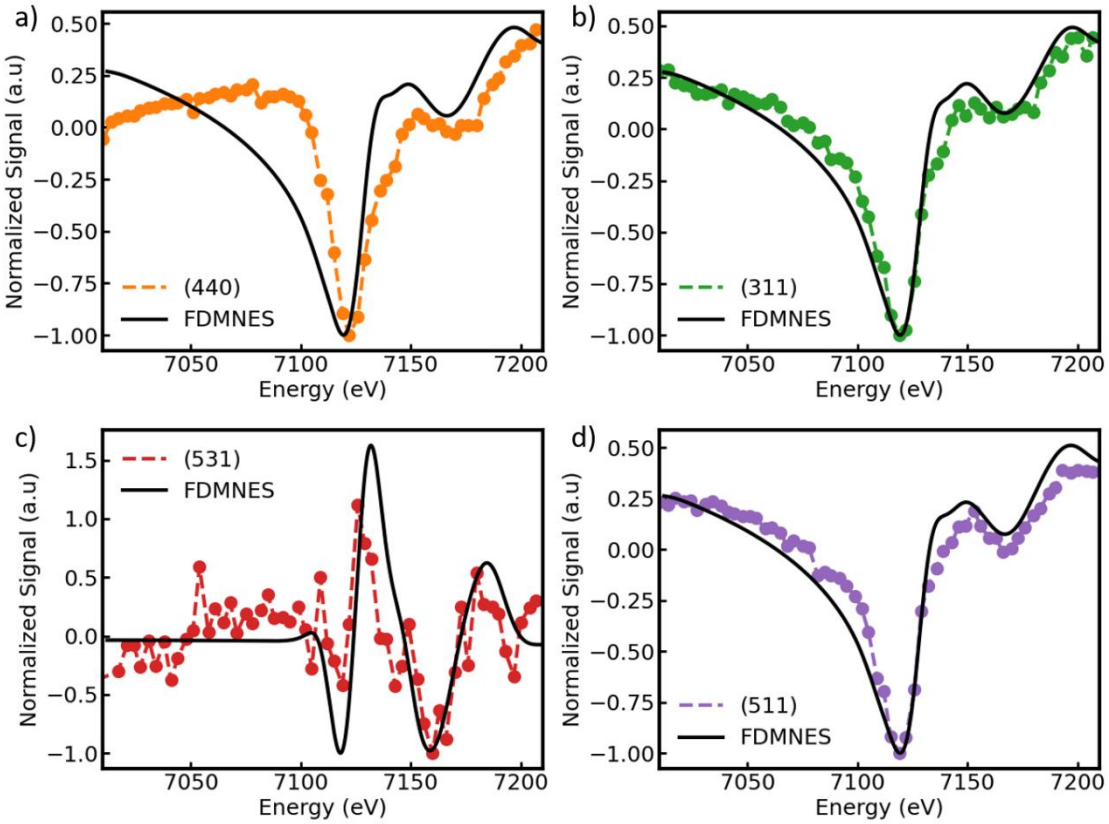

Figure 5.22: Normalized RXD signal at the Fe K edge and comparison with FDMNES calculations for the $Fe_{2.43}Ni_{0.21}Cr_{0.36}O_4$ sample.

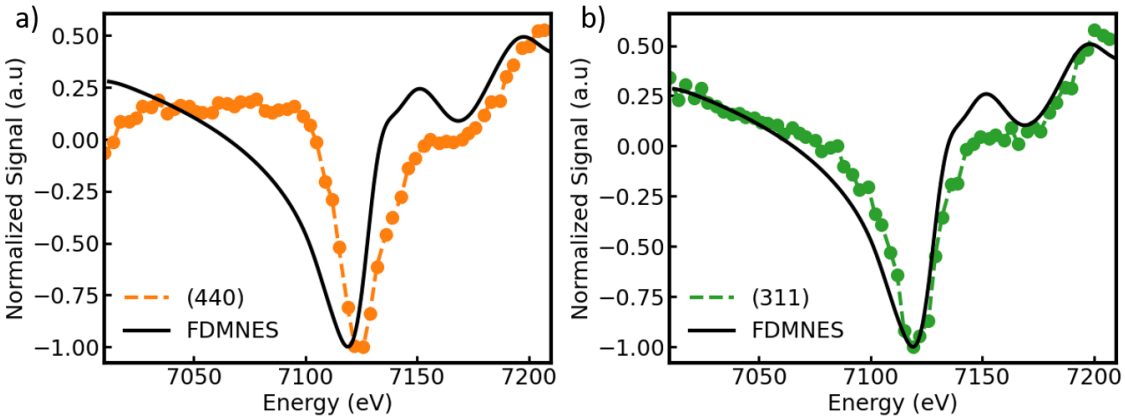

Figure 5.23: Normalized RXD signal at the Fe K edge and comparison with FDMNES calculations for the $Fe_{1.44}Ni_{0.45}Cr_{1.11}O_4$ sample

For the last $Fe_{1.44}Ni_{0.45}Cr_{1.11}O_4$ sample (Figure 5.23), the same observation applies to the (440) and (311) peaks, as the (440) is flat in the pre-edge region and subsequently decreases significantly, and the (311) signal is in close agreement with the simulation.

The FDMNES calculations are in good agreement with the RXD experimental signals at the Fe K edge. This signifies that the hypothesized cationic distribution (ratio of iron in O_h and T_d sites) is correct. The exception is the (440) peak for all samples, where the pre-edge slope of the calculations exhibit a significant discrepancy with the experimental curves.

5.2.6 Cationic distribution with (531) signal features

The (531) peak exhibit an opposite sign between the T_d (768) and O_h (-1086) contributions (see Table 5.9). Consequently, in function of the ratio between the occupancy of the two sites, the curve shape will be different.

The RXD signal was simulated with FDMNES for different hypothetical samples of $Fe_{3-y}Cr_yO4$ with different ratios of Fe in the T_d and O_h sites. Four variations have been tested:

- The initial variation entails the alteration of the Fe fractional occupancies in both the T_d and O_h sites, with the ratio of T_d to O_h sites maintained at one: $(Fe_yCr_{1-y})[Fe_{2y}Cr_{2-2y}]O_4$.
- The second variation concerns the fractional occupancy of Fe in the T_d site, while the Fe located in the O_h site is maintained at 100 %: $(Fe_yCr_{1-y})[Fe_2]O_4$.
- The third variation is about the repartition of the iron, passing from a 100% occupancy of the O_h to a 100 % occupancy of the T_d site: $(Fe_yCr_{1-y})[Fe_{2-2y}Cr_{2y}]O_4$.
- The last variation concerns the quantity of Fe in O_h site, while maintaining a 100% occupancy of the T_d site: $(Fe_1)[Fe_{2y}Cr_{2-2y}]O_4$.

The normalized signals for the aforementioned variations are presented in Figure 5.24. The progressive filling of both the T_d and O_h sites (a) results in signals that are highly analogous. While there is a slight variation in the peaks, this will be overshadowed by the noise present in the experimental RXD, rendering it undetectable in practical applications.

The gradual filling of the T_d site (b) is more interesting. The shape change, in particular the a and b peaks increase in intensity with the filling of T_d sites. In particular, the amplitude between the a and b peaks may provide insight into the cationic repartition.

The third variation and the fourth variation ((c) and (d)) are particularly noteworthy, as the curve exhibits a significant shift in shape, evolving from a single c peak to two peaks one negative a peak and one positive b peak. The c peak disappears in this process, undergoing a shift in position to form the b peak, moving from 7119 eV to 7133 eV. The amplitude difference between the c peak (obtained at 0 % O_h and 100 % T_d) and the a peak demonstrates variations with the progressive filling of the O_h site.

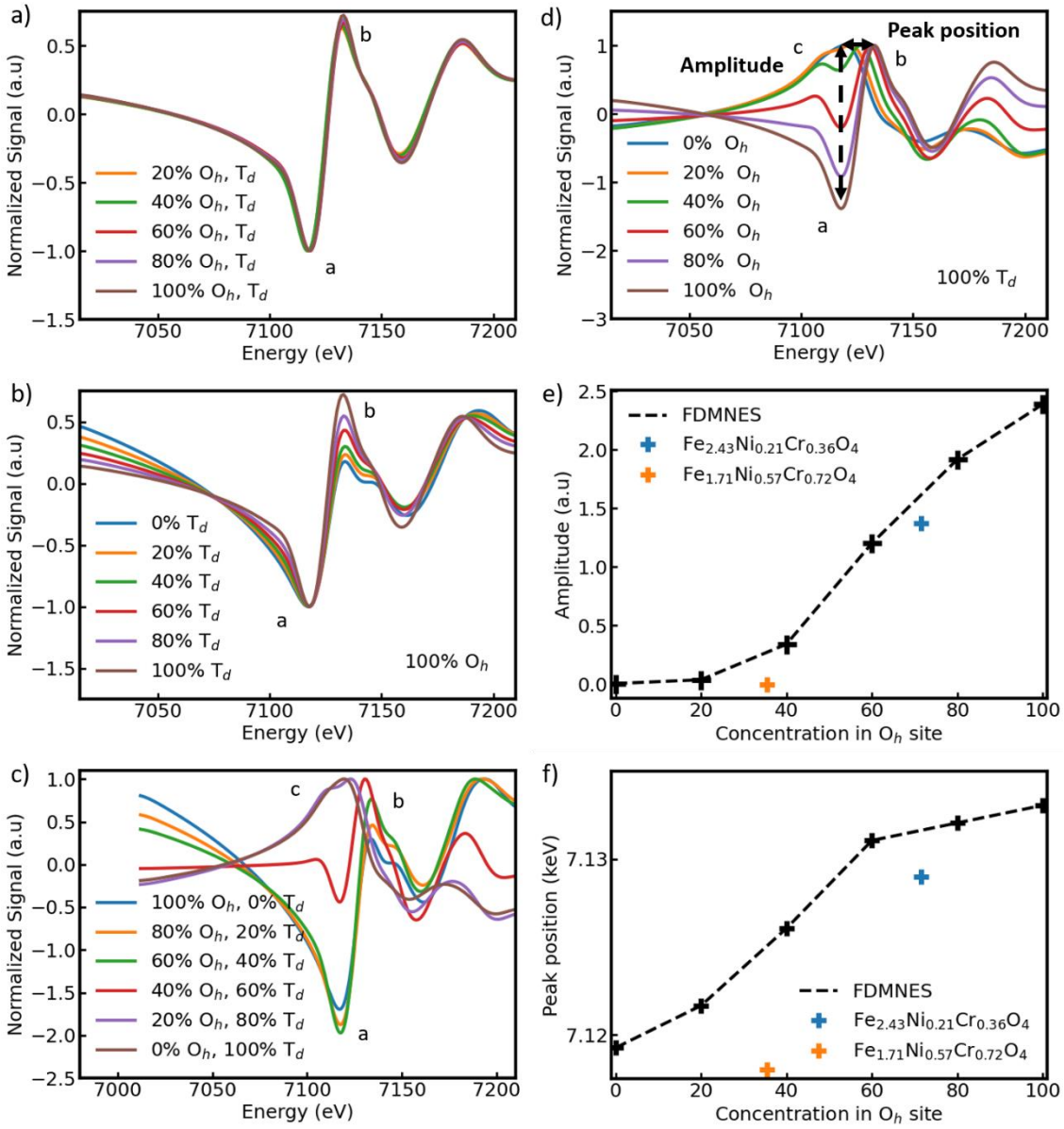

Figure 5.24: Variations of the normalized (531) signal for different cationic repartition. The curves presented in a) and b) have been divided by their minimums, while the curves presented in c) and d) have been divided by their maximums.

The amplitude variations during the transformation of the c peak into a peak with the filling of the O_h site is presented in (e), while the peak position variations peak with the filling of the O_h site are presented in (f). The curves are not linear; however, they can be employed to estimate the cationic repartition of experimental data. As the samples under investigation appear to contain only Fe in the T_d site, the colored crosses in (e) and (f) indicate the experimental point for $Fe_{1.71}Ni_{0.57}Cr_{0.72}O_4$ and $Fe_{2.43}Ni_{0.21}Cr_{0.36}O_4$ samples. The data are in good agreement with the amplitude method, while there is a slight discrepancy in the case of the peak position. This discrepancy can be attributed to the high noise levels in the (531) signals and the difficulty in determining the peak position for the $Fe_{1.71}Ni_{0.57}Cr_{0.72}O_4$ sample.

5.2.7 Comparison between RXD and XMCD regarding the cationic distribution

The RXD and XMCD cationic distributions are presented in the Table 5.12. The XMCD distribution was obtained by a fitting process, while the RXD distribution was presupposed and the resulting simulated curves were compared to the experimental curves, with success. The two cationic distributions are in good agreement. The total sum of iron species in both sites are in close proximity, and no techniques have detected the presence of Ni in T_d sites.

Table 5.12 Summary of the cationic distribution obtained through XMCD and RXD fits.

Sample	Technique	$\Sigma\, Fe_{T_d}$	$\Sigma\, Fe_{O_h}$	Ni_{T_d}
$Fe_{2.43}Ni_{0.21}Cr_{0.36}O_4$	XMCD	0.98	1.45	No
	RXD	1	1.4	No
$Fe_{1.71}Ni_{0.57}Cr_{0.72}O_4$	XMCD	1.15	0.56	No
	RXD	1	0.65	No
$Fe_{1.44}Ni_{0.45}Cr_{1.11}O_4$	XMCD	0.95	0.49	No
	RXD	1	0.5	No

5.3 CONCLUSIONS

5.3.1 Conclusions on the XMCD experiment

From XMCD experiments, the probed cationic ordering is the following:.

- The chromium cations have been identified to be exclusively located on the O_h sites, with oxidation state Cr^{+3}.
- The nickel cations have been described as Ni^{2+} in O_h sites for the majority of samples. For samples with the highest Cr content, the analysis shows potentially a low Ni content in T_d sites.
- The iron cations have displayed occupancies of both the T_d and O_h sites, with Fe^{2+} and Fe^{3+}, depending of the sample stoichiometry. From these occupancies and a theoretical model of cationic occupancy, the inversion parameter has been obtained and its variation with the stoichiometry has been discussed. With the methodology employed, the $Fe_{T_d}^{3+}$ contribution had a non-negligible contribution in the peak of $Fe_{O_h}^{3+}$. Consequently, the $Fe_{O_h}^{3+}$ contribution was relatively low, thus increasing the other contributions.

It was also possible to identify some trends for specific series of samples:

- In the $Ni_{\beta}Fe_{3-\beta}O_4$ series, the $Fe_{T_d}^{3+}$ remains constant at 1 and $Fe_{T_d}^{2+}$ at 0. The two other contributions decrease with β increasing.
- In the $Ni_{\beta}Fe_{2.50-\beta}Cr_{0.50}O_4$ series, the $Fe_{T_d}^{3+}$, $Fe_{T_d}^{2+}$, $Fe_{O_h}^{3+}$ and $Fe_{O_h}^{2+}$ contributions starts at 0.85, 0.05 0.40 and 1 respectively. The $Fe_{T_d}^{2+}$ remains near 0, before increasing to 0.25 at β = 1.0. The $Fe_{T_d}^{2+}$ increase until β = 0.50, before decreasing to 0.8 at β =1.0. The $Fe_{O_h}^{2+}$ contribution decreases from 1 to 0.40, while the $Fe_{O_h}^{3+}$ decreases from 0.40 to 0.20 until β = 0.50, and remains constant at 0.20 with the increase of β to 1.
- In the $Fe_{3-\gamma}Cr_{\gamma}O_4$ series, the $Fe_{T_d}^{3+}$, $Fe_{T_d}^{2+}$, $Fe_{O_h}^{3+}$ and $Fe_{O_h}^{2+}$ starts respectively at 1, 0, 0.8 and 1.2 at γ = 0. The $Fe_{T_d}^{2+}$ increases gradually, while $Fe_{T_d}^{3+}$ and $Fe_{O_h}^{2+}$ decreases gradually. The $Fe_{O_h}^{3+}$ decreases until γ = 0.50 (α = 2.50) and increases between γ = 0.50 and γ = 0.75 (α = 2.25). It ends by a decreases after γ = 0.75.

Finally, preliminary XMCD magnetic hysteresis loops have been recorded for each species and compared to VSM hysteresis loops.

5.3.2 Conclusions on the RXD experiment

The RXD experiment represents an effective methodology for investigating the cationic site distribution within the spinel structure. A methodology was developed for the extraction of both the background and the RXD signal. The background spectrum is analogous to that observed in XAS spectrum at a K edge. The extracted data underwent further processing (removal of the linear increase and normalization) to facilitate comparison with the FDMNES simulations.

The experimental data, despite the presence of noise, exhibit a satisfactory degree of correlation with the FDMNES calculations. This induces that the hypothesized cationic distribution in FDMNES simulations is correct. Precisely, the RXD samples possess only Ni cations in O_h sites. The hypothesized ratio of iron occupancies in the T_d and O_h sites is correct. These observations are also in agreement with those of the XMCD technique. The XMCD is able to differentiate between Fe^{2+} and Fe^{3+}, which is not possible for RXD due to the noise in RXD signals.

The (531) peak at the Fe K edge is markedly different between the two samples where this peaks has been recorded. This is related to the discrepancy in ratio of iron in T_d and O_h site. By using FDMNES simulations, a model has been developed to extract site occupancy in relation to the parameters governing the shape of the curve, like the peak position and the amplitude between the edge and the peak.

A continuation of this work will be to perform RXD experiments on peaks exhibiting only T_d contribution ((220) peak) at the Ni K edge for sample presenting $Ni_{T_d}^{2+}$ in XMCD to verify if this contribution is correct or an artefact.

5.4 BIBLIOGRAPHY

(1) Navrotsky, A.; Kleppa, O. J. The Thermodynamics of Cation Distributions in Simple Spinels. *Journal of Inorganic and Nuclear Chemistry* **1967**, *29* (11), 2701–2714. https://doi.org/10.1016/0022-1902(67)80008-3.

(2) Dunitz, J. D.; Orgel, L. E. Electronic Properties of Transition-Metal Oxides-II: Cation Distribution amongst Octahedral and Tetrahedral Sites. *Journal of Physics and Chemistry of Solids* **1957**, *3* (3), 318–323. https://doi.org/10.1016/0022-3697(57)90035-5.

(3) Haverkort, M. W.; Sangiovanni, G.; Hansmann, P.; Toschi, A.; Lu, Y.; Macke, S. Bands, Resonances, Edge Singularities and Excitons in Core Level Spectroscopy Investigated within the Dynamical Mean-Field Theory. *EPL* **2014**, *108* (5), 57004. https://doi.org/10.1209/0295-5075/108/57004.

(4) Haverkort, M. W.; Zwierzycki, M.; Andersen, O. K. Multiplet Ligand-Field Theory Using Wannier Orbitals. *Phys. Rev. B* **2012**, *85* (16), 165113. https://doi.org/10.1103/PhysRevB.85.165113.

(5) Lu, Y.; Höppner, M.; Gunnarsson, O.; Haverkort, M. W. Efficient Real-Frequency Solver for Dynamical Mean-Field Theory. *Phys. Rev. B* **2014**, *90* (8), 085102. https://doi.org/10.1103/PhysRevB.90.085102.

(6) Retegan, M.; Kuschel, S. Mretegan/Crispy: V0.7.4, 2023. https://doi.org/10.5281/ZENODO.1008184.

(7) Pinho, P. V. B.; Chartier, A.; Menut, D.; Barbier, A.; Hunault, M. O. J. Y.; Ohresser, P.; Marcelot, C.; Warot-Fonrose, B.; Miserque, F.; Moussy, J.-B. Stoichiometry Driven Tuning of Physical Properties in Epitaxial Fe3-xCrxO4 Thin Films. *Applied Surface Science* **2023**, *615*, 156354. https://doi.org/10.1016/j.apsusc.2023.156354.

(8) Pinho, P. V. B. Experimental and Theoretical Study on Fe-Cr-O Thin Films : From Fine Structure to Macroscopic Behavior. phdthesis, Université Paris-Saclay, 2022. https://theses.hal.science/tel-03917144 (accessed 2024-04-19).

(9) Verwey, E. J. W.; Heilmann, E. L. Physical Properties and Cation Arrangement of Oxides with Spinel Structures I. Cation Arrangement in Spinels. *The Journal of Chemical Physics* **1947**, *15* (4), 174–180. https://doi.org/10.1063/1.1746464.

(10) *International Tables for Crystallography*, 2016th ed.; Vol. A.

6 RELATIONS BETWEEN THE FINE STRUCTURE AND CRYSTALLOGRAPHY OR MAGNETIC BEHAVIOR

This final Chapter of the thesis will discuss the relations between the fine structure described in the chapter 5 and the crystallographic and magnetic properties. At first, the link between the fine structure and the lattice parameter will be established through a revisited model. The structural parameters derived from these models will be employed to elucidate the variation in lattice parameter across different isoconcentrations in iron, nickel, and chromium. Ultimately, the various angles between the cations within the structure will be calculated in order to elucidate the variations in magnetic properties.

6 RELATIONS BETWEEN THE FINE STRUCTURE AND CRYSTALLOGRAPHY OR MAGNETIC BEHAVIOR

6.1 FINE STRUCTURE RELATION WITH CRYSTALLOGRAPHIC STRUCTURE

In this section, the cationic site distribution as function of the spinel composition determined in the chapter 5 will be employed in a theoretical model allowing the calculation of the lattice parameters of all spinel compositions. The calculated lattice parameters will the compared to the experimental ones.

6.1.1 Model of theoretical lattice parameter

Models that link the cationic distribution and the spinel lattice parameter have been already been established in the past[1,2]. Once the cationic distribution at the O_h and T_d sites has been determined, the mean ionic radius on O_h (r_{O_h}) or T_d (r_{T_d}) sites can be calculated with the following relationship:

$$r_{T_d} = C_{Td}^{Fe^{2+}} * r_{Td}^{Fe^{2+}} + C_{Td}^{Fe^{3+}} * r_{Td}^{Fe^{3+}} + C_{Td}^{Ni^{2+}} * r_{Td}^{Ni^{2+}}$$

$$r_{O_h} = \frac{C_{Oh}^{Fe^{2+}} * r_{Oh}^{Fe^{2+}} + C_{Oh}^{Fe^{3+}} * r_{Td}^{Fe^{3+}} + C_{Oh}^{Cr^{3+}} * r_{Oh}^{Cr^{3+}} + C_{Oh}^{Ni^{2+}} * r_{Oh}^{Ni^{2+}}}{2} \quad (6.1)$$

With C_{Site}^{X} represents the concentration of the cationic species X at the designated atomic site ". The sum of these concentrations is normalized at one for T_d sites and at two for O_h sites. r_{Site}^{X} represents the effective ionic radius of the species X in the specified atomic site . The effective ionic radii found in the literature are summarized in Table 6.1. The selected effective ionic radii were always high spin compared to low spin (as usually made in the literature[3]). In addition the oxygen anion has four bonds with its neighboring metallic cations, resulting in a value of ionic radius of 1.38 Å for O^{2-} anions.

Table 6.1: Effective ionic radius extracted from Shannon[4] for the different species.

Site	Species	Effective ionic radius (Å)
O_h	$Fe_{O_h}^{3+}$	0.64
	$Fe_{O_h}^{2+}$	0.78
	$Ni_{O_h}^{2+}$	0.69
	$Cr_{O_h}^{3+}$	0.62
T_d	$Fe_{T_d}^{3+}$	0.49
	$Fe_{T_d}^{2+}$	0.63
	$Ni_{T_d}^{2+}$	0.55
Anion	O^{2-}	1.38

In the case of a perfectly close packed assembly of oxygen anions, the oxygen positional parameter u is valued at 0.375 in the case of an origin at $\bar{4}3m$ (origin choice 1). u can be calculated with the following relations[2]:

$$u' = \frac{r_{T_d} + r^O}{\sqrt{3} * c_{exp}} + \frac{1}{4}$$
$$u'' = \frac{5}{8} - \frac{r_{O_h} + r^O}{c_{exp}} \qquad (6.2)$$
$$u_{avg} = \frac{u' + u''}{2}$$

In equation (6.2), r^O represent the ionic radius of oxygen anions. u' is the anion parameter obtained from the T_d site, while u'' is the anion parameter derived from the O_h site. c_{exp} represents the experimental lattice parameter. u_{avg} designates the mean value between u' and u''. As described by Sickafus *et al.*[1] a strong empirical correlation exists between u and the ratio of r_{O_h} on r_{T_d}. This correlation has the advantage to not necessitate the c_{exp}, and is the following:

$$u = 0.3876 \left(\frac{r_{O_h}}{r_{T_d}}\right)^{-0.07054} \qquad (6.3)$$

u_{avg} can be employed in the estimation of the bond length at the tetrahedral (R_{T_d})and octahedral (R_{O_h}) sites through the following relations:

$$R_{T_d} = \sqrt{3} c_{exp} \left(u_{avg} - \frac{1}{4}\right)$$
$$R_{O_h} = c_{exp} \sqrt{2\left(u_{avg} - \frac{3}{8}\right)^2 + \left(\frac{5}{8} - u_{avg}\right)^2} \qquad (6.4)$$

These lengths can be calculated with the u definition on the equation (6.3). Finally, the theoretical value of the lattice constant c_{th} can be estimated using the following relation:

$$c_{th} = \frac{8R_{T_d}}{3\sqrt{3}} + \frac{8R_{O_h}}{3} \qquad (6.5)$$

6.1.2 Application to $Fe_\alpha Ni_\beta Cr_\gamma O_4$ spinel thin films

The comparison between the results of this model applied to all spinel composition on which a XMCD measurement has been conducted, and the theoretical lattice parameter is presented in Figure 6.1. The theoretical and experimental values of the c parameter are in good agreement. A few samples exhibit a small misalignment related to oxides for which the value: Σ $Species_{Td}$ exceeds one.

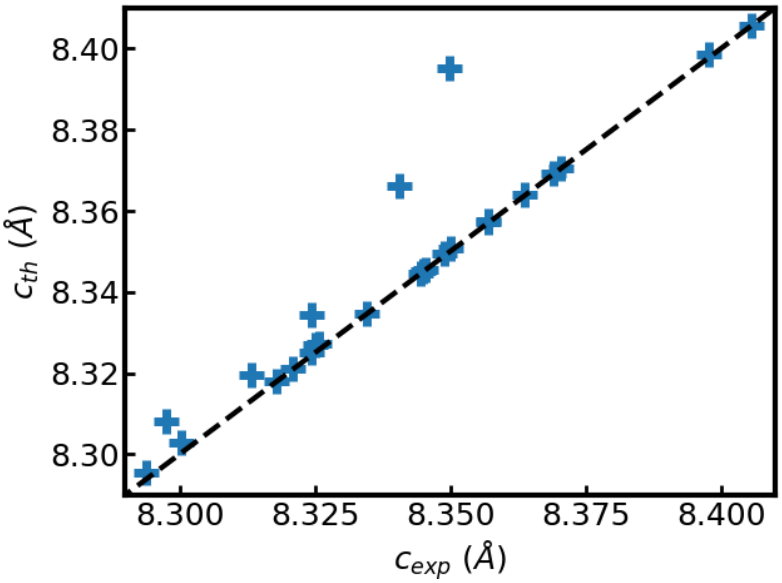

Figure 6.1: Theoretical lattice parameter (c_{th}) compared to the experimental lattice parameter (c_{exp}) for the different samples.

The discrepancy observed in Figure 6.1 can be addressed by providing a revised definition of the mean effective ionic radius at T_d and O_h sites, r_{T_d} and r_{O_h}. Indeed, the samples, exhibiting the greatest discrepancies, are those with the greatest excess of species in the T_d sites. Consequently, the new r_{T_d} definition includes a division by the total number of species in T_d sites, while the r_{O_h} is normalized by the total number of species in O_h sites. The new equations are the following:

$$r_{T_d} = \frac{C_{Td}^{Fe^{2+}} * r_{Td}^{Fe^{2+}} + C_{Td}^{Fe^{3+}} * r_{Td}^{Fe^{3+}} + C_{Td}^{Ni^{2+}} * r_{Td}^{Ni^{2+}}}{C_{Td}^{Fe^{2+}} + C_{Td}^{Fe^{3+}} + C_{Td}^{Ni^{2+}}}$$
$$r_{O_h} = \frac{C_{Oh}^{Fe^{2+}} * r_{Oh}^{Fe^{2+}} + C_{Oh}^{Fe^{3+}} * r_{Td}^{Fe^{3+}} + C_{Oh}^{Cr^{3+}} * r_{Oh}^{Cr^{3+}} + C_{Oh}^{Ni^{2+}} * r_{Oh}^{Ni^{2+}}}{C_{Oh}^{Fe^{2+}} + C_{Oh}^{Fe^{3+}} + C_{Oh}^{Cr^{3+}} + C_{Oh}^{Ni^{2+}}} \quad (6.6)$$

In equation (6.6), the revised definition ensures that r_{Td} is equal to 0.49 when only Fe^{3+} is present at T_d sites. The revised model applied to the samples are presented in Table 6.2.

*Table 6.2: Revised model applied on different spinel oxide thin films probed by XMCD. * indicates a $Ni^{2+}_{T_d}$ contribution.*

Cationic distribution $\{(T_d)[O_h]_2O_4\}$	u′ (T_d)	u″ (O_h)	c_{th} (Å)	c_{exp} (Å)
$(Fe^{3+}_{0.95})[Fe^{3+}_{0.63}Fe^{2+}_{0.63}Ni^{2+}_{0.78}]O_4$	0.3794	0.3755	8.3461	8.3455
$(Fe^{3+}_{0.94})[Fe^{3+}_{0.85}Fe^{2+}_{1.03}Ni^{2+}_{0.18}]O_4$	0.3784	0.3759	8.4061	8.4057
$(Fe^{3+}_{0.99})[Fe^{3+}_{0.92}Fe^{2+}_{0.73}Ni^{2+}_{0.36}]O_4$	0.3786	0.3773	8.3986	8.3978
$(Fe^{3+}_{0.96})[Fe^{3+}_{0.97}Fe^{2+}_{0.92}Ni^{2+}_{0.15}]O_4$	0.3790	0.3757	8.3709	8.3704
$(Fe^{3+}_{0.98})[Fe^{3+}_{0.47}Fe^{2+}_{0.98}Ni^{2+}_{0.21}Cr^{3+}_{0.36}]O_4$	0.3792	0.3750	8.3574	8.3570
$(Fe^{3+}_{0.89}Fe^{2+}_{0.27})[Fe^{3+}_{0.20}Fe^{2+}_{0.35}Ni^{2+}_{0.57}Cr^{3+}_{0.72}]O_4$	0.3824	0.3774	8.2997	8.2975
$(Fe^{3+}_{0.70}Fe^{2+}_{0.25})[Fe^{3+}_{0.21}Fe^{2+}_{0.28}Ni^{2+}_{0.45}Cr^{3+}_{1.11}]O_4$	0.3828	0.3791	8.2971	8.2939
$(Fe^{3+}_{0.74}Fe^{2+}_{0.24})[Fe^{3+}_{0.11}Fe^{2+}_{0.40}Ni^{2+}_{0.90}Cr^{3+}_{0.60}]O_4$	0.3821	0.3770	8.3276	8.3257
$(Fe^{3+}_{0.78}Fe^{2+}_{0.23})[Fe^{3+}_{0.13}Fe^{2+}_{0.39}Ni^{2+}_{1.02}Cr^{3+}_{0.45}]O_4$	0.3819	0.3765	8.3267	8.3251
$(Fe^{3+}_{0.93})[Fe^{3+}_{0.14}Fe^{2+}_{0.74}Ni^{2+}_{0.69}Cr^{3+}_{0.51}]O_4$	0.3795	0.3753	8.3351	8.3345
$(Fe^{3+}_{1.0})[Fe^{3+}_{0.19}Fe^{2+}_{0.88}Ni^{2+}_{0.39}Cr^{3+}_{0.54}]O_4$	0.3791	0.3756	8.3642	8.3637
$(Fe^{3+}_{0.98})[Fe^{3+}_{0.46}Fe^{2+}_{0.78}Ni^{2+}_{0.42}Cr^{3+}_{0.36}]O_4$	0.3794	0.3756	8.3450	8.3445
$(Fe^{3+}_{0.98})[Fe^{3+}_{0.38}Fe^{2+}_{0.89}Ni^{2+}_{0.21}Cr^{3+}_{0.54}]O_4$	0.3790	0.3762	8.3697	8.3691
$*(Fe^{3+}_{0.64}Fe^{2+}_{0.32}Ni^{2+}_{0.85})[Ni^{2+}_{0.08}Cr^{3+}_{1.11}]O_4$	0.3838	0.3835	8.3071	8.3003
$(Fe^{3+}_{0.64}Fe^{2+}_{0.32})[Ni^{2+}_{0.93}Cr^{3+}_{1.11}]O_4$	0.3833	0.3802	8.3045	8.3003
$(Fe^{3+}_{0.58}Fe^{2+}_{0.78})[Fe^{3+}_{0.20}Fe^{2+}_{0.31}Ni^{2+}_{0.14}Cr^{3+}_{1.01}]O_4$	0.3848	0.3809	8.3556	8.3498
$(Fe^{3+}_{0.48}Fe^{2+}_{0.74})[Fe^{3+}_{0.17}Fe^{2+}_{0.23}Ni^{2+}_{0.33}Cr^{3+}_{1.07}]O_4$	0.3853	0.3810	8.3467	8.3406
$(Fe^{3+}_{0.63}Fe^{2+}_{0.42})[Fe^{2+}_{0.38}Ni^{2+}_{0.27}Cr^{3+}_{1.29}]O_4$	0.3838	0.3794	8.3173	8.3133
$*(Fe^{3+}_{0.52}Fe^{2+}_{0.37}Ni^{2+}_{0.19})[Fe^{2+}_{0.32}Ni^{2+}_{0.05}Cr^{3+}_{1.56}]O_4$	0.3838	0.3813	8.3296	8.3245
$(Fe^{3+}_{0.52}Fe^{2+}_{0.37})[Fe^{2+}_{0.32}Ni^{2+}_{0.24}Cr^{3+}_{1.56}]O_4$	0.3837	0.3809	8.3293	8.3245
$(Fe^{3+}_{0.90})[Fe^{3+}_{0.84}Fe^{2+}_{1.26}]O_4$	0.3793	0.3730	8.3501	8.3500
$(Fe^{3+}_{0.84}Fe^{2+}_{0.06})[Fe^{3+}_{0.67}Fe^{2+}_{1.23}Cr^{3+}_{0.20}]O_4$	0.3799	0.3735	8.3493	8.3490
$(Fe^{3+}_{0.80}Fe^{2+}_{0.13})[Fe^{3+}_{0.40}Fe^{2+}_{1.18}Cr^{3+}_{0.50}]O_4$	0.3811	0.3732	8.3184	8.3180
$(Fe^{3+}_{0.74}Fe^{2+}_{0.18})[Fe^{3+}_{0.55}Fe^{2+}_{0.81}Cr^{3+}_{0.70}]O_4$	0.3817	0.3765	8.3225	8.3210
$(Fe^{3+}_{0.47}Fe^{2+}_{0.38})[Fe^{3+}_{0.45}Fe^{2+}_{0.49}Cr^{3+}_{1.20}]O_4$	0.3837	0.3805	8.3496	8.3450

Figure 6.2 illustrates the plot of the theoretical lattice parameter as a function of the experimental one. With this revised model, all the sample are aligned with the $c_{th} = c_{exp}$ relation. The lattice parameter measurement in this system can be the only measurement needed to have the cationic distribution. Using this revised model, the $Fe_{0.96}Ni_{0.93}Cr_{1.11}O_4$ composition showing a $Ni^{2+}_{T_d}$ contribution exhibits a calculated lattice parameter in better agreement with the experimental one. However its (u′,u″) values are above the values of all other compositions. For this

reason, it will be discarded for the rest of discussion.

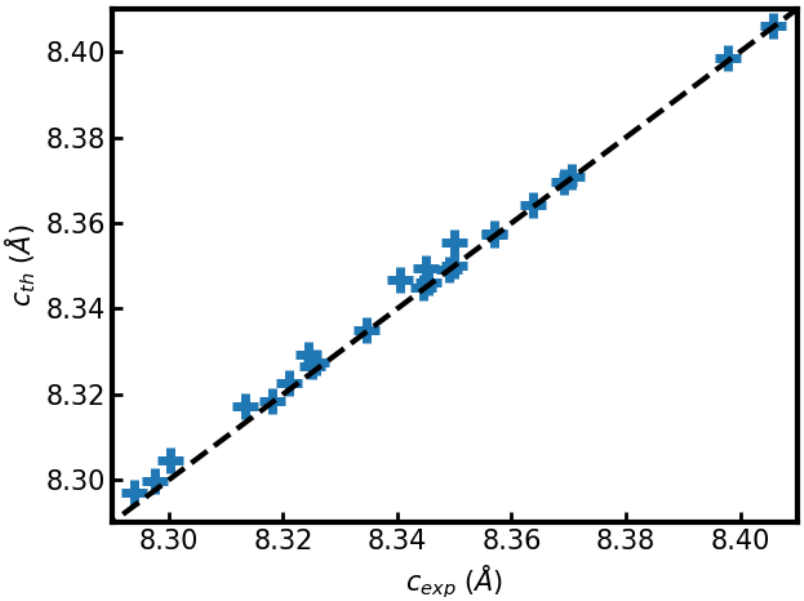

Figure 6.2: Theoretical lattice parameter compared to the experimental lattice parameter, in the revised model.

The variation of u" in function of u', in the revised model, is presented on the Figure 6.3. Three zones can be observed.

The first zone ($\delta \geq 0.95$) is characterized by an inversion parameter close to one. A decrease in the u" as a function of u' is noticeable. In this region, the T_d site is only occupied by Fe^{3+} cations. The values of u' are very close (between 0.3784 and 0.3799), with the variations in u' attributed to those in c_{exp}. The variations in the lattice parameter are solely attributable to the effective ionic radius on O_h sites. An increase in r_{Oh} results in a decrease in u", as evidenced in the equation (6.2).

In the zone II, the inversion parameter exhibits a decrease ($0.95 \geq \delta \geq 0.45$), whereas the pair (u',u") has a significant increase. An inversion parameter lower than one results in an increase in r_{Td}, which in turn leads to an increase in u'. Concurrently, a reduction in the number of cations in the oxidation state 2+ at the O_h site results in a decline in r_{Oh}. A reduction in r_{Oh} consequently results in an increase in u". Consequently, the couples (u', u") exhibit an increase.

In the zone III, the value of u" remains constant, while u' continues to increase. Given that the O_h sites are less occupied by iron species, r_{Oh} tends to an asymptote and exhibits minimal variations. At the opposite, the increased presence of $Fe_{T_d}^{2+}$ leads to greater u'.

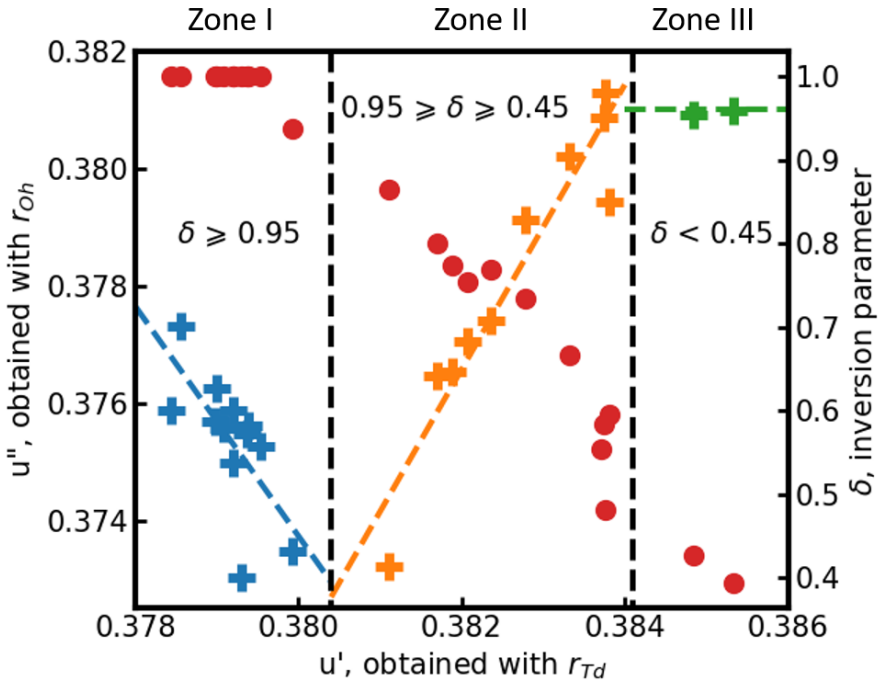

Figure 6.3: Anion parameter u" obtained through r_{Oh} in function of u', obtained through r_{Td}. The crosses represent the different parts, which can be read on the left. The red circles represent the inversion parameter.

The variation of the anion parameter as a function of the inversion parameter is presented in Figure 6.4. The linear fit is also displayed. A repartition of the variation in three regions is also discernible. This is a consequence of the separation in three regions of the (u',u") couple. As expected, this correlation indicates that the cationic disorder within the structure is managed through the adaptation of the oxygen anion position.

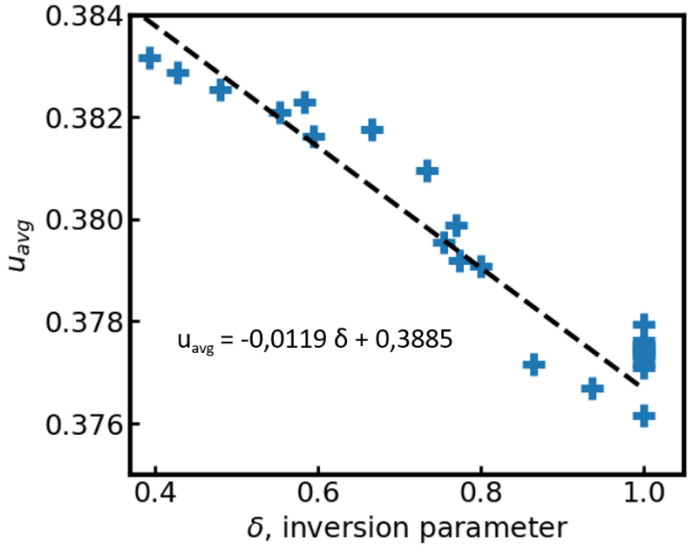

Figure 6.4: Average anion parameter (u_{avg}) as a function of the inversion parameter (δ). The black line is a linear fit without the points at δ = 1.

The Figure 6.5 illustrates in the quaternary diagram the u_{avg} values. The anion parameter exhibits an increase when moving leftward and upward.

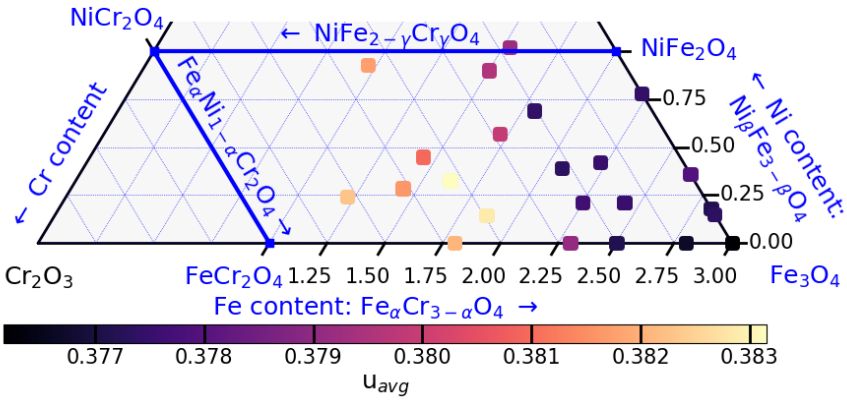

Figure 6.5: u_{avg} for the revised model is represented in the quaternary plot.

6.1.3 Cationic distribution with lattice parameter

Given that c_{th} is in good agreement with c_{exp}, a lattice parameter measurement in this system can be the only measurement needed to access to the cationic site distribution. The veracity of this hypothesis can be determined through empirical testing. The XMCD technique has not be employed in the study of two samples with varying compositions of nickel, chromium, and iron. c_{th} values can be calculated with different cationic distributions, resulting in different degrees of agreement with the value of c_{exp}. For example, the first line of Table 6.3 shows the cationic distribution obtained with XMCD for the $Fe_{1.62}Ni_{0.33}Cr_{1.05}O_4$ sample, along with another distribution. The two values of c_{th} and c_{exp} are indicated.

In the Chapter 5, it has been observed that $Cr_{O_h}^{3+}$ = γ and at the exception of two samples, $Ni_{O_h}^{2+}$ = β. The first sample is $Fe_{2.31}Ni_{0.15}Cr_{0.54}O_4$. Given that α > 2, it can be supposed that only Fe^{3+} are present in T_d sites. The second sample is $Fe_{1.23}Ni_{0.96}Cr_{0.78}O_4$. Given that α < 2, a little contribution of $Fe_{T_d}^{2+}$ can be expected. All the previous defined variables can be calculated for distinct cationic distributions. Given that the c_{exp} is known, it must be compared to the c_{th} calculated with the different cationic repartitions.

The different cationic repartitions tested and the resulting c_{th} are indicated in Table 6.3. Only cationic distribution with discrepancies in lattice parameters less than 0.002 Å are presented for the samples. For $Fe_{2.31}Ni_{0.15}Cr_{0.54}O_4$ sample, the best result exhibits 0.15 discrepancy with regards to the ideal charge distribution (1.15 against $\sum cations^{2+} = 1$ for ideal charge distribution). For this sample, it is evident that the introduction of additional $Fe_{O_h}^{3+}$ leads to a greater gap between

the calculated and experimental values. Concerning the $Fe_{1.23}Ni_{0.96}Cr_{0.78}O_4$ sample, the best agreement is found with sum of 2+ cations valued at 1.20. Introducing more $Fe_{O_h}^{3+}$ or $Fe_{T_d}^{2+}$ lead to greater discrepancies.

Table 6.3: Summary of the cationic distribution tested for the two samples not previously examined in XMCD.

Sample	Cationic distribution $\{(T_d)[O_h]_2O_4\}$	c_{th} (Å)	c_{exp} (Å)
$Fe_{1.62}Ni_{0.33}Cr_{1.05}O_4$	$(Fe_{0.48}^{3+}Fe_{0.74}^{2+})[Fe_{0.17}^{3+}Fe_{0.23}^{2+}Ni_{0.33}^{2+}Cr_{1.05}^{3+}]O_4$	8.3467	8.3406
	$(Fe_{0.50}^{3+}Fe_{0.50}^{2+})[Fe_{0.62}^{2+}Ni_{0.33}^{2+}Cr_{1.05}^{3+}]O_4$	8.3439	
$Fe_{2.31}Ni_{0.15}Cr_{0.54}O_4$	$(Fe_{1.0}^{3+})[Fe_{0.30}^{3+}Fe_{1.0}^{2+}Ni_{0.15}^{2+}Cr_{0.54}^{3+}]O_4$	8.3205	8.3202
	$(Fe_{1.0}^{3+})[Fe_{0.40}^{3+}Fe_{0.90}^{2+}Ni_{0.15}^{2+}Cr_{0.54}^{3+}]O_4$	8.3207	
	$(Fe_{1.0}^{3+})[Fe_{0.50}^{3+}Fe_{0.80}^{2+}Ni_{0.15}^{2+}Cr_{0.54}^{3+}]O_4$	8.3209	
	$(Fe_{1.0}^{3+})[Fe_{0.60}^{3+}Fe_{0.70}^{2+}Ni_{0.15}^{2+}Cr_{0.54}^{3+}]O_4$	8.3211	
	$(Fe_{1.0}^{3+})[Fe_{0.70}^{3+}Fe_{0.60}^{2+}Ni_{0.15}^{2+}Cr_{0.54}^{3+}]O_4$	8.3213	
$Fe_{1.23}Ni_{0.96}Cr_{0.78}O_4$	$(Fe_{1.0}^{3+})[Fe_{0.24}^{2+}Ni_{0.96}^{2+}Cr_{0.78}^{3+}]O_4$	8.3087	8.3073
	$(Fe_{1.0}^{3+})[Fe_{0.12}^{3+}Fe_{0.12}^{2+}Ni_{0.96}^{2+}Cr_{0.78}^{3+}]O_4$	8.3091	
	$(Fe_{0.95}^{3+}Fe_{0.05}^{2+})[Fe_{0.24}^{2+}Ni_{0.96}^{2+}Cr_{0.78}^{3+}]O_4$	8.3089	
	$(Fe_{0.95}^{3+}Fe_{0.05}^{2+})[Fe_{0.12}^{3+}Fe_{0.12}^{2+}Ni_{0.96}^{2+}Cr_{0.78}^{3+}]O_4$	8.3093	
	$(Fe_{0.9}^{3+}Fe_{0.10}^{2+})[Fe_{0.24}^{2+}Ni_{0.96}^{2+}Cr_{0.78}^{3+}]O_4$	8.3091	
	$(Fe_{0.85}^{3+}Fe_{0.15}^{2+})[Fe_{0.24}^{2+}Ni_{0.96}^{2+}Cr_{0.78}^{3+}]O_4$	8.3093	

This suggests that the experimental AO-MBE setup may have issues with oxidation, which could result in samples being sub-oxidized. Consequently, a greater number of Fe^{2+} charges are present in the samples. This is also evident in iron L_3 edge XMCD fits, where the sum of Fe^{2+} species is consistently greater that the ideal value of 1-β. This provide a supplementary explanation to the previous hypothesis made to explain the excess of 2+ charges, *i.e.* the contribution of $Fe_{T_d}^{3+}$ in the peak of $Fe_{O_h}^{3+}$.

6.2 CORRELATIONS BETWEEN THE LATTICE PARAMETER AND THE CATIONIC ORDERING OF THE SPINEL THIN FILMS

This part is focused on the evolution of the lattice parameter as a function of the stoichiometry. More precisely, some isoconcentration lines will be discussed, as illustrated in Figure 6.6. The red line is the nickel isoline, the green line represents the iron isoline and the orange line depicts the chromium isoline. Unfortunately, the iron isolines contain too few samples to draw some trends. It will not be analyzed in the following.

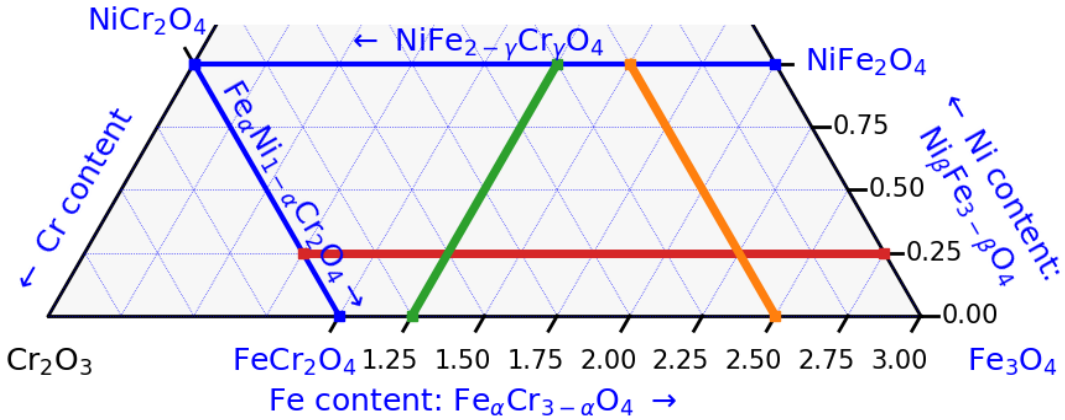

Figure 6.6: Schematic illustration of several isolines in the quaternary system.

6.2.1 Isoconcentrations in chromium: $Fe_\alpha Ni_\beta Cr_\gamma O_4$ with γ fixed

Three isolines of chromium concentrations will be analyzed. The three selected lines are: γ = 0, γ = 0.5, γ = 1.04 and are represented by the following colors in Figure 6.7: red, pink, and purple, respectively.

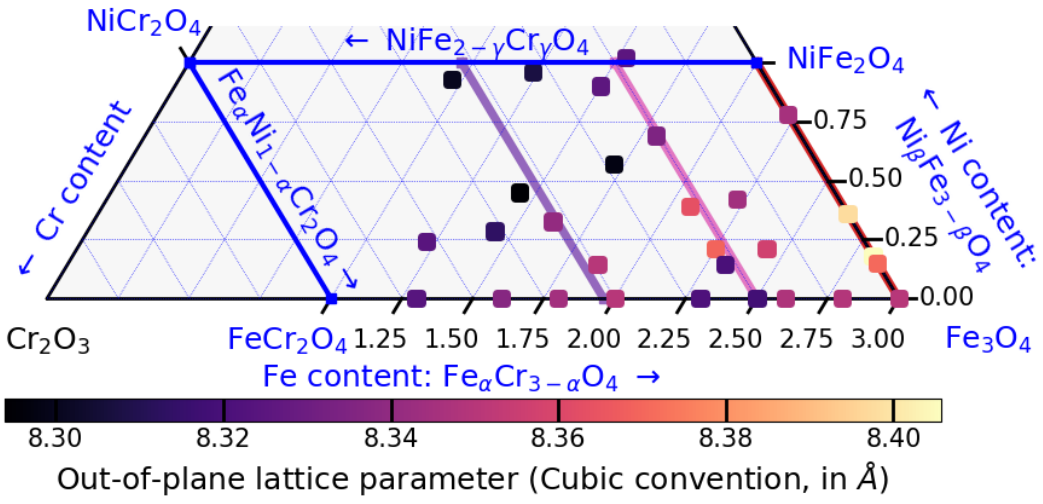

Figure 6.7: Isolines of chromium concentration.

The lattice parameter variations for the three isolines are illustrated in Figure 6.8. Two regions can be discerned. In the first region (β < 0.4), the lattice parameter increases for red and pink curves, while the purple curve remains constant. In the second region (β > 0.4), the lattice parameter decreases for red and pink curves. The purple curve remains constant, after a drop at β = 0.4.

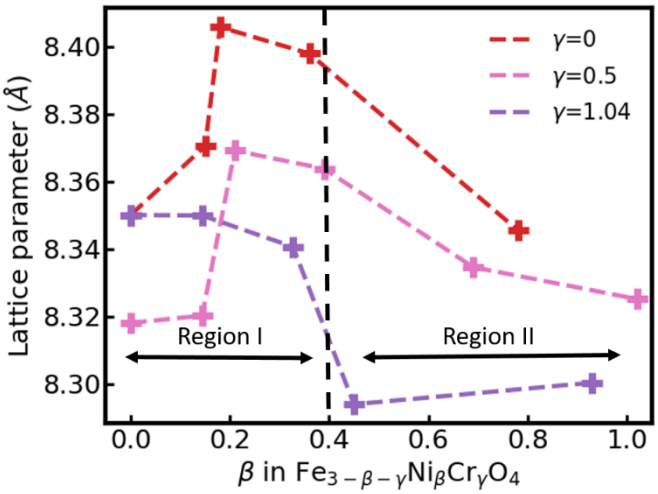

Figure 6.8: Lattice parameter variations as a function of β in the series $Fe_{3-\beta-\gamma}Ni_{\beta}Cr_{\gamma}O_4$.

6.2.1.1 Chromium isoline $Fe_{3-\beta}Ni_{\beta}Cr_0O_4$ (γ = 0)

This isoline corresponds to the binary Fe_3O_4-$NiFe_2O_4$ system. This binary system has been the subject of numerous studies on nanoparticles (NPs) or thin films (TFs)[5–9]. The summary of different results is illustrated in Figure 6.9.

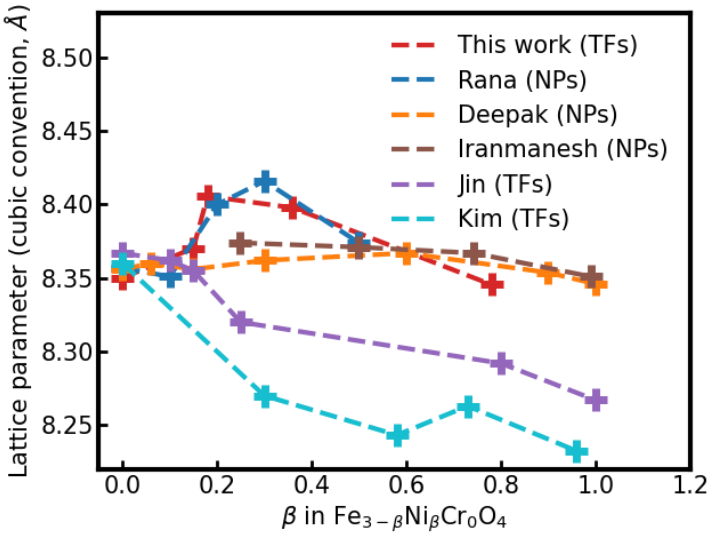

Figure 6.9: Lattice parameter evolution as a function of β in the Fe_3O_4-$NiFe_2O_4$ binary system extracted from [5–9].

As observed by Kim *et al.*[9], the samples exhibited a tetragonal structure. In order to facilitate comparison with the present work, an equivalent cubic lattice parameter has been calculated as follows: $a_{cubic}^3 = a_{tetra}^2 c_{tetra}$. Following the NPs or TFs samples, two types of curves are discernible. NPs exhibit lattice parameters higher than these observed in TFs. However, in this work, the measured lattice parameters are in good agreement with those observed in nanoparticles. The thin film samples elaborated by Jin *et al.*[8] or Kim *et al.*[9] exhibited a thickness of around 300 nm, and are polycrystalline. This is strongly different from our AO-MBE monocrystalline thin films with a thickness around 10 nm.

Figure 6.10 shows the variations of the lattice parameter with respect to the O_h or T_d cationic radius. Two regions seems discernible, separated at β = 0.40. The region I exhibits a stark decline in the occupancy of $Fe_{O_h}^{2+}$ (cationic radius of 0.78 Å), accompanied by small variations in $Fe_{O_h}^{3+}$ (0.64 Å) occupancy (≈ 0.9), and a progressive increase of $Ni_{O_h}^{2+}$ (0.69 Å) which results in a decrease for r_{Oh}. Due to the decrease of r_{Oh}, the anion parameter is increasing, as observed for the lattice parameter.

The region II displays a net decrease in $Fe_{O_h}^{3+}$ occupancy, while the $Fe_{O_h}^{2+}$ occupancy is slightly decreased. This missing occupancy is filled with $Ni_{O_h}^{2+}$, which results in a slight increase in r_{Oh}. Given that r_{Td} remains constant, the variation in u is solely due to the variation in r_{Oh}. This results in an overall decrease of the lattice parameter.

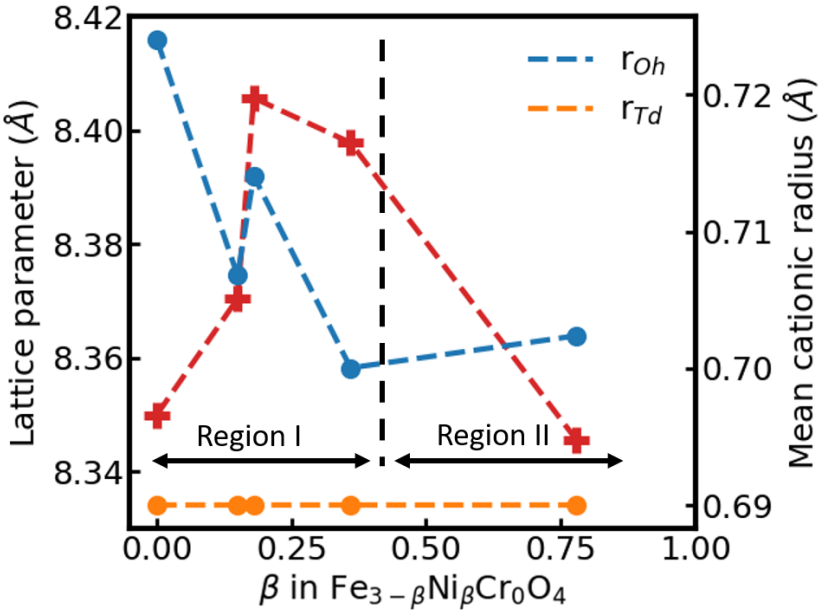

Figure 6.10: Variations of the lattice parameter with the mean cationic radius in $Fe_{3-\beta}Ni_\beta Cr_0O_4$. The lattice parameter (red curve) is indicated at the left, the mean cationic radius at the right. r_{Td} is shifted by +0.2 Å.

6.2.1.2 Chromium isoline $Fe_{2.5-\beta}Ni_\beta Cr_{0.5}O_4$ ($\gamma = 0.5$)

The variations within the mean cationic radius are illustrated in Figure 6.11. The variations can be separated in two regions, with the boundary at β = 0.40. In the region I, there is a decrease in Fe^{2+} (0.78 Å) and Fe^{3+} (0.64 Å) in O_h sites occupancies, with the progressive increase of $Ni_{O_h}^{2+}$ (0.69 Å). With regard to the T_d site, there is a slight increase in the occupancy of Fe^{3+} (0.49 Å) and a slight decrease in that of Fe^{2+} (0.63 Å). The resulting mean radius decreases for both sites. Despite the decrease in r_{Td}, the anion parameter shows a slight increase due to the reduction in r_{Oh}, resulting in an overall augmentation of the lattice parameter, until β = 0.40.

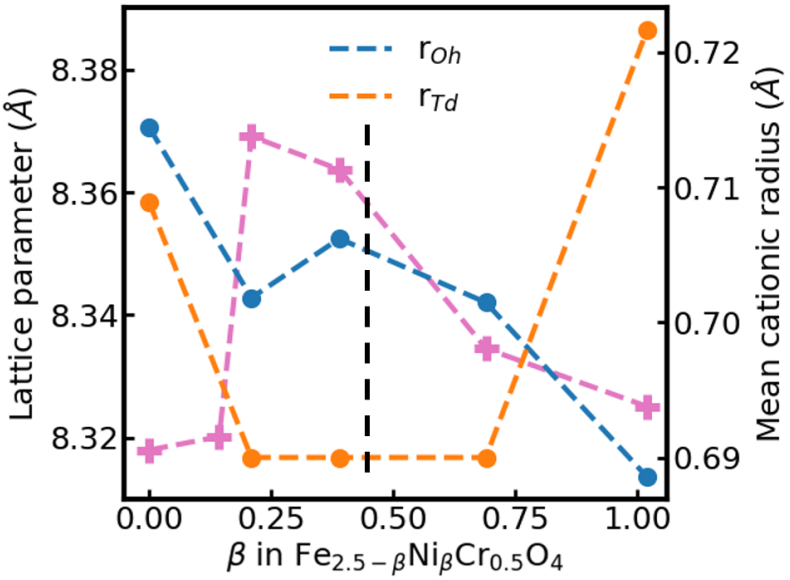

Figure 6.11: Variations of the lattice parameter with the mean cationic radius in $Fe_{2.5-\beta}Ni_\beta Cr_{0.5}O_4$. The lattice parameter (pink curve) is indicated at the left, the mean cationic radius at the right. r_{Td} is shifted by +0.2 Å.

Subsequently in the region II, the O_h occupancy of iron continues to decrease for both species, and some $Fe_{T_d}^{2+}$ is discernible. r_{Td} exhibits a significant increase due to the presence of $Fe_{T_d}^{2+}$, while r_{Oh} continues to decline. The anion parameter then increases due to this dual influence, resulting in an overall reduction in the lattice parameter.

6.2.1.3 Chromium isoline $Fe_{1.96-\beta}Ni_\beta Cr_{1.04}O_4$ ($\gamma = 1.04$)

The variations within the mean cationic radius are illustrated in Figure 6.12. The sample $Fe_{2.00}Cr_{1.00}O_4$ was not probed by an XMCD experiment. However, its fine structure has been deduced from a pondered mean between the fine structure of two samples situated on its Cr isoline: $Fe_{2.30}Cr_{0.70}O_4$ and $Fe_{1.80}Cr_{1.20}O_4$. The retained

fine structure is $(Fe^{3+}_{0.59}Fe^{2+}_{0.31})[Fe^{3+}_{0.4}Fe^{2+}_{0.61}Cr^{3+}_{1.00}]O_4$. This yields to a theoretical lattice parameter of 8.3533 Å. The fine structure retained for the sample $Fe_{0.96}Ni_{0.93}Cr_{1.11}O_4$ was the one without $Ni^{2+}_{T_d}$ contribution for reasons explained in section 6.1.2.

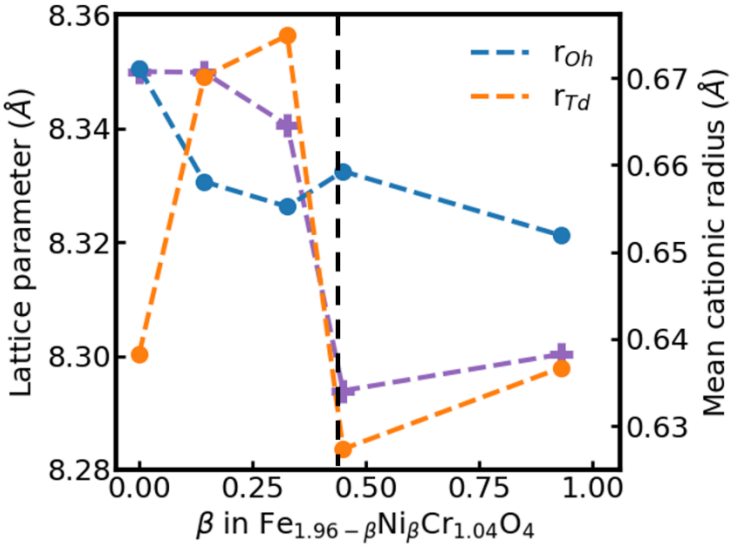

Figure 6.12: Variations of the lattice parameter with the mean cationic radius in $Fe_{1.96-y}Ni_yCr_{1.04}O_4$. The lattice parameter (purple curve) is indicated at the left, the mean cationic radius at the right. r_{Td} is shifted by +0.2 Å.

The cationic radius exhibits a two-region variation, separated at β= 0.40. In the region I, the $Fe^{3+}_{T_d}$, $Fe^{3+}_{O_h}$ (0.64 Å) and $Fe^{2+}_{O_h}$ (0.78 Å) occupancies exhibit a decrease, while the $Fe^{2+}_{T_d}$ contribution increases. This results in a decrease of the inversion parameter δ. The mean cationic radius at the T_d site increases due to the presence of $Fe^{2+}_{T_d}$, while the cationic radius at O_h site decreases as a result of the overall decrease in iron species at the O_h site. Consequently, the anion parameter increases from the two contributions, resulting in a slight reduction of the lattice parameter.

In the subsequent region (II), the O_h occupancy of iron cations continues to decrease, while the contribution of $Fe^{3+}_{T_d}$ increases, and that of $Fe^{2+}_{T_d}$ decreases. The inversion parameter therefore increases. The abrupt increase in $Fe^{3+}_{T_d}$ occupancy results in a decline in the mean cationic radius within the T_d sites, while the r_{Oh} exhibits a decrease in the overall region II. Consequently, the anion parameter in region II is observed to increase from the two contributions of cationic radius. The consequence of this u variation for the corresponding lattice parameter is a notable decline from region I to region II, before remaining almost constant at 8.295 Å.

In summary, the variations for the fine structure and lattice parameter are indicated in Table 6.4. From the increase in chromium content, the number of iron cation exhibiting a decline in the first region increase (only $Fe_{O_h}^{2+}$ for γ = 0, then $Fe_{O_h}^{2+}$ and $Fe_{O_h}^{3+}$ for γ = 0.5 and finally $Fe_{O_h}^{2+}$, $Fe_{O_h}^{3+}$ and $Fe_{T_d}^{3+}$ for γ = 1.04). The second region is marked by the apparition of the $Fe_{T_d}^{2+}$ for γ > 0. In γ = 0, $Fe_{O_h}^{3+}$, in γ = 0.5, $Fe_{O_h}^{2+}$ and in γ = 1.04, $Fe_{O_h}^{3+}$ and $Fe_{O_h}^{2+}$ are the responsible for the decreasing of the lattice parameter.

Table 6.4: Variations of cationic iron species for the different chromium isolines. LP means lattice parameter.

Isoline		LP	$Fe_{T_d}^{3+}$	$Fe_{T_d}^{2+}$	$Fe_{O_h}^{3+}$	$Fe_{O_h}^{2+}$
γ=0	Region I	↗	1	0	≈	↘
	Region II	↘	1	0	↘	≈
γ=0.5	Region I	↗	↗	↘	↘	↘
	Region II	↘	↘	↗	≈	↘
γ=1.04	Region I	≈	↘	↗	↘	↘
	Region II	↘ then ≈	↗ then ≈	↘ then ≈	↘	↘

6.2.2 Isoconcentrations in nickel: $Fe_\alpha Ni_\beta Cr_\gamma O_4$ with β fixed

Four isolines of nickel concentrations have been traced. The four selected lines are β = 0, β = 0.25, β = 0.40, and β = 0.95 and are represented by the following colors in Figure 6.7: red, cyan, pink and purple, respectively.

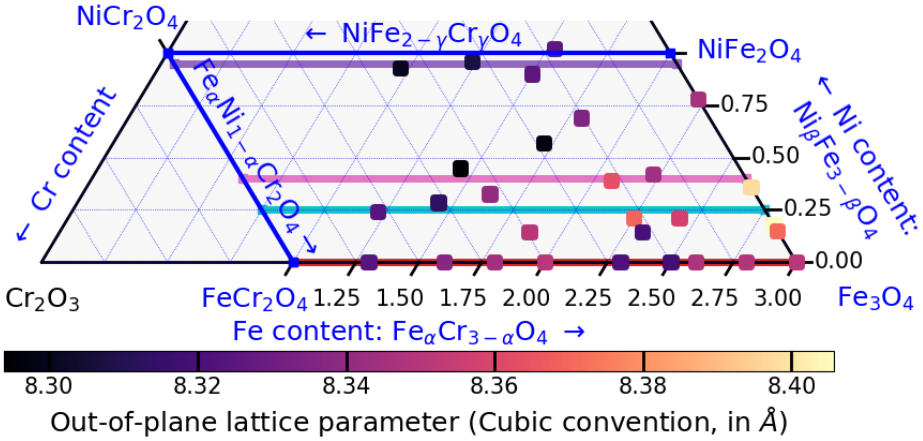

Figure 6.13: Isolines of nickel concentration.

Figure 6.14 presents the lattice parameter variations for the four isolines. The three regions indicated are the regions identified for β = 0. These regions have a distinct behavior when β >0.

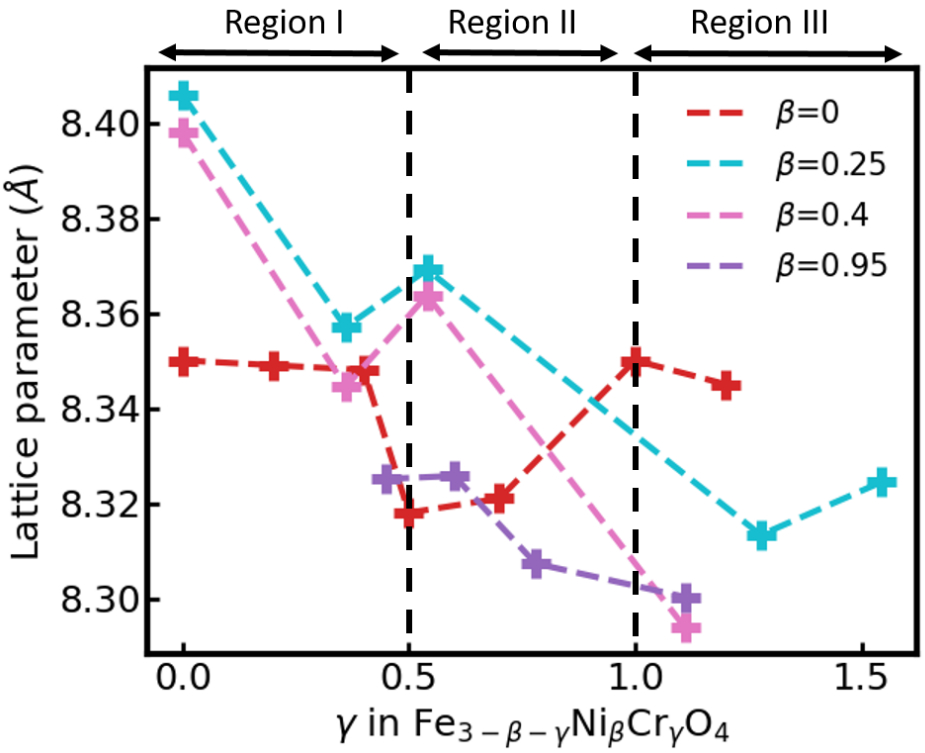

Figure 6.14: Lattice parameter variations function of γ in $Fe_{3-\beta-\gamma}Ni_{\beta}Cr_{\gamma}O_4$.

6.2.2.1 Nickel isoline $Fe_{3.0-\gamma}Ni_0Cr_{\gamma}O_4$ (β = 0)

This isoline corresponds to the binary Fe_3O_4-$FeCr_2O_4$ system. This binary system has been previously explored in our laboratory, and many articles describe this binary system[10,11]. A comparison with the results from the literature is presented in Figure 1.7.

Three regions are observed, in accordance with the fine structure, illustrated in Figure 6.16. The region I extends from γ = 0 to γ = 0.5 in bulk (Francombe *et al.*) and in thin films (Pinho *et al.*). The decreased in lattice parameter is associated with the progressive filling of O_h site by Cr^{3+} (0.62 Å), which replace $Fe_{O_h}^{3+}$ (0.64 Å). The second region extends from γ = 0.5 to γ = 1.0 in thin films, and to γ = 1.3 in bulk. This region exhibits an increase of the lattice parameter linked to a decrease of the inversion parameter. The last region exhibits a new decrease. The iron occupancies continue to decrease, at the exception of $Fe_{T_d}^{2+}$ occupancy that would continue to increase to reach 1.0 when γ = 2.0. Therefore, the $FeCr_2O_4$ will exhibit a normal spinel structure.

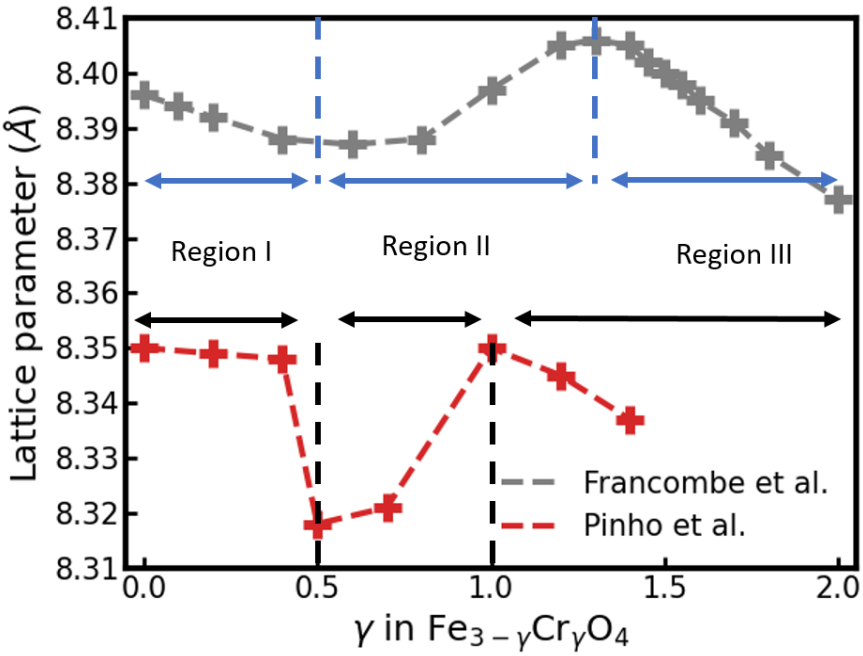

Figure 6.15: Evolution of the lattice parameter as a function of the Cr doping. The red crosses present the bulk variations, while the gray crosses depict the thin film variations. Adapted from Pinho[12].

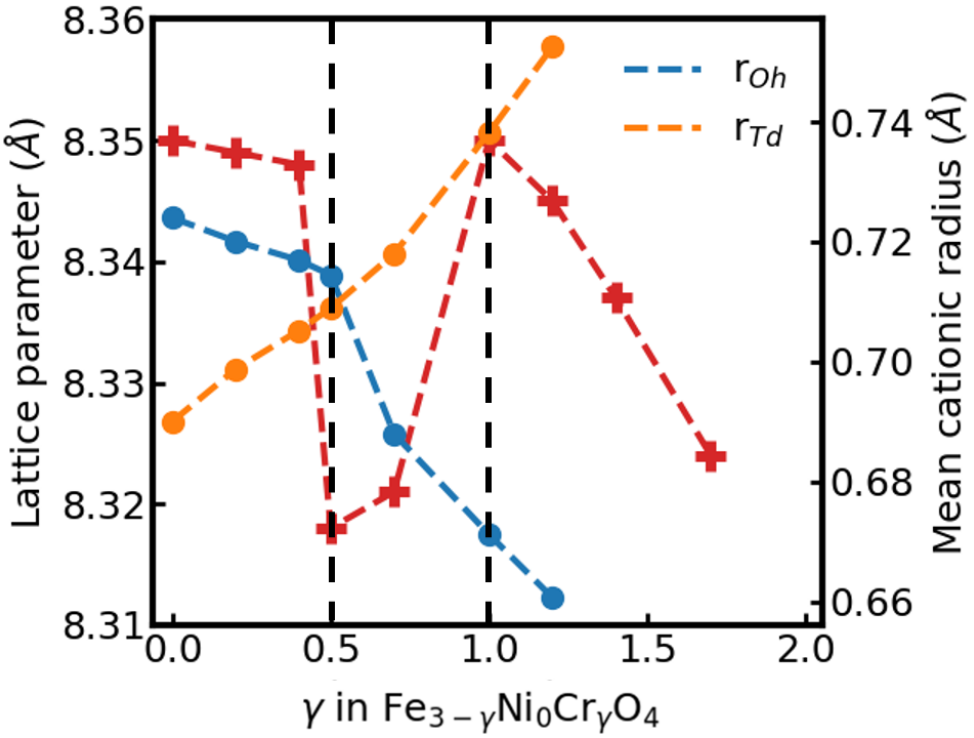

Figure 6.16: Variations of the lattice parameter with the mean cationic radius in $Fe_{3.0-\gamma}Ni_0Cr_\gamma O_4$. The lattice parameter (red curve) is indicated at the left, the mean cationic radius at the right. r_{Td} is shifted by +0.2 Å.

6.2.2.2 Nickel isolines $Fe_{2.75-\gamma}Ni_{0.25}Cr_\gamma O_4$ (β=0.25) and $Fe_{2.60-\gamma}Ni_{0.40}Cr_\gamma O_4$ (β=0.40)

Figure 6.17 shows the variations of the mean cationic radius and the lattice parameters of the revised model in the case of the $Fe_{2.75-\gamma}Ni_{0.25}Cr_\gamma O_4$ and $Fe_{2.60-\gamma}Ni_{0.40}Cr_\gamma O_4$ series. The two black dotted lines present the regions identified for the case where β = 0.

In these cases, no samples exhibit a stoichiometry corresponding to the region II have been synthesized. Nevertheless, two distinct regions in the two isolines are observed, separated at γ = 0.50. In region I, no $Fe_{T_d}^{2+}$ is observed. The $Fe_{O_h}^{3+}$ decrease starkly (as more $Cr_{O_h}^{3+}$ is introduced in the structure), the $Fe_{O_h}^{2+}$ remains around 1.0 for (a) and 0.80 for (b), and $Fe_{T_d}^{3+}$ occupancy remains constant at 1.0. Consequently, the inversion parameter remains constant at 1.0. Overall, the lattice parameter decrease in this region, related to the r_{Oh} decrease.

In the region II, there is a notable decrease in $Fe_{O_h}^{3+}$, $Fe_{O_h}^{2+}$, and $Fe_{T_d}^{3+}$ occupancies. $Fe_{O_h}^{3+}$ occupancy even reaches zero. However, once in the region III, the occupancy of these three species is almost constant, with a slight decrease observed for $Fe_{O_h}^{2+}$ and $Fe_{T_d}^{3+}$. Fe^{2+} begins to occupy the T_d sites. Consequently, the inversion parameter starts to decrease. The resulting lattice parameter exhibits the same variations than r_{Oh}: a pronounced decreasing in the region II, followed by a near-constant value. r_{Td} exhibits an invert variation: a stark increase followed by a near constant value.

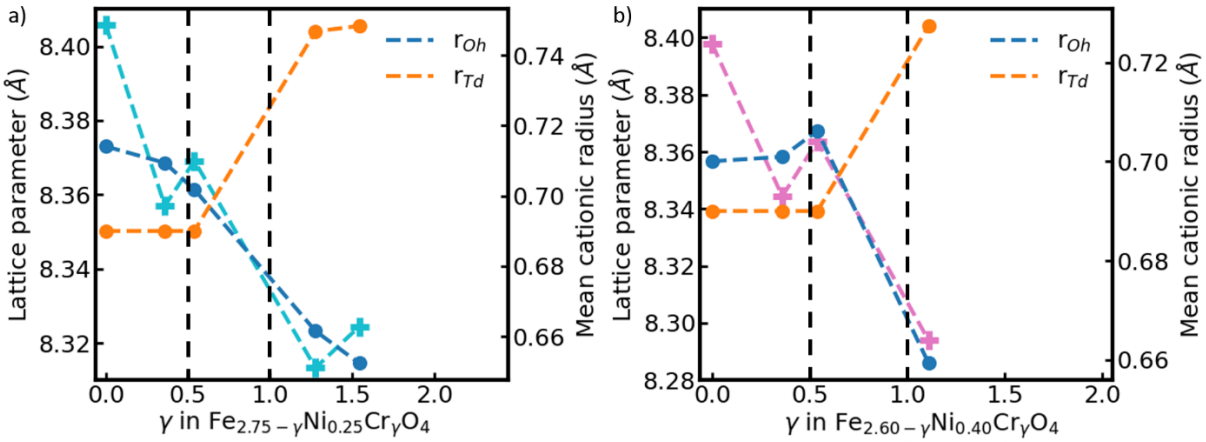

Figure 6.17: Variations of the lattice parameter with the mean cationic radius in $Fe_{2.75-\gamma}Ni_{0.25}Cr_\gamma O_4$ (a) and in $Fe_{2.60-\gamma}Ni_{0.40}Cr_\gamma O_4$ (b). The lattice parameter (cyan and pink curves) is indicated at the left, the mean cationic radius at the right. r_{Td} is shifted by +0.2 Å.

6.2.2.3 Nickel isoline $Fe_{2.05-\gamma}Ni_{0.95}Cr_\gamma O_4$ (β = 0.95)

This isoline corresponds to the $NiFe_2O_4$-$NiCr_2O_4$ binary system. A comparison of the samples extracted from this work and the literature[13–18] is shown in Figure 6.18. The variations are divided into two regions, with a boundary at γ = 1.0.. The region I exhibits a decrease of the lattice parameter, due to the replacing of $Fe_{O_h}^{3+}$ (0.64 Å) by $Cr_{O_h}^{3+}$ (0.62 Å), while the region II exhibits an increase due to the progressive replacing of $Fe_{T_d}^{3+}$ (0.49 Å) by $Fe_{T_d}^{2+}$ (0.63 Å). The samples of this study demonstrate the same variations observed in the literature, *i.e.* an overall decrease until γ = 1.0. The purple points are situated at the mean of the other studies from the literature, with the exception of the x = 0.6 data point. The samples from this study exhibit a relatively low Cr content (up to γ =1.0), which excludes the observation of the aforementioned increase.

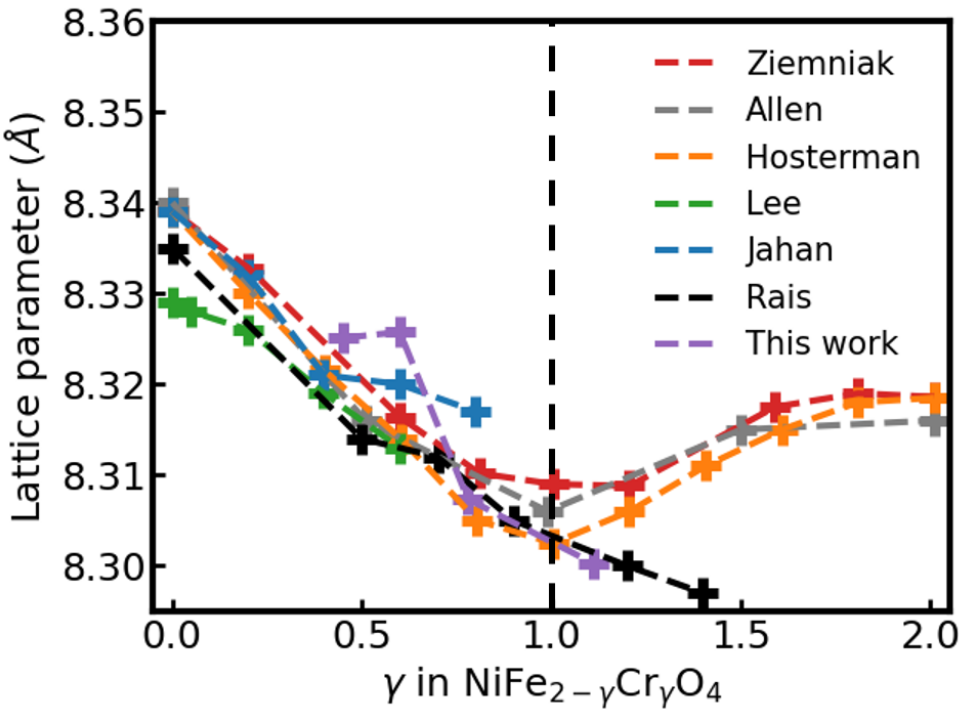

Figure 6.18: Evolution of the lattice parameter as a function of the chromium content in the $Fe_{2.0-\gamma}Ni_{1.0}Cr_\gamma O_4$ series in this work and coming from different authors.

Figure 6.19 shows the variations of the mean cationic radius in the case of the $Fe_{2.05-\gamma}Ni_{0.95}Cr_\gamma O_4$ series. The slight jump at γ = 0.6 is linked to the slight drop in Ni stoichiometry (see Figure 6.19). The occupancy of all iron species decreases slightly, at the exception of $Fe_{T_d}^{2+}$. The inversion parameter also decreases. Unfortunately, no samples was synthetized in the region II, but it can be expected that $Fe_{T_d}^{2+}$ will replace $Fe_{T_d}^{3+}$, thus decreasing the inversion parameter.

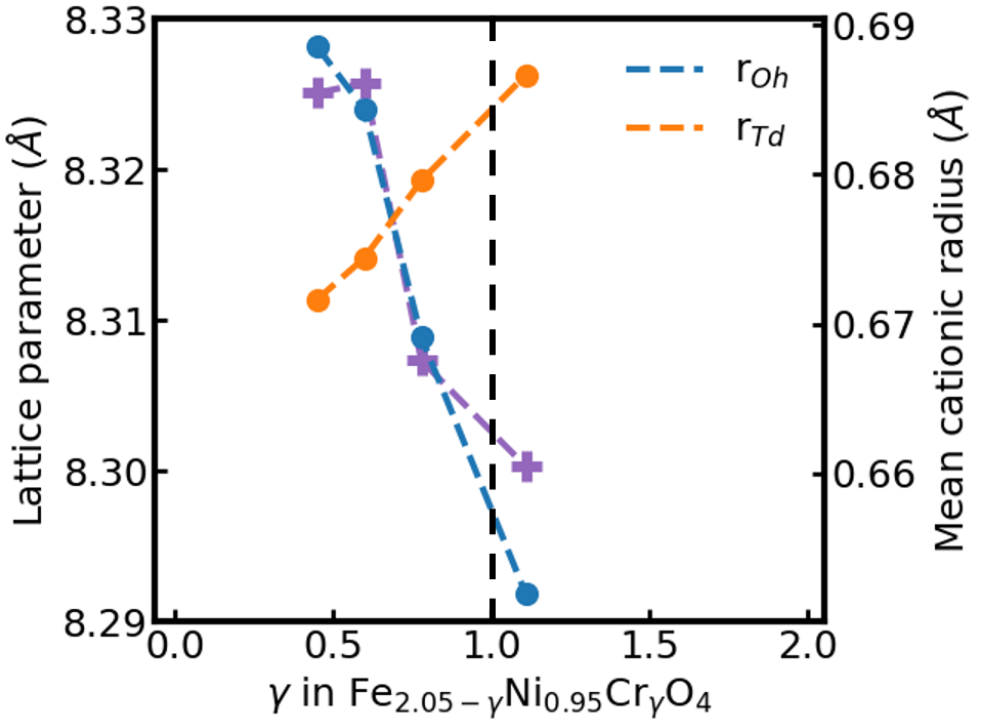

Figure 6.19: Variations of the lattice parameter with the mean cationic radius in $Fe_{2.05-\gamma}Ni_{0.95}Cr_{\gamma}O_4$. The lattice parameter (purple curve) is indicated at the left, the occupancies at the right. r_{Td} is shifted by +0.15 Å.

The overall variation of cationic species in function of the nickel isoline is presented in Table 6.5. Increasing β results in the disappearing of a region (region II). The region II for β = 0.25 and β = 0.40 requires more samples to be analyzed.

Table 6.5: Variations of cationic iron species for the different nickel isolines.

Isoline		LP	$Fe_{T_d}^{3+}$	$Fe_{T_d}^{2+}$	$Fe_{O_h}^{3+}$	$Fe_{O_h}^{2+}$
β=0	Region I	↘	↘	↗	↘↘	↘
	Region II	↗	↘↘	↗↗	≈	↘↘
	Region III	↘	↘↘	↗↗	↘↘	↘↘
β=0.25 and β=0.40	Region I	↘	1	0	↘↘	≈
	Region II	↘	↘↘	↗↗	↘↘	↘↘
	Region III	≈	≈	≈	0	↘
β=0.95	Region I	↘	↘	↗	↘	↘↘
	Region II	↗	↘↘	↗↗	0	0

6.2.3 Conclusions on the relation between the fine structure and the cationic ordering

Some series of samples with identical content of nickel and chromium has been analyzed. However, the iron isolines contain few samples and it is not possible to draw some tendencies from these isolines.

For the chromium isolines, three of them have been analyzed. Two region of variations (separated at β = 0.40) are present in all of them, but the variations of the lattice parameter evolves with the increase of γ.

- In the γ = 0 isoline (corresponding to Fe_3O_4-$NiFe_2O_4$ binary system), our samples present lattice parameter in agreement with those of the literature of nanoparticles. The region I show an increase of the lattice parameter, related to a decrease of $Fe_{O_h}^{2+}$ occupancy. The region II present a decrease of the lattice parameter linked to a decrease of $Fe_{O_h}^{3+}$. The T_d site is solely occupied by Fe^{3+}.
- In the γ = 0.50 isoline, the region I exhibits an increase of the lattice parameter, related to a decrease of iron cations in O_h sites ($Fe_{O_h}^{3+}$ and $Fe_{O_h}^{2+}$). The region II shows a decrease of the lattice parameter link with the decrease of $Fe_{O_h}^{2+}$ and the increase of $Fe_{T_d}^{2+}$ occupancies.
- In the γ = 1.04 isoline, the region I exhibits few variations of the lattice parameter. The iron decreases in O_h sites ($Fe_{O_h}^{3+}$ and $Fe_{O_h}^{2+}$), and the $Fe_{T_d}^{2+}$ increases. From these two influences, the lattice parameter remains identical. The region II shows a decrease of the lattice parameter compared to the first region, but exhibits few variations overall. link with the decrease of $Fe_{O_h}^{2+}$ and the increase of $Fe_{T_d}^{2+}$ occupancies. The drop is link to the drop of $Fe_{T_d}^{2+}$ occupancy. After this drop, the T_d occupancy does not vary, and the progressive disappearance of Fe in O_h site is filled with $Ni_{O_h}^{2+}$, which results in no variations for the lattice parameter.

For the nickel isolines, four of them have been analyzed. At β = 0, three regions are discernible (boundaries at γ = 0.50 and γ = 1.0), but at β = 1.0, only two regions are visible.

- In the β = 1 isoline (corresponding to Fe_3O_4-$FeCr_2O_4$ binary system), our samples present lattice parameter below bulk samples. The region I exhibits a decrease of the lattice parameter link to the decrease of $Fe_{O_h}^{3+}$. The region II exhibits an increase of the lattice parameter, related to a $Fe_{O_h}^{2+}$ decrease. The region III exhibits a decrease of the lattice parameter, link to the overall decrease of $Fe_{O_h}^{2+}$, $Fe_{O_h}^{3+}$ and $Fe_{T_d}^{3+}$.
- In the β = 0.25 and β = 0.40 isolines, the region II progressively merge with the region I. These two regions exhibits a decrease of the lattice parameter,

related to a significant decrease of $Fe_{O_h}^{3+}$ occupancy. In the region III, the lattice parameter seems to remain identical. The iron cationic distribution sees the presence of $Fe_{T_d}^{2+}$, but does not evolve in this region.

- In the β = 0.95 isoline (corresponding to $NiFe_2O_4$-$NiCr_2O_4$ binary system), our samples present lattice parameter in agreement with those of the literature. The region II has disappeared, and only two region of variations appears (separated at γ = 1.0). The region I exhibits a decrease of the lattice parameter, related to the decrease of $Fe_{O_h}^{2+}$, while the region II should display an increase, related to an increase of $Fe_{T_d}^{2+}$, according to the literature.

6.3 CORRELATIONS BETWEEN CATIONIC ORDERING AND MAGNETIC PROPERTIES

The magnetic properties and specifically the double-exchange, super-exchange interactions in spinel oxides are dependent of the angles between the different cations in the interstitial sites. Consequently, these angles are key parameters and the literature provides different equations which can be used to calculate their values[19]. The first part of this section will be dedicated to the calculations of the angles, the subsequent subsections will examine the variations of the magnetic properties as a function of these different angles.

6.3.1 Angle calculation

The different angles in the spinel structure indicated in the Figure 6.20 are the more favorable angles for an effective magnetic interaction[20,21].

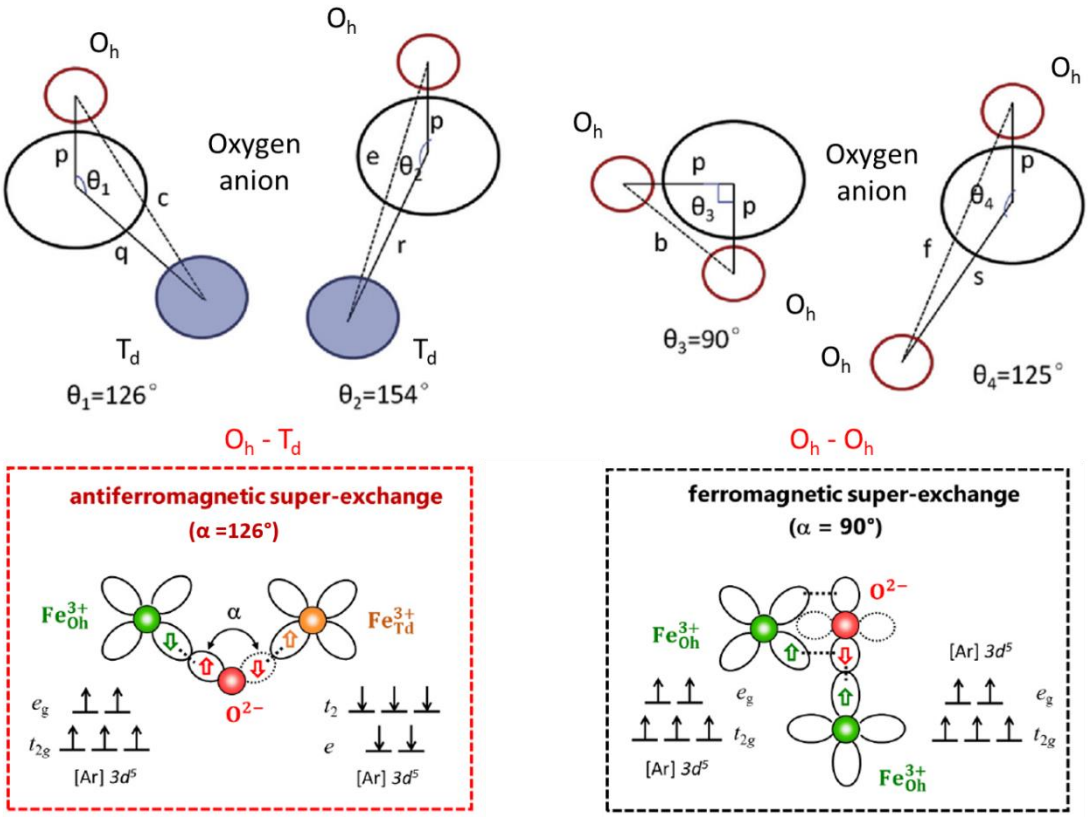

Figure 6.20: Most favorable bond angles for effective magnetic interactions and super-exchanges mechanisms. Extracted from Yan et al.[22]

The distances and angles indicated in Figure 6.20 can be calculated from the equations displayed in Table 6.6.

Table 6.6: Equations for distances and angles displayed in Figure 6.20.

Distance Cation-Cation	Distance Cation-Oxygen	Angles
$b = \frac{2a\sqrt{2}}{8}$	$p = R_{Oh} = a\sqrt{2\left(u-\frac{3}{8}\right)^2+\left(\frac{5}{8}-u\right)^2}$	$\theta_1 = cos^{-1}\left(\frac{p^2+q^2-c^2}{2pq}\right)$
$c = \frac{a\sqrt{11}}{8}$	$q = R_{Td} = \frac{a}{\sqrt{3}}\left(u-\frac{1}{4}\right)$	$\theta_2 = cos^{-1}\left(\frac{p^2+r^2-e^2}{2pr}\right)$
$e = \frac{3a\sqrt{3}}{8}$	$r = \frac{a}{\sqrt{11}}\left(u-\frac{1}{4}\right)$	$\theta_3 = cos^{-1}\left(\frac{2p^2-b^2}{2p^2}\right)$
$f = \frac{2a\sqrt{6}}{8}$	$s = \frac{a\sqrt{3}}{3}\left(u+\frac{3}{8}\right)$	$\theta_4 = cos^{-1}\left(\frac{p^2+s^2-f^2}{2ps}\right)$

For a first approximation, only the O_h-O_h, and O_h-T_d nearest neighbors exchanges interactions will be studied (lengths b and c with angles θ_3 and θ_1, respectively). The T_d-T_d distance is more important than O_h-O_h, and O_h-T_d distances, this is why the T_d-T_d interaction will be disregarded. These formulae are applied on samples for which the fine structure and magnetic properties are known, and the results are presented in Table 6.7.

Table 6.7: Angles between the different sites for sample studied in XMCD.

Stoichiometry	O_h-O_h (°)	O_h-T_d (°)
$Fe_{2.22}Ni_{0.78}O_4$	91.12	124.47
$Fe_{2.82}Ni_{0.18}O_4$	90.99	124.56
$Fe_{2.64}Ni_{0.36}O_4$	91.35	124.30
$Fe_{2.85}Ni_{0.15}O_4$	91.08	124.50
$Fe_{2.43}Ni_{0.21}Cr_{0.36}O_4$	90.96	124.58
$Fe_{1.44}Ni_{0.45}Cr_{1.11}O_4$	92.76	123.29
$Fe_{1.50}Ni_{0.90}Cr_{0.60}O_4$	92.11	123.76
$Fe_{1.53}Ni_{1.02}Cr_{0.45}O_4$	91.94	123.88
$Fe_{1.80}Ni_{0.69}Cr_{0.51}O_4$	91.10	124.48
$Fe_{2.07}Ni_{0.39}Cr_{0.54}O_4$	91.07	124.50
$Fe_{2.22}Ni_{0.42}Cr_{0.36}O_4$	91.15	124.45
$Fe_{2.25}Ni_{0.21}Cr_{0.54}O_4$	92.56	123.43
$Fe_{0.96}Ni_{0.93}Cr_{1.11}O_4$	91.21	124.40
$Fe_{1.86}Ni_{0.15}Cr_{0.99}O_4$	93.14	123.01
$Fe_{1.62}Ni_{0.33}Cr_{1.05}O_4$	93.66	122.63
$Fe_{1.44}Ni_{0.30}Cr_{1.29}O_4$	93.79	122.53
$Fe_{1.20}Ni_{0.24}Cr_{1.56}O_4$	93.07	123.06

The quaternary diagrams of these three angles are shown in Figure 6.21. It can be observed that the addition of chromium results in a decrease in both θ_1 and θ_5, while θ_3 has an inverse trend, increasing with the addition of chromium.

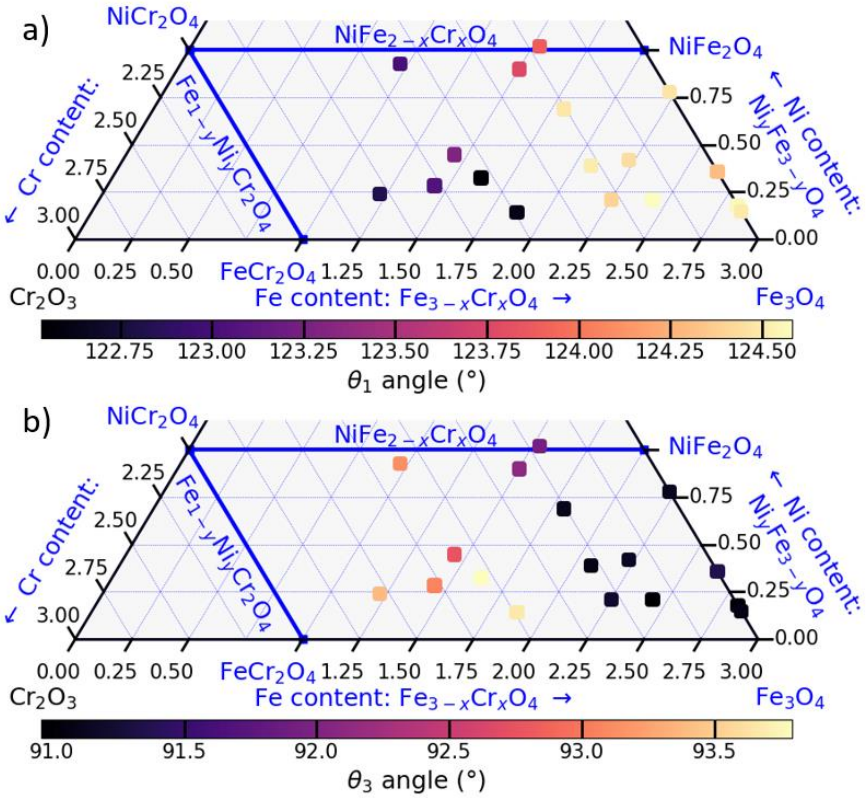

Figure 6.21: Various angles presented in the quaternary diagram. θ_1 (a), θ_3 (b), and θ_5 (c) correspond to the angle between O_h and T_d sites, O_h and O_h sites and T_d and T_d sites, respectively.

6.3.2 Link between magnetic properties and calculated angles

The M_S parameters obtained at T = 300 K (see chapter 4) are presented as a function of the various theta angles and the anion parameter (from revised model), in Figure 6.22.

The optimal magnetic properties are achieved when u_{avg} is approximately 0.375, which represents the ideal value. The aforementioned ideal value of the anion parameter thus implies ideal values of 126° for θ_1 and 90° for θ_3. It is evident that the ideal values are not reached. Nevertheless, the highest magnetic properties are obtained when the various angles move to the ideal value. The asymptotes for θ_1, and θ_3 are 124.5°, 91°, respectively. Similar variations are observed at lower temperatures.

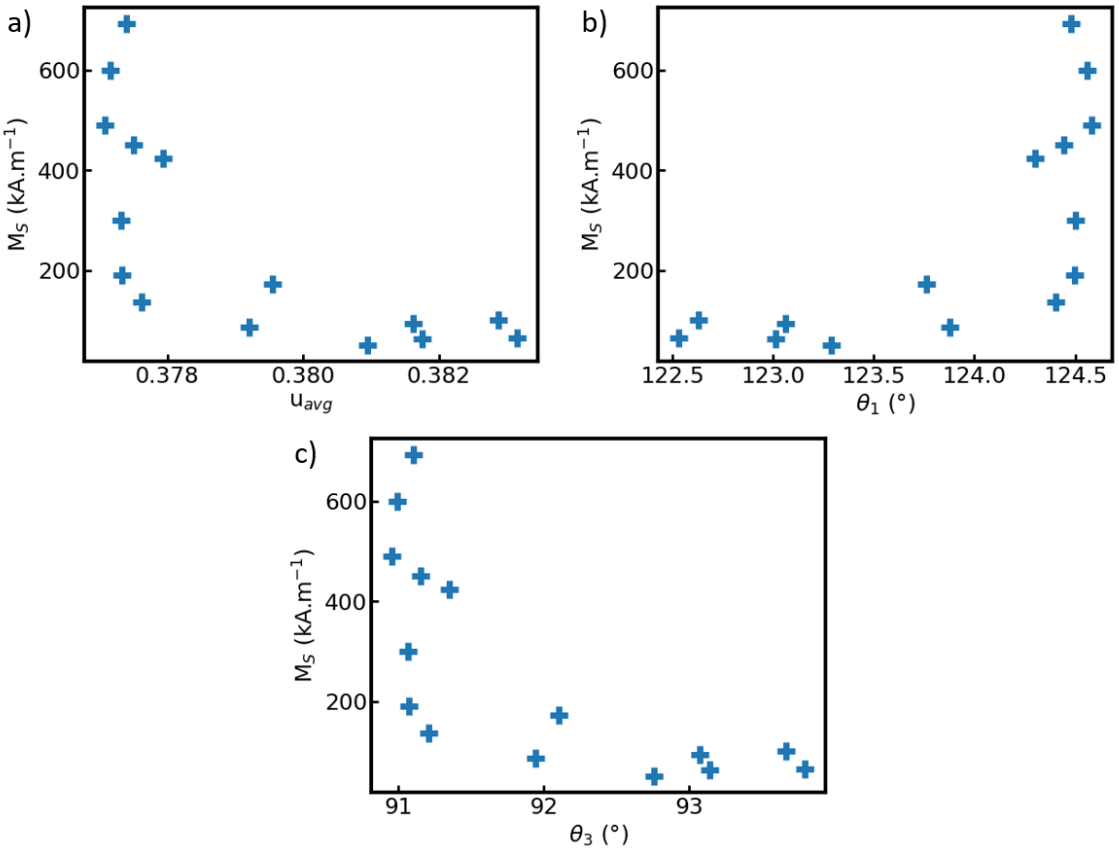

Figure 6.22: M_S variations at T = 300 K as a function of u_{avg} (a), θ_1 (b), θ_3 (c), and θ_5 (d).

Figure 6.23 shows the variations of M_R and H_C as a function of the u_{avg}. Similarly to variations observed in M_S, the highest magnetic properties are obtained for u_{avg} approaching 0.375.

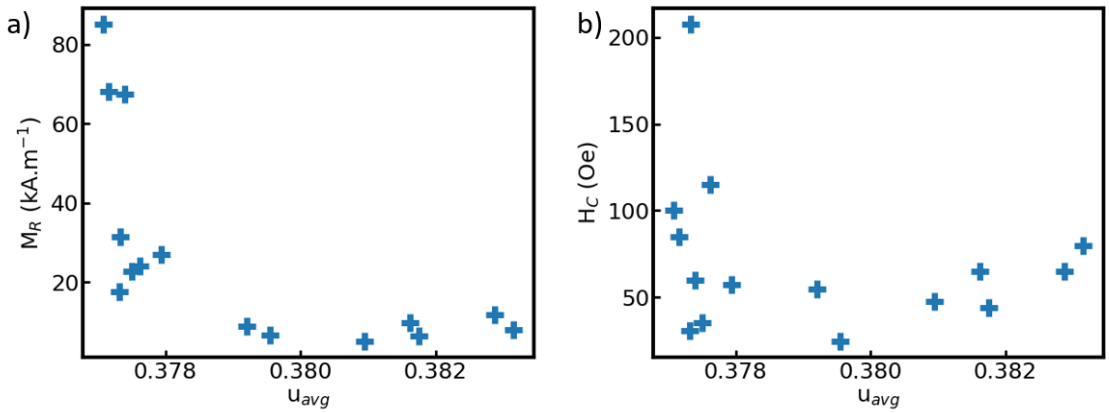

Figure 6.23: M_R (a) and H_C (b) variations at 300 K as a function of u_{avg}.

Two regions concerning these magnetic evolutions can be defined. The first region is the region where M_S is below 200 kA.m^{-1} (M_R below 20 kA.m^{-1} and H_C below 80 Oe, horizontal line). The subsequent region is the vertical line, where $u_{avg} < 0.378$ ($\theta_1 > 124°$, $\theta_3 < 91.5°$, and $\theta_5 > 77°$). The separation in two zones is indicated in Figure 6.24.

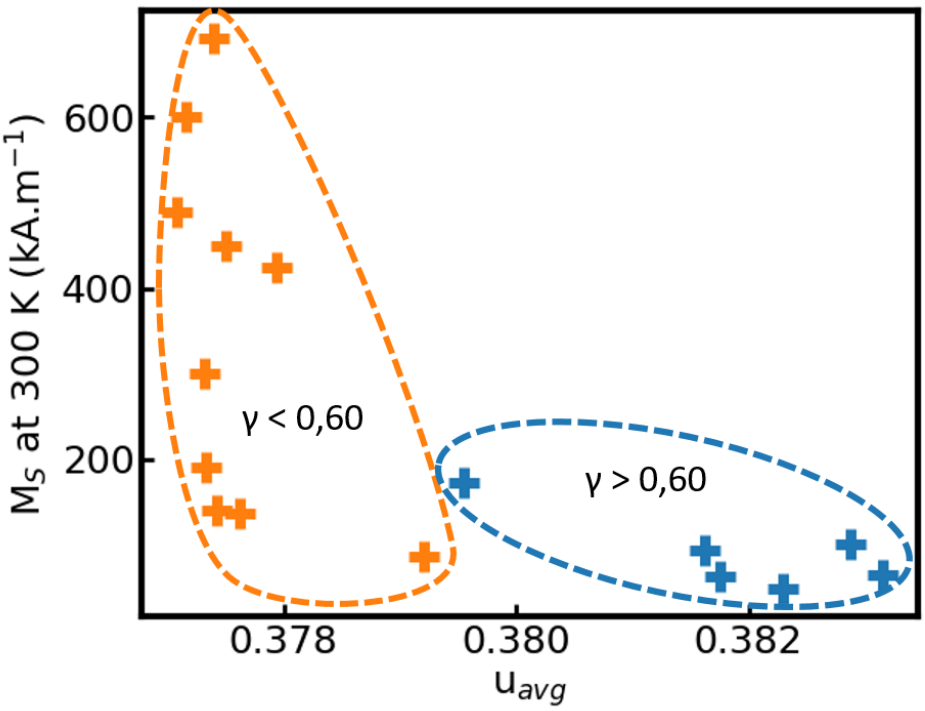

Figure 6.24: Separation in two zone of magnetic properties variations.

6.3.3 Magnetic properties variation for chromium enriched samples

All the samples in this region present a chromium content (γ) superior to 0.60. The different magnetic parameters as a function of the chromium content are presented in Figure 6.25 (a), (b) and (c), while the M_R variation as a function of nickel content (β) is presented in (d). The best correlations are obtained for H_C and M_S values in function of the chromium content, while the best relationship is obtained for M_R in function of the Ni content. M_S is decreasing with the increasing chromium content, while H_C exhibits an inverse trend. M_R displays no correlation with the chromium content (c), but exhibits a slight decrease with nickel stoichiometry. One of the explanation of the lowered magnetic properties with the addition of chromium is the distortion in the anion parameter induced by the chromium cations.

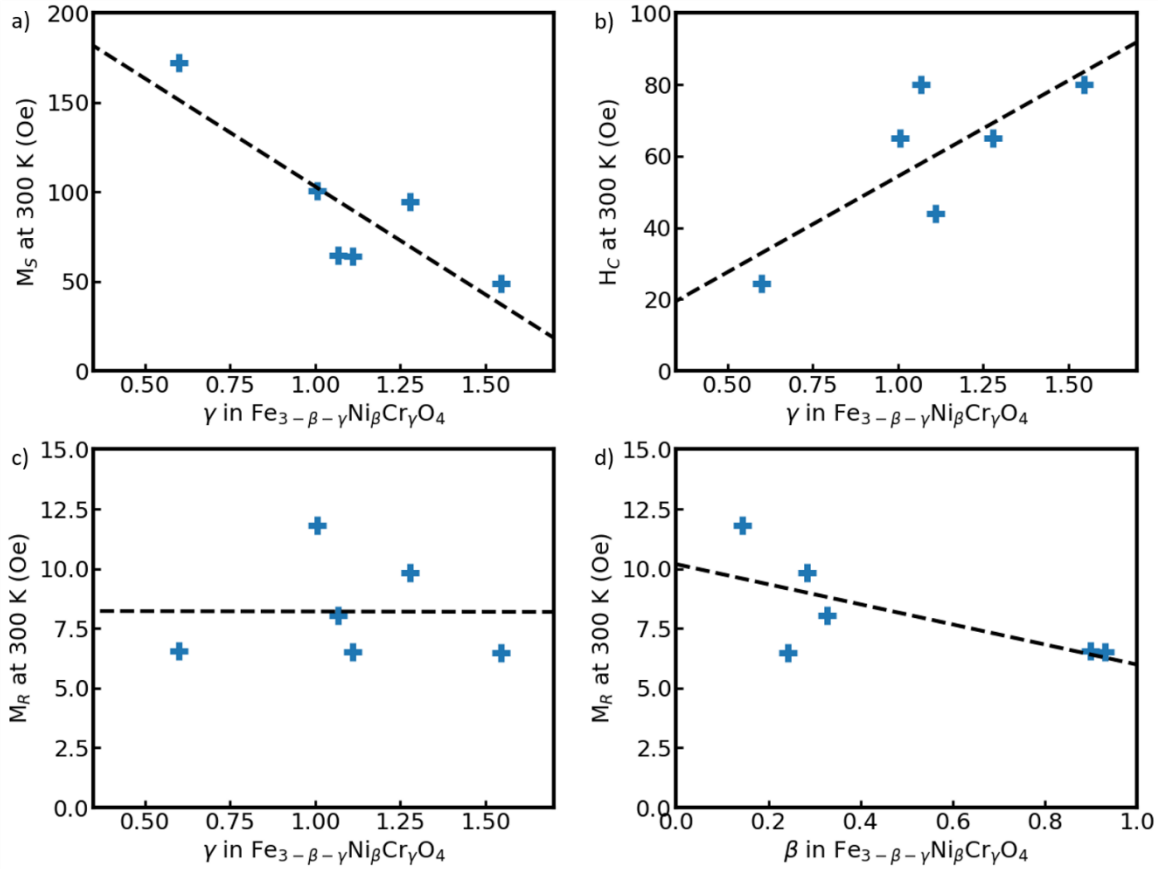

Figure 6.25: Variations of M_S (a) and H_C (b) as a function of the chromium content and variations of M_R (c) and (d) as a function of the chromium and nickel content respectively.

6.3.4 Magnetic properties variation for low chromium content sample

The second region exhibits two different behaviors, in function of the chromium content. The first behavior is represented with blue crosses and is composed of samples with γ < 0.45. The second behavior is composed of samples with 0.45 < γ < 0.60. The variations of the magnetic properties as a function of the relevant parameters is presented in Figure 6.26. The M_S and M_R properties are influenced by the occupancy of $Fe_{O_h}^{2+}$. Additionally, the sample possessing the lowest M_R and M_S (at $Fe_{O_h}^{2+}$ = 0.40) exhibits some Fe^{2+} in T_d site, whereas all the other blue sample exhibit a $Fe_{T_d}^{3+}$ of 1.0.

In regard of H_C, the variations are not evident and the separation in two regions is not clear for this parameter.

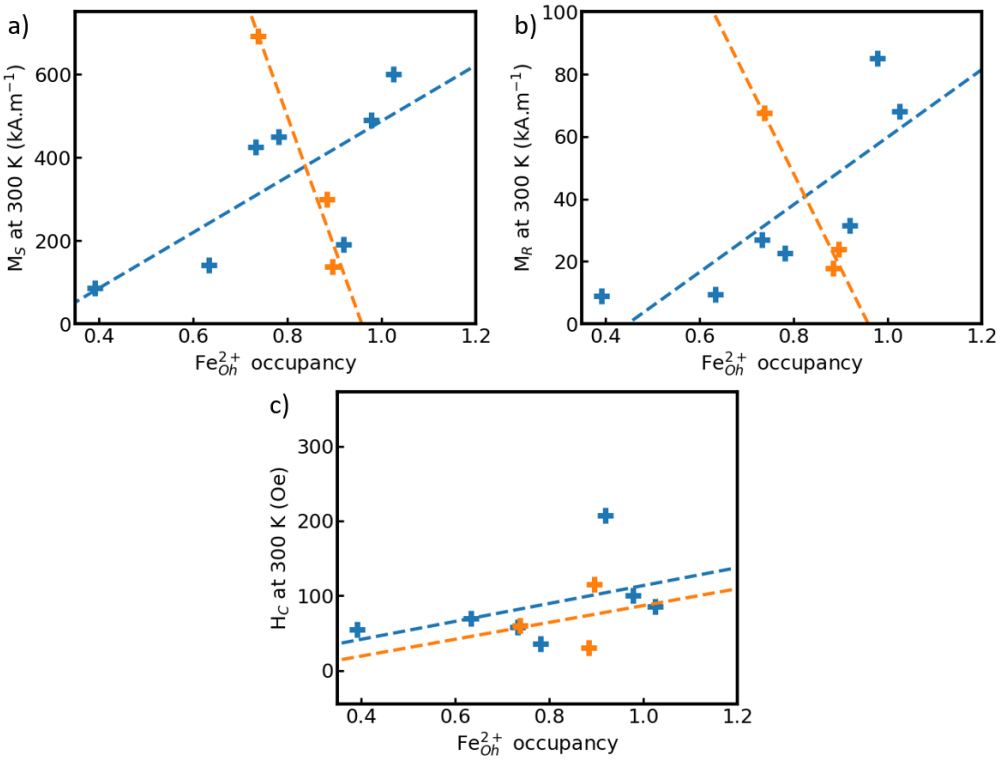

Figure 6.26: Variations of M_S (a), M_R (b), and H_C (c) as a function of the $Fe^{2+}_{O_h}$ content.

6.3.5 Conclusions on the relation between fine structure and magnetic properties

The requisite angles for super-exchange interactions have been calculated on the basis of the fine structure and the experimental lattice parameter. The magnetic parameters exhibit a two-regions variation with the angles. We deduce that the geometry is one of the factors in the degradation of magnetic properties with the increase in chromium content.

The initial region is defined by values of u greater than 0.378, which corresponds to a chromium content exceeding 0.60. In this region, the magnetic properties are influenced by the chromium content for M_S and H_C and by the nickel content for M_R.

The second region exhibits two distinct behaviors. The first behavior is observed for samples with chromium contents below 0.45, with the magnetic properties being highly influenced by $Fe^{2+}_{O_h}$ occupancy for M_S and M_R. The second region is composed of samples presenting between 0.45 and 0.60 chromium content, and the magnetic properties are also significantly influenced by $Fe^{2+}_{O_h}$ occupancy, however in an inverse trend. The H_C value does not exhibit a notable variation in response to any of the different parameters within this region.

6.4 BIBLIOGRAPHY

(1) Sickafus, K. E.; Wills, J. M.; Grimes, N. W. Structure of Spinel. *Journal of the American Ceramic Society* **1999**, *82* (12), 3279–3292. https://doi.org/10.1111/j.1151-2916.1999.tb02241.x.

(2) Hill, R. J.; Craig, J. R.; Gibbs, G. V. Systematics of the Spinel Structure Type. *Phys Chem Minerals* **1979**, *4* (4), 317–339. https://doi.org/10.1007/BF00307535.

(3) Al Maashani, M. S.; Khalaf, K. A.; Gismelseed, A. M.; Al-Omari, I. A. The Structural and Magnetic Properties of the Nano-CoFe2O4 Ferrite Prepared by Sol-Gel Auto-Combustion Technique. *Journal of Alloys and Compounds* **2020**, *817*, 152786. https://doi.org/10.1016/j.jallcom.2019.152786.

(4) Shannon, R. D. Revised Effective Ionic Radii and Systematic Studies of Interatomic Distances in Halides and Chalcogenides. *Acta Cryst A* **1976**, *32* (5), 751–767. https://doi.org/10.1107/S0567739476001551.

(5) Iranmanesh, P.; Tabatabai Yazdi, Sh.; Mehran, M. Effect of Ni Substitution on Structural, Optical and Magnetic Properties of Ferrite Nanoparticles Synthesized by Co-Precipitation Route. *Materials Science and Engineering: B* **2019**, *251*, 114442. https://doi.org/10.1016/j.mseb.2019.114442.

(6) Rana, G.; Johri, U. C. A Study on Structural and Magnetic Properties of Ni-Substituted Magnetite Nanoparticles. *Journal of Alloys and Compounds* **2013**, *577*, 376–381. https://doi.org/10.1016/j.jallcom.2013.05.184.

(7) Deepak, F. L.; Bañobre-López, M.; Carbó-Argibay, E.; Cerqueira, M. F.; Piñeiro-Redondo, Y.; Rivas, J.; Thompson, C. M.; Kamali, S.; Rodríguez-Abreu, C.; Kovnir, K.; Kolen'ko, Y. V. A Systematic Study of the Structural and Magnetic Properties of Mn-, Co-, and Ni-Doped Colloidal Magnetite Nanoparticles. *J. Phys. Chem. C* **2015**, *119* (21), 11947–11957. https://doi.org/10.1021/acs.jpcc.5b01575.

(8) Jin, C.; Zhang, Q.; Mi, W. B.; Jiang, E. Y.; Bai, H. L. Tunable Magnetic and Electrical Properties of Polycrystalline and Epitaxial $Ni_x Fe_{3-x} O_4$ Thin Films Prepared by Reactive Co-Sputtering. *J. Phys. D: Appl. Phys.* **2010**, *43* (38), 385001. https://doi.org/10.1088/0022-3727/43/38/385001.

(9) Kim, K. J.; Kim, M. H.; Kim, C. S. Structural Phase Transition, Electronic Structure, and Magnetic Properties of Sol-Gel-Prepared Inverse-Spinel Nickel-Ferrites Thin Films. *Journal of Magnetics* **2014**, *19* (2), 111–115. https://doi.org/10.4283/JMAG.2014.19.2.111.

(10) Francombe, M. H. Lattice Changes in Spinel-Type Iron Chromites. *Journal of Physics and Chemistry of Solids* **1957**, *3* (1), 37–43. https://doi.org/10.1016/0022-3697(57)90045-8.

(11) Robbins, M.; Wertheim, G. K.; Sherwood, R. C.; Buchanan, D. N. E. Magnetic Properties and Site Distributions in the System FeCr2O4-Fe3O4(Fe2+Cr2−xFex3+O4. *Journal of Physics and Chemistry of Solids* **1971**, *32* (3), 717–729. https://doi.org/10.1016/S0022-3697(71)80412-2.

(12) Pinho, P. V. B.; Chartier, A.; Menut, D.; Barbier, A.; Hunault, M. O. J. Y.; Ohresser,

P.; Marcelot, C.; Warot-Fonrose, B.; Miserque, F.; Moussy, J.-B. Stoichiometry Driven Tuning of Physical Properties in Epitaxial Fe3-xCrxO4 Thin Films. *Applied Surface Science* **2023**, *615*, 156354. https://doi.org/10.1016/j.apsusc.2023.156354.

(13) Ziemniak, S. E.; Gaddipati, A. R.; Sander, P. C. Immiscibility in the NiFe2O4–NiCr2O4 Spinel Binary. *Journal of Physics and Chemistry of Solids* **2005**, *66* (6), 1112–1121. https://doi.org/10.1016/j.jpcs.2005.01.009.

(14) Allen, G. C.; Jutson, J. A.; Tempest, P. A. Characterization of Nickel-Chromium-Iron Spinel-Type Oxides. *Journal of Nuclear Materials* **1988**, *158*, 96–107. https://doi.org/10.1016/0022-3115(88)90159-6.

(15) Hosterman, B. D. Raman Spectroscopic Study of Solid Solution Spinel Oxides, University of Nevada, Las Vegas. https://doi.org/10.34917/2476131.

(16) Lee, S. H.; Yoon, S. J.; Lee, G. J.; Kim, H. S.; Yo, C. H.; Ahn, K.; Lee, D. H.; Kim, K. H. Electrical and Magnetic Properties of NiCrxFe2ÀxO4 Spinel (0 x 0.6). *Materials Chemistry and Physics* **1999**, 6.

(17) Jahan, N.; Chowdhury, F.-Z.; Zakaria, A. K. M. Structural and Electrical Properties of Chromium Substituted Nickel Ferrite by Conventional Ceramic Method. *Materials Science-Poland* **2016**, *34* (1), 185–191. https://doi.org/10.1515/msp-2016-0028.

(18) Rais, A.; Gismelseed, A. M.; Al-Omari, I. A. Cation Distribution and Magnetic Properties of Nickel-Chromium Ferrites NiCrxFe2-xO4 (0 ≤x ≤ 1.4). *phys. stat. sol. (b)* **2005**, *242* (7), 1497–1503. https://doi.org/10.1002/pssb.200440022.

(19) Lakhani, V. K.; Pathak, T. K.; Vasoya, N. H.; Modi, K. B. Structural Parameters and X-Ray Debye Temperature Determination Study on Copper-Ferrite-Aluminates. *Solid State Sciences* **2011**, *13* (3), 539–547. https://doi.org/10.1016/j.solidstatesciences.2010.12.023.

(20) Goodenough, J. B. Theory of the Role of Covalence in the Perovskite-Type Manganites [La, M(II)]MnO$_{3}$. *Phys. Rev.* **1955**, *100* (2), 564–573. https://doi.org/10.1103/PhysRev.100.564.

(21) Kanamori, J. Theory of the Magnetic Properties of Ferrous and Cobaltous Oxides, I. *Prog. Theor. Phys.* **1957**, *17* (2), 177–196. https://doi.org/10.1143/PTP.17.177.

(22) Yan, Z.; Luo, J. Effects of CeZn Co-Substitution on Structure, Magnetic and Microwave Absorption Properties of Nickel Ferrite Nanoparticles. *Journal of Alloys and Compounds* **2017**, *695*, 1185–1195. https://doi.org/10.1016/j.jallcom.2016.08.333.

7 CONCLUSIONS AND PERSPECTIVES

This PhD thesis was divided in two distinct parts. The first part is the study of the magnetic domain walls in an antiferromagnetic model compound: NiO. In the second part, a thorough study of the structural and magnetic properties of epitaxial $Fe_{\alpha}Ni_{\beta}Cr_{\gamma}O_4$ thin films was performed in correlation with the fine structure (*i.e.* cationic distribution) and the lattice parameter. This last chapter briefly summarizes the mains results of each chapter and discusses the perspectives of this work.

7 CONCLUSIONS AND PERSPECTIVES

This thesis is comprised of two distinct parts, each employing a unique methodology. This section presents an overview of each part, followed by an examination of the insights and implications deduced from this research.

The initial section of this thesis (Chapter 2) was dedicated to the examination of magnetic Domain Walls (DWs) in the NiO antiferromagnetic (AFM) oxide by using atomic spin dynamics.

NiO was selected as it represents one corner of the Fe-Cr-Ni-O quaternary phase diagram explored in this thesis. In order to simulate the complex magnetic structure of domains, two uniaxial anisotropy constants were introduced, which allowed for the simulation of both the called "T" and "S" magnetic domains. The second decision was to use high values for these anisotropy constants, in order to simulate DWs in reasonable simulation cell. Once the methodology described, the S and T DWs were simulated.

The 60° and 120° S DWs were successfully simulated, whereas the 180° S DW, was only obtained through parasitic interferences. At the atomic scale, the structure reveals a 60° or 120° rotation of the AFM vector. The physical properties of these S DWs with pseudo XMLD-PEEM and NVM is obtained. The pseudo XMLD-PEEM displays a symmetrical behavior from the two sides of the DW, whereas NVM image exhibits variations in the components of the signal, while the norm remains constant through the DW.

The T DWs exhibit a more complex behavior. The width of the DW is the result of two distinct contributions. The first part is a rotation of the AFM vector, which passes through the common direction at the two T planes. The most intriguing part concerns the splitting zone. This zone is a consequence of the AFM nature of NiO. The atomic spins maintains their AFM alignment between T planes, while breaking their FM alignment in each T-plane in order to move from one T plane to the other. This splitting zone is geometrically mandatory. The widths observed in XMLD-PEEM exhibit an asymmetrical behavior, which can be attributed to the presence of the splitting zone. The higher the rotation to reach the two S directions, the higher the width.

The identified mechanism between width and rotations provides a relevant criterion to distinguish between T DWs. This allows the four DWs of each $T_{(100)}$ and $T_{(110)}$ walls, which are independent by symmetry, to be separated into a singlet and a triplet. The separation into singlet/triplet was not performed in experiments by Arai *et al.*[1] for their estimations of widths. The calculations, conducted with varying K_u^T, from J_2 to 1/10 J_2, indicate a linear dependency between the DW width and the square of $1/K_u^T$.

The fitting of the spinglet and triplet identified allows for the estimation of the experimental width, with a distinction made in the distribution of the DW widths measured by Arai *et al.*[1].

The study of NVM signal reveals a strong signal of approximately 20 µT. This signal is exclusively observed when the T side is aligned in FM formation. The signal diminishes rapidly to zero following the passage of the domain wall.

Some perspectives, opened by this work, can be discussed. A custom version of the Vampire simulation code[2–4] was used to study the AFM NiO with two anisotropy constants. In the same manner, other AFM systems have two anisotropy constants such as CoO or MnO. These systems are interesting for spintronics applications even if their Néel temperature (T_N) is below 300 K. Another AFM system potentially interesting for spintronic is Cr_2O_3. Different teams have tried to increase the T_N by strain engineering[5]. The Vampire code could be used to study the internal AFM structure and the different parameter influencing the DW width in these systems. A complex structure observed in NiO can be simulated such a crossing between a $T_{(100)}$ and a $T_{(110)}$ wall. On others codes, the addition of spin dynamic with atomic dynamic in the LAMMPS code for example can open the possibility to simulate the formation of DWs l, for example from an oxidation of a Ni alloy.

The second part of this thesis was devoted to the crystalline growth and the relations between the fine structure and the structural or magnetic properties of thin films in the Fe-Ni-Cr-O quaternary phase diagram.

In Chapter 4, we have first shown that it is possible to grow epitaxial $Fe_\alpha Ni_\beta Cr_\gamma O_4$ (111) thin films on α-Al_2O_3 (0001) for different (α, β, γ) compositions. For a high chromium content (γ), the use of a spinel-type substrate: $MgAl_2O_4$ ((001) or (111) orientations) has been necessary for elaborating spinel oxides. The α, β or γ content has been precisely controlled by using individual effusion cells in an oxygen-assisted molecular beam epitaxy (OA-MBE) setup. The high energy electron diffraction (RHEED) images recorded in real-time have shown a good epitaxy of the oxide layers with a 2D growth mode and low roughnesses, as confirmed by the X-ray reflectivity analysis. The chemical composition of each sample has been carefully probed by using X-ray photoemission spectroscopy (XPS). The center and bottom of the spinel zone in the Fe-Ni-Cr-O quaternary diagram has been explored, while the top left (zone around $NiCr_2O_4$, with different iron content) and top right corner (zone around $NiFe_2O_4$ with different chromium content) more difficult to investigate. A thorough structural analysis by X-ray diffraction (XRD) allowed to put on view the high crystalline quality of the layers and to determine the epitaxial relationships according to the selected substrates and the lattice parameter as a function of the stoichiometry.

7 CONCLUSIONS AND PERSPECTIVES

In Chapter 5, the cationic site distribution in the different $Fe_\alpha Ni_\beta Cr_\gamma O_4$ samples has been investigated using two synchrotron-based techniques: X-ray magnetic circular dichroism (XMCD) and Resonant X-ray diffraction (RXD). In XMCD, the fit of each cation (Fe, Ni, Cr) L_3 edge has been successfully performed by using theoretical contributions of each cation. The chromium is solely Cr^{3+} in O_h sites. The nickel has the Ni^{2+} valence state and localized in O_h sites, even if for two samples, the presence of Ni^{2+} in T_d sites can be observed without a clear explanation. By developing RXD experiments (on Ni and Fe K edges), the careful study of several diffraction peaks allowed us to probe again the cationic site distribution. The simulations of RXD spectra with FDMNES has been performed. The experimental curves and the calculated ones are in good agreement. The hypothesized cationic distribution in FDMNES is therefore correct. It signifies that no Ni^{2+} in T_d sites is observed in the three RXD samples, and that the ratio of iron in O_h and in T_d sites is correct. Additionally, these two techniques are in good agreement with each other.

In Chapter 6, the cationic site distributions obtained previously have been used in a model, linking the fine structure and the experimental lattice parameter. This allows us to calculate the anion parameter and the theoretical lattice parameter. From these two values, it is also possible to calculate the different angles between the cationic sites within the spinel structure. With this model and the knowledge of the experimental lattice parameter, a first approximation of the cationic distribution can be established. The lattice parameter and the fine structure have been studied in two different cases: isoconcentration of chromium and nickel. The isoconcentrations in iron have too few samples to draw some tendencies. The isoconcentration in nickel revealed interesting mechanisms. Indeed, at $\beta = 0$, three regions (boundaries at 0.5 and 1.0) have been identified. Increasing β resulted in the progressive merging of the region II with the region I for $\beta = 0.25$ and $\beta = 0.40$. At $\beta = 1$, the region II has disappeared and only two regions have been observed. Concerning the chromium isolines, at $\gamma = 0$, the lattice parameter exhibited two regions (increase followed by a decrease) with a boundary at $\beta = 0.4$. The same trend has been observed for $\gamma = 0.5$, whereas at $\gamma = 1.04$, two regions of nearly identical lattice parameter are separated by a drop in lattice parameter, passing from region I to region II. Concerning the magnetic properties, two regions were observed. The samples having an oxygen localization parameter, u, close to the ideal value of 0.375 exhibited the highest magnetic properties. This ideal u value is linked with the different angles associated to the super-exchange interactions. By decreasing the u value, the magnetic exchange interaction is decreasing. The samples with a high chromium content ($\gamma > 0.60$) showed poor magnetic properties due to the differences between the experimental angles and the ideal theoretical values. The M_S and H_C parameters are related to the chromium content while the M_R parameter seems to be link

with the nickel content. In the samples having the best magnetic properties (*i.e.* for γ < 0.60), a correlation with $Fe_{O_h}^{2+}$ has been identified for M_S and M_R. The H_C parameter did not show a clear correlation with $Fe_{O_h}^{2+}$.

In conclusion, some comments and perspectives on this work can be discussed. For the $Fe_\alpha Ni_\beta Cr_\gamma O_4$ thin films growth, one zone has not yet been explored ($NiCr_2O_4$ samples with low iron content). The selection of a spinel-type substrate ($MgAl_2O_4$ with (001) or (111) orientations) has been a good decision for the elaboration of the $NiCr_2O_4$ stoichiometry, with the spinel structure. The XPS spectra should be more exploited. In particular, the Ni *2p* spectra present a different curve shape compared to the reference $NiFe_2O_4$ for several samples, with some spectra exhibiting a mix between Ni^{2+} in O_h sites and Ni^{2+} in T_d sites. Concerning the Fe *2p* spectra, the utilization of XMCD to obtain the cationic distribution can serve as a reference in the fitting of the XPS spectra, with contributions coming from the four iron species. The final objective of this kind of study is to obtain the cationic distribution with only the XPS spectra, thus elimination the need to perform XMCD experiments.

The XMCD L edges analysis can be completed with the implementation of 'constraint fit', which has been developed. This allows the study of the cationic environment of iron cations and its eventual deformation related to the substrate. It will necessitate the development of new parameters such as D_σ and D_τ in C_{3v} geometry for example. The study of the crystal field environment can be confirmed with the measure of in-plane and out-of-plane lattice parameters obtained in XRD. The chromium $L_{2,3}$ edges spectra were also roughly adjusted. A more precise analysis should help to better understand the O_h environment of this cation. This can be used in the better assessment of the cationic environment of the iron species.

The RXD experiments can be further detailed with complementary studies. It will be interesting to study the Ni K edge for peaks exhibiting solely a T_d contribution such as the (220) diffraction peak for samples exhibiting Ni^{2+} in T_d sites contribution in XMCD experiment. This approach will enable a clear distinction to be made between measure artefacts and the actual Ni^{2+} contribution in T_d sites.

Another experiment to perform on $Fe_\alpha Ni_\beta Cr_\gamma O_4$ thin films, specifically in the corrosion field, concerns the electrical resistivity measurement. One of the key parameter controlling the corrosion is the electrical conductivity of the intermediate layer between the alloy and the corroding environment. To assess these values, resistivity measurements as a function of the temperature, magnetic field, should be performed in the future. The understanding of the resistivity behavior and its correlation with the fine structure could be used later in

theoretical models. Magnetic fields favor the magnetic order within the crystal, which is in turn linked to the crystalline structure (phenomenon of magnetostriction in NiO, intrication of crystallographic and magnetic low-temperature transitions in $FeCr_2O_4$). In these stoichiometries, the magnetic field should not be disregarded.

In the spintronics context, this work should allow to better understand the magnetic properties of $Fe_\alpha Ni_\beta Cr_\gamma O_4$ thin films by carefully selecting the stoichiometries in nickel and chromium.

Spinel oxides containing Fe, Ni and Cr cations have also other potential applications in biomedical, catalyzer for organic synthesis, geology among other fields. In these different research fields, a comprehensive study from a microscopic to a macroscopic point of view is fundamental. For example, the addition of Mn in Fe_3O_4 nanoparticles results in greater rate of catalytic reduction of nitroarenes compounds[6]. We hope that this work will help other research fields.

7 CONCLUSIONS AND PERSPECTIVES

7.1 BIBLIOGRAPHY

(1) Arai, K.; Okuda, T.; Tanaka, A.; Kotsugi, M.; Fukumoto, K.; Ohkochi, T.; Nakamura, T.; Matsushita, T.; Muro, T.; Oura, M.; Senba, Y.; Ohashi, H.; Kakizaki, A.; Mitsumata, C.; Kinoshita, T. Three-Dimensional Spin Orientation in Antiferromagnetic Domain Walls of NiO Studied by x-Ray Magnetic Linear Dichroism Photoemission Electron Microscopy. *Phys. Rev. B* **2012**, *85* (10), 104418. https://doi.org/10.1103/PhysRevB.85.104418.

(2) Evans, R. F. L.; Fan, W. J.; Chureemart, P.; Ostler, T. A.; Ellis, M. O. A.; Chantrell, R. W. Atomistic Spin Model Simulations of Magnetic Nanomaterials. *J. Phys.: Condens. Matter* **2014**, *26* (10), 103202. https://doi.org/10.1088/0953-8984/26/10/103202.

(3) Evans, R. F. L.; Atxitia, U.; Chantrell, R. W. Quantitative Simulation of Temperature-Dependent Magnetization Dynamics and Equilibrium Properties of Elemental Ferromagnets. *Phys. Rev. B* **2015**, *91* (14), 144425. https://doi.org/10.1103/PhysRevB.91.144425.

(4) Jenkins, S.; Chantrell, Roy. W.; Evans, R. F. L. Atomistic Simulations of the Magnetic Properties of Ir x Mn 1 − x Alloys. *Phys. Rev. Materials* **2021**, *5* (3), 034406. https://doi.org/10.1103/PhysRevMaterials.5.034406.

(5) Kota, Y.; Imamura, H.; Sasaki, M. Strain-Induced Néel Temperature Enhancement in Corundum-Type Cr_2O_3 and Fe_2O_3. *Appl. Phys. Express* **2013**, *6* (11), 113007. https://doi.org/10.7567/APEX.6.113007.

(6) Ibrahim, I.; Ali, I. O.; Salama, T. M.; Bahgat, A. A.; Mohamed, M. M. Synthesis of Magnetically Recyclable Spinel Ferrite (MFe2O4, M = Zn, Co, Mn) Nanocrystals Engineered by Sol Gel-Hydrothermal Technology: High Catalytic Performances for Nitroarenes Reduction. *Applied Catalysis B: Environmental* **2016**, *181*, 389–402. https://doi.org/10.1016/j.apcatb.2015.08.005.